

SELECTIVE LASER SINTERING OF A STAINLESS STEEL POWDER

By
Carl Hauser BEng (Hons)

Submitted in accordance with the requirements for the degree of
Doctor of Philosophy

University of Leeds
School of Mechanical Engineering
Leeds, UK.

July 2003

The candidate confirms that the work submitted is his own and that appropriate credit has been given where reference has been made to the work of others.

To be conscious that you are ignorant
is a great step to knowledge.

Benjamin Disraeli Sybil.

ACKNOWLEDGEMENTS

The acknowledgements are the optional but essential part of this thesis because it allows thanks to go to those people that have helped and given their support during the years that go together to construct a PhD.

I would first like to thank my supervisor Professor Tom Childs for his help, guidance, encouragement and particularly patience during the practical works and, more importantly, during the writing of this thesis. Thanks must also go to Dr Kenny Dalgarno for his support and his views that gave a different, but valuable, direction of thought.

Technicians Phil Wood, Abbas Ismail and Dave Instrill also deserve recognition for their astonishing ability to turn thoughts, sketches and babble into anything you want, no matter how badly described or drawn (*which was more often than not*). Thanks must again be given to Phil Wood for giving me the chance to expel some of my energy by making me run around a squash court like a headless chicken (*I will beat you one day!*). Tony Wiese must also be acknowledged for his help in the metallography lab and to Mr. John Harrington (School of Materials) for his guidance during the preparation and capturing of images when using the Scanning Electron Microscope.

Paul Pilling must also be thanked for his work in constructing key aspects of the research SLS machine and to Radu Eane for his help in polishing some of my samples – not many people would have been persuaded to do that...I'll buy you that pint sometime! I must also acknowledge the Engineering and Physical Science Research Council (EPSRC) and to all collaborating companies of the joint EPSRC IMI aerospace „LastForm“ program for their funding.

I would also like to thank my parents for their support, both financial and personal, and for their encouragement over the last however many years.

Finally, thanks must go to my new wife, Katherine (June 10th 2000), who has given me so much while receiving so little from me during the writing of this thesis - I will love you forever XXXXX.

ABSTRACT

The research presented in this thesis was part of a larger collaborated project (LastForm Programme) to research engineering solutions for the rapid manufacture of large scale (0.5m – 5.0m in length) low, medium and high temperature tooling (from room temperature to 1000°C) for use in the automotive and aerospace industry. All research was conducted using small scale investigations but with a final discussion including implications of the work in future large scale planning.

The aim of the work presented in this thesis was to develop current understanding about the sintering and melting behaviour of metal powders by Selective Laser Sintering (SLS). The powder used in the research was an argon atomised austenitic stainless steel of type 314s HC. The powder was supplied in four batches, each differentiated by particle size distribution; -300+150 μ m, -150+75 μ m, -75+38 μ m and -38 μ m. The characteristics of each powder, in particular flow properties, differed considerably allowing powder handling and powder flow during melting to also be explored in this work. Three different environmental conditions were also investigated to assess the role of atmospheric and residual (powder) oxygen: (1) air atmosphere (control), (2) argon atmosphere and (3) argon atmosphere with argon percolation through the powder layer. In this, the design of an environmental control chamber and its integration into a research SLS machine was central to the work.

Experimental studies of the selective laser sintering/melting process on room temperature stainless steel 314s powder beds has been successfully carried out. The methodology was progressive; from tracks to layers to multiple layers. Single tracks were produced by melting the powder by varying laser power and scan speed. Results from experiments have been used to construct a series of process maps. Each map successfully charts the heating and melting behaviour of the irradiated powder. Behaviours can now be predicted with reasonable accuracy over a dense power and speed range, including laser powers up to 200W and scan speeds up to 50mm/s. The experiments also allowed melt pool geometries to be investigated. Three types of melt cross-section were categorised; flattened, rounded and bell shape. Flat tracks generally

occurred at low speed (0.5mm/s) but also occurred up to 4mm/s at lower power (77W). Rounded tracks occurred between 1mm/s and 4mm/s and had a much larger area than expected. In the rounded track regime tracks sink well into the powder bed. Powder to either side of a track collapses into it, leaving a trench surrounding the track. The admission of extra powder is thought to be one cause of increased mass. However, a remaining question that still needs answering is what causes the change from a flattened to a rounded track.

Values of laser absorptivity were also estimated from track mass per unit length data and from melting boundaries displayed within the process maps. The results showed that absorptivity changed considerably depending on the powder, process conditions and atmospheric conditions. Within an argon atmosphere an „effective“ absorptivity from mass data was estimated to range from 0.1 to 0.65, the lower value at low speed scanning (0.5mm/s) and the higher value from high speed scanning (>4mm/s). These values were much higher than expected for a CO₂ laser.

Melt pool balling was found to be a big problem, limiting the process speed at which continuous tracks could be successfully constructed (<12mm/s). Comparisons between a mathematical model developed in this work and experimental results suggested that balling within an air environment occurred when the ratio of melt pool length to width reached a critical value close to π . Balling within an argon atmosphere was more difficult to model due to higher viscous melts caused by the take up of surrounding powder.

Melted single layers were produced by varying laser power, scan speed, scan length and scan spacing or melt track overlap. Scan length proved to be a significant factor affecting layer warping and surface cracking. Provided the scan length remained below 15mm, layer warping could be largely avoided.

Multiple layer blocks were produced by melting layers, one on top of the other. They were constructed over a range of conditions by varying laser power, scan speed, scan spacing and layer thickness. Layer thickness was a crucial parameter in controlling the interfacial bond between layers, but the spreading mechanism proved to be the overriding factor affecting layer thickness and therefore the quality and density of the blocks.

TABLE OF CONTENTS

ACKNOWLEDGEMENTS.....	III
ABSTRACT	IV
TABLE OF CONTENTS.....	VI
LIST OF FIGURES	XII
LIST OF TABLES	XXII
NOTATION AND ABBREVIATIONS.....	XXIII
CHAPTER ONE.....	1
INTRODUCTION AND LITERATURE REVIEW	1
1.1 INTRODUCTION AND PROJECT OVERVIEW.....	1
1.2 DIRECT METAL LASER SINTERING: THEORY AND PROCESS OVERVIEW	4
1.3 PRE-ALLOYED METAL POWDER CONSOLIDATION.....	7
1.4 HEAT AND FLUID FLOW	10
1.4.1 Surface Tension Driven Fluid Flow	10
1.4.1.1 Effects on Melt Pool Shape and Melt Penetration	10
1.4.2 Aerodynamic Drag Forces.....	16
1.4.3 Buoyancy Forces	17
1.4.4 Summary	17
1.5 SCANNING PARAMETERS: EFFECTS ON MELT POOL SIZE, MELT POOL STABILITY AND	
DENSITY	19
1.5.1 Spot Diameter.....	19
1.5.2 Laser Power and Scan Speed.....	19
1.5.2.1 Melting in Absence of an Underlying Substrate	21
1.5.2.2 Melting to an underlying substrate.....	26
1.5.3 Scan spacing	29
1.5.3.1 Effects on Melt Pool Behaviour.....	29

1.5.3.2	Effects on Surface Morphology	30
1.5.4	Layer Thickness	34
1.6	OXIDATION: EFFECTS AND METHODS OF PREVENTION	35
1.6.1	Vacuum	37
1.6.2	Inert Gas	40
1.7	POWDER BED BEHAVIOUR.....	43
1.7.1	Powder Properties.....	43
1.7.1.1	Particle Size and Shape.....	44
1.7.1.2	Powder Packing Density.....	46
1.7.1.3	Powder Fluidity	46
1.7.2	Powder Deposition and Spreading	47
1.7.3	Laser Energy Absorption.....	50
1.7.3.1	Introduction	50
1.7.3.2	Coupling	50
1.7.3.3	Heat Penetration.....	52
1.8	SOLIDIFICATION MECHANISMS	53
1.8.1	Grain Structure	53
1.8.2	Heat Extraction.....	56
1.8.3	Solidification Control.....	59
1.9	SUMMARY OF BACKGROUND	63
1.10	AIMS AND OBJECTIVES OF THE THESIS.....	64
1.11	ORGANISATION OF THE THESIS	65
CHAPTER TWO		66
EXPERIMENTAL METHODS.....		66
2.1	INTRODUCTION.....	66
2.2	EXPERIMENTAL POWDER	68
2.2.1	Storage and Use.....	69
2.2.2	Preparation	69
2.2.3	Handling.....	70
2.3	EXPERIMENTAL APPARATUS	70
2.3.1	Selective Laser Sintering Equipment	70
2.3.1.1	Laser and Focussing Optics.....	71
2.3.1.2	X-Y Scan Head.....	75
2.3.1.3	Process Chamber and Powder Handling Apparatus.....	77

2.3.1.4	Motion Control Table	83
2.3.2	Pin fixture Array.....	84
2.3.3	Powder Mixing Equipment.....	85
2.3.4	Microscopy and Materials Preparation Equipment	86
2.3.5	Measurement Equipment.....	86
2.4	SCANNING AND SCANNING SOFTWARE.....	87
2.4.1.1	Scan Length and Laser Beam Offset.....	88
2.5	EXPERIMENTAL PROCEDURE.....	92
2.5.1	Scanning Conditions.....	92
2.5.1.1	Single Layer Test Conditions.....	94
2.5.1.2	Multiple Layer Test Conditions	94
2.5.2	Environmental Conditions.....	95
2.5.2.1	Air Atmosphere	95
2.5.2.2	Argon Rich Atmosphere	95
2.5.2.3	Argon Rich Atmosphere with Argon Percolation	96
2.5.3	Repeatability of Results.....	96
2.5.4	Reproducibility of Results.....	97
2.5.5	Dimensional Measurement.....	97
2.5.5.1	Single Tracks	97
2.5.5.2	Single and Multiple Layers.....	98
2.5.6	Sample Preparation for Microscopy Inspection	99
2.5.6.1	Powder.....	99
2.5.6.2	Melt Tracks.....	99
2.5.7	Measurement of Grain Size	99
2.5.8	Powder Mixing Procedure.....	100
2.5.8.1	Mixing Time Calibration	101
2.6	MACHINE CALIBRATION PROCEDURES AND RESULTS	103
2.6.1	Galvanometer and Beam Velocity.....	103
2.6.2	Laser Power.....	103
2.7	SUMMARY	105
CHAPTER THREE		107
RESULTS OF SINGLE TRACK MELT TESTS USING DIFFERENT ENVIROMENTAL CONDITIONS, SCANNING CONDITIONS AND POWDERS.....		107
3.1	INTRODUCTION.....	107

3.2	POWDER MIXING CALIBRATION RESULTS.....	107
3.3	POWDER MICROSCOPY RESULTS	110
3.4	SELECTIVE LASER SINTERING OF SINGLE TRACKS SCANNED IN AN AIR ATMOSPHERE... 113	
3.4.1	Qualitative Observations	113
3.4.2	Process Maps.....	127
3.4.3	Characteristics of the Melt Pool	135
3.4.3.1	Melt Pool Form.....	135
3.4.3.2	Width and Depth Changes	136
3.4.3.3	Mass Changes	144
3.4.4	Powder Trenching and Melt Pool Irregularities	145
3.4.4.1	Powder Trenching.....	145
3.4.4.2	Melt Pool Irregularities.....	147
3.4.5	Microscopy studies.....	150
3.5	SELECTIVE LASER SINTERING OF SINGLE TRACKS SCANNED IN AN ARGON ATMOSPHERE	
	157	
3.5.1	Qualitative Observations	157
3.5.2	Process Maps.....	164
3.5.3	Characteristics of the Melt Pool	171
3.5.3.1	Melt Pool Form.....	171
3.5.3.2	Width and Depth Changes	173
3.5.3.3	Mass Changes	186
3.5.4	Powder Trenching and Melt Pool Irregularities	188
3.5.5	Microscopy Studies	188
3.6	SELECTIVE LASER SINTERING OF SINGLE TRACKS SCANNED IN AN ARGON PERCOLATED	
	ATMOSPHERE.....	191
	CHAPTER FOUR.....	192
	SINGLE AND MULTIPLE LAYER CONSTRUCTION	192
4.1	INTRODUCTION.....	192
4.2	SINGLE LAYER BUILD STRATEGY.....	193
4.2.1	Layer Distortions and Methods of Reduction.....	193
4.3	SINGLE LAYER AIR ATMOSPHERE RESULTS.....	199
4.4	SINGLE LAYER ARGON ATMOSPHERE RESULTS.....	209
4.5	MULTIPLE LAYER EQUIPMENT AND BUILD STRATEGY.....	215
4.5.1	Powder Spreading, Deposition and Layer Displacement	215

4.5.2	Build Strategy.....	217
4.6	MULTIPLE LAYER RESULTS.....	219
CHAPTER FIVE.....		223
DISCUSSION AND CONCLUSIONS.....		223
5.1	INTRODUCTION.....	223
5.2	PRELIMINARY STUDIES.....	224
5.3	SINGLE TRACK EXPERIMENTS.....	224
5.3.1	Track Cross-Section Observations	224
5.3.2	Track Masses per Unit Length	226
5.3.3	Process Maps.....	228
5.3.4	Melting Boundary.....	230
5.3.4.1	Melt Pool Fragmentation and Balling Boundaries	234
5.4	MULTI-LAYERS AND SCALE UP.....	239
5.5	CONCLUSIONS.....	242
5.6	FUTURE WORK.....	243
REFERENCES.....		244
APPENDIX A		244
ENGINEERING DRAWINGS AND POWDER MIXING CALCULATIONS.....		244
A1 PISTON HEAD ASSEMBLY		244
A2 PIN FIXTURE ARRAY.....		248
A3 POWDER MIXER ASSEMBLY AND ROTATIONAL SPEED CALCULATIONS.....		249
APPENDIX B		252
HPGL SOURCE CODE		252
B1 AN EXAMPLE OF HPGL CODE		252
APPENDIX C		256
MACHINE PARAMETER SETTINGS AND BEAM VELOCITY CALCULATIONS		256
C1 MACHINE PARAMETER SETTINGS.....		256
C2 SCAN SPEED CALCULATIONS.....		257
APPENDIX D		260

10	MELT TRACK DIMENSIONAL AND MASS MEASUREMENTS.....	260
	D1 AIR ATMOSPHERE RESULTS.....	260
	D1.1 300/150 POWDER BATCH.....	260
	D1.2 150/75 POWDER BATCH.....	261
	D1.3 75/38 POWDER BATCH.....	263
	D1.4 38 POWDER BATCH.....	264
	D2 ARGON ATMOSPHERE RESULTS.....	266
	D2.1 300/150 POWDER BATCH.....	266
	D2.2 150/75 POWDER BATCH.....	268
	D2.3 75/38 POWDER BATCH.....	271
	D2.4 -38 POWDER BATCH.....	273
	APPENDIX E	276
	POWDER DENSITY DATA AND PARTICLE GRAIN SIZE MEASUREMENTS	276
	E1 POWDER BED DENSITY DATA.....	276
	E2 PARTICLE GRAIN SIZE MEASUREMENTS	279

LIST OF FIGURES

Figure 1.1: Schematic view of a typical selective laser sintering arrangement.	5
Figure 1.2: Range of laser processes mapped against power density per unit time (Steen, 1998).	5
Figure 1.3: Selective laser sintering scanning strategy and sign convention.	6
Figure 1.4: Shapes and geometrical parameters for (a) stable melt bead, (b) an unstable melt bead, (c) a perturbed bead maintaining with a constant contact angle and (d) a perturbed bead with arrested parallel contact lines.	9
Figure 1.5: Schematic diagram illustrating the Heiple-Roper theory for weld penetration. The views are in a direction normal to the direction of scan (Heiple and Roper, 1982).	11
Figure 1.6: The d/b ratio as a function of the linear energy (Mills et al., 1998), where LS is low sulphur, HS is high sulphur and MS is some middle value (medium sulphur).	12
Figure 1.7: A Visual definition of inter-run porosity when (a) melt tracks are shallow and (b) melt tracks are deep and narrow.	15
Figure 1.8: SEM images of laser sintered HSS surfaces using a scan speed of 1mm/s and a scan spacing of 0.15mm for (a) water atomised 100 μ m particles at 10W, (b) gas atomised 117 μ m particles at 10W, (c) water atomised 100 μ m particles at 30W and (d) gas atomised 117 μ m particles at 30W (Niu and Chang 1999a).	15
Figure 1.9: SEM images of laser sintered HSS surfaces using a scan speed of 1mm/s and a scan spacing of 0.15mm for (a) water atomised 32 μ m particles at 10W, (b) as milled 11 μ m particles at 10W, (c) water atomised 32 μ m particles at 30W and (d) as milled 11 μ m particles at 30W (Niu and Chang 1999a).	16
Figure 1.10: Single track building within (a) a deep powder layer and (b) on a solid substrate.	21
Figure 1.11: SEM images of single track melt pool cross sections showing fused powder agglomerates around their periphery. Tracks were produced using (a) gas atomised M2-117 powder at 50W and 10mm/s and (b) water atomised M2-94 powder at 40W and 10mm/s (Niu and Chang, 1999b).	22

Figure 1.12: Break up kinetics of the liquid cylinder (Singer, 1997).	25
Figure 1.13: SEM images of laser sintered single line tracks of gas atomised M2 High Speed Steel powders (117 μ m) using a CO ₂ laser with a spot size of 0.5mm. The laser power and scan speeds are; (a) 50W at 5.0mm/s, (b) 50W at 20mm.s, (c) 150W at 5mm/s and (d) 150W at 20mm/s (Niu and Chang, (1999b))......	25
Figure 1.14: The three generalised cross sections of single track melt bead profiles when bonded to a solid substrate (Steen, 1998).....	27
Figure 1.15: (a) single track width vs. scan speed, (b) single track width vs. laser power, (c) single track depth vs. scan speed and (d) single track depth vs. laser power (Yevko et al., 1998).....	28
Figure 1.16: Variations in single layer porosity with changes in laser power and scan speed (Niu and Chang, 2000).....	30
Figure 1.17: Model of overlapping process (Li and Ma, 1997).....	32
Figure 1.18: Surface roughness as a function of overlapping ratio (Li and Ma, 1996). 32	
Figure 1.19: Section profiles of overlapped cladding layers at some critical ratios (Li and Ma, 1996).	33
Figure 1.20: Section profiles of overlapped cladding layers at some critical ratios (Li and Ma, 1997).	33
Figure 1.21: Theoretical estimation of the position of the melt front during laser irradiation of a pre-placed powder layer (Steen, 1998).....	34
Figure 1.22: SLM processed nickel superalloy powder with (a) no powder conditioning and (b) after 12 hours vacuum conditioning at temperatures of 450°C (Wohlert et al., 1999).	38
Figure 1.23: Transverse cross-section showing a typical SLS processed nickel superalloy cylinder at the interface between bottom cap, side wall and core (Wohlert et al., 1999).	39
Figure 1.24: Microstructure of the wall of a HIP cylinder produced by SLS showing (a) columnar grains orientated vertically in the build direction and (b) equiaxed grains across the surface of a single layer. The height of each image is representative of seven layers (Wohlert et al., 1999).....	39
Figure 1.25: Sample cross sections of SLM parts made from (a) stainless steel 316L and (b) titanium (TiAl6V4) powders (Meiners et al., 1999).....	42

Figure 1.26: Micrographs showing single layer pads of stainless steel powder produced within an argon atmosphere using lasing conditions of (a) continuous wave at 20A and 15W, (b) pulsed at 20kHz at 20A and 10W, (c) pulsed at 40kHz at 20A and 11W (O'Neill et al., 1998).	42
Figure 1.27: Micrographs showing cross sections of blocks produced using twenty layers of 80 μ m thick. Average power 12W, speed 100mm/s, overlap 25% of beam diameter, laser pulse frequency of (a) 48kHz and (b) 53kHz (O'Neill et al., 1999).	43
Figure 1.28: A qualitative description of possible powder particle shapes (German, 1994).	44
Figure 1.29: SEM images of laser sintered high speed steel powders using laser powers of 50W and a scan rate of 5.0mm/s and a scan line spacing of 0.15mm. Particle sizes were: (a) as supplied form atomiser (full range), (b) 53 μ m - 150 μ m, (c)>150 μ m and (d) <38 μ m (Niu and Chang, 2000).....	45
Figure 1.30: Three solutions for powder deposition and spreading during SLS, based on (a) scraper blade, (b) counter rotating roller and (c) slot feeder (Van Der Schueren and Kruth, (1995).	48
Figure 1.31: Effects of layer position accuracy during powder compaction.	50
Figure 1.32: Absorptivity as a function of wavelength for normal incidence, smooth surface and at room temperature. Metals 1 are those with full inner electron shells (Au, Ag, Cu,...) and Metals 2 are transition metals (Fe, Ni, Cr,...) (Hügel and Dausinger, 1996).	51
Figure 1.33: Microstructure of cladding melt beads, in a direction normal to the direction of scan, showing evidence of epitaxial grain growth from attached satellite particles (Smugeresky et al., 1997).....	54
Figure 1.34: Epitaxial and columnar growth near the fusion line in an iridium alloy (Brody, 1986).	55
Figure 1.35: Supercooling in alloy solidification (a) stable interface and (b) unstable interface (Steen, 1998).	55
Figure 1.36: Representation of planar to equiaxed growth through changes in G/R (temperature gradient/solidification rate) and solute content C_o (Lancaster, 1999).	58

Figure 1.37: Plot of temperature gradient versus solidification rate and solidification morphology (Minkoff, 1986).	59
Figure 1.38: The macrostructure observed in flat sections of gas tungsten arc welds in low carbon steel (Lancaster, 1999).	61
Figure 1.39: The dependence of G/R (a) and T (b) versus dimensionless melt depth z/H at the interface in the plane $y = 0$: (1) $u = 0.8\text{mm/s}$, (2) $u = 1.7\text{mm/s}$ and (3) 3.3mm/s (Berjeza, 1995).	63
Figure 2.1: (a) Powder storage container, as supplied and (b) spent and mixed powder storage. A 6inch rule is pictured.	69
Figure 2.2: Schematic diagram showing the principle subsystems of the SLS research	68
Figure 2.3: Photograph showing the SLS apparatus used to melt powders in this study.	74
Figure 2.4: Photograph showing the laser head and BEZ 10 beam expander.	74
Figure 2.5: Photograph showing the UC-1000 laser controller with the additional potentiometer and numerical counter.	75
Figure 2.6: Photograph showing the X-Y scan head.	76
Figure 2.7: Schematic diagram of the X-Y scan head control system.	76
Figure 2.8: Schematic diagram of the process chamber.	80
Figure 2.9: Schematic diagram showing the passage of gas flow through the process chamber.	81
Figure 2.10: Schematic diagram and photographs of the power handling apparatus. .	77
Figure 2.11: Stainless steel pin fixture used for securing the first layer of a multi layer build.	84
Figure 2.12: V-cone mixer assembly used for mixing of powders.	85
Figure 2.13: Programme flow chart for HPGL file generation (Part A).	89
Figure 2.14: Programme flow chart for HPGL file generation (Part B).	90
Figure 2.15: Example scanning routines (a) single lines and (b) single layers.	86
Figure 2.16: Intended size and excess dimension due to beam offset.	92

Figure 2.17: Chart showing the scanning conditions used during the experimental works. Each node represents 1 of 374 different conditions.	93
Figure 2.18: Position of measurement for single tracks.	98
Figure 2.19: Area cross-sections of single lines for microscopic inspection.	100
Figure 2.20: Showing relative position and sample identity numbers of powder samples taken for mixing calibration.	102
Figure 2.21: Filling of nylon cup during powder density calibration.	102
Figure 2.22: Deviation of scan speed experimental results from calculated results. .	104
Figure 2.23: Calibration graph for manual laser power modulation. Error bars show 97% confidence limits.	106
Figure 2.24: Calibration graph showing laser power deviance during manual power modulation over an 18 month period.	106
Figure 3.1: Density variation with mixing time for (a) 300/150 powder batch, (b) 150/75 powder batch, (c) 75/38 powder batch and (c) 38 powder batch.	109
Figure 3.2: Particle shape and grain structure in powder batches (a/b) 300/150, (c/d) 150/75 and (e/f) 75/38.	112
Figure 3.3: Variation of grain size with particle diameter for particles contained within the 300/150, 150/75 and 75/38 powder batches. The calculated curve has been plotted with a constant of proportionality of 1.0.	113
Figure 3.4: Part A: Tracks melted in air atmosphere using 300/150 μ m powder batch at different scanning conditions.	115
Figure 3.5: Part A: Tracks melted in air atmosphere using 150/75 μ m powder batch at different scanning conditions.	117
Figure 3.6: Part A: Tracks melted in air atmosphere using 75/38 μ m powder batch at different scanning conditions.	119
Figure 3.7: Part A: Tracks melted in air atmosphere using -38 μ m powder batch at different scanning conditions.	121
Figure 3.8: Qualitative classification of the three types of solidification observed in the experimental works.	127
Figure 3.9: Process map for the 300/150 powder batch processed within a laboratory „air“ atmosphere.	131

Figure 3.10: Process map for the 150/75 powder batch processed within a laboratory „air“ atmosphere.	132
Figure 3.11: Process map for the 75/38 powder batch processed within a laboratory „air“ atmosphere.	133
Figure 3.12: Process map for the -38 powder batch processed within a laboratory „air“ atmosphere.	134
Figure 3.13: Melt pool dimensions as a function of scan speed and laser powder. Results for the 300/150 powder batch are shown.	137
Figure 3.14: Melt pool dimensions as a function of scan speed and laser power. Results for the 150/75 powder batch are shown.	137
Figure 3.15: Melt pool dimensions as a function of scan speed and laser powder. Results for the 75/38 powder batch are shown.	138
Figure 3.16: Melt pool dimensions as a function of scan speed and laser powder. Results for the -38 powder batch are shown.	138
Figure 3.17: Melt pool aspect ratio as a function of scan speed for the 300/150, 150/75, 75/38 and -38 powder batches.	141
Figure 3.18: Images showing melt track aspect ratio. All tracks were removed from powder beds containing the 150/75 powder size distribution. The Images are approximately at X8 magnification.	142
Figure 3.19: A plot showing contours of constant track width superimposed onto the process maps for the 300/150, 150/75, 75/38 and -38 powder batches.	143
Figure 3.20: Melt pool mass per unit length plotted as a function of laser energy density for the 150/75 and 75/38 powder batches. LS represents the Low Speed slope (0.5mm/s) and HS represents the High speed slope (>4mm/s).	144
Figure 3.21: Trench formation during SLS.	146
Figure 3.22: Stages of powder collapse and trench formation during SLS.	146
Figure 3.23: Melt pool irregularities during air melting.	147
Figure 3.24: Bobble formation in melt tracks produced using the 300/150 and 150/75 powder batches.	148
Figure 3.25: Bobble formation in melt tracks produced using the 75/38 powder batch.	149

Figure 3.26: Bobble formation in melt tracks produced using the -38 powder batch.	149
Figure 3.27: Bobble formation in melt tracks.....	149
Figure 3.28: Particle necking and consolidation (images a,c,e) and microstructure coarsening (images b,d,f) during melting of the 75/38 powder batch in air. The laser power was fixed at 50W and the scan speed changed from (a/b) 35mm/s, (c/d) 30mm/s and (e/f) 25mm/s.	153
Figure 3.29: Microstructure of melt tracks scanned at low power densities (typically 110W at 4mm/s).....	154
Figure 3.30: Microstructure of melt tracks scanned at medium power densities (typically 125W at 1mm/s).....	155
Figure 3.31: Microstructure of melt tracks scanned at high and very low power densities (typically 189W at 1mm/s).....	156
Figure 3.32: Percentage of columnar growth in melt tracks produced using the 300/150, 150/75 and 75/38 powder batches as scanning conditions change.	156
Figure 3.33: Tracks melted in an argon atmosphere using -300+150 μ m powder batch at different scanning conditions	160
Figure 3.34: Tracks melted in an argon atmosphere using -150+75 μ m powder batch at different scanning conditions	161
Figure 3.35: Tracks melted in an argon atmosphere using -75+38 μ m powder batch at different scanning conditions	162
Figure 3.36: Tracks melted in an argon atmosphere using -38 μ m powder batch at different scanning conditions.	163
Figure 3.37: Process map for the 300/150 powder batch processed within a argon atmosphere.	167
Figure 3.38: Process map for the 150/75 powder batch processed within a argon atmosphere.	168
Figure 3.39: Process map for the 75/38 powder batch processed within a argon atmosphere.	169
Figure 3.40: Process map for the 75/38 powder batch processed within a argon atmosphere.	170

Figure 3.41: Melt pool dimensions as a function of scan speed and laser powder. Results for the 300/150 powder batch are shown.	174
Figure 3.42: Melt pool dimensions as a function of scan speed and laser powder. Results for the 150/75 powder batch are shown.	175
Figure 3.43: Melt pool dimensions as a function of scan speed and laser powder. Results for the 75/38 powder batch are shown.	176
Figure 3.44: Melt pool dimensions as a function of scan speed and laser powder. Results for the -38 powder batch are shown.	177
Figure 3.45: Melt pool aspect ratio as a function of scan speed for the 300/150, 150/75, 75/38 and -38 powder batches.	179
Figure 3.46: Track cross sections: before and after image processing.	179
Figure 3.47: Images showing melt track aspect ratio. All tracks were removed from powder beds containing the 150/75 powder size distribution.	180
Figure 3.48: Images showing melt track aspect ratio. All tracks were removed from powder beds containing the 150/75 powder size distribution.	181
Figure 3.49: Images showing melt track aspect ratio. All tracks were removed from powder beds containing the 150/75 powder size distribution.	182
Figure 3.50: Images showing melt track aspect ratio. All tracks were removed from powder beds containing the 150/75 powder size distribution.	183
Figure 3.51: Images showing melt track aspect ratio superimposed onto the 150/75 process map.	186
Figure 3.52: Melt pool mass per unit length plotted as a function of laser energy density. LS represents the Low Speed slope (0.5mm/s) and HS represents the High speed slope (>4mm/s).	187
Figure 3.53: Typical examples of microstructure found in melt pools that exhibit a low melt aspect ratio.	190
Figure 3.54: An overview of typical microstructures found in melt pools that exhibit a „bell“ shaped cross section i.e. 110W to 143W at 4mm/s to 5mm/s in the 150/75 powder batch.	191
Figure 4.1: Layer distortions and solidification tearing in (a) a layer with a scan length of 80mm, (b) a layer with a scan length of 50mm and (c) a layer with a longer progression length of 60mm. All layers were produced with a scan spacing	

ratio, s_b , of 0.5, a laser power of 77W and a scan speed of 5mm/s. The atmosphere was argon.	194
Figure 4.2: Layers produced with a short scan length and a long progression length.	196
Figure 4.3: Distortions in layers created within an air atmosphere.	197
Figure 4.4: Layers with a short scan length, created within a argon atmosphere.	198
Figure 4.5: 150/75 single track process map showing superimposed regions of differing single layer melting behaviour. The map has been produced using a scan spacing ratio, s_b , of 0.25.	201
Figure 4.6: 150/75 single track process map showing superimposed regions of differing single layer melting behaviour. The map has been produced using a scan spacing ratio, s_b , of 0.5.	202
Figure 4.7: 150/75 single track process map showing superimposed regions of differing single layer melting behaviour. The map has been produced using a scan spacing ratio, s_b , of 0.75.	203
Figure 4.8: 150/75 single track process maps showing superimposed regions of differing single layer melting behaviour. The map has been produced using a scan spacing ratio, s_t , of 0.75 and 0.5.	207
Figure 4.9: Single layers produced at low power, with a 75% scan spacing as a percentage of beam diameter.	210
Figure 4.10: Single layers produced at high power, with a 75% scan spacing as a percentage of beam diameter.	210
Figure 4.11: Single layers produced at low power, with a 50% scan spacing as a percentage of beam diameter.	211
Figure 4.12: Single layers produced at high power, with a 50% scan spacing as a percentage of beam diameter.	211
Figure 4.13: Single layers produced at low power, with a 25% scan spacing as a percentage of beam diameter.	212
Figure 4.14: Single layers produced at high power, with a 75% scan spacing as a percentage of beam diameter.	212
Figure 4.15: Powder displacement during single layer scanning.	213

Figure 4.16: Layer delamination caused by oversized melt tracks at the start of each new layer.	214
Figure 4.17: (a) Misalignment and (b) rotation and skew of melted layers processed within deep powder beds. The shape should be that of a pyramid.	217
Figure 4.18: Layer building using supporting pins.....	219
Figure 4.19: Multiple layer block consisting of 18 layers.....	220
Figure 5.1: Variation of laser effective absorptivity, α^* , with powder particle size.	228
Figure 5.2: Generalisation of melting behaviour within an argon atmosphere.	229
Figure 5.3: Variation of α with powder particle size. Results calculated from slopes of melting boundaries a-a in air and b-b in argon.	232
Figure 5.4: (a) temperature field and heat balance around a moving heat source and (b) a simplified melt pool shape.....	235
Figure 5.5: Process map for the 150/75 powder batch processed in air showing the calculated boundary when $a = 9.65$ and $b = 14.68$	238

LIST OF TABLES

Table 2.1: Composition of the experimental material.....	69
Table 3.1: Temper colorations observed during the heating of the powder (Monypenny, 1954).	123
Table 4.1: Values of $s_t=0.25$, calculated from $s_t = \frac{s}{b} = 1.1 \times 0.25 / b$	208
Table 4.2: Values of $s_t = 0.5$, calculated from $s_t = \frac{s}{b} = 1.1 \times 0.5 / b$	208
Table 4.3: Values of $s_t=0.75$ calculated from $s_t = \frac{s}{b} = 1.1 \times 0.75 / b$	208
Table 5.1: Material property data used in calculations throughout this chapter.	227
Table 5.2: LS and HS boundary gradients and α^* values calculated from mass/length vs. P/U figures in Chapter 3.	228
Table 5.3: Calculated values of constant energy density along boundary line b-b on the air process maps and the boundary line a-a on the argon process map.....	230
Table 5.3: Values of α calculated from the a-a and b-b boundaries on the process maps in Chapter 3.	232
Table 5.4: Calculated values for constants, a, and, b, using experimental data obtained from the 150/75 process maps created using an air atmosphere.....	238

NOTATION AND ABBREVIATIONS

3DP	Three Dimensional Printing
3DP	Three-Dimensional printing
300/150	-300+150 μ m Powder Batch
150/75	-150+75 μ m Powder Batch
75/38	-75+38 μ m Powder Batch
-38	-38 μ m Powder Batch
DAC	Data Acquisition Controller
DSC	Digital Scanner Controller
DMLS	Direct Metal Laser Sintering
FDM	Fused Deposition Manufacturing
LOM	Laminated Object Manufacturing
LPS	Liquid Phase Sintering
LSB	General Scanning Units
RGA	Residual Gas Analysis
RP	Rapid Prototyping
RT	Rapid Tooling
SEM	Scanning Electron Microscope
SLA	Stereolithography
SLM	Selective Laser Melting
SLPR	Selective Laser Powder Remelting
SLS	Selective Laser Sintering
SPF	Super Plastic Forming
a	laser beam radius
b	melt track width
C_p	Specific Heat
d	melt track depth/diameter of powder mixer
$d\gamma/dT$	surface tension temperature coefficient

E_s	Specific energy density
F_c	centrifugal force
F_g	gravitational force
G	Temperature Gradient
H	minimum height of overlapped track
HAZ	Heat Affected Zone
I	welding current
k	overlap ratio
L	single layer length (y direction)/ length of traverse
m	mass of a single powder particle
m_L	mass per unit length of a melt track
n	number of repetitions
N	rotational speed of powder mixer/ number of grain boundaries
N_c	critical rotational speed of a cylinder powder mixer
N_o	optimal rotational speed of powder mixer
P	laser power
ρ	density of solid
$\bar{\rho}$	Average density
ρ_{powder}	Powder density
r	Particle Radius
R	Solidification Velocity
RP_L	Rayleigh-Plateau limit for stability
s	scan spacing (mm)
s_b	ratio of scan spacing to the beam diameter ($s/2a$)
s_t	ratio of scan spacing to the melt track width (s/b)
S	Length/diameter ratio of molten pool (w/d)
T	maximum height of overlapped track
T	temperature
u	scan speed
v	speed of melt front (y direction)
V	Volume
V	Welding arc voltage/rotational velocity of powder mixer

V	Rotational speed of mixer
w	Length of molten pool or length of solidified melt track (x direction)
w_c	Weight of cup
w	weight of powder
x,y,z	Cartesian coordinates in space (see Figure 1.3)
z	deposited layer thickness
z''	position of melt relative to powder layer surface
λ	Length of Liquid Bridge
ΔH	Change in Melt Bead Height
\bar{d}	grain size
\dot{q}	Heat Flux
γ	surface tension
α	Absorptivity
α^*	Effective absorptivity
τ	Growth Time of Liquid Bridge Disturbance
ϕ	laser spot diameter (2a)
θ	Liquid Contact Angle
σ	Surface Tension
h	Height Difference Between two Static Builds
h	Surface Heat Transfer Coefficient
K	Thermal Conductivity
L	Latent Heat
L_m	length of molten region
m^*	Track Mass per unit Length
P_b	Laser Power Conducted into Bed
P_m	Laser Power Conducted into Melt
S	Slenderness of a Liquid Bridge
T_m	Melt Temperature
T_o	Ambient Temperature
V	Volume of Powder Particle

CHAPTER ONE

INTRODUCTION AND LITERATURE REVIEW

Introduction and Project Overview

Conventional tool production techniques can be expensive and often slow, and therefore contribute significantly to the cost and lead times of product manufacture. In an attempt to address these issues, several existing Rapid Prototyping (RP) technologies are being developed further to exploit their construction speed and process flexibility for applications in direct tooling production. This phase of RP development, known as Rapid Tooling (RT), aims to initially support but then ultimately replace traditional tool making methods and bring about reductions in manufacturing lead times and cost.

RP technologies use a layer by layer material additive manufacturing methodology to build up shapes defined by a three-dimensional CAD model. The CAD model is numerically sliced into a stack of layers and each layer is sequentially converted into a physical layer and bonded to the preceding layer without the need for additional tooling or fixtures. In the Selective Laser Sintering (SLS) process, layers are created by melting a pre-placed powder, or partially melting a powder mixture by scanning an infrared laser beam. In the Laminated Object Manufacturing (LOM) process, cut to shape laminates are bonded together. In the Stereolithography process (SLA), a photosensitive polymer resin is cured, layer on layer, using a scanning ultraviolet laser beam. In Three-Dimensional Printing (3DP), layers are created from powders, onto which a traversing ink jet head prints a bonding agent. Tooling made by these methods can be used for the following (Childs et al., 1998; Radstok, 1999):

1. making sacrificial patterns for investment casting (SLA, SLS, LOM);
2. making polymer and ceramic based investment casting shells or patterns for sand casting directly (SLS, LOM, 3DP);

3. making injection moulding tooling from polymer/metal composites (SLA, SLS, 3DP); and
4. recently, for making injection mould and pressure die casting tooling directly from metal materials (SLS, LOM).

In response to the growth of RP for tooling applications the IMI/EPSRC LAST-FORM research programme was started. LAST-FORM is an acronym for: Large Scale Tooling For Rapid Manufacture. This project is a collaboration between three Universities (Leeds, Liverpool and Warwick), each with its own expertise in layer manufacturing, in researching routes for the rapid manufacture of tooling to be of use to four aerospace (BAe (MAD), BAe Airbus, Rolls Royce Plc and Short Bros. Plc) and one automotive industrial partner (Rover Plc), one CAD/CAM software developer (Delcam) and a machine manufacturer exploiter (Quantum Laser Engineering).

The project's aim is to develop strategies and to research engineering solutions for the direct rapid creation of tooling for prototype and small batch aerospace and automotive manufacture. Tooling requirements include sheet metal forming tools (room temperature at $\sim 75\text{MPa}$), plastics injection mould tooling ($250^\circ\text{C} - 350^\circ\text{C}$ at 200MPa) and tooling for Super Plastic Forming (SPF) and diffusion bonding of titanium alloys (900°C at gas pressures around 30MPa). In all cases, solutions must be practical for future scale up (tools ranging from $0.5\text{m} - 5.0\text{m}$ in length).

LOM techniques are investigated in the LAST-FORM programme as prime routes for RT due to their inherent relatively low materials cost, ease of materials handling and short fabrication time. This process, like many other RP technologies, is also capable of incorporating complex tooling features, including conformal cooling channels, which are otherwise difficult to fabricate by conventional means.

A feasibility study is also being developed to assess the impact of introducing thick sectioned ($3\text{mm} - 8\text{mm}$) laminate sheets into the LOM build cycle to help ease material handling issues when constructing larger tooling. Therefore, in supporting this research, slant laser cutting, laser cladding and welding techniques are also being developed to either avoid, remove or fill in the steps that are present on angled surfaces created by the thickness of the layers.

The LOM process, however, could prove ineffective as a method for producing high temperature tooling. Many adhesives and brazing alloys currently used to bond laminates have poor mechanical strength and low working temperatures. High temperature brazing materials, clamping methods or welding techniques could provide possible solutions but these techniques are either largely unproven, could disrupt tool alignment or increase the number of manufacturing stages respectively.

The expertise in RP at Leeds University is in the SLS process. Metal powder routes potentially offer more freedom of material choice and are likely to be more suitable for the more demanding high temperature tooling requirements. However, the proposed route of melting pre-alloyed powders is not without complications. Firstly, single stage, high density pre-alloyed powder consolidation is only feasible with full particle melting. This often produces a melt volume which is unpredictable and difficult to control, where the actions of surface properties and internal heat and fluid flow can cause melt pool balling, induce layer distortions, compromise accuracy and affect surface quality (Kruth et al., 1998a; Radstok, 1999). Secondly, the components produced are often porous, even with large melt volumes inter-run porosity can often be high due to the directional construction strategy and the cylindrical shape of the melt pool. Therefore, research on issues concerning changes in melt pool morphology and break-up kinetics are still taking place.

In supporting this research, it is important to identify conditions where the effects of surface tension forces can be controlled and melt pool morphology can be predicted, allowing the tailoring of melt pool shape. In this work, the aim of the research is twofold. Firstly, to provide a detailed empirical study that maps the melt history of a pre-alloyed stainless steel powder during laser exposure and to identify conditions where melt pool stability, repeatability and reproducibility can be maximised. Secondly, to apply the information presented in the maps and discuss construction strategies and equipment issues geared towards large scale tool production.

Direct Metal Laser Sintering: Theory and Process Overview

Figure 1.1 shows a schematic diagram detailing primary components of a typical SLS machine that is configured for use in Direct Metal Laser Sintering (DMLS). The process begins by spreading and levelling a thin layer of metal powder on top of a piston unit. Spreading usually occurs by traversing a rotating or counter-rotating roller across the build zone. This is generally the most popular method but other mechanisms are in use; a wiper blade or slot feeder being the most common (Van der Schueren and Kruth, 1995). The thickness of each deposited layer typically falls within the range of 50 μ m to 1.5mm. Its value is often constant throughout a build and is a parameter that plays an important part in affecting construction speed, part resolution and the quality and strength of the bond between layers.

Once environmental conditions have been achieved (see Section 1.6), an infrared laser beam, directed by a scanning mirror system, delivers power, P , to the powder bed surface to selectively reproduce the first numerical layer. The inherently rough surface of the powder layer improves laser absorptivity and so surface energy values required for melting are often lower than those used in other laser machining and laser welding processes. For comparative reasons, Figure 1.2 maps regional values of the laser power density per unit time used in a number of laser based machining, welding and surface marking processes; DMLS has been superimposed onto the figure. It illustrates the phase change (if any) associated with each process and the required energy (power density/interaction time) to produce this change.

However, care must be taken when considering the layout of this Figure. Firstly, SLA creates layers by photo-polymerisation and not through heating. Secondly, layers are often cured at scan speeds, u , in excess of 0.7m/s (3D Systems). Assuming a beam diameter, $2a$, of 0.3mm (3D Systems), calculations reveal that the interaction time ($P/2a.u$) is more likely to be two orders of magnitude lower than values given in Figure 1.2. It is therefore unclear whether this is an isolated error, or whether power density values displayed in Figure 1.2 are defined at some maximum depth of heat penetration rather than at the irradiated surface; the latter often being the method of choice..

Figure 1.3 shows the surface layer in plan. Every layer is reproduced by traversing the laser beam in a back and forth motion, creating overlapping tracks line by line. This technique, called raster scanning, allows for a progressive and systematic coverage of the powder bed surface. Other scanning routines have also been investigated, but layer geometry often dictates the benefits (Crawford, 1993) and therefore, alternative techniques are not discussed in this Thesis.

During rastering, the laser beam scans at a speed of u in the direction of $\pm x$, over the current layer width, w , (scan length), while indexing with a spacing, s , in the direction of $+y$. The rastering motion of the beam therefore develops a process front that moves in the $+y$ direction at a speed of v ; assuming negligible laser toggling transients. The effective diameter of the laser, or heat source width, is difficult to define because it will increase as the peak temperature it creates increases (including a heat affected zone). Therefore, the effective diameter is often equated to the beam diameter, $2a$, which can be measured using a beam profileometer.

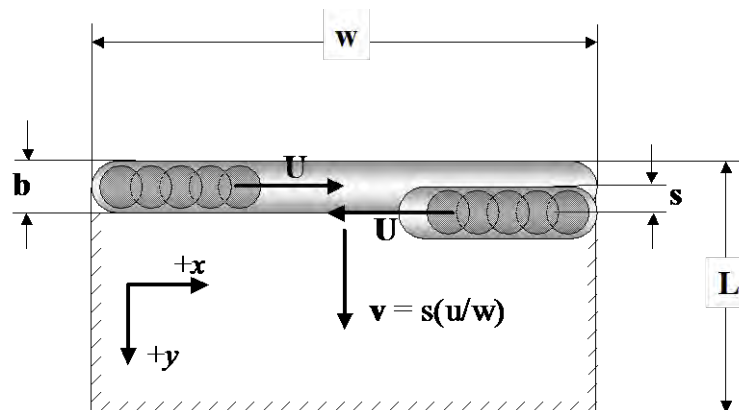


Figure 1.3: Selective laser sintering scanning strategy and sign convention.

Every time a new layer is to be added, both the melted and non-melted areas are moved downwards by one layer thickness and a new layer of powder is spread over the surface: building always occurs in the plane $z = 0$. Powder areas not sintered remain in position suspending and supporting the part at every level of its construction. When all layers in a build are complete, the supporting powder can be brushed away revealing the completed component.

Pre-Alloyed Metal Powder Consolidation

There are two approaches to metal powder consolidation by SLS. Both fall under the general heading of Direct Metal Laser Sintering (DMLS). The first method, and arguably the easier route, uses a mixture of two metal powders: a high melting point metal (structural material) and a low melting point „binder“ metal. Controlled heating of the metal powder mixture by the laser beam causes irradiated binder particles to melt and flow into surrounding porosity formed by the non-molten structural particles. This method of powder densification is known as Liquid Phase Sintering (LPS) (German, 1994). LPS is used extensively in conventional powder metallurgy processing where a strong literature database has been the driving force for this avenue of research (Kruth et al., 1998). However, this method of consolidation often creates an inhomogeneous component or green product with mechanical strength suitable only for further post processing i.e. metal infiltration or furnace sintering (Kruth et al., 1998; Lauwers et al., 1998a; Wieters et al., 1996). However, for large scale high temperature tooling infiltration would be impractical. The reasons are twofold. Firstly, achieving homogeneity of mechanical and physical properties during metal infiltration has been found to be extremely difficult. Stewart et al., (1998) demonstrated that material properties generally degrade with increasing distance from the point of infiltration. Stewart also added that infiltration is strongly time dependant with parts in excess of 2 inches thick (a negligible value when compared to the sizing requirements of LAST-FORM tools) would require special attention and increased infiltration times. For reference, the DTM default infiltration time of 1.5 hours at 1156°C is for a typical 6 inch square block with a 2 inch thickness (DTM Corporation, 1996). Secondly, tooling would be restricted by the working temperature of the binder particles or infiltrate.

The second DMLS materials route, known more specifically as Selective Laser Powder Remelting (SLPR) or Selective Laser Melting (SLM)¹ uses higher laser powers to create a conduction limited melt volume sourced from directly irradiated particles and from a large number of surrounding particles (Fuesting et al., 1996a/b; Niu and Chang, 1999a/b; Meiners et al., 1999; Abe et al., 2000). As the laser traverses the metal powder bed, surface tension forces localise the melt volume creating a series of highly dense

¹ This abbreviation will be used in this work.

tracks, each having an appearance analogous to deposited weld or clad melt beads (see Figure 1.4a (Steen, 1998; Yevko et al., 1998)).

However, the melt bead created may or may not be stable, depending on the processing and environmental conditions. For example, if processing speeds are high or if the melt is in contact with a cooler substrate or if there is an addition of solute oxygen (Mills et al., 1998; Steen, 1998; Meiners et al., 1999), then the melt bead will typically be unstable, and will quickly reshape itself into a series of sessile drops or balls, much like a liquid jet (Schiaffino and Sonin, 1997) (see Figure 1.4b). Other liquid and material problems may yield further different results: the bead may develop bulges but not separate into pieces (see Figure 1.4c/d), or it may show no signs of instability at all and remain perfectly uniform along its entire length (see Figure 1.4a). Generally speaking, the processing parameters and localised conditions act to determine the thermal profile and temperature time history of the localised melt pool which in turn affects melt pool behaviour and solidification. Furthermore, during pre-placed powder cladding, the collapse of powder into the melt volume plays an additional role (Steen, 1998).

The remainder of this chapter discusses the response of the melt pool to changes in the process conditions outlined above. Given the shortage of information in the SLM literature, this chapter also discusses and compares literature from welding, laser welding and laser cladding sources. It may, however, be beneficial to begin with a discussion on melt pool heat and fluid in order to help in the understanding of the effects of changing the process conditions.

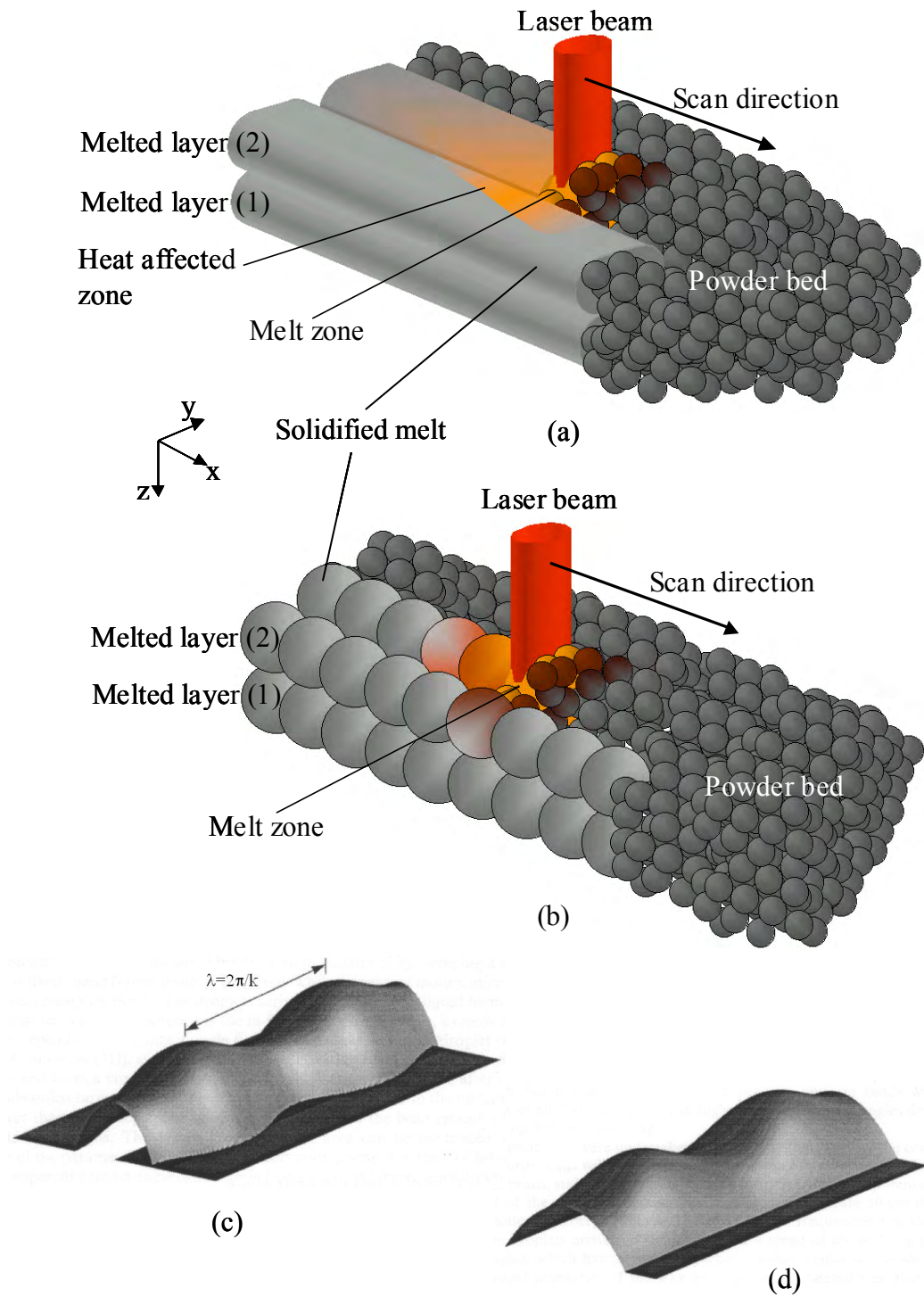


Figure 1.4: Shapes and geometrical parameters for (a) stable melt bead, (b) an unstable melt bead, (c) a perturbed bead maintaining with a constant contact angle and (d) a perturbed bead with arrested parallel contact lines.

Heat and Fluid Flow

1.1.1 Surface Tension Driven Fluid Flow

When an interface between two immiscible fluids is subjected to a temperature (or concentration) gradient, its interfacial tension will vary from point to point. These surface tension gradients will induce shear stresses that result in fluid motion. This will cause fluid to be drawn along the surface from regions of low surface tension (hot areas) to regions of high surface tension (cold areas) (Mills et al., 1998). Since liquids are viscous, they are dragged along causing bulk fluid motions and local reciprocal stirring of the melt pool; a phenomena commonly known as Marangoni convection.

Marangoni convection has been shown to trigger circulatory flows in weld pool deposits causing changes to the temperature gradient and cooling rate in the melt pool, and therefore affecting the solidification microstructure (see Section 1.8) (Welch, 1997). These flows also lead to changes in the depth/width ratio (d/b) of the melt pool and so Marangoni convection is often used as a measure to predict weld penetration into underlying layers (El-Batahgy, 1997; Mills et al., 1998).

1.1.1.1 Effects on Melt Pool Shape and Melt Penetration

Heiple and Roper, (1982) first developed the theories that weld penetration into a substrate is a result of differences in the fluid flow in the weld pool resulting from variations in the direction and magnitude of thermocapillary forces. Furthermore, they suggested that these were controlled by concentrations of surface active elements such as oxygen in the metal. Most pure metals and many alloys with low oxygen and sulphur contents exhibit a decrease in surface tension as the temperature increases, resulting in what is termed a negative surface tension temperature coefficient (Heiple and Roper, 1981/1990).

In such molten beads, the surface tension is at its maximum at the pool surface (the coldest part), and lowest under the heat source (the hottest part). Under these conditions, an outward fluid flow would result, producing a wide, shallow geometry (see Figure 1.5a). However, the additions of surface active impurities, sulphur and oxygen being the most notable in steels (Zacharia & David, 1993), can segregate

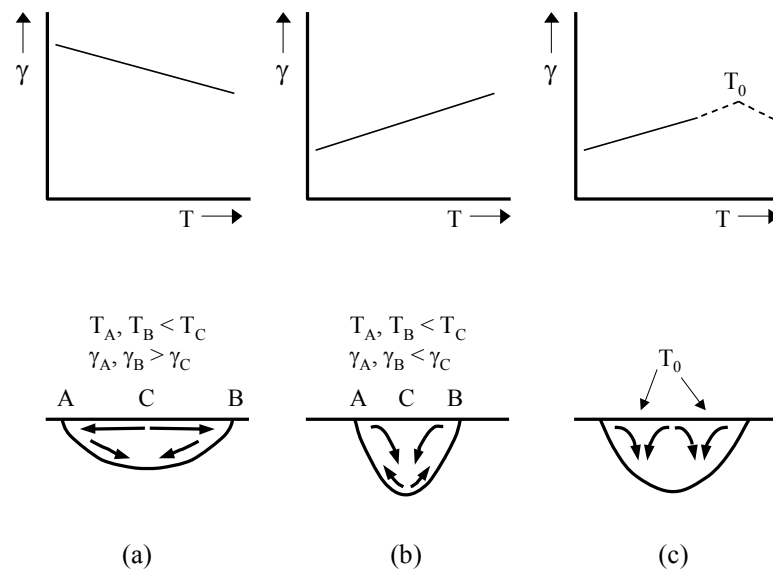


Figure 1.5: Schematic diagram illustrating the Heiple-Roper theory for weld penetration. The views are in a direction normal to the direction of scan (Heiple and Roper, 1982).

preferentially to the surface of the liquid alloy and lower the surface tension. Burgardt and Heiple, (1986) suggested that oxygen and sulphur concentrations exceeding ~ 50 ppm will change the temperature coefficient of surface tension ($d\gamma/dT$) from negative to positive. They further suggested that since a large temperature gradient exists between the centre and the edges of the weld pool, a large surface tension gradient will be produced across the surface. This will cause the surface tension to be greater in the high temperature region (at the centre of the pool) causing an inward fluid flow along the surface and down to the centre of the weld pool. This will transfer hot metal to the bottom of the weld pool resulting in a deep narrow weld (see Figure 1.5b). Systems which exhibit a positive surface tension temperature coefficient must go through a maximum at some temperature and thus produce a complex flow similar to that shown in Figure 1.5c. Therefore, a negative surface temperature coefficient only occurs for a limited range of temperatures above the melting point (Heiple and Roper, 1982;1990). Mills et al., (1998) also noted that Marangoni convection is only affected by the concentration of soluble oxygen and not the combined oxygen in the form of surface films. They added that surface films tend to suppress surface flows and thus produce stagnant regions at the edges of the weld pool.

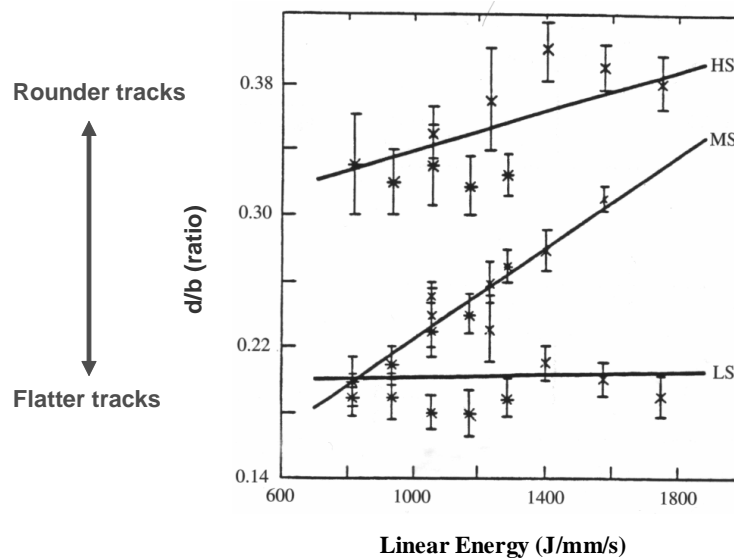


Figure 1.6: The d/b ratio as a function of the linear energy (Mills et al., 1998), where LS is low sulphur, HS is high sulphur and MS is some middle value (medium sulphur).

Mathematical models and empirical investigations have shown that the fluid flow in the weld pool is complex, despite the fact that thermocapillary forces tend to dominate (Ergy et al., 1998; Wahab et al., 1998; Longtin et al., 1999; Ricci et al., 1998). Nevertheless, on the basis of the Heiple-Roper theory some correlation between d/b and the temperature gradient ($\partial T/\partial x$) can be expected. Burgardt and Heiple, (1986) suggested that since Marangoni forces are typically dominant, the effects of altering welding conditions can be best explained in terms of the impact these changes would have on the temperature gradient. Therefore, any change which brings about an increase in the temperature gradient i.e. an increase in linear energy, would cause an increase in weld pool penetration depth (and a decrease in width) in high oxygen or high sulphur metals and increased width (and a decrease in depth) in low oxygen or low sulphur metals. Mills et al., (1998) agreed, and further suggested that the linear energy allows the effect of $I \cdot V$ and u on the Marangoni forces to be taken into account simultaneously, but they emphasised that this does not account for other forces that act in the weld pool; where, I , is the arc current and, V , is the voltage. Figure 1.6 shows these relationships. It illustrates the rate of change of the d/b ratio with linear energy and how this rate change alters with sulphur content. Mills also discusses that the change in

melt pool shape can be large with respect to its actual size, and hence the angle of contact between the melt and its substrate will also change (see 1.5.2.2).

On the basis of these experiments, Mills concluded that the temperature gradient ($\partial T/\partial x$) is related to the power input ($I \cdot V$), but added that the travel speed, u , primarily affects the rate of heat input and so it is this quantity that controls ($\partial T/\partial x$) (see also Sections 1.5 and 1.8). Mills added that these results are essentially in agreement with the earlier proposals by Burgardt and Heiple, (1986).

O'Neill et al., (1998) were the first to recognise that an awareness of weld pool heat and fluid flow could be the key to a better understanding of melt pool behaviour during SLM. They further cautiously added that changes in melt pool fluid flow may also help explain why large discrepancies are frequently found in the quality of fusion bonds between rastered tracks; though they admitted that at the time of writing no evidence could be found in their work or in the literature to support this claim.

In more recent experimental works, Niu and Chang, (1999a) concluded that Marangoni convection was the driving phenomena causing shape changes in melt pools that they had been observing. They reported that the d/b ratio of melt pools, in absence of an underlying substrate, changed from a wide shallow geometry to a deep narrow geometry when switching from gas atomised high speed steel powders to water atomised high speed steel powders. Niu and Chang argued that these shape changes were a direct consequence of a changing temperature coefficient of surface tension (from negative to positive) which was triggered by differences in the oxygen concentration of each powder being irradiated (200ppm in gas atomised powders and 1000ppm in water atomised powders). When referring to the concluding remarks made by Mills et al., (1998) (see page 11 of this thesis), Niu and Chang's results imply that the oxygen concentration of the powder dictates the amount of soluble oxygen in the melt and that more importantly, the change in soluble oxygen was sufficient to influence fluid flow behaviour in the SLM generated melt pool. Niu and Chang reported that the consequence of changing from a wide, shallow melt pool to one with a deep narrow geometry reduced the bond between neighbouring melt tracks causing an increase in inter-run porosity (see Figures 1.7, 1.8 and 1.9). This caused single layers to have a furrowed surface morphology. They also added that the problem of inter-run

porosity became particularly evident at higher laser powers ($>30\text{W}$) (see Figure 1.8c and Figure 1.9c/d). However, it is not clear in their work how the phenomena is affected by scan speed.

Niu and Chang also reported additional increases in inter-run porosity and directional surface morphology when irradiating two different batches of High Speed Steel (HSS) powder, both of which contained smaller particles (see Figure 1.9). One batch contained $32\mu\text{m}$ water atomised powder particles (see Figure 1.9a/c) and the other contained $11\mu\text{m}$ particles produced by milling a percentage of the first batch. They reported that residual gas analysis (RGA) revealed an oxygen concentration of 1700ppm for the first batch, but results for the second batch were not given. Nevertheless, it can be speculated that a smaller particle size, together with the milling operation, are likely to yield even higher oxygen concentrations (German, 1994). This would account for the additional increases in inter-run porosity observed by Niu and Chang when irradiating the latter powder. They therefore concluded that a positive surface tension temperature coefficient, invoked by residual oxygen and causing a deep narrow melt pool geometry, was a significant factor affecting surface morphology and inter-run porosity during SLM.

The Heiple-Roper theory makes two further important assumptions that strengthens the concluding remarks made by Niu and Chang. These assumptions are: (1) that the heat transfer in the weld pool is controlled by the fluid flow in the pool and not the heat conduction into the work piece and, (2) that Marangoni or thermocapillary forces are the dominant forces within a weld pool. The first of these assumptions suggests that observations of shape change triggered by Marangoni convection will occur irrespective of the locality of solid material and secondly, that other mechanisms known to affect melt pool behaviour, namely aerodynamic drag forces and buoyancy forces can be considered as negligible. Aerodynamic drag and buoyancy forces are briefly discussed in the following sections.

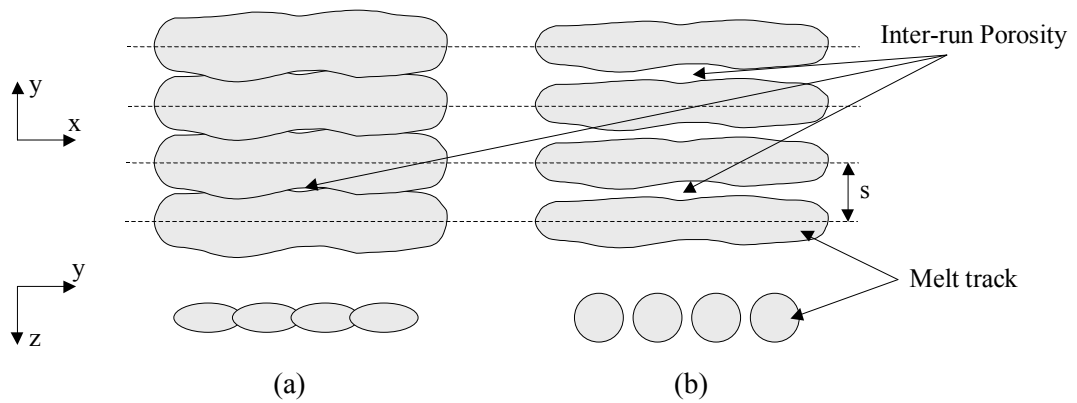


Figure 1.7: A Visual definition of inter-run porosity when (a) melt tracks are shallow and (b) melt tracks are deep and narrow.

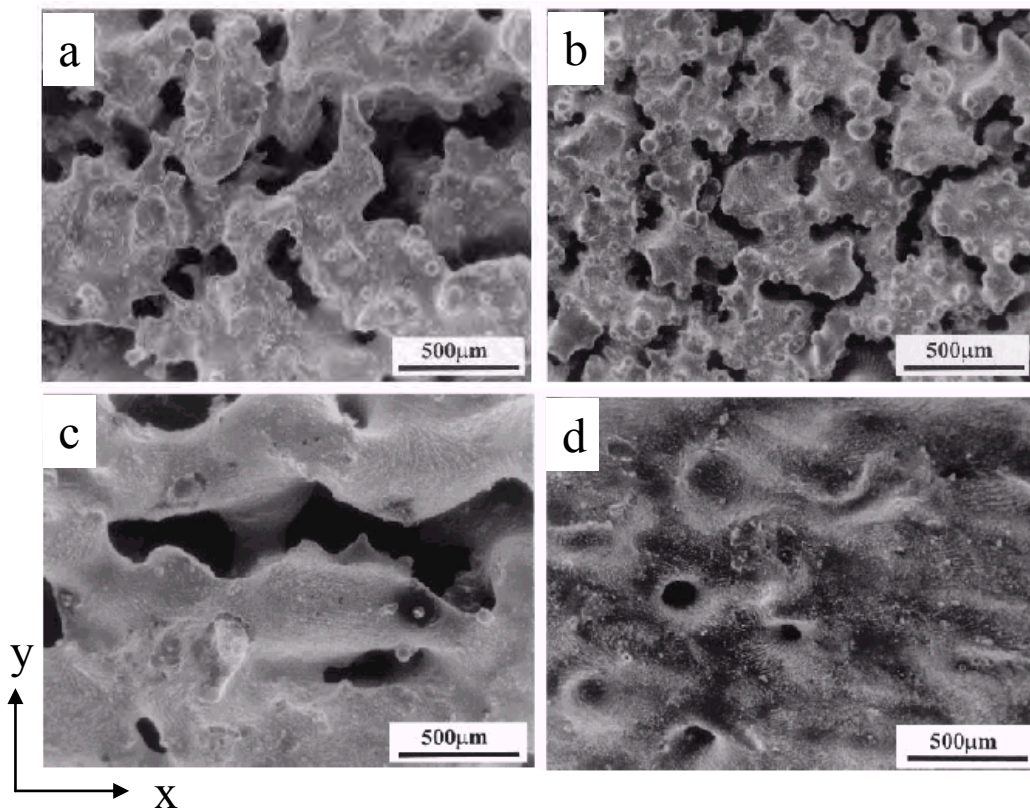


Figure 1.8: SEM images of laser sintered HSS surfaces using a scan speed of 1mm/s and a scan spacing of 0.15mm for (a) water atomised 100µm particles at 10W, (b) gas atomised 117µm particles at 10W, (c) water atomised 100µm particles at 30W and (d) gas atomised 117µm particles at 30W (Niu and Chang 1999a).

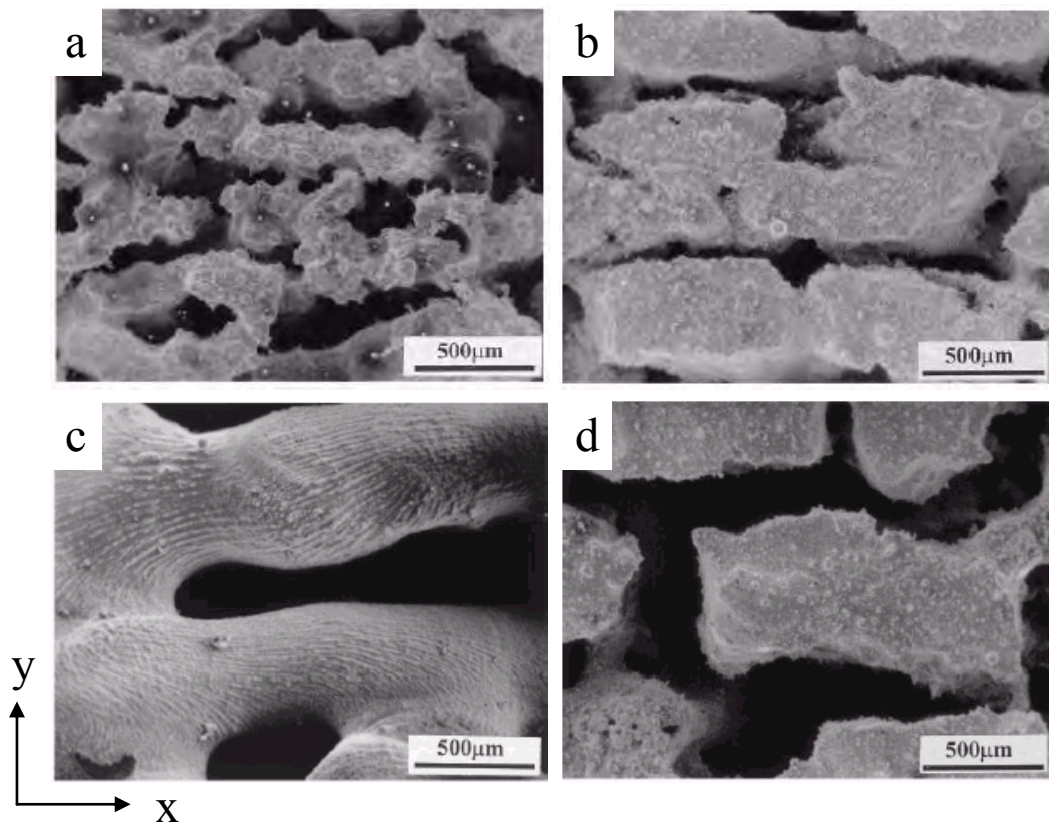


Figure 1.9: SEM images of laser sintered HSS surfaces using a scan speed of 1mm/s and a scan spacing of 0.15mm for (a) water atomised 32µm particles at 10W, (b) as milled 11µm particles at 10W, (c) water atomised 32µm particles at 30W and (d) as milled 11µm particles at 30W (Niu and Chang 1999a).

1.1.2 Aerodynamic Drag Forces

Aerodynamic drag forces during conventional arc welding can occur from frictional forces between the molten pool and the plasma stream. This frictional force produces very fast stirring and a rapid outward radial flow. The concept and potential of a plasma stream during SLM has been reported by O'Neill et al., (1998; 1999). They discussed that a laser operating in pulsed mode creates a plasma shock wave, directed towards the melt, which bombards the melt and causes geometry modifications. The process is currently somewhat hypothetical, and lacks physical interpretation, but the results are promising with reports of improved fluid flow that is creating layers with good surface quality and high levels of densification. However the occurrence of the

plasma stream, in a sufficient capacity to bring about change, is only thought possible when the laser operates in pulsed mode.

1.1.3 Buoyancy Forces

Buoyancy forces occur when the heat flux from the welding arc generates spatial and temporal density gradients in the molten bead which causes thermally activated driven flows. The hotter liquid metal (near the centre of a weld pool) under the influence of the buoyancy force floats up to the surface. The cooler liquid metal (near the pool boundary) has a higher density and so sinks to the bottom. This produces fluid flow on a weld pool surface. However, the radially outward driven flow is relatively slow and is suppressed by high cooling rates and is therefore thought to be the least dominate force in weld pools, especially when the melt pool is less than 10mm in depth (Welch, 1997; Mills et al., 1998).

1.1.4 Summary

The results presented by Niu and Chang are based on the extent of inter-run porosity rather than providing direct evidence of melt pool width and depth changes. Furthermore, because it is not clear how effective their protective atmosphere was, nor is there any evidence to suggest the use of a degassed powder, it is possible that their results were a product of poor wetting through oxide formation (as discussed by Abe and Osakada, 1996a) rather than through Marangoni convection. It is therefore unclear in their work whether Marangoni convection, surface oxidation or some combination of the two are responsible for increased inter-run porosity and reduced surface quality. Furthermore, the size and shape of powder particles used in their study varied considerably. Discussions in Section 1.7 reveal that changes in powder characteristics in addition to the amount of residual oxygen can also greatly influence melting.

Furthermore, if a positive surface tension temperature gradient can exist without significantly affecting the balance of surface energies i.e. reducing wetting, then providing any geometric changes are constant along the length of the melt pool, it is likely that inter-run porosity can be reduced by simply altering the scan spacing to maintain a smaller scan overlap. Therefore, if Marangoni convection is the singular

problem as implied by Niu and Chang, then scanning routines may compensate for geometry changes and the inherent problem may be easily controlled.

It is apparent that a large majority of current SLM literature considers Marangoni convection and related fluid flow phenomena to be a negative aspect of the process. However, discussions in Section 1.5.2 reveal that melt pool shape changes can also be advantageous, leading to surface quality improvements and reduced porosity during area coverage.

Scanning Parameters: Effects on Melt Pool Size, Melt Pool Stability and Density

1.1.5 Spot Diameter

Steen, (1998) discusses that the principle parameters in laser processing are power (P), scan speed (u) and spot size or spot diameter (2a), the most important is spot size. This acts in two ways; firstly, a decrease in spot size will increase the power density ($P/(\pi a^2)$) which increases energy absorption and secondly, a decrease will lead to a reduction in exposure area. Generally, a smaller spot size for a given power density allows for increased part definition during laser sintering, but will equally increase build time during area coverage (Miller et al., 1997). No literature could be found that discusses the effects of spot size on melt pool shape and stability.

1.1.6 Laser Power and Scan Speed

The overall effect of increasing power is to allow melting at faster speeds and/or greater depths of heat penetration. The faster the scan speed, the less time there is for heating and therefore, for a given laser power, less time for the heat to diffuse sideways, causing a narrowing of the melt region and heat affected zone. With a Gaussian laser beam there is a „sharpened pencil“ effect in that as the speed increases there becomes only sufficient energy at the tip of the Gaussian curve, or centre of the beam, to cause melting (Steen, 1998). To readdress the balance, a corresponding increases in laser power is required.

Because of this strong association between power and speed, a suitable way of expressing their influences on powder interaction is in the form of a compound variable which is referred to as the specific energy density (E_s) (Williams and Deckard, 1998), where:

$$E_s = \frac{P}{2a \cdot u} \quad \left(\frac{J}{\text{mm}^2} \right) \quad (1.1)$$

It is obvious from Equation 1.1 that the energy received at the powder surface will increase with increasing power or decrease with decreasing spot size and/or scan speed. Gedda, (2000) found Equation 1.1 to be a useful tool to compare the melting responses of different powders. However, he added that Equation 1.1 was rather limited as a universal predictor and instead only introduces a linear model that gives a semi-quantitative idea of the melting response. This is because a number of assumptions have to be made in order to arrive at its solution. These assumptions include (Miller et al., 1997):

1. There are no considerations of a melting model and so the physical and chemical properties of the material are assumed to be fixed;
2. The optical properties of the powder bed and melted areas are assumed identical and remain fixed throughout the duration of the build cycle (see Section 1.7.2);
3. Changes in layer geometry or vector length have no influence on the melting response;
4. There are no heat losses due to convection, conduction or radiation.

For the purposes of modelling, these assumptions often lead to a great many inaccuracies. However, despite these obvious drawbacks, changes in laser power and scan speed are often used to observe and correlate empirical data, allowing strong trends to be forged. It is these observations and trends that will now be discussed. Before this however, it is important to note that it is apparent in the literature that there are two approaches to the production of a single track melt bead; melting of pre-placed powder in absence of an underlying substrate (see Figure 1.10a) and melting of pre-placed powder on top of an underlying substrate (see Figure 1.10b). A substrate, in this case, refers to a consolidated or melted powder layer or a flat plate machined from solid. The former method presents itself when melting the first layer of an unanchored build or when constructing the first layer of any overhanging feature(s). The latter method presents itself when the aim is to overlay one layer with another to form a strong interfacial bond when building up layers. The first layer of a build is also often bonded to an underlying plate to form an anchorage point for successive layers. Since each approach affects melt pool behaviour differently, it is appropriate to channel forthcoming discussions accordingly. Here the former method is treated first.

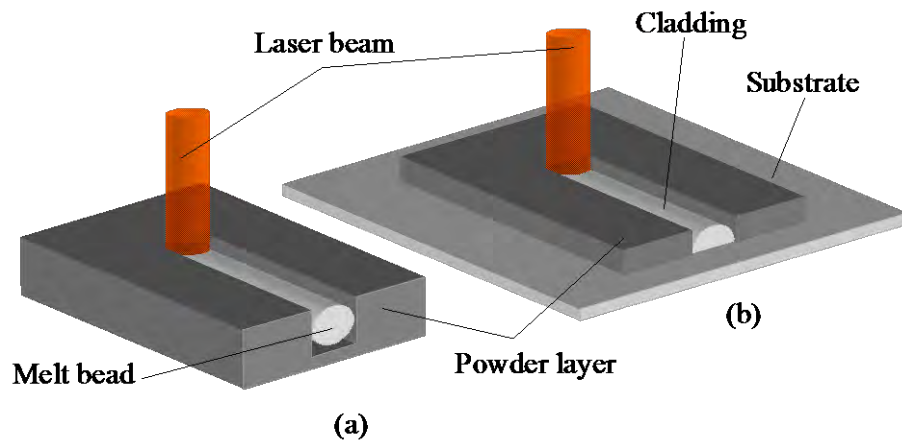


Figure 1.10: Single track building within (a) a deep powder layer and (b) on a solid substrate.

1.1.6.1 Melting in Absence of an Underlying Substrate

When the melt bead is supported by the surrounding powder (see Figure 1.10a), Abe and Osakada, (1996a), Karapatis et al., (1998) and Niu and Chang, (1999b) have reported that surface tension forces and surface tension driven fluid flows (see Section 1.4) dictate melt pool geometry and stability. Therefore, since surface tension forces are strong in liquid metals, the melt track will assume a form such that its surface area will be a minimum and its volume a maximum i.e. cylindrical in shape with an area cross section equal to that of an ellipse or circle. However, due to heat transfer and capillary flows, Niu and Chang found that a large number of surrounding particles will bond to the already molten core, and subsequently distort its final overall shape (see Figure 1.11). Niu and Chang further added that the strong surface tension forces will act to minimise the surface area further by breaking up the liquid bead into a series of balls (a shape where its surface area is a minimum and its volume a maximum). This phenomenon was found to be a major concern during early DMLS research (Manriquez-Fayre and Bourell, 1990;1991; Agarwala et al., 1995a). Nevertheless, Niu and Chang demonstrated, like Deckard and Miller, (1995) before them, that this problem could generally be controlled by maintaining a low scan speed. They reported that a continuous CO₂ laser scanning at speeds lower than 20mm/s was sufficient to suppress

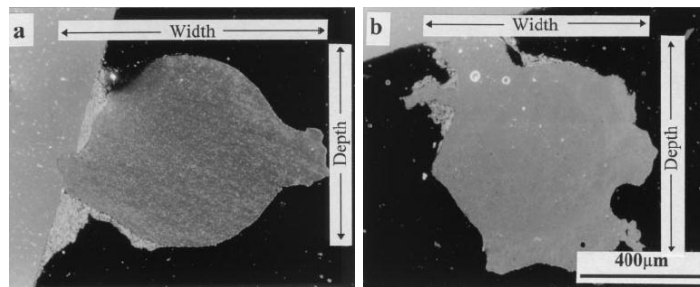


Figure 1.11: SEM images of single track melt pool cross sections showing fused powder agglomerates around their periphery. Tracks were produced using (a) gas atomised M2-117 powder at 50W and 10mm/s and (b) water atomised M2-94 powder at 40W and 10mm/s (Niu and Chang, 1999b).

balling in a HSS over a power range not exceeding 80W. At greater powers balling was again difficult to control. These observations also held when processing a number of different powder batches fabricated by different means (gas atomisation, water atomisation and milling). Although, they added that balling became more difficult to control when irradiating powders containing smaller particles, they speculated that these problems occurred due to Marangoni convection, triggered by the high oxygen content of the powder and the high linear energy respectively, and causing a radially inward driven fluid flow (see Section 1.4). However, they further added that both problems could be easily solved by simply reducing the temperature gradient within the melt i.e. reducing power or increasing scan speed, with the required size of the reduction increasing with decreasing particle size; although a large increase in speed would again trigger balling.

With further testing, Niu and Chang also found that a reduction in scan speed could also suppress balling when irradiating powders at high laser powers. However, since this action would increase the temperature gradient in the melt, it would seem that this method would only appear viable in a low oxygen environment where the effects of the parameters which trigger circulatory flows are seemingly reversed (see Section 1.4.1.1). Despite these latter observations, which currently lack a full understanding in the SLM literature, Niu and Chang argued that balling could generally be expected when the diameter of the melt was small, since the melt diameter substantially reduced at high scan speeds. Niu and Chang furthered this discussion by suggesting, like others

before them (Gratzke et al., 1992) that the balling phenomena of a liquid cylinder closely follows Plateau's theory on the collapse of cylindrical structures.

In the 18th century Plateau, and later Raleigh, found that a neutrally buoyant liquid bridge is stable to small perturbations as long as its length, λ , is less than its circumference $2\pi r$, such that; (see Figure 1.13a)

$$\lambda < 2\pi r \quad (1.2)$$

If in the case the wave length exceeds the circumference of the cylinder instabilities will commence and the perturbations will be begin to grow. Eventually the cylinder will break up into a series of droplets. Furthermore, the analysis provides a growth time, τ , of that disturbance which grows fastest where

$$\tau = 3\sqrt{\frac{\rho}{\sigma}} r^3 \quad (1.3)$$

where, ρ , is the liquid density and σ is the surface tension. Note that $\sqrt{(\rho/\sigma)}r^3$ is a characteristic time constant whenever surface tension is the dominant driving force. In laser welding it also characterises the collapse of a keyhole after the laser is switched off (Gratzke et al., 1992). If we assume the weld bead to have the shape of a cylinder, and associate the wavelength, λ , of the disturbance with the length of the molten region in the weld pool, then for stability, $S < \pi$ where $S = \lambda/2r$. Hence S is often known as the slenderness of the bridge (Burcham et al., 1998). When $\lambda/2r = \pi$ the liquid bridge becomes unstable and breaks. This critical condition is known as the Rayleigh-Plateau limit (RPL) or pinch effect (Marr-Lyon et al., 1998). Since a liquid bridge is a liquid mass supported solely by capillary forces (surface tension and wetting constraints), a liquid cylinder will tend to minimise its surface area by forming spheres. As the liquid cylinder grows in length, surface tension forces cause the cylinder to take a form similar to that of an hour glass (see Figure 1.12b). Due to high curvature stresses in the neck

region and an increased internal pressure due to the contracting diameter, the liquid cylinder will become unstable and will fragment when the length of the cylinder reaches RP_L (see Figure 1.12c). Often, smaller spheres will form between the larger spheres due to the neck region forming further independent liquid cylinders (Singer, 1997). This formation is called a spider web structure and has been observed in early metal SLS studies (Deckard and Miller, 1995).

Results presented by Niu and Chang, appear to agree with Raleigh's theory, although their concluding remarks that the diameter of the melt is the critical factor appear a little misleading. To explain, Figure 1.13 shows examples of their results and implies that tracks produced at conditions of 50W and 5mm/s and 150W and 20mm/s, giving specific energy densities of 20J/mm^2 and 15J/mm^2 respectively (with a spot diameter of 0.5mm), are of a similar size, yet only the track produced at the higher scan speed showed signs of balling. Nevertheless, it is possible for the faster travelling melt front to have an extended molten region, hence the condition $\lambda/2r = \pi$ is met and the melt front will solidify into a series of balls.

Earlier discussion by Abe and Osakada, (1996a/b) agreed with the results presented by Niu and Chang, (1999b). However, they also suggested that since balling was difficult to control at high linear energies, the apparent increase in surface tension related activity is likely to be linked to a lower melt viscosity, though they failed to prove this experimentally. Also, this argument disagrees with Niu and Chang's results presented above. Nevertheless, Abe and Osakada speculated that a pre-alloyed powder when melted to a mushy state i.e. in the region of its phase diagram bounded by the solidus and liquidus lines, would resist tendencies to ball because of increased melt viscosity caused by the precipitation of solid from the liquid. They concluded that it would therefore be beneficial to heat a pre-alloyed powder to a temperature which just exceeds its melting point, presumably however, provided the scan speed remains low.

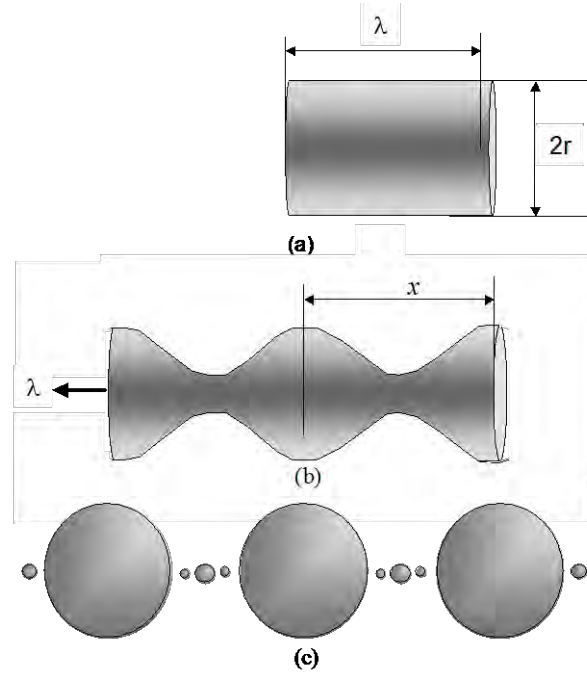


Figure 1.12: Break up kinetics of the liquid cylinder (Singer, 1997).

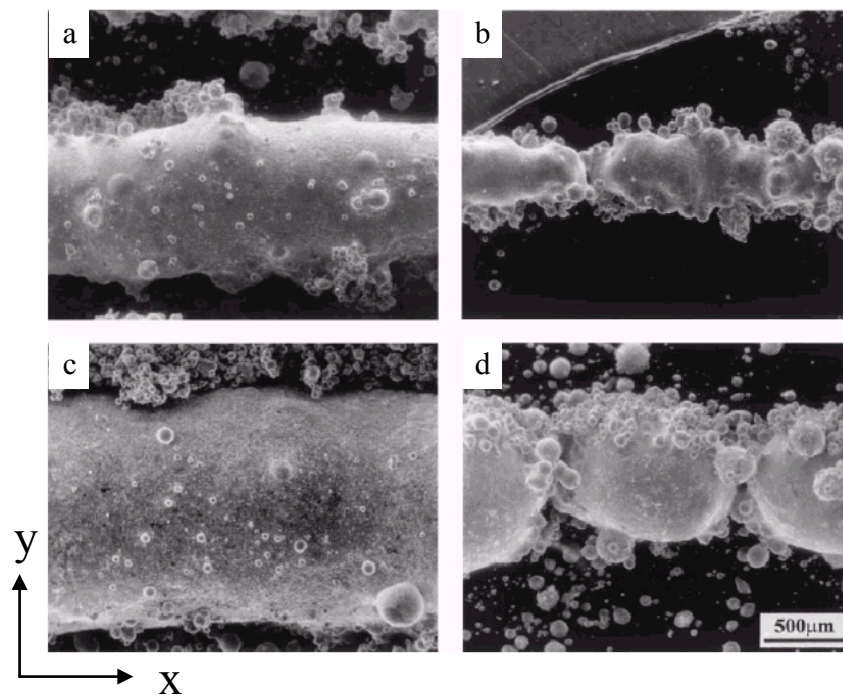


Figure 1.13: SEM images of laser sintered single line tracks of gas atomised M2 High Speed Steel powders (117 μm) using a CO₂ laser with a spot size of 0.5mm. The laser power and scan speeds are; (a) 50W at 5.0mm/s, (b) 50W at 20mm/s, (c) 150W at 5mm/s and (d) 150W at 20mm/s (Niu and Chang, (1999b).

1.1.6.2 Melting to an underlying substrate

When the melt bonds to a flat underlying substrate, Steen, (1998) reported that the shape of a single track clad bead can be summarised by three general area cross sections (see Figure 1.14). For rastering to be achieved without porosity between tracks the angle θ (wetting angle) must be acute, as shown in Figure 1.14a; this can be defined by the aspect ratio (depth/width). If the energy density is extremely high then a strong fusion bond with the underlying layer can be achieved for a given powder layer thickness (see Figure 1.14b). Steen further discusses that the strength of the fusion bond is primarily dependant on Marangoni convection (See Section 1.4.1.1) and heat penetration.

When the scan speed is extremely high, and often, when the laser power is low, a discontinuous melt bead will occur (balling). This phenomena forms through insufficient wetting due to poor heating of the substrate. A wetting liquid has a small contact angle θ , defined by the equilibrium of surface energies (German, 1985);

$$\gamma_{SV} = \gamma_{SL} + \gamma_{LV}\cos(\theta) \quad (1.4)$$

where γ_{SV} is the solid-vapour surface energy, γ_{SL} is the solid-liquid surface energy and γ_{LV} is the liquid-vapour surface energy. If a balance of these surface energies creates a large contact angle θ (wetting angle), then the liquid will not spread and wet the solid surface (see Figure 1.14c). Schiaffino and Sonin, (1997) also discussed that the stability of the bead also depends upon the boundary conditions at its contact line. Davis, (1980) used a linearised hydrodynamic theory to derive sufficient conditions for stability for three cases: (a) beads whose contact angle, θ , remains fixed at an equilibrium value while the contact lines are free to move, as in Figure 1.4c; (b) beads whose contact angle depends on the contact line speed, but reduces to an equilibrium value at zero speed, and (c) beads whose contact lines are arrested in a parallel state while the

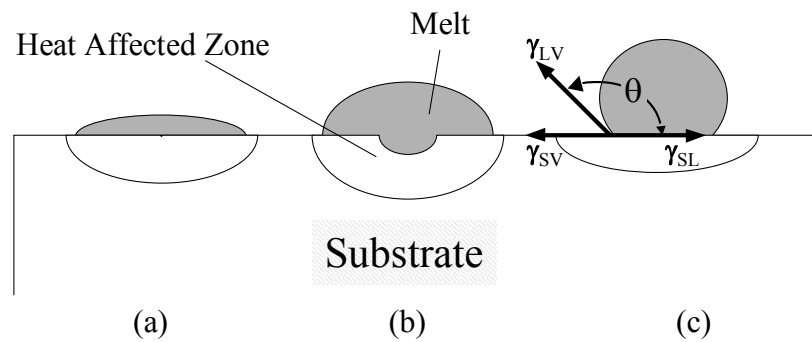


Figure 1.14: The three generalised cross sections of single track melt bead profiles when bonded to a solid substrate (Steen, 1998).

contact angle is free to change, as in Figure 1.4d. Davis showed that, like Raleigh's liquid cylinder, cases (a) and (b) will always be unstable at some disturbance wavelengths, but that case (c) will be stable if $\theta < \frac{1}{2}\pi$. Furthermore, Schiaffino and Sonin, (1997) observed severe undulations on the surfaces of melt pools when $\theta > \frac{1}{2}\pi$. These undulations have been observed by numerous authors, including Gratzke et al., (1992) during welding processes where this disturbance phenomenon is known as humping. Humping again appears to occur at higher heat inputs and/or higher scanning speeds, and are thus thought to be strongly associated with Raleigh's theory of instability (Gratzke et al., 1992). On the other hand, Mills and Keane, (1990) proposed Marangoni convection as the underlying physical mechanism for humping. However, their suggestion that the entire flow in the weld pool is determined solely by the increase of surface tension with temperature in the range 1440°C to 1800°C appears somewhat extreme in view of the fact that the surface of the weld pool will not lie entirely in this range, but can reach 3300°C near the central region of the pool where the surface tension is likely to decrease with temperature. Their conjecture also suggests humping even for a stationary arc, but this has not so far been observed. Therefore, Gratzke et al., (1992), concluded that humping cannot be fully explained as surface elevation due to Marangoni convection. However, Marangoni flow as a substantial contributor to the fluid flow in a weld pool is a totally different matter, and certainly has an impact of weld pool shape and therefore may be indirectly related to the humping phenomenon.

For a continuous melt bead, Yevko et al, (1998) demonstrated that the change in the width of the melt pool was almost linear with changes in both power and scan speed (increasing with increasing power and decreasing speed) (see Figure 1.15a/b). As they predicted, a similar relationship was also observed for the height of the bead. However, at very high laser powers the relationship changed and the height was found to decrease with further increases in power (see Figure 1.15c/d). They tentatively suggested that this sudden drop in height was caused by an insufficient volume of powder for melting, since the width was still increasing. They admitted that there was no evidence for this theory, yet they thought it appeared to be a logical explanation since the volume of powder available for melting is fixed, and so would choke expansion of the melt pool at high energy densities. However, it would also seem equally probable that a similar occurrence would occur at low scan speeds, since at low scan speeds the energy density is also very high, but this is clearly not shown in the results by Yevko.

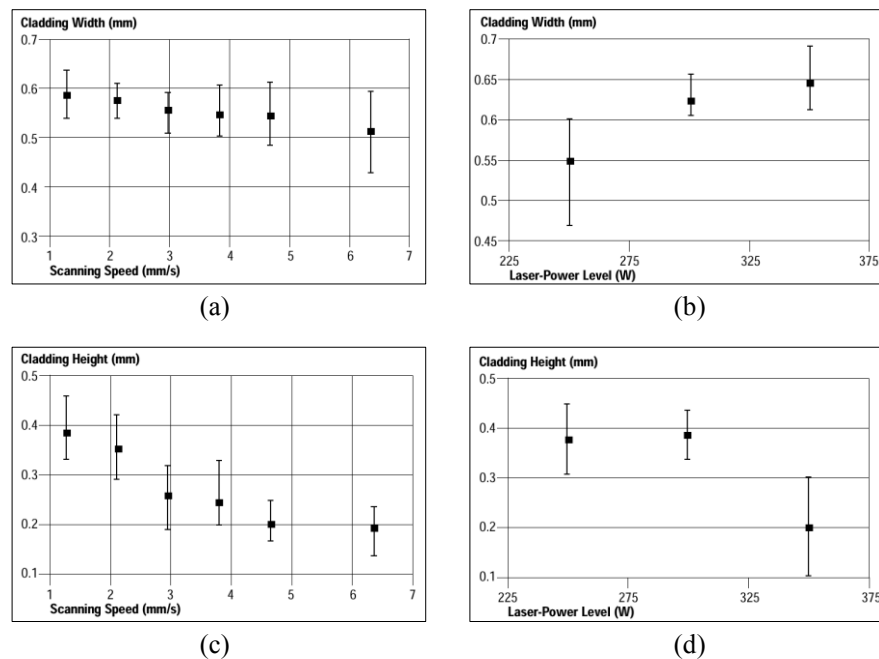


Figure 1.15: (a) single track width vs. scan speed, (b) single track width vs. laser power, (c) single track depth vs. scan speed and (d) single track depth vs. laser power (Yevko et al., 1998).

1.1.7 Scan spacing

If area coverage is to be achieved, overlapping of melt pool tracks will have to take place. Research concerning the selection and optimisation of the overlapping ratio (scan spacing) to achieve uniform density and track layer thickness has been well documented and some of this research will be reviewed in this section. However, more important to the work of this thesis is the understanding of melt pool behaviour during overlap. This is an area containing little research. Nevertheless, there are some general observations that have been made, and it is these observations that will be discussed first.

1.1.7.1 Effects on Melt Pool Behaviour

Niu and Chang, (2000) reported that high levels of porosity within a single layer generally occurred at conditions where single tracks were found to ball i.e. at high scan speeds (see Section 1.5.1.1), implying that both a rastered and unrastered spot influences the behaviour of the melt in much the same way. They constructed a process map which summarises, for a scan overlap of 0.15mm, the change in surface morphology of a single layer melted using a range of laser powers (0 - 100W) and process speeds (1.0mm/s – 36mm/s) (see Figure 1.16). The map consists of five zones (Z1 – Z5), with each zone representing a different, and presumably generalised, mode of solidification; (Z1) interconnected porosity (predominantly occurring at temperatures below the melting point), (Z2) inter-run porosity, (Z3) a highly dense structure but with small areas of isolated porosity, (Z4) a highly dense structure but with large areas of isolated porosity and (Z5) a fully dense structure with no porosity. Z1 covers an area bounded by low laser powers (<20W). Furthermore, and to some surprise, this boundary is shown to be impervious to changes in scan speed. With increasing power, Z4, Z3 and Z2 occur next with Z4 occurring at low scan speeds (<6mm/s) and low laser powers (<40W), Z3 primarily covers an area mapped out by an intermediate speed and power range (6mm/s – 26mm/s and 20W - ~70W) but extending to a higher speed range at higher laser powers and Z2 is concentrated over a high scan speed range (>16mm/s). Finally, zone 5 covers a large scan speed range at powers above 40W. Within this regime, the speed range increased with increasing power.

Since Niu and Chang argued that melt pool balling was the key to single layer porosity, then it would appear possible to gauge the effects that rastering has on melt behaviour by comparing Figure 1.16 with melting results obtained when traversing an unrastered spot (see Sections 1.4.1 and 1.5.2). Such comparisons reveal large differences in the speed and power range over which balling takes place. In Section 1.5.2 it was reported that Niu and Chang had discussed that balling could generally be controlled at speeds below 20mm/s and laser powers below 80W. However, in Figure 1.16 it is clear that a single layer can be produced without porosity (and therefore without balling) over a much larger speed and power range (up to 30mm/s at 100W). This would seem logical since the behaviour of the melt changes when it comes into contact with an underlying substrate (see Sections 1.5.2.1 and 1.5.2.2).

1.1.7.2 Effects on Surface Morphology

Li and Ma, (1997) found that a strong relationship exists between the surface roughness, scan spacing and clad height. In their simulation, a series of clad melt beads were assumed to be symmetrically parabolic in shape and deposited onto a solid substrate. The overlapping process was described as that schematically shown in Figure 1.17, where T is the maximum height of the overlapped track, H is the minimum height of the overlapped track, s is the scan spacing, d and b are the depth and width of the first

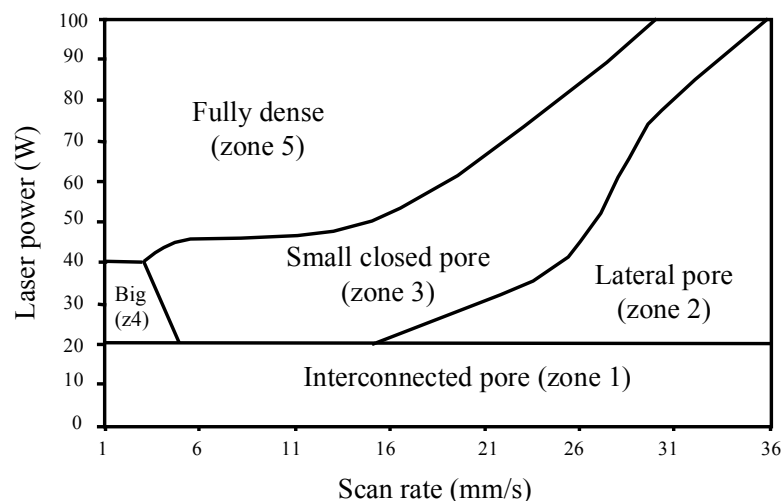


Figure 1.16: Variations in single layer porosity with changes in laser power and scan speed (Niu and Chang, 2000).

clad track respectively (control) and k is a scan overlap parameter depicting the overlapping ratio ($k = (b-s)/b$). It was found in their analysis that surface roughness was dependant on the height, d , and the overlapping ratio, k , but independent of single clad track width, b . Figure 1.18, shows the relationship between the surface roughness, $\Delta H/d$ ($\Delta H = T - H$), and k . It illustrates that the surface roughness is oscillatory in nature with a maximum surface roughness occurring at $\Delta H = d(1 - k)$ i.e. at overlapping ratios of 50%, 66%, 75% etc.

In contrast, when $\Delta H = 0.24d(1 - k)$ the surface roughness was found to be a minimum i.e. at overlapping ratios of 29.3%, 59.2%, 71.7% etc. Figure 1.19, shows these results graphically, which were later verified with an empirical study observing changes in surface roughness of deposited stainless steel particles.

Li and Ma further discussed that surface roughness will generally become smaller with increasing scan overlap, whether the overlapping ratio takes the optimised value or not. However, they added that a very large scan overlap can be impractical because this will decrease the covering speed of the melt front, implying that a trade off between surface quality and surface coverage speed needs to be considered. They also added that the overlapping ratio should not be too high because inter run porosity defects will be produced. Niu and Chang agreed, and further suggested that an increase in linear energy would counteract the problem of inter-run porosity, presumably, because it would increase the amount of material melted. However, this action is also likely to increase the size of the layer produced, and it would therefore seem more preferential to reduce the scan overlap.

Li and Ma also simulated the overlapping process with different area cross section profiles, including (1) an asymmetric profile composed of two parabolic ones; (2) a symmetric circle segment and (3) a symmetric profile composed of two circle segments with different radii. Using the same model as before they found that the relationships between $\Delta H/d$ and k were comparable to the results obtained in the first experiment. They therefore concluded that the two optimised scan overlap ratios are 29.3% and 59.2%. The high tolerance of these ratios further suggests that the geometry of the tracks are highly reproducible.

Finally, Li and Ma also found that a scan overlap ratio of 29.3% produces an effective clad layer thickness of $0.82d$. Alternatively, when the overlapping ratio takes a value of 59.2%, the effective layer thickness was found to increase to $1.56d$, implying that the height of the clad track relative to the surface of the powder layer increases, which may prove to hinder the recoating of fresh powder layers during SLM. Figure 1.20, shows the relationship between the ratio of H/d , and the overlapping ratio, k .

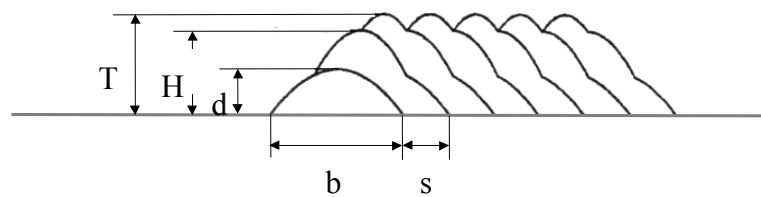


Figure 1.17: Model of overlapping process (Li and Ma, 1997).

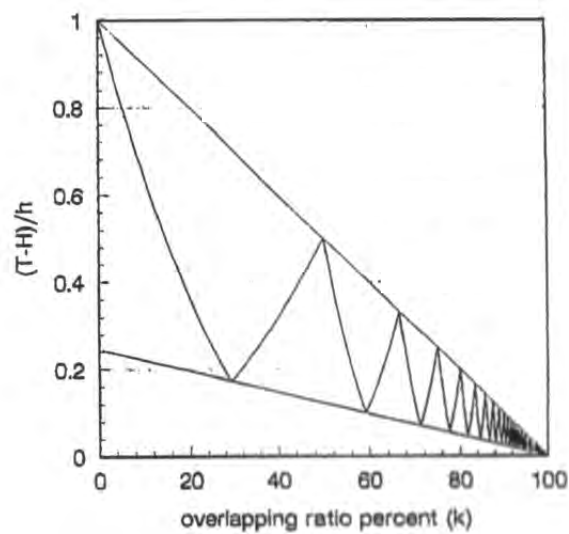


Figure 1.18: Surface roughness as a function of overlapping ratio (Li and Ma, 1996).

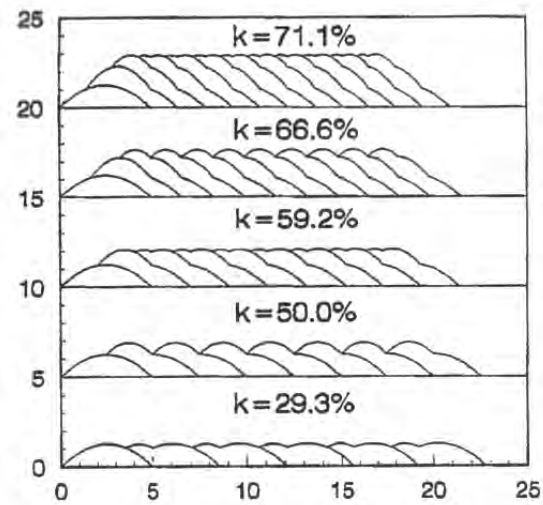


Figure 1.19: Section profiles of overlapped cladding layers at some critical ratios (Li and Ma, 1996).

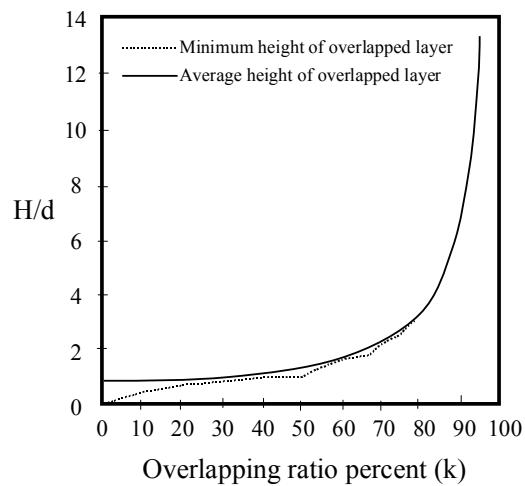


Figure 1.20: Section profiles of overlapped cladding layers at some critical ratios (Li and Ma, 1997).

1.1.8 Layer Thickness

Steen, (1996) discusses that a thin layer of powder is an important requirement during layer manufacturing because the bond required to fuse consecutive layers is often difficult to achieve by virtue of the pre-placed powder layer. This is because the underlying solidified layer needs to be remelted in order to achieve a strong fusion bond. But, since the substrate is not directly irradiated, the degree of remelting will depend on the transmitted energies through the powder layer. Hence, there is a general agreement in the literature, backed up by empirical studies, that a smaller layer thickness will increase the bond between layers, resulting in higher density components (Marcus et al., 1994; Agarwala et al., 1995a/b; Lauwers et al., 1998).

Steen further discusses that this problem heightens as the underlying layer increases in density. As the molten front of the current layer proceeds through the powder to the underlying layer, it will refreeze at the point of contact due to the additional thermal load caused by the high thermal conductivity of the lower layer; to ensure a strong fusion bond the current layer must be remelted before the substrate melts. If the current layer refreezes prematurely, then a lower penetration liquid-solid bond will form. However, Steen adds that if the lower layer remains cold, then the current layer will not wet the substrate and balling can be expected. Figure 1.21 shows the theoretical position of the melt front during pre-placed powder cladding. It

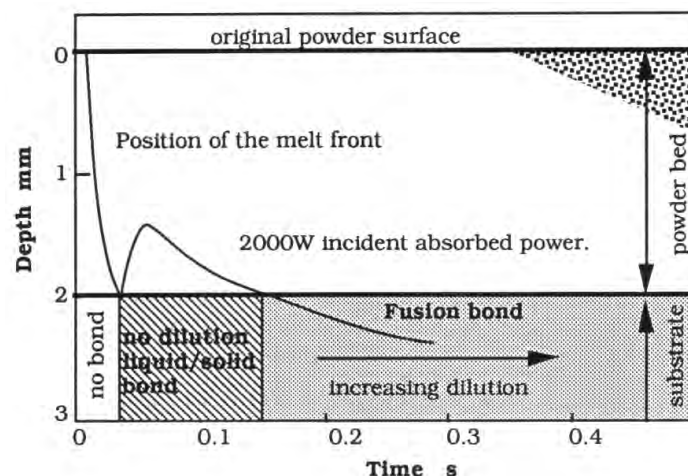


Figure 1.21: Theoretical estimation of the position of the melt front during laser irradiation of a pre-placed powder layer (Steen, 1998).

illustrates the importance of how an increase in dwell time, caused by a reduction in scan speed, will allow sufficient melting at the interface between layers to cause a good fusion bond.

Benda, (1994) also found that the melt depth or penetration depth of the melt front changed depending on the value of the scan spacing. He found that an increase in scan overlap caused a reduction in melt depth and a decrease in scan overlap resulted in an opposite effect. He suggested that the phenomena occurred due to changes in the absorptivity of the laser light since the surface roughness and porosity of the bed changes drastically when powder is melted. He found that increasing the scan spacing or reducing the layer thickness counteracted the problem of reduced penetration. He also discussed that an increase in linear energy may also prove beneficial, but since the understanding of laser absorptivity during SLM and other powder based processes is currently in a state of infancy, this possibility is only speculative. The factors affecting laser absorptivity are discussed in greater detail in Section 1.73.

Finally, Hu and Baker, (1999) also noted that the melt depth tended to fluctuate within a layer, particularly at the beginning where the depth was found to increase with an increasing number of tracks, only reaching steady state conditions after about 10 consecutive scans. Hu and Baker failed to provide an explanation for this behaviour, though it is plausible that the natural preheating of the powder layer that takes place during scanning may have some bearing over these observations. Hu and Baker concluded that a variable melt depth made it difficult to choose an adequate layer thickness to maintain a consistency in the bonds between layers.

Oxidation: Effects and Methods of Prevention

The high specific surface area of a powder allows a large amount of material to be directly exposed to the surroundings. Therefore, during powder production, storage, handling and processing many contaminants can be easily picked up from the surrounding medium through adsorption and chemisorption processes (Thümmeler and Oberacker, 1993; German, 1994). In many cases these impurities segregate to the particle surface, giving rise to two powder specific problems:

1. The reaction between the powder melt and the impurities.

2. The effect of impurities on the final material properties.

Oxygen is one of the most damaging impurities during metal powder melting (Carter and Jones, 1993). It can be present within the processing atmosphere, in the form of an oxide created on particle surfaces during powder production or as a gas that has become absorbed during inadequate storage and careless handling. If no measures are taken to reduce oxygen or oxide levels, severe further oxidation can take place since raster scanning and the progressive construction of layers causes every melted layer to run through a temperature cycle which is very conducive to oxide formation. This will lead to poor wetting conditions and at worse, melt pool balling, which often proves impossible to stop once it occurs (Carter and Jones, 1993; Das et al., 1998a/b; Niu and Chang, 1998). Furthermore, if oxygen is absorbed to excess during melting, it will combine with deoxidants and become rejected in the form of a slag (Lancaster, 1999). It is therefore generally accepted that a metal powder (in most circumstances) cannot be directly exposed to high levels of laser radiation without firstly establishing a protective atmosphere.

There are several criteria which need to be considered when selecting a suitable atmosphere, including prevention and/or removal of oxides, removal of contaminants and by-products, chemistry control and finally cost. Because current SLM research is largely focused on process and melt phase control rather than chemistry or metallurgical control, atmospheric selection is principally driven by the need for oxide prevention and/or removal only. However, due to a poor literature coverage, the choice of atmosphere for use in SLM still remains diverse with little cohesion. The most common types of atmosphere currently used are:

1. Vacuum.
2. Vacuum with inert/reducing gas backfill.
3. Inert gasses (including argon or nitrogen)
4. Oxide reducing gasses (including hydrogen, forming gas or dissociated ammonia).

In most cases each system has proven to be an effective route to oxide reduction, removal or in some cases prevention, causing vast improvements in wetting conditions and general fluid flow behaviour (Agarwala et al., 1994; Das et al., 1997a/b; O'Neill et

al., 1998; Niu and Chang, 2000). However, the suitability and relative importance of each of the different systems and the degree of effort required to maintain each system has been the source of much debate. The most common arguments occur between a vacuum based atmosphere and an inert gas based atmosphere. Sections 1.6.1 and 1.6.2 discusses the advantages and disadvantages of both.

1.1.9 Vacuum

Vacuum sintering or vacuum sintering with inert and/or reducing gas backfill has been identified as being the most reliable, repeatable and controllable atmosphere during SLS (Zong et al., 1992; Das et al., 1997a/b; Das et al., 1998a/b; Wohlert et al., 1999). Furthermore, a vacuum is a useful means of producing a non reactive environment, though Das et al., (1998b) demonstrated that a high vacuum and the use of specialist equipment was required to achieve this (a pressure of $<5 \times 10^{-5}$ Torr when melting a cobalt based superalloy).

In addition to atmospheric control, Carter and Jones, (1993), Das et al., (1997a), Wohlert et al., (1999) and others have also discussed that powder conditioning prior to SLS processing is a further important step in the control of oxidation and increased melt fluidity. In particular, Carter and Jones speculated that interlayer porosity would always be a problem if powder pre-processing steps were not implemented since enough residual oxygen would be present in each freshly deposited powder layer to cause the interface between melted layers to oxidise during cooling and prevent a good interfacial bond. This will also lead to melt pool shape changes (see Section 1.4).

Powder treatments often involve vacuum outgassing or exposure to a stream of inert or reducing gases. The reported processing times and gas flow rates are however not specific and range from several hours to several days. The gas flow rates are also wide ranging, making it difficult to determine the most reliable method. Nevertheless, Wohlert summarised by stating that more effort spent at the pre-processing level will lead to greatly increased long term benefits during SLS, since an untreated or coarsely treated powder will tend to produce parts with solidification cracks and a large amount of porosity, irrespective of the processing environment used (see Figure 1.22). Wohlert also added that the application of heat during pre-processing, values again varying

widely between 100°C and 1000°C, will hasten powder cleansing allowing overnight treatment.

Using a pre-processed powder (exact processing conditions were not given), Wohlert produced a „thin walled“ pressure cylinder from a nickel based superalloy powder. The pressure cylinder concept created a vehicle for which the unmelted powder contained in its core could be increased to full density by a post processing route known as HIPing (Hot Isostatic Pressing). HIPing worked by exposing the cylinder to very high pressures and temperatures, creating a cylinder exhibiting a fully dense core and integral wall. However, success could only be achieved if the leak rate of the pressurised gas through the cylinder wall did not exceed $1 \times 10^{-9} \text{ cm}^3/\text{s}$. This translated to a required wall density of 98.5% (Das et al., 1997a). The reported success of the work by Wohlert et al. (1999) implies that powder conditioning allows for improvements in both melt density and perhaps more importantly, in density homogeneity.

Figure 1.23 shows the shape and surface quality of an SLS processed pressure cylinder produced by Wohlert et al. (1999). It clearly illustrates the difference in density between the wall and the core. Micrographs showing the microstructure of the wall of the cylinder, prior to HIPing, in both a transverse and longitudinal direction to the powder layer orientation are also shown in Figure 1.24. These micrographs illustrate

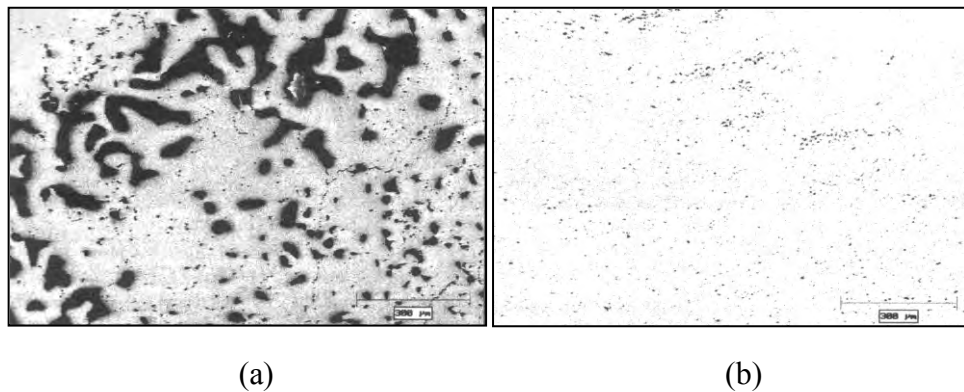


Figure 1.22: SLM processed nickel superalloy powder with (a) no powder conditioning and (b) after 12 hours vacuum conditioning at temperatures of 450°C (Wohlert et al., 1999).

The dark shading represent areas of porosity and trailing black lines show solidification cracking.

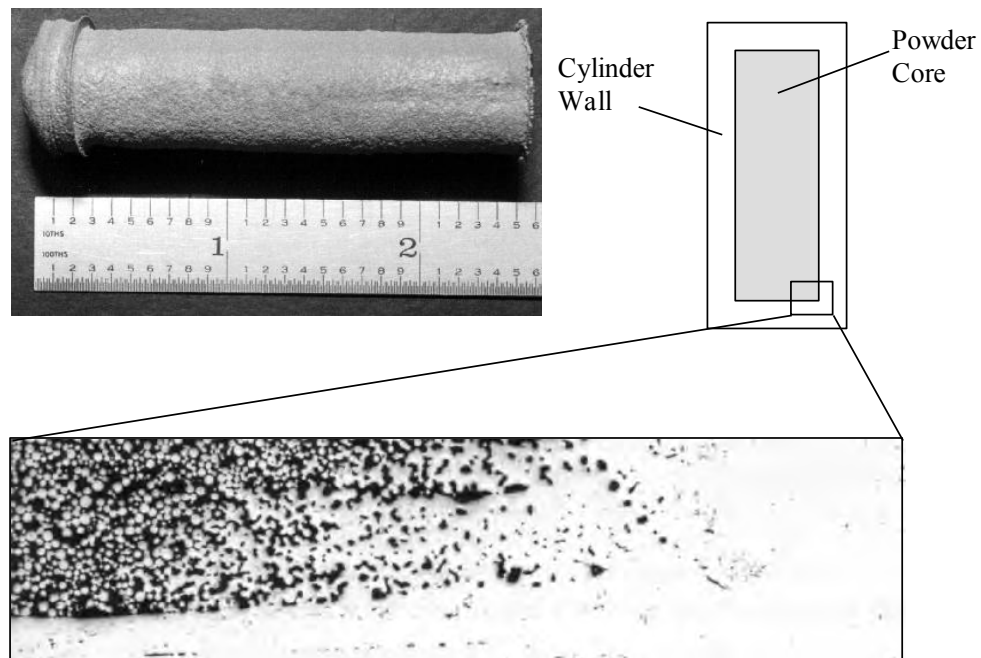


Figure 1.23: Transverse cross-section showing a typical SLS processed nickel superalloy cylinder at the interface between bottom cap, side wall and core (Wohlert et al., 1999).

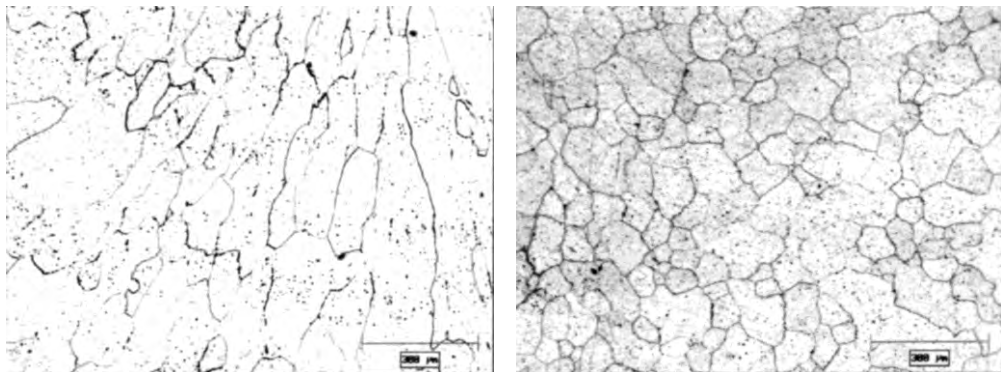


Figure 1.24: Microstructure of the wall of a HIP cylinder produced by SLS showing (a) columnar grains orientated vertically in the build direction and (b) equiaxed grains across the surface of a single layer. The height of each image is representative of seven layers (Wohlert et al., 1999).

elongated columnar grain growth orientated vertically in the build direction (see Figure 1.24a), and an equiaxed grain structure growing in a direction parallel to the powder layers (see Figure 1.24b). Wohlert added that the orientation of the columnar grains

indicates that the solidification front originates from the surface of the underlying layer. It is also interesting to note that no distinct boundaries between the layers or adjacent scan tracks are visible, re-emphasising the quality of the fusion bonds obtained in this work. Prior work on SLS/HIP development for titanium alloy powders (Ti-6Al-4V) has also been reported with equally successful results under the same atmospheric conditions (Das et al., 1998d; Das et al., 1999).

Although Wohlert failed to suggest reasons for the observed improvements in melt fluidity, there is however some general information available explaining the detrimental effects of solid films on fluid flow. Some of these effects have been listed below (Barlow, 1970):

1. Strong films can form a continuous layer around the liquid phase, raising the apparent surface tension, thereby reducing fluidity and decreasing the effective cross-sectional area of the melt volume.
2. Solid films can be entrained in the metal, restricting flow and increasing turbulence.
3. A film can act as a thermally insulating barrier, reducing temperature and therefore increasing viscosity. However, growing evidence suggests that surface oxide films often increase laser energy absorptivity, thereby counteracting the insulating properties of the film (see Section 1.7.2).

1.1.10 Inert Gas

Work by Meiners et al., (1999) dismissed results and observations presented by Wohlert by demonstrating success in constructing single and multiple layer components, with high densities and reasonable surface finishes, whilst shielding the build cylinder with argon gas. Furthermore, they discussed that powder pre-conditioning was not necessary, and therefore they chose to process untreated powder; the only powder requirement reported in their work was the use of a powder containing spherical particles with sizes ranging from 20 μ m to 50 μ m, though they failed to explain the significance of these particular powder properties nor did they give any indication of the „as received“ condition of the powder or the method by which it was stored.

Nevertheless, Meiners reported component densities exceeding 99% of theoretical density with linear accuracy's of ± 0.1 mm. Post processes like infiltration were thought unnecessary and machining steps to improve surface roughness yielded mirror like finishes. However, Meiners stressed the importance of scanning strategies and gas flow rates when attempting to achieve and maintain such high tolerances, though no further information was relayed in their work.

Figure 1.25, shows the typical structure, in a direction normal to the direction of scan, of components produced from stainless steel (316L) and titanium alloy (TiAl6V4) powders when melted in an argon atmosphere. It illustrates the quality of the fusion bonds between both tracks and layers, where arguably, the titanium samples appear analogous to samples produced by Das et al., (1999) under more strict environmental conditions (see Section 1.6.1).

Laser melted samples produced from stainless steel powders also show great promise, but it is not clear whether the boundary lines visible in Figure 1.25a represent areas of inter-run porosity formed through inadequate fusion or just differences in grain orientation (see Section 1.9). However, due to the reported homogeneity of material properties, this would suggest that the boundary lines are formed through changes in grain orientation rather than through inter-run porosity. Furthermore, no explanation was given as to why boundary lines between tracks only appear on alternate layers, though this is likely to be caused by a rotational build technique where every alternative layer is built on a 90° rotation. If this is the case, then this build method would also account for the high tensile strength measurements taken in a direction normal to the direction of scan; raster scanning often produces inhomogeneous layer properties (Kruth et al, 1998a). Tensile strength values for both orientations were within the range of the materials specification ($490 - 690 \text{ N/mm}^2$ for stainless steel 316L).

In comparison, O'Neill et al. (1998;1999) observed large differences when comparing the density between adjacent rastered tracks and between consecutive layers when melting untreated stainless steel powders in an argon gas stream (see Figures 1.26 and 1.27). They concluded that layer warping together with their inability to maintain a constant layer thickness were the primary causes for inter-layer porosity, although it is equally likely that the porosity was caused by powder contamination.

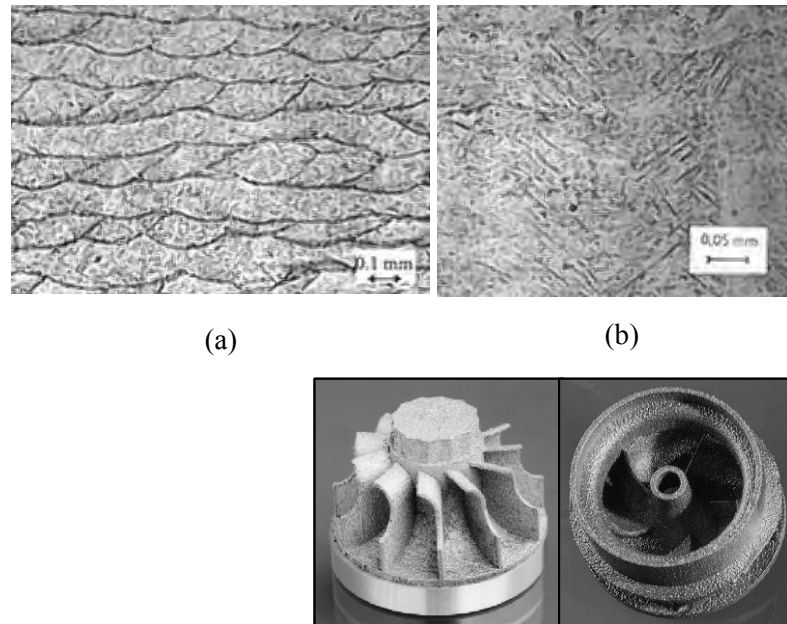


Figure 1.25: Sample cross sections of SLM parts made from (a) stainless steel 316L and (b) titanium (TiAl6V4) powders (Meiners et al., 1999).

The insert shows an aeronautical component which is representative of parts produced from titanium powders: note the surface roughness.

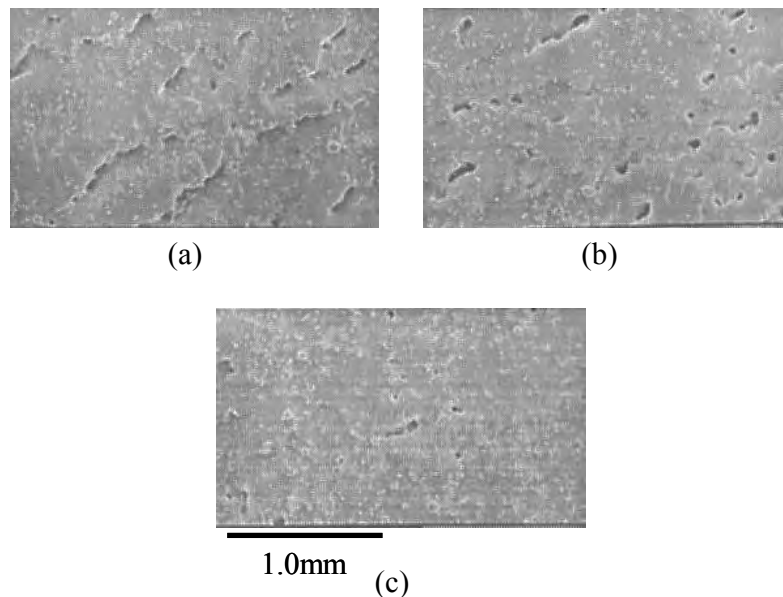


Figure 1.26: Micrographs showing single layer pads of stainless steel powder produced within an argon atmosphere using laser conditions of (a) continuous wave at 20A and 15W, (b) pulsed at 20kHz at 20A and 10W, (c) pulsed at 40kHz at 20A and 11W (O'Neill et al., 1998).

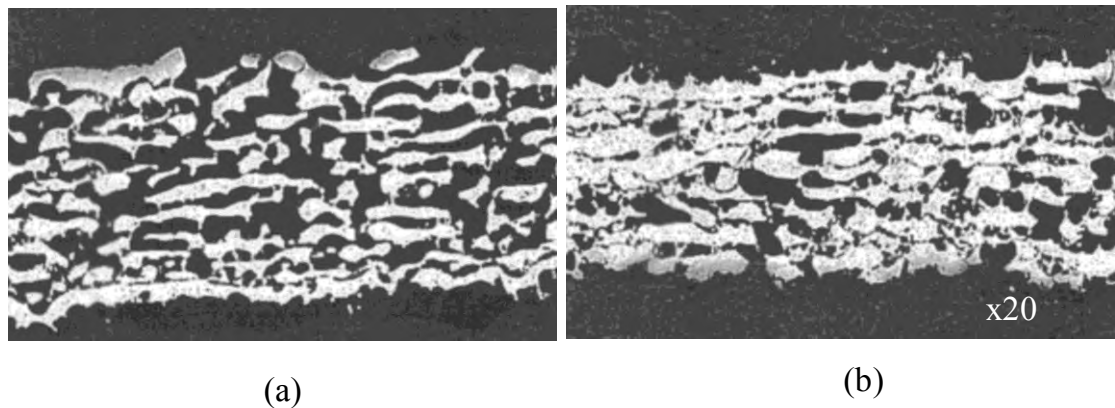


Figure 1.27: Micrographs showing cross sections of blocks produced using twenty layers of 80µm thick. Average power 12W, speed 100mm/s, overlap 25% of beam diameter, laser pulse frequency of (a) 48kHz and (b) 53kHz (O'Neill et al., 1999).

Powder Bed Behaviour

1.1.11 Powder Properties

An exhaustive literature database of conventional powder metallurgy research often underlines the benefits of tailoring specific powder properties, through simple steps, to allow significant improvements in the properties of the sintered component and to increase efficiencies during powder handling, packing and compacting (Goetzel, 1949; Tsukerman, 1965; Thummler and Oberacker, 1993; German, 1994). The strength of results from this literature has directed several researchers to recognise similar benefits during DMLS. In particular, the properties of individual particles (such as size and shape) and the collective (bulk) properties of a powder (such as packing density, and flowability) can be customised leading to changes in melt pool behaviour, sintering kinetics and laser absorptivity (Van der Schueren and Kruth, 1995; Smugeresky et al., 1997; Lauwers et al., 1998; Karapatis et al., 1998; Niu and Chang, 1998; Karapatis et al., 1999). The impact of these powder property changes will be discussed here.

1.1.11.1 Particle Size and Shape

Powder metallurgy techniques generally deal with powder particles that are larger than smoke particles (0.01 to 1.0 μm), but smaller than sand (0.1 to 3mm). They can be supplied in a vast number of shapes, where each shape is determined by the production parameters and method (German, 1994). Because it is difficult to quantify every particle shape, several qualitative descriptors are frequently used, the most common of which are given in Figure 1.28.

In the context of SLM, the size distribution of metal particles within a bulk powder generally range from 20.0 μm up to 200 μm and they are often produced by gas atomisation techniques. This production method produces spherical shaped particles with smooth surfaces and due to the inert production gasses, the powder often has low levels of residual oxygen and surface oxidation (German, 1998). These characteristics allow for ideal flow properties and reduced surface contamination which are arguably, the primary concerns when selecting powders for use in SLM (see Section 1.7.1.3).

Reports concerning the effects of particle size and shape on melt pool behaviour are however limited and generally restricted to powder contamination issues rather than actual particle size effects (see Sections 1.4 and 1.72). However, those reports that do

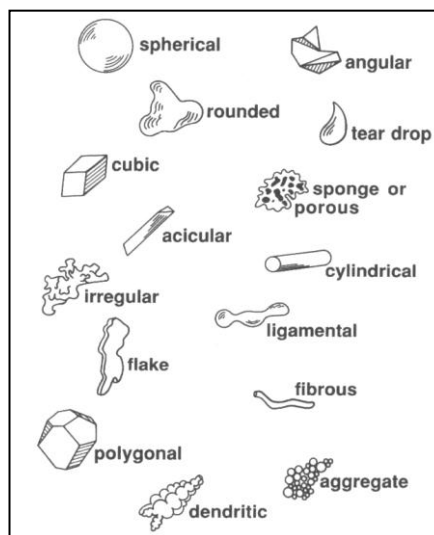


Figure 1.28: A qualitative description of possible powder particle shapes (German, 1994).

attempt to address the effects of particle size and shape often leave the reader wondering whether contamination through oxidation is the real issue. For example, Niu and Chang, (2000) found that melting of HSS powders produced a highly porous structure when the particle size was small ($<38\mu\text{m}$). Since oxidation is more prevalent when heating powders containing smaller particles, it is likely that the porous structure has formed through inefficient wetting rather than by some mechanism governed solely by particle size effects.

Niu and Chang also reported that large particles ($>100\mu\text{m}$) required higher laser powers for melting since heat transfer into the powder layer was lower. Therefore, for a given energy density, the structure produced was generally more porous than a structure produced using smaller particles (See Figure 1.29c/d). Discussions in Section 1.7.1 also reveal a further mechanism by which surface oxidation strongly affects laser absorptivity.

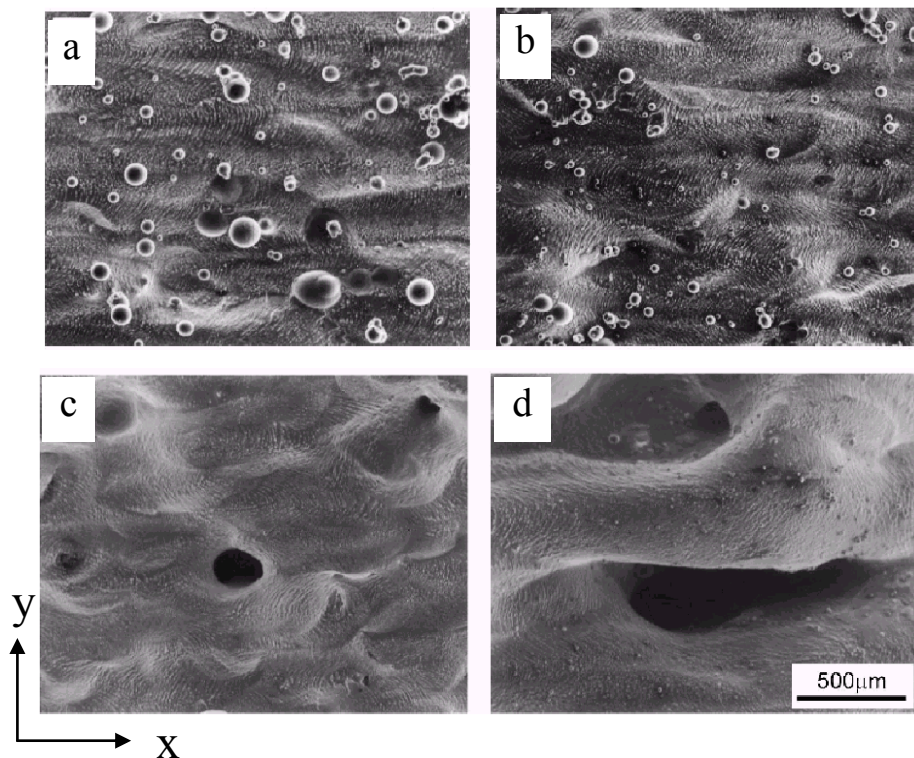


Figure 1.29: SEM images of laser sintered high speed steel powders using laser powers of 50W and a scan rate of 5.0mm/s and a scan line spacing of 0.15mm. Particle sizes were: (a) as supplied form atomiser (full range), (b) $53\mu\text{m} - 150\mu\text{m}$, (c) $>150\mu\text{m}$ and (d) $<38\mu\text{m}$ (Niu and Chang, 2000).

In addition to the effects of particle size and shape on melting, Wieters et al., (1996), Das et al., (1999), Karapatis et al., (1998) and others have also found that particle size often dictates the surface roughness of the finished article. Due to local heat transfer, surrounding particles will fuse to the molten region and hence the surface roughness is often found to be a direct function of particle size, implying that finer particles will produce the best surface finish under ideal melting conditions. Van der Schueren and Kruth, (1995) and Lauwers et al., (1999) generally agreed with these results, but they also highlighted that surface quality is ultimately governed by the flowability characteristics of the bulk powder. If the particle size is too small and the shape too irregular, then these characteristics will impede the smooth deposition of layers which in turn will affect the quality of the irradiated layer (see Section 1.7.1.3).

Finally, Agarwala et al., (1995a/b), Van der Schueren and Kruth, (1995) and Karapatis et al., (1998) have also established that the particle size and the presence of any agglomerated particles will determine the dimensions of the minimum layer thickness that can be deposited during a build. Agarwala concluded that if the layer thickness falls below the dimensions of the largest powder agglomerates, then deposition of fresh layers, without disturbing previously melted areas becomes difficult.

1.1.11.2 Powder Packing Density

A deposited powder layer that exhibits a high packing density has been identified as making an important contribution to the density of the sintered or melted layer following laser exposure. In this, particle size, particle size distribution and mixing can affect its value. For liquid phase sintered metal powders the relationship between powder and sintered density is often direct (Wieters et al., 1996; Lauwers et al., 1998), with final consolidated part densities often equating to the initial density of the powder bed. However, during full melt processing of pre-alloyed powders, where part densities can approach theoretical density, the effects of particle packing on melt density is less clear.

1.1.11.3 Powder Fluidity

Powder deposition and spreading is a critical step during SLS. The surface morphology and density of the melted layers together with the fusion bond between

them is ultimately dependant upon the uniformity, packing efficiency and smoothness of every deposited powder layer, implying that any surface irregularities present in the deposited powder layer will be echoed in the sintered or melted surface, though the sensitivity of this transfer is not clear. In this, the choice of deposition mechanism and the efficiency of powder fluidity play a decisive role. Here the second is discussed first.

Powder fluidity or flow rate is usually expressed as the time taken for 50g of powder to flow through a Hall flow meter (German, 1994). Short flow times indicate free flowing powders while long flow times suggest high interparticle friction. The friction between particles is dominated by particle shape, surface area, surface roughness and surface chemistry. As the surface roughness and surface area increases, or the particle size decreases, the amount of friction within a powder mass will increase.

There are also a number of weak forces, namely van der Waals attraction forces, electrostatic charges, magnetic forces and capillary liquid forces which all act to reduce powder fluidity by causing particle agglomeration. Each of these forces becomes more noticeable as the particle size decreases e.g. $<100\mu\text{m}$ for capillary forces and $<0.05\mu\text{m}$ for van der Waals forces (German, 1994). In general, a bulk powder containing spherical particles greater than $45\mu\text{m}$ can usually be considered as free flowing, but there will be an inherent resistance to de-agglomeration up to particle sizes of $100\mu\text{m}$ (Tsukerman, 1965; German, 1994).

1.1.12 Powder Deposition and Spreading

There are three powder deposition mechanisms in general use during SLS. The first is based on the use of a scraper blade. A predefined shot of powder is placed in front of the blade and swept across the build zone, spreading and levelling in one operation (See Figure 1.30a). This system is capable of depositing a uniform powder layer but there are some basic problems related to this solution (Van der Schueren and Kruth, 1995):

1. The quantity of powder required is not regulated or controlled during each sweep and so a surplus is needed to ensure complete coverage of the build cylinder;

2. Surplus powder increases the weight of the powder shot causing an increase in friction between the moving powder heap and the underlying melted layer: this can cause shearing and displacement leading to misalignment of layers;
3. A fixed line contact between the blade and the surface of the powder bed can cause irregularities in the powder (such as agglomerated particles) to be swept along tracing furrows in the powder surface; and
4. The approach offers no means to compact the powder during deposition.

The problem of the fixed contact line is solved with a counter rotating roller (see Figure 1.30b). In this second approach, the rotary motion of the roller will cause irregularities appearing on the contact line between the powder and the roller to leave this contact line a few moments later, giving only small traces of disturbance. Another

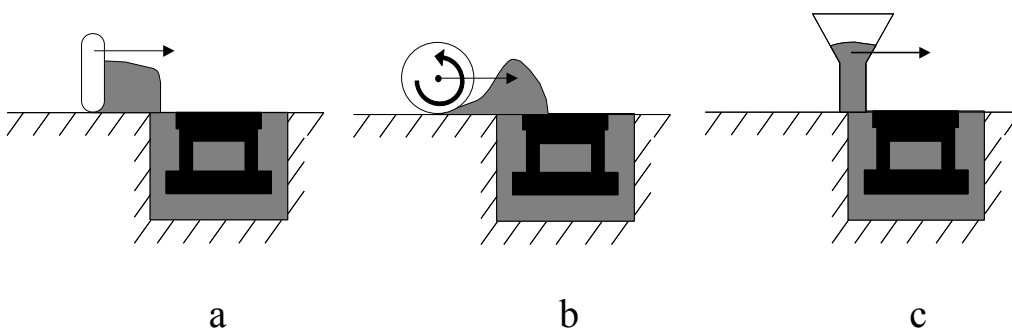


Figure 1.30: Three solutions for powder deposition and spreading during SLS, based on (a) scraper blade, (b) counter rotating roller and (c) slot feeder (Van Der Schueren and Kruth, (1995).

advantage of the roller mechanism is the ability to apply, simultaneously, a vertical vibratory motion. This vibration resembles a tapping operation which should yield a higher powder density, known as the tap density.

To minimise friction between the moving powder heap and the previously deposited layer, a slot feed mechanism can be used (see Figure 1.30c). Unlike the first two techniques, this third mechanism continually deposits powder during transit rather than pushing a heap of powder across the build cylinder, minimising the interaction between powder and melted layer. The outflow from the hopper acts as a natural blade

to deliver a final levelling action. There is no tapping operation to increase powder density but this mechanism often proves successful in reducing layer displacement.

Because no single system fulfils all the deposition requirements imposed by SLS, Van Der Schueren and Kruth, (1995) planned a two phase deposition, spreading and compacting mechanism which combines a slot feeder and a rotating roller. They proposed a four stage deposition cycle as follows:

1. The build cylinder piston lowers to a depth just below the required layer thickness.
2. The slot feeder deposits a layer of loose, uncompacted powder.
3. The piston raises up to the required layer thickness.
4. A roller, rotating in the direction of motion, traverses across the powder bed and compacts the projecting powder layer.

Van Der Schueren and Kruth speculated that such a mechanism should achieve a powder bed density that approaches the powder tap density. In a previous study, research by Lee et al., (1993) found evidence which supports this theory by performing compaction experiments on Alumina powder layers with a rotating roller. They found that the tap density for irregular shaped particles could be reached using this method (40% of theoretical density). However, Lee et al., (1993) also reported that powder layer compaction, which is difficult to achieve consistently due to the irregular distribution of particles, can cause previously melted layers to displace vertically from their suspended positions. Lee concluded that object dimensional accuracy could not be guaranteed during compaction. Figure 1.31 shows the effect of vertical layer displacement during powder compaction. It illustrates how the static height, h , between two remote features cannot be guaranteed during layer compaction.

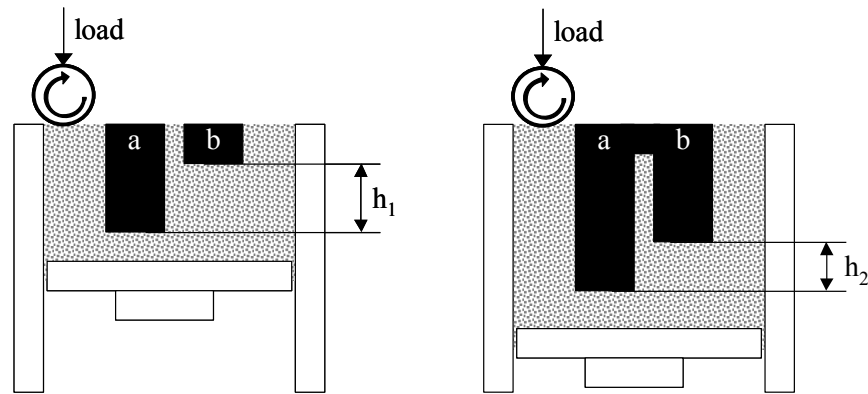


Figure 1.31: Effects of layer position accuracy during powder compaction.

1.1.13 Laser Energy Absorption

1.1.13.1 Introduction

Kruth et al., (1998b) stated that a study of powder absorptivity is of a particular interest to SLS because it allows for the creation of more accurate sintering windows. Furthermore, prior knowledge of such information will lead to improved levels of experimental and process reproducibility and uniformity, and therefore its understanding has been considered important for the work of this thesis.

1.1.13.2 Coupling

Since a laser beam is a light source, when it falls incident on the surface of an opaque powder bed, a part of its heat energy reflects to the surroundings, away from the powder surface. The remainder will be absorbed by the powder particles. The ratio of the laser absorptivity to reflectivity, commonly termed „laser coupling“ or „energy coupling“ is a measure of the transfer efficiency of the laser’s radiant energy into the surface of the work piece. For opaque matter the incident laser power, P , will be partially absorbed (P_A) and partially reflected (P_R) according to (Hügel and Dausinger, 1996):

$$P = P_R + P_A = \alpha P + \beta P \quad (1.4)$$

where α and β are the absorptivity and reflectivity ratios respectively, hence $\alpha + \beta = 1$. The thermal energy per unit time released into the interaction zone is therefore equivalent to the absorbed power. Figure 1.32, gives a first approximation for the magnitude of α for both CO₂ and Nd:YAG lasers. It illustrates, for normal angles of incidence, how the absorptivity changes with both laser wavelength, λ , and the materials chemical composition. It also illustrates the low efficiency of the energy transfer into the workpiece, especially for those metals which are commonly used in SLM (iron, nickel, chromium). The depth penetration of the absorbed radiation (excluding heat transfer) is also very small for opaque materials, typically of the order of 10nm - 1 μ m over the range of wavelengths having industrial interest (Tolochko et al., 2000).

Similar to fully dense materials, only a fraction of the incident radiation will be directly absorbed by a singular metal particle surface. However, within a powder layer, which contains many hundreds of particles, a high proportion of the remaining or reflected energy will penetrate surrounding porosity where multi-reflections between particles will increase the overall absorptivity, thus allowing the radiation to interact with underlying particles (Hügel et al., 1994). In this, an irregular particle shape also plays a decisive role (Steen, 1998; Niu and Chang, 2000). This phenomena is perhaps

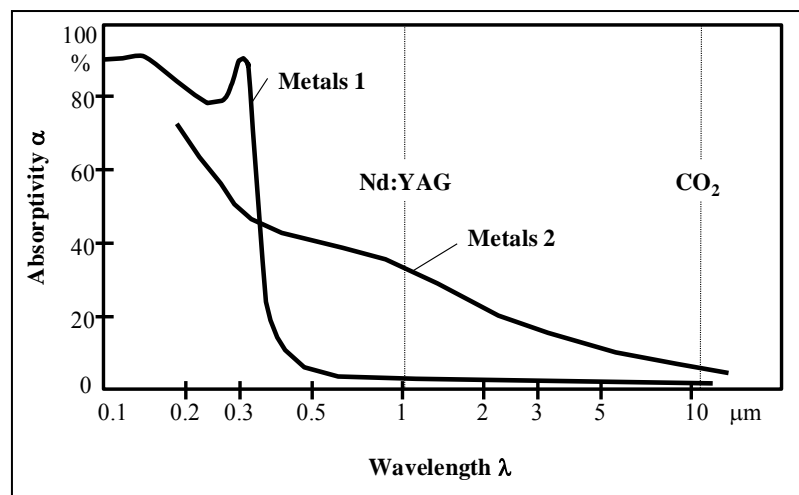


Figure 1.32: Absorptivity as a function of wavelength for normal incidence, smooth surface and at room temperature. Metals 1 are those with full inner electron shells (Au, Ag, Cu,...) and Metals 2 are transition metals (Fe, Ni, Cr,...) (Hügel and Dausinger, 1996).

analogous to the observations of increased absorptivity when a keyhole forms during laser drilling or cutting. Again, the beam is subjected to many reflections down the hole due to the irregularity of the walls. Interestingly, as the depth of the key hole increases, the number of reflections increase and the effects of radiation wavelength become less significant (Hügel and Dausinger, 1996).

Simulation studies by Sih and Barlow, (1995) and empirical research by Tolochko et al., (2000) independently discussed that the laser absorption into a metal powder, particularly if the powder bed is pre-heated, can approach idealised values i.e. $\alpha = 1$ (black body). However, Hügel et al., (1994) disagreed by stating that tabulated data for powder absorptivity must be approached with caution because results are strongly influenced by a great many processing conditions. In particular, the surface condition, temperature and optical properties of the workpiece together with the radiation wavelength, polarisation, power and mode quality have all been shown to affect absorptivity. Therefore, Hügel tentatively suggested that the coupling efficiency for CO₂ laser radiation, at values far below those to reach surface melting, will realistically approach values of 35% and 45% for a pure metal and a pre-alloyed powder respectively.

Hügel added that oxidation is likely to be the decisive factor affecting absorptivity accuracy due to the difficulties when trying to maintain a reproducible, oxygen free atmosphere. Tolochko et al., (2000) agreed and presented data showing an increase in absorptivity, reaching almost idealised values, for CO₂ radiation when incident on the surface of a number of oxidised alloyed samples. Hügel also suggested that oxidation, or the lack of it, is the primary reason for reduced energy coupling when the incident laser power is high. At these conditions an enhanced convective stirring of the melt volume limits the growth of oxide layers.

1.1.13.3 Heat Penetration

Wang and Kruth, (2000) proposed through simulations that a strong relationship exists between the energy absorption, penetration depth and the lasing wavelength. In their simulation a powder bed which was a mixture of Fe and Cu (30wt%) with porosity of 0.75 was irradiated by two types of laser source: CO₂ and Nd:YAG. Absorption of the Nd:YAG laser was 54% into the Fe and 12% into the Cu or in coupling, 66%. In

contrast, absorption of the CO₂ laser was 26% into the Fe and 7% into the Cu or in coupling, 33%. Their theoretical results predicted, as first hypothesized, that an increase in energy absorption will be followed by an increase in depth of penetration. However, their results also showed that for the same energy absorption, Nd:YAG lasers gave a lower depth penetration than a CO₂ laser. This may be caused by a larger number of inter-particle reflections during CO₂ radiation which penetrate the bed more readily.

Both Benda, (1994) and Bunnell et al., (1996) independently discussed that in-situ changes of the laser absorptivity during scanning, triggered by the changes in density and surface quality of the melted powder, is likely to affect wetting between the liquid and the solid phases. During raster scanning, if the powder absorbs all of the laser energy, then the molten metal may not wet the cooler solid resulting in non fusion bonding and balling of the melt phase. Benda suggested that this is a particular problem when melting powder in close proximity to solidified powder. They added that ideally the amount of power required to uniformly sinter the powder should be modulated depending on the proximity and amount of the previously melted powder. Part growth near the edges, layer warping and poor adhesion between layers are probable detrimental effects. Benda chose to keep track of the temperature history of the powder as it is melted. This was accomplished by analysing the reflected laser beam emitted from the powder surface. This proposed method was still in its early stages of development, but improvements in layer warping were noticeable.

Solidification Mechanisms

1.1.14 Grain Structure

During welding and laser cladding, and therefore likely during SLM, the melt pool can be considered as a small casting, often a continuous casting formed under specialised conditions: melt pool stirring (Marangoni convection), high temperature gradients, rapid solidification, intimate contact between the molten alloy and the underlying layer including partial melting of the underlying layer (Brody, 1986; McLean et al., 1997).

Grain formation in alloys is usually presented as a nucleation and growth process. However, in weld zone solidification the nucleation step is not required. Instead, the crystals that form are nucleated by the solid crystals located at the solid-liquid interface (s/l). This type of crystal growth is known as „epitaxial“. Hence, each crystal in the melt pool forms initially as a continuation of one of the grains that lie along the s/l interface. (Brody, 1986; Berjeza et al., 1995; Lancaster, 1999). Additionally, unmelted powder particles, often found fused to the surface of clad melt pools, have been implicated by Smugeresky et al., (1997) as being ideal sites for nucleation (these „satellite“ particles occur due to an excess of blown powder), implying that melt tracks created by SLM will be nucleated by the surrounding powder bed. Smugeresky reported that observations of the re-solidified melt pool, in a direction normal to the direction of scan, revealed a localisation of the microstructure in areas adjacent to fused particles (see Figure 1.33). They also added that the hardness of solidified tracks increased with decreasing particle size. Since hardness is a function of grain size (Cottrell, 1995) and that the grain structure of an individual particle is dependent upon its diameter (German, 1994), this observation strengthens the previous argument concerning epitaxial growth.

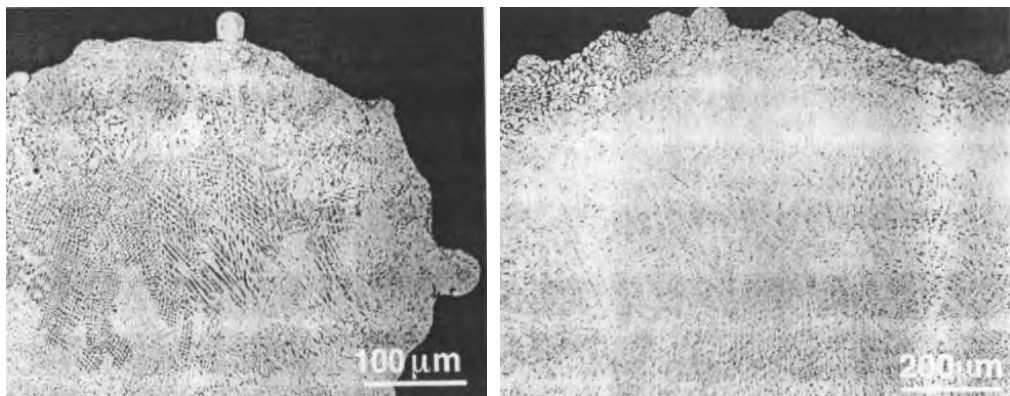


Figure 1.33: Microstructure of cladding melt beads, in a direction normal to the direction of scan, showing evidence of epitaxial grain growth from attached satellite particles (Smugeresky et al., 1997).

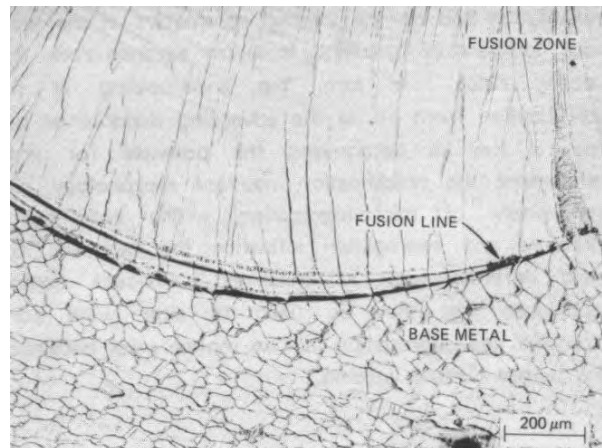


Figure 1.34: Epitaxial and columnar growth near the fusion line in an iridium alloy (Brody, 1986).

As the fusion line progresses through the melt, the primary grain structure continues to grow in a columnar fashion. Competition between grains results in some change in relative size, but in general the primary grain size and crystallographic orientation of the solidified melt pool is determined by the grains in the underlying metal at the fusion line (Brody, 1986). Figure 1.34, shows epitaxial and columnar grain growth in a solidified weld pool. It illustrates the relationship between underlying layer grains and primary weld zone grains at the fusion line.

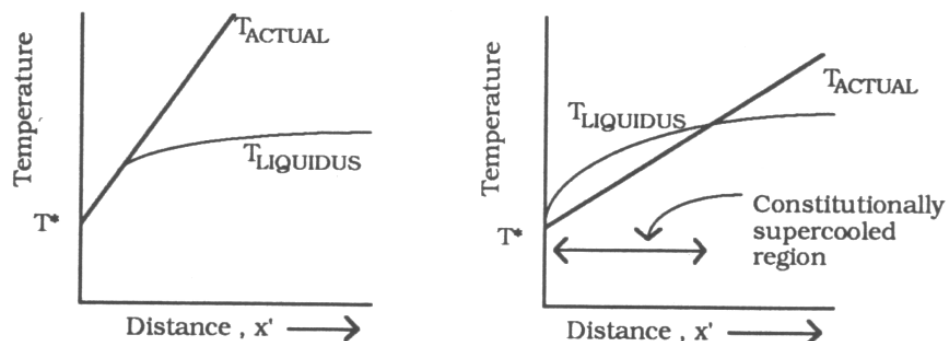


Figure 1.35: Supercooling in alloy solidification (a) stable interface and (b) unstable interface (Steen, 1998).

A fusion weld or clad melt pool has a primary grain structure, and individual grains have a structure that results from micro segregation (Lancaster, 1999). The type of substructure that forms is determined by the conditions of heat transport. Solidification at the solid/liquid (*s/l*) boundary will proceed as either a stable planar front or an unstable front leading to dendritic or cellular grains. The type of solidification interface morphology that forms depends on supercooling. Supercooling is achieved by extracting heat without nucleating the solid phase and is a measure of the actual temperature below the equilibrium transformation temperature. If the liquid is cooled significantly below the equilibrium temperature then the solidification front will become unstable (see Figure 1.35). Hence, two key parameters with respect to the resulting microstructure are solute content, C_o , and a solidification parameter which is equal to the temperature gradient, G , in the direction of solidification divided by the rate of advance, R , of the solidification front. Both G and R are related to the cooling rate which is determined by heat extraction (German, 1994; Steen, 1998; Lancaster, 1999).

1.1.15 Heat Extraction

Heat extraction changes the energy of the phases (solid and liquid) in two ways (Kurz and Fisher, 1989):

1. There is a decrease in the enthalpy of the liquid or solid, due to cooling, which is given by: $\Delta H = \int cdT$ where c is the specific heat.
2. There is a decrease in enthalpy, due to the transformation from liquid to solid, which is equal to the latent heat of fusion per mole, ΔH_f .

Heat extraction is achieved by applying a suitable means of cooling to the melt in order to create an external heat flux, q_e . The resultant cooling rate dT/dt , can be deduced from a simple heat balance if the metal is isothermal and the specific heats of the liquid and the solid are the same. Using the latent heat of fusion per unit volume $\Delta hf = \Delta H_f / v_m$, and also the specific heat per unit volume, c , in order to conform with the dimensions of other factors, then:

$$q_e \left(\frac{A'}{v} \right) = -c \left(\frac{dT}{dt} \right) + \Delta h_f \left(\frac{df_s}{dt} \right) \quad (1.5)$$

so that:

$$\frac{dT}{dt} = -q_e \left(\frac{A'}{vc} \right) + \left(\frac{df_s}{dt} \right) \cdot \left(\frac{\Delta h_f}{c} \right) \quad (1.6)$$

The first term on the right hand side of equation 1.6 reflects the effect of melt geometry (ratio of surface area, A' , to its volume v) upon the extraction of sensible heat, while the second term takes account of the continuing evolution of latent heat of fusion during solidification. For an alloy, where solidification occurs over a range of temperatures, the variation of solid as a function of time (df_s / dt) must be calculated from the relationship:

$$\frac{df_s}{dt} = \left(\frac{dT}{dt} \right) \left(\frac{df_s}{dT} \right) \quad (1.7)$$

since f_s is a function of temperature, the cooling rates becomes:

$$\frac{dT}{dt} = \frac{-q_e \left(\frac{A'}{vc} \right)}{1 - \left(\frac{\Delta h_f}{c} \right) \cdot \left(\frac{df_s}{dT} \right)} \quad (1.8)$$

It can be seen from Equation 1.8 that solidification decreases the cooling rate since df_s / dT is negative. With a moving heat source the cooling rate at a given located and time is given by (Kurz and Fisher, 1989):

$$\left(\frac{dT}{dt}\right) = \left(\frac{dT}{dx} \times \frac{dx}{dt}\right) = G \cdot R \quad (1.9)$$

where R is the rate of movement of the (s/l) interface (solidification growth rate) and G is the thermal gradient across the s/l interface. At high solidification rates ($>10^2$ K/s), typical of laser melting (Steen, 1998), the microstructure tends to become more dendritic as the ratio G/R decreases (see Figure 1.36), while the dendrite spacing tends to increase as the freezing time (expressed as $1/\sqrt{GR}$) increases. Hence increasing $G \cdot R$ will lead to a finer microstructure (Minkoff, 1986; Steen, 1998). Eventually, at high values of $1/\sqrt{GR}$ (increasing supercooling) the dendrites nucleate at a point and the structure becomes equiaxed. Figure 1.37, illustrates these relationships and further introduces the concept of „absolute stability“ when the solidification rate, R , is so large that there is insufficient time for diffusion.

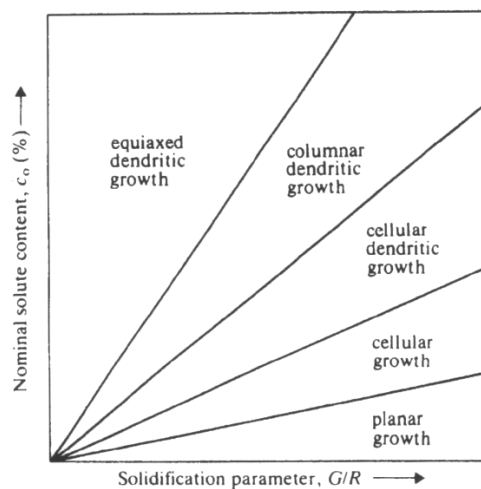


Figure 1.36: Representation of planar to equiaxed growth through changes in G/R (temperature gradient/solidification rate) and solute content C_o (Lancaster, 1999).

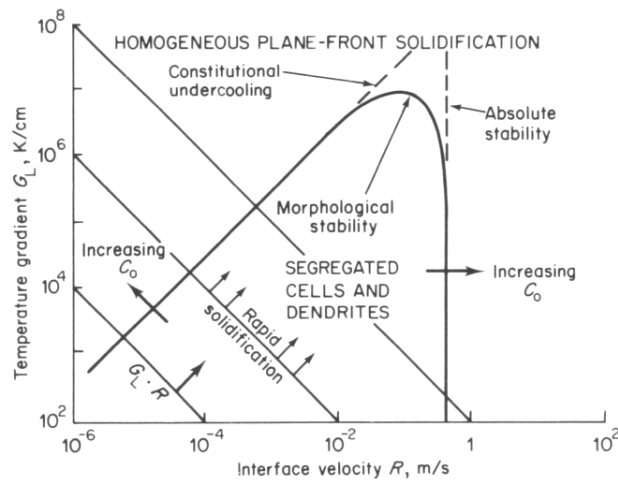


Figure 1.37: Plot of temperature gradient versus solidification rate and solidification morphology (Minkoff, 1986).

1.1.16 Solidification Control

In laser welding the solidification velocity, R , is equal to the scan speed, u , multiplied by the epitaxial growth angle, ϕ , (Lancaster, 1999; Steen, 1998):

$$R = u \sin\phi \quad (1.10)$$

where, ϕ , is the angle between the tangent of the growth vector and the scanning direction. The temperature gradient, G , from equation 1.9 is:

$$G = \frac{dT}{dx} \quad (1.11)$$

this can be written as:

$$G = \frac{dT}{dt} \cdot \frac{dt}{dx} = \frac{dT}{dt} \bigg/ u = \frac{1}{u} \cdot \frac{dT}{dt} \quad (1.12)$$

For three dimensional heat flow, the gradient at the rear of the melt pool is, numerically:

$$G = \frac{1}{u} \cdot \frac{dT}{dt} = \frac{T_p}{x_1} \quad (1.13)$$

where T_p is the melt pool temperature, and x_1 is the distance between the heat source and the rear of the weld pool (see Figure 1.38). At this point $\sin \phi = 1$ and:

$$\frac{G}{R} = \frac{T_p}{ux_1} \quad (1.14)$$

hence, if the rate of movement of the solidification interface, R , increases, the solidification parameter, G/R , decreases.

The structure of a weld pool for a range of scanning conditions is shown in Figure 1.38. At the lowest scan rates and thus the highest value of the solidification parameter, the central part of the weld is occupied by grains running longitudinally, and this is associated with a nearly circular weld pool (see Figure 1.38a). With higher scan speeds and a more elongated pool, the grains established near the fusion boundaries are later blocked by grains growing from the rear of the melt pool, giving a random grain orientation (see Figure 1.38b). At still higher speeds, the melt pool becomes kite shaped and the grains form a herringbone pattern. Equiaxed grains can sometime be observed as shown in Figure 1.38e; these are thought to be nucleated by heterogeneous and are not necessarily related to the solidification parameter. Planar growth structures have also been observed at the fusion boundaries since G/R can have high values in this region (Lancaster, 1999). Since solidification is largely directional, McLean et al., (1997) found that identifying adjacent scan tracks and layers during the Laser

Engineered Net Shaping (LENS™) process becomes easy due to changes in dendritic growth.

A preparatory study by Fuesting et al., (1996a/b) indicated that the solidification microstructure of a melt bead produced by SLM could also be influenced by controlling the laser energy density. A series of test coupons (1”x0.5”x0.06”) containing two types of titanium coated ceramic abrasive grit, a nickel alloy matrix and a lower melting point cobalt brazed material, were melted and prepared for metallographic examinations. Fuesting found that energy densities between 2000J/cm² and 4000J/cm² were required to eliminate porosity. Within this range energy densities of 2500 - 3500J/cm² will produce a dendritic microstructure and energy densities in the range of 1900 – 2200J/cm² will produce an equiaxed microstructure. These reported changes in microstructure show an early potential of the process as a method to control solidification, though at this stage, the results are rather crude and differentiated only by large changes in laser energy density.

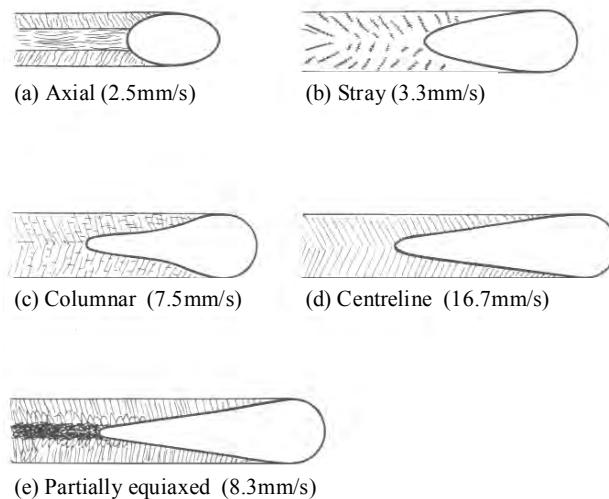


Figure 1.38: The macrostructure observed in flat sections of gas tungsten arc welds in low carbon steel (Lancaster, 1999).

The work by Fuesting et al., (1996a/b) was later continued and refined by Das et al., (1998a/b) who demonstrated more accurate control in the type, scale and directionality of the solidification microstructure with changes in the scanning conditions. However, there was still no direct evidence in the work presented by Das to suggest the sensitivity or reproducibility of these changes. Das further added that powder pre-heating also plays an influential role in affecting the cooling rate of the melt pool. Because no further results were presented, it remains unclear whether the changes in microstructure reported by Das were influenced by laser scanning routines or powder pre-heating. However, the directionality of the microstructure in results presented by Das appears to have been lost, suggesting continued grain growth after the laser heat source has passed. This effect can be observed in a number of papers, each being linked by the use of powder-preheating (Wohlert et al., 1999; Das et al., 1998c/d; Das et al., 1997a).

Finally, Berjeza et al., (1995) has also shown that a transition from a planar front to a cellular structure also forms when observing the solidified melt in a direction normal to the direction of scan. The transitions from a planar front to a cellular structure and from a cellular structure to a dendritic structure were found to occur at dimensional depths of 0.6 – 0.8 ($u = 0.8\text{mm/s}$), 0.8 – 0.9 ($u = 1.7\text{mm/s}$) and 0.9 ($u = 3.3\text{mm/s}$) respectively (see Figure 1.39). Hence, the depth of transition from a cellular to cellular dendritic structure depends on the scan speed, with a decrease in transition depth with decreasing beam velocity. Hence at the solid/liquid boundary the G/R ratio is greatest and a planar front is possible. As the point of interest shifts towards the surface, a cellular structure begins to emerge. However, Steen suggests that this will only occur if convective mixing forces (Marangoni convective forces) are low, implying that a well defined boundary between different solidification microstructures is a good measure that Marangoni convection is not acting in the weld pool.

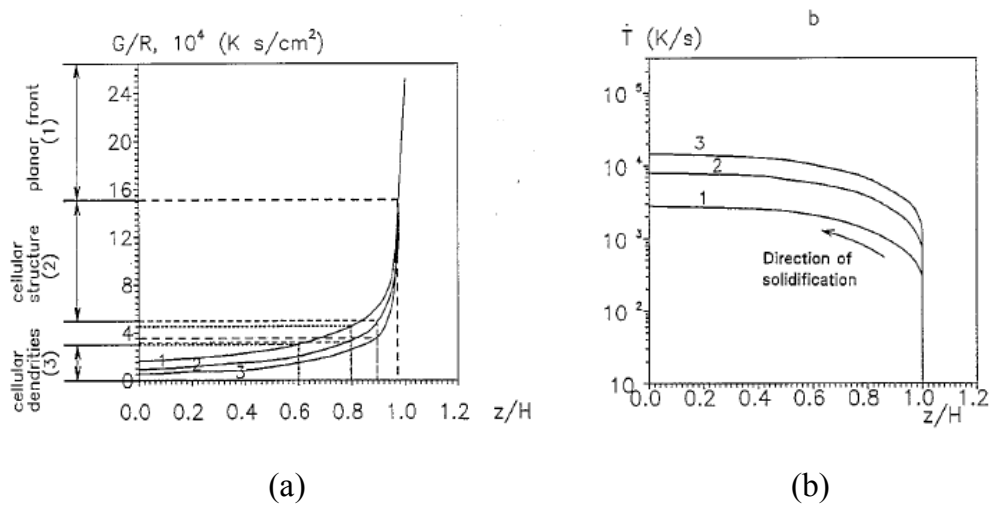


Figure 1.39: The dependence of G/R (a) and T (b) versus dimensionless melt depth z/H at the interface in the plane $y = 0$: (1) $u = 0.8 \text{ mm/s}$, (2) $u = 1.7 \text{ mm/s}$ and (3) 3.3 mm/s (Berjeza, 1995).

Summary of Background

Previous SLM research geared towards the development and production of high density layers and multiple layers by fully melting a pre-alloyed metal powder bed has highlighted the importance of being able to predict melt pool shape and control melt pool stability (Meiners et al., 1999). It has been shown that if these two criteria are met, then among other things, the size of the fusion zone between adjacent melt beads can be maximised leading to minimal or complete elimination of inter-run porosity. This research has led to the recognition of five influential process parameters; environmental, powder characteristics, scanning variants, layer thickness and material properties. Research in other areas, namely laser welding and cladding, have also demonstrated that melt pool shape is adversely affected by the conditions and locality of an underlying substrate. This is likely, though not evidentially conclusive in the literature, to cause two possible outcomes during SLM since construction of objects with overhanging features or with complex geometries can yield melting of powder both local to and remote from underlying layers.

Clearly, each of the properties reported above have been implicated throughout the literature as having strong influences on melt pool behaviour with their effects being linked to what influence each has over melt pool wetting conditions, surface tension

forces and surface tension driven fluid flows. However, this research has also raised many questions concerning the benefits and importance of each. Ongoing studies are debating whether construction and scanning issues or contamination within the surrounding atmosphere and within the powder layer are the more dominant. Nevertheless, it has become apparent in the literature that oxygen concentrations within the powder bed play a decisive role due to the high variability and ease of contamination. However, these concerns are yet to be proven because investigations studying the effects of each of the variables in question are often conducted independently, making discussions and conclusions biased. It is therefore difficult when reviewing the literature to gauge the relative importance of each. It is this lack of a full understanding that has led to the formulation of this research.

Aims and Objectives of the Thesis

This thesis is concerned with the study of the SLS process specifically geared towards stainless steel 314s HC powder processing. Its purpose is to develop an understanding of the dependence of suspended melt pool stability on contamination by oxidation, laser scanning parameters of power, speed, scan spacing and spot size and on the properties of the powder bed. Results from this work will then be used to develop and discuss construction strategies which would become central to future SLS technology scale-up involving the production of large scale tooling (Progression of the SLS technology to large scale production was not part of the objectives of this thesis). To achieve this end it was decided, with full agreement with the industrial partners, that the following research objectives should be met:

1. Observe changes during the heating of the powder and to assess melt pool behaviour over a wide range of scanning conditions. The results are to be presented as a series of process maps.
2. Develop the results in (1) for a number of environmental conditions and bulk powders differentiated by oxygen content and flow characteristics respectively.
3. An analysis of melt pool solidification behaviour for all the conditions covered, aiming towards improving the understanding of solidification and melt pool fluid flow during SLM.
4. Develop mathematical tools which model the behaviour of the melt pool.

Organisation of the Thesis

This thesis consists of five chapters. Chapter one contains an introduction and a literature review. Chapter two describes material, experimental methods and equipment design. This involves powder mixer design, operating protocol, Scanning Electron Microscope (SEM) studies, optical microscopy, and experimental works on a research SLS machine. Chapter three contains the results of the experimental works and microscopy studies described in Chapter two for single track melt pool behaviour studies. Chapter four contains the results from single layer studies discussed in Chapter two. Chapter five discusses the results from the work carried out in this thesis. In this chapter discussions are focused on the effects of the powder bed, environmental control and scanning issues including a discussions concerning their potential impact during large scale production. Chapter five is closed with conclusions and future work.

CHAPTER TWO

EXPERIMENTAL METHODS

Introduction

In order to accomplish the objectives set out in this research (see Chapter 1, Section 1.10) several distinct tasks had to be completed. The first encompassed a number of SLS machine related tasks; including equipment design (see Section 2.3), the compilation of software to perform several duties during machine set-up and scanning (see Section 2.4) and several machine calibration procedures (see Section 2.6).

The second task comprised single track melting experiments, melting experiments conducted under conditions agreed upon by the industrial partners (see Section 2.5.1). Four batches of powder, each differing in particle size and particle size distribution were examined, melted by systematically tracing a series of single line scans in air and argon atmospheres, at different laser powers, scan speeds and scan lengths and remote from solid material or an underlying substrate. The experiment also included depth, width and mass measurements of the tracks, observational studies of melt pool behaviour and surface morphology, comparative studies between the different powder batches and microscopy studies observing changes in the solidification microstructure.

Dimensional measurement was performed particularly to determine the effects of powder, scanning and atmospheric and environmental conditions on melt pool shape and growth. The observational studies have been conducted to gather information about the change in behaviour of the melt pool, forming a foundation on which to construct process maps that detail the melt history of each of the powder batches for single line scanning. The optical microscopy experiments have been carried out to determine the mode of solidification and to help identify the effects of the processing conditions on solidification behaviour.

The third task expanded on the results from task two, with an aim of examining the effects of single track morphological changes on surface roughness and porosity during single and multiple layer construction. The experiments also included observational studies of melt pool behaviour during rastering and dimensional measurements of individual tracks within a layer to verify, or otherwise, that the melt pool morphological changes observed during single track production are also applicable during single and multiple layer construction.

Since it was necessary to consider the role of oxygen on melt pool behaviour, the design and use of environmental conditioning equipment became central to this work. The design required both independent and coupled control over oxygen levels in the powder layer and within the processing atmosphere. The development of equipment was carried out in partnership with a parallel project (see Section 2.3). Initial concepts, the design of a piston assembly and the structuring of environmental control strategies to ensure accurate and repeatable results during operational use of the equipment was the focus of this study.

It was also necessary to design a powder deposition and spreading mechanism for use in the multiple layer experiments. This work was again carried out in collaboration with the parallel project. Several designs for the spreading mechanism and supporting apparatus were generated and prototyped. Each design proved successful for the deposition of the first powder layer, but were found to be unsuccessful during the recoating stages, thereby making multiple layer construction difficult. These difficulties significantly reduced the number of experiments conducted in this area (see Sections 2.3.1.3 and 2.5.1).

Finally, since it was important at the onset of this study to establish a sufficient level of consistency in and between deposited powder layers it was thought necessary to design and use powder mixing equipment to break down agglomerated particles and in doing so, regain particle distribution homogeneity in the stored powder prior to its deposition (see Section 2.3.3). The mixing equipment proved successful, and was found to maximise and balance the particle packing density between deposited powder layers. Previous research has identified that a high variance in particle size distribution and packing density between powder deposits can alter the effects of melt pool behaviour

(see Chapter 1, Section 1.7). The levels of testing required to investigate these observations was outside the scope of this research; however, in order to maintain consistency in a potentially changeable variable, it was agreed by the industrial partners to employ powder mixing prior to all melt tests.

This chapter outlines the materials, equipment, software compilation, experimental procedures and calibration procedures listed above. Section 2.2 describes the experimental powder, Section 2.3 describes the experimental apparatus used in each section of the research, Section 2.4 describes the software compilation and the conditions for scanning, Section 2.5 describes the procedures followed in each case and Section 2.6 describes the calibration procedures and displays the results in each case.

Experimental Powder

The powder used in this research was an argon atomised austenitic stainless steel alloy of type 314s HC, supplied by Osprey Metals Ltd (West Glamorgan, UK). The abbreviation, HC, denotes its high carbon content. A breakdown of the materials composition is given in Table 2.1. The material was selected, as instructed by the industrial partners (Chapter 1, Section 1.1), for its high creep and corrosion resistant properties at elevated temperatures, making it ideally suited for SPF (Super Plastic Forming) tooling manufacture. The melting temperature of the material is approximately 1350°C (Monypenny, 1954). The powder was received from the supplier in four batches, each batch differentiated by particle size distribution; (1) -300+150 μ m, (2) -150+75 μ m, (3) -75+38 μ m and (4) -38 μ m. Each batch will be referred to in this work as 300/150, 150/75, 75/38 and 38 respectively. These distributions were chosen because they are representative of a large proportion of particle sizes typically encountered in the SLM literature and because they differ in flow properties, giving rise to important powder handling issues which will need to be considered upon technology scale-up. Gas atomisation was the powder production method of choice because the particles that are produced are generally spherical in shape, have smooth surfaces and generally exhibit low surface oxidation. These characteristics allow for a more accurate comparison of flow properties between batches and reduce the problems associated with powder contamination (see Chapter 1, Section 1.71).

Table 2.1: Composition of the experimental material.

Elements	Fe	Ni	Cr	C	Si
Wt.%	Bal.	20.0	25.0	0.4	1.0

2.1.1 Storage and Use

The powder was supplied in 5.0kg capacity self-sealing plastic containers (see Figure 2.1). These containers were also used for storing the powder. Used powder was sieved to remove solidified melt debris then stored separately. The spent powder was used only for proving trials and machine calibration procedures where required.

2.1.2 Preparation

The powder was used in its „as received state“ and hence no attempts were made to heat treat the powder, condition the powder by inert gas exposure or add fluxes or lubricants to the powder prior to its deposition and spreading in the build zone, build tray or pin fixture (see Sections 2.3.1.3 and 2.3.2). However, in some experiments the powder was degassed by percolating argon gas through the bed during irradiation (see Section 2.5.2.3).



Figure 2.1: (a) Powder storage container, as supplied and (b) spent and mixed powder storage. A 6inch rule is pictured.

2.1.3 Handling

Powder handling was kept to a minimum throughout the duration of this research. Reasons for this safeguarded approach were twofold. Firstly, to limit the adsorption of contaminants from the atmosphere, and secondly, to maintain the reproducibility of data by limiting particle segregation and exposure during handling. To achieve these ends, the caps of storage containers were only removed when powder was required and the pouring height of the powder from its container into the hopper or build tray was kept to a minimum to limit aeration of the powder.

Experimental Apparatus

2.1.4 Selective Laser Sintering Equipment

Melting of all powder reported in this thesis was carried out using a research SLS machine. The machine was constructed specifically for use in the LAST-FORM programme and was the focus of a parallel research project running concurrently with the work presented in this thesis. Figures 2.2 and 2.3 show an overview of the experimental set-up. An introductory explanation of how an SLS machine works is given in Chapter 1, Section 1.2.

The machine consisted of four principle subsystems; the laser and focusing optics (see Section 2.3.1.1), the X-Y scan head (see Section 2.3.1.2), the process chamber and powder handling apparatus (see Section 2.3.1.3) and finally the motion control table (see Section 2.3.1.4). The control module was centred around a Pentium PC running X-Y scan head driver and calibration software (PC-Mark MT and Postgrid), motion control software for the positioning table (Talk2bus) and software (L-Scan) written specifically for this research to configure system level commands and to generate a list of input commands to control the direction of the mirrors (see Section 2.4).

The remainder of this section details the equipment, arrangement and coupling of each subsystem together with the design of additional equipment to assist in the experimental works listed in Section 2.1.

2.1.4.1 Laser and Focussing Optics

The laser used in this study was a SYNRAD 240 Watt “Duo - Lase®” CO₂ Laser emitting an infrared beam with a wavelength of 10.6µm. The laser head and its control hardware and software was supplied by Laser Lines (Banbury, UK). The laser head consisted of two 60-1 series 125W laser tubes mounted side by side. Each tube is controlled by a water cooled solid state RF power supply, each delivering 1.4kW of RF through two RG 8 type coax cables to the laser head. Within the laser head both tubes feed an optical beam combiner. The beam combiner is nearly 100% efficient in combining the two linearly polarised beams, giving a maximum output power of 250W and a beam mode quality of TEM₀₀ (Transverse Electromagnetic Mode) at 90% purity. However, difficulties with one of the three Synrad DC-100 power packs feeding the RF power supplies reduced the maximum output power to 200W over the duration of this research. Laser lines ensured that only the power output would be effected by this. The laser was water cooled by a closed loop NESLAB CFT-300 re-circulating chiller unit.

The beam diameter at the laser head aperture was 4.4mm. A BEZ 10 beam expander supplied by V&S Scientific Ltd (London, UK), located at a distance of 0.35m from the laser aperture (distance to focussing optic), was used to focus the propagating beam onto the powder bed surface (see Figure 2.3). At the powder bed surface (a distance of 0.85m from the laser output aperture including passage through mirrors) the spot size was 1.1mm. The large spot size was selected as a means to speed up surface coverage during raster scanning. The spot size was fixed throughout the duration of this research.

Power Output Control

In this research the laser power was controlled by the operator. This was achieved by using a Synrad UC-1000 Laser Controller. However, to increase accuracy, a potentiometer and integral 1000 division counter was added which bypassed the factory fitted potentiometer and fascia mounted controller (see Figure 2.5). Calibration of the mechanical scale with the output power rating is described in Section 2.6.2. To avoid toggling delays between power switching and scanning, the gate input on the UC-1000 was provided with a TTL (Transistor-Transistor logic) signal (+3.5 – 5v high and 0 – 0.5V low). The TTL signal, sourced from the computer’s power supply, and modulated

by signals sent from the PCMARK MT scanning software to the X-Y scan head HC/2 hardware (see Section 2.4), synchronised laser toggling with end of scan markers located in the HPGL file(s) (see Section 2.4.2).

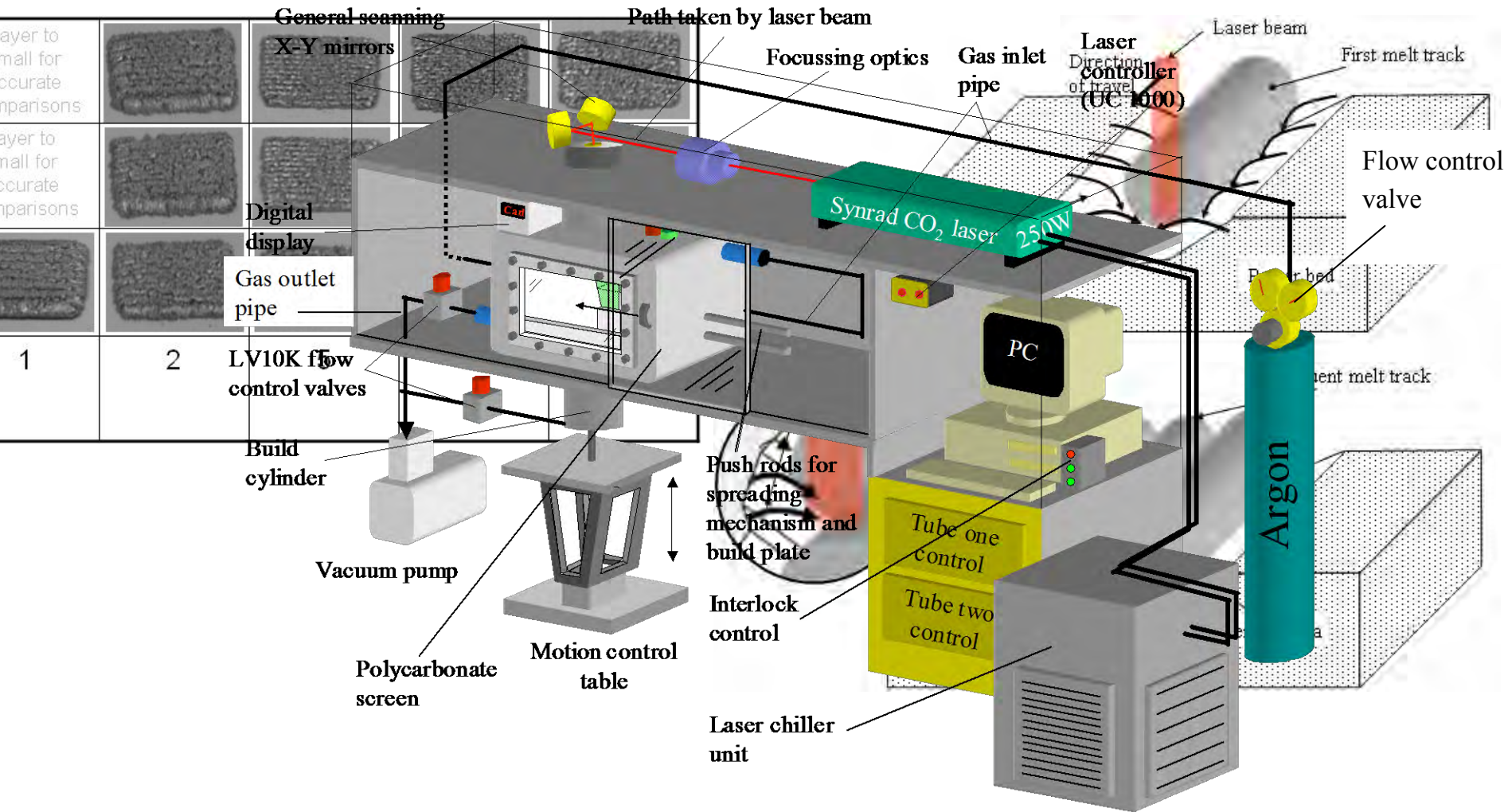


Figure 2.2: Schematic diagram showing the principle subsystems of the SLS research machine.

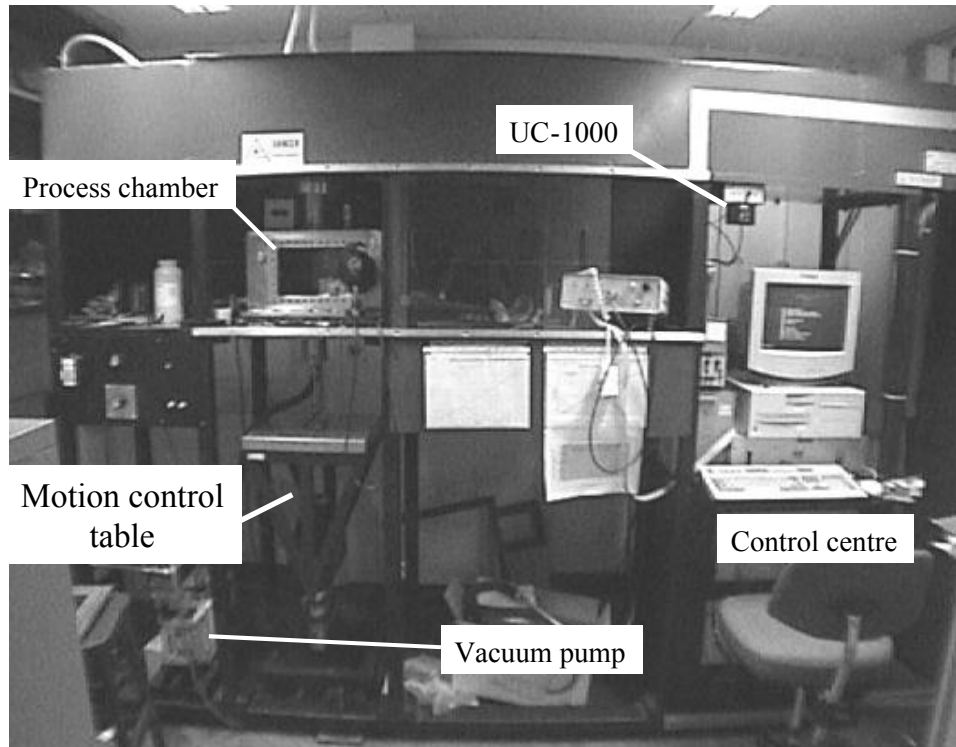


Figure 2.3: Photograph showing the SLS apparatus used to melt powders in this study.

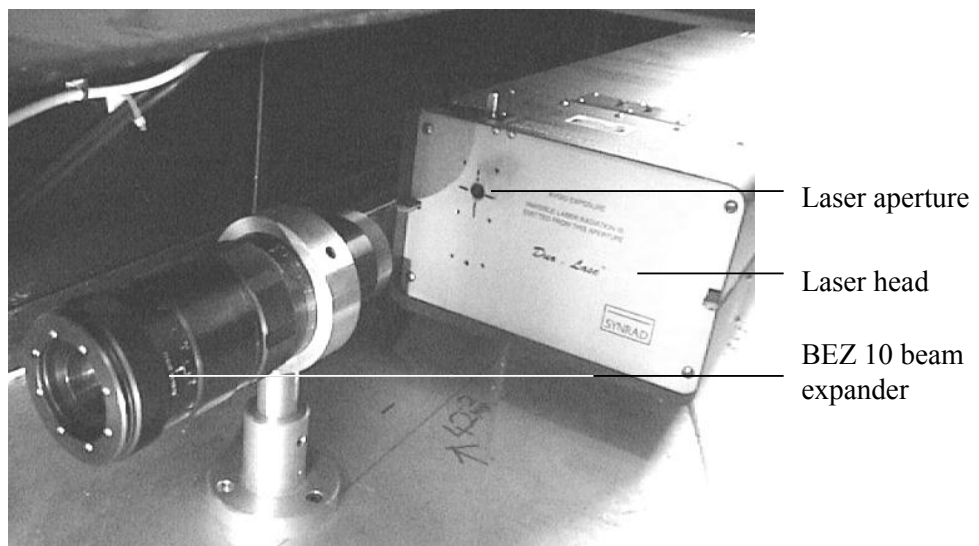


Figure 2.4: Photograph showing the laser head and BEZ 10 beam expander.

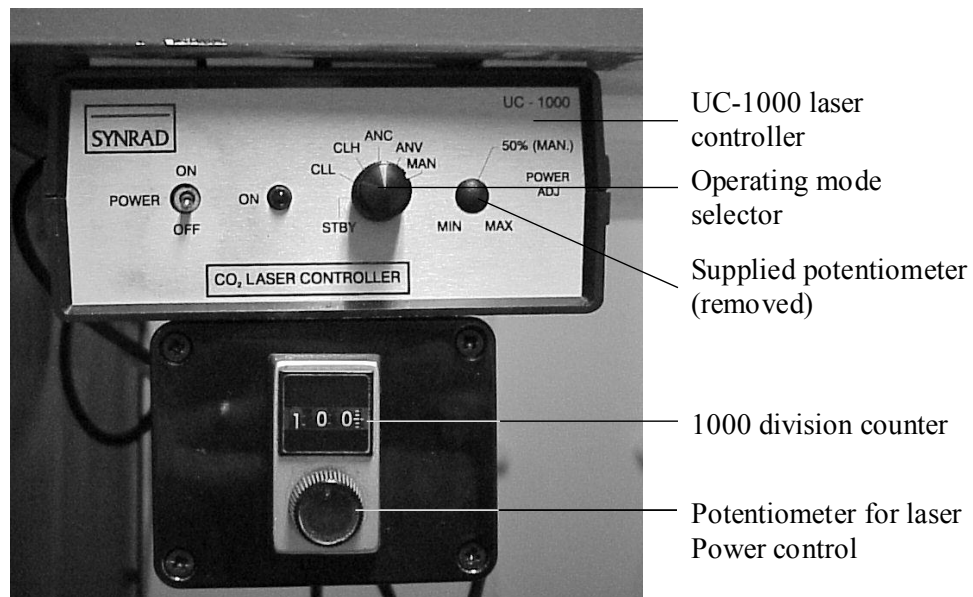


Figure 2.5: Photograph showing the UC-1000 laser controller with the additional potentiometer and numerical counter.

2.1.4.2 X-Y Scan Head

The scan head used to direct the laser beam over the powder bed surface is of type G325DT supplied by General Scanning Inc (Banbury, UK). The mirrors within the scan head are placed orthogonal to each other and each have a scan angle of 40° peak to peak. The lower mirror produces the X scan and the larger upper mirror reflects the X axis in the Y direction, producing the Y axis beam (see Figure 2.6). As the beam passes through the mirrors it translates through 90° and onto the powder bed surface. The movements of both mirrors are achieved by limited rotation closed loop galvanometers which are driven by the Digital Scanner Controller (DSC) and controlled by PC based software (see Figure 2.7). The software programme is called PC-Mark MT and is described in Section 2.4.

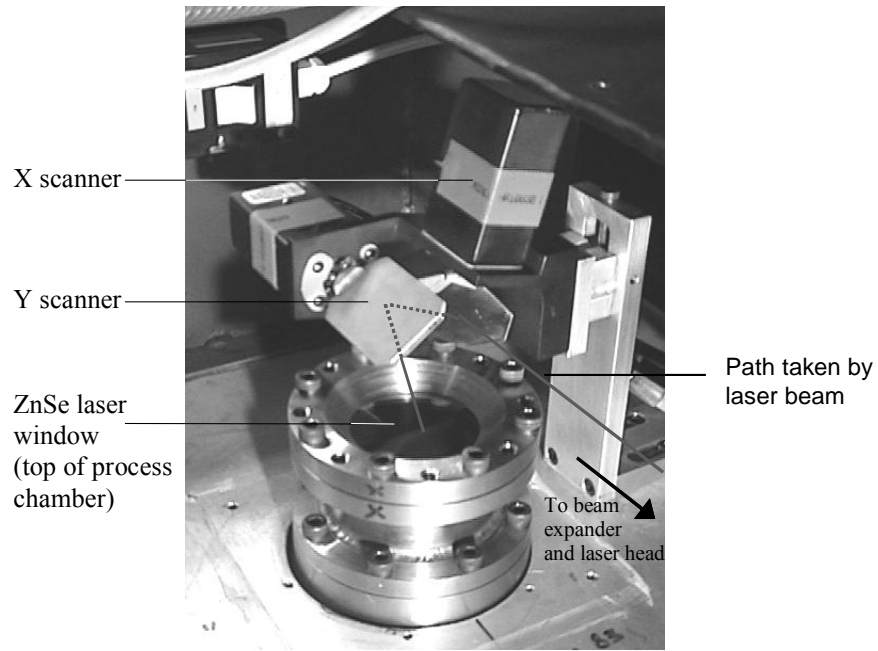


Figure 2.6: Photograph showing the X-Y scan head.



Figure 2.7: Schematic diagram of the X-Y scan head control system.

2.1.4.3 Process Chamber and Powder Handling Apparatus

Figures 2.8 to 2.10 show a picture of the process chamber, a schematic diagram detailing the gas flow through the chamber and pictures of the powder handling apparatus respectively. The chamber and powder handling apparatus were designed to store, deposit and condition, on-demand, layers of powder while maintaining a controlled atmosphere. The process chamber consisted of four key elements; the build chamber, the build cylinder, the powder handling equipment and the build tray. Each piece of apparatus is discussed in the following paragraphs.

Build Chamber

The walls and roof of the build chamber were constructed using 10mm thick stainless steel (AISI 304L) plate which was welded together then bolted to a 25mm thick stainless steel base plate to form an air tight cavity 460mm long, 260mm high and 250mm deep. This cavity housed the powder handling apparatus and two build areas: the build zone and the build tray. A doorway, 250mm long and 150 mm high was machined into the front wall of the chamber to give access to the powder handling equipment and both build areas. During operation an access plate fitted with a polycarbonate viewing window and sealing ring was located over the doorway and secured and sealed to the chamber wall using eight equally spaced M8 cap head bolts. All tapped holes were blind to ensure no leakage at the fixation points during operation.

A 75mm diameter hole was machined into the base plate of the build chamber to give access to the build cylinder and piston unit. The laser beam entered the build chamber through an identical hole machined into the roof of the build chamber. Both holes were located on the same centre line. A 180mm long stainless steel cylinder with flanged ends, a wall thickness of 6.0mm and an inner diameter of 75mm was located on the outside of the chamber roof and was sealed around the upper hole using twelve M8 cap head bolts. The open end of the assembly was capped and sealed using a flanged collar which housed a Zinc/Selenium laser window (see Figure 2.9). The window was sealed into the collar using rubber o-rings.

Inert gas entering the build chamber was regulated using a flow control valve. The exhaust flow was regulated using a vacuum pump and a fine leak control valve, both supplied by Edwards High Vacuum International (Sussex, UK). The vacuum pump

was an RV3 rotary vane pump capable of a maximum pumping speed of 3.3 m³/hour. The pressure inside the chamber was monitored using an Edwards pressure sensor connected to an Edwards Active Digital Display (ADD) unit.

Build Cylinder

The build cylinder had two functions; firstly to house the piston assembly and secondly, to store the deposited powder and the sintered component during multiple layer construction. The cylinder comprised of a 150mm long stainless steel cylinder with a bore ground to a diameter of 75mm. The wall thickness of the cylinder was 6.0mm. A stainless steel flange was welded to the cylinder at one end. The flange was located and sealed to a machined surface on the underside of the build chamber base plate using eight M8 cap head bolts. The opposite end of the cylinder was sealed using a threaded end cap and vacuum seal. The end cap was fitted with a gas outlet pipe which was connected via an Edwards fine leak control valve to the vacuum pump. The end cap also housed a sealed linear bearing, located axially, which positioned the connecting rod which linked the motion control table to the piston head.

The piston head, onto which the powder was deposited, consisted of a conical stainless steel shell which housed a 3065/15M sintered ceramic disc sandwiched between two perforated stainless steel plates. The ceramic disc had a porosity rating of 5µm (P10) and was supplied by Bibby Sterilin Ltd (Staffordshire, UK). The design allowed for inert gas (and not powder) to be drawn from the build chamber, through the piston head assembly, and exhausted through the outlet pipe located in the end cap of the build cylinder. The piston head was moved by the Motion Control Table (see Section 2.3.1.4) An engineering drawing of the piston head is given in Appendix A.

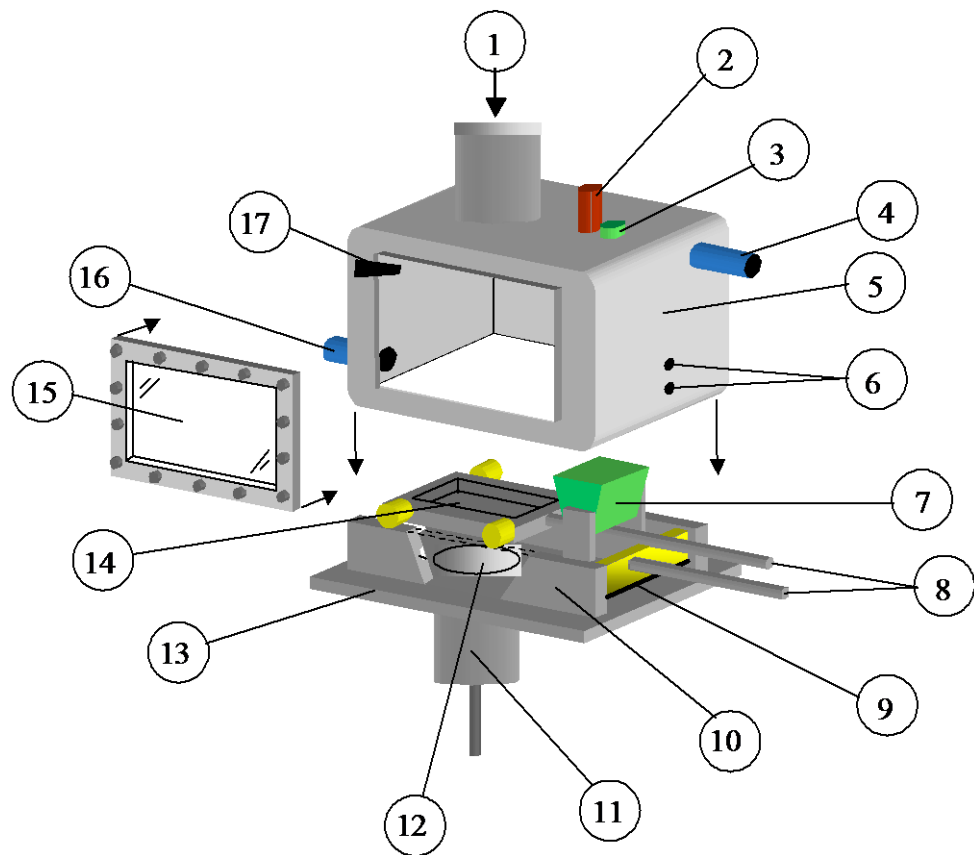
Powder Handling Equipment

The storage, deposition and levelling of powder over the build zone was accomplished using a hopper and wiper blade (see Figure 2.10). The design and use of a counter rotating roller in addition to the blade was also investigated; however, this design proved unsuccessful, and so was not used in the main body of research. The results from studies investigating the use of both arrangements is discussed in detail in Chapter 4.

The blade was made of a 5mm thick stainless steel plate with a round rubber strip (diameter 3mm) bonded to its working edge. The blade was mounted onto a docking cradle which was located between two parallel runners, positioned either side of the cradle using sealed roller bearings. This assembly was designed to ensure smooth passage of the cradle and blade when traversed across the build zone. The cradle was moved using a hand operated push rod which exited through a sealed brass fitting located in the wall of the upper chamber.

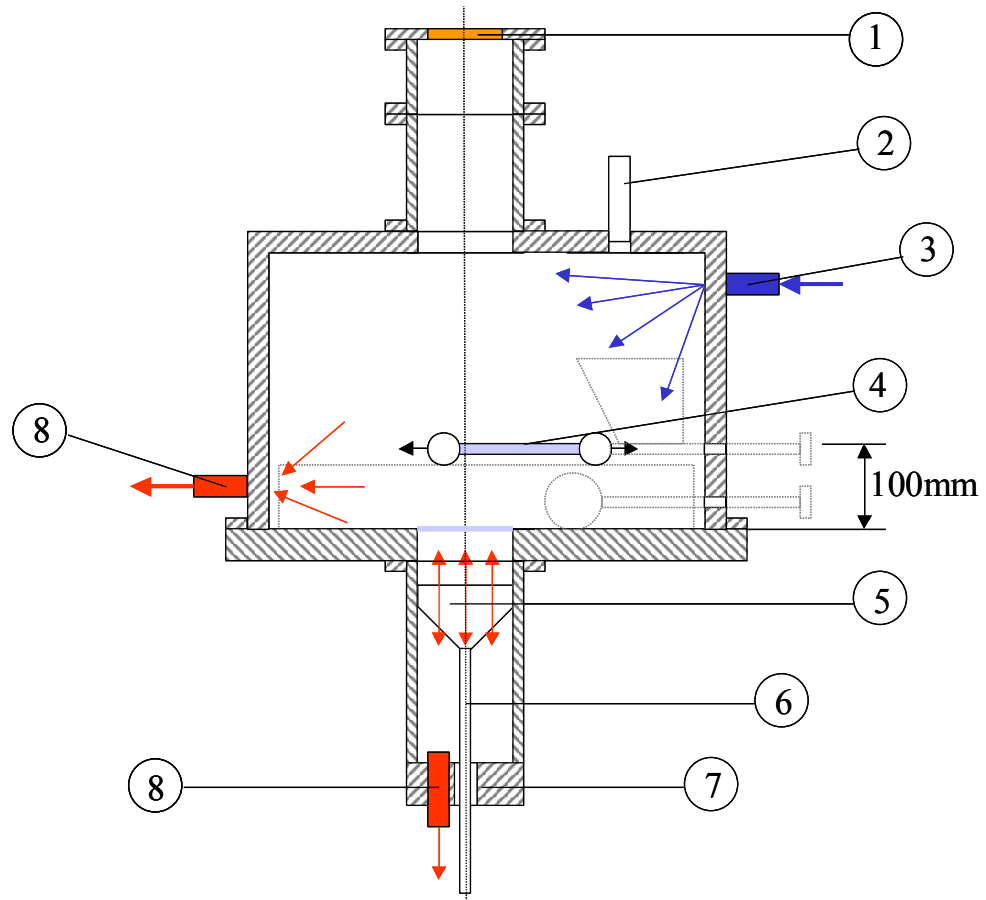
The roller mechanism consisted of a ground 50mm diameter (outer diameter) stainless steel tube which was closed at both ends using weighted end caps. A shaft was welded about the central axis of the roller which located the roller into the docking cradle. Also located and locked onto the axial shaft, either side of the roller, were two 15 tooth spur gears. These gears engaged two 15 tooth driver gears mounted on the docking cradle. Sealed roller bearings were attached to the ends of the axial shaft. The bearings located the roller and cradle apparatus into the parallel runners while the driver gears engaged the toothed racks (6 tpi) running along each side of the build zone. The roller was again pushed by hand across the build zone where the action of the spur gears and rack reversed the direction of rotation of the roller.

The powder used for spreading was stored in a Perspex hopper located inside the chamber. When required, powder was deposited in front of the blade/roller by rotating a spool (through 90°) located at the hopper outlet. The spool had a machined slot which transferred then dropped a predefined volume of powder from the hopper to the front edge of the blade/roller respectively (see Figure 2.10). The spool was rotated by hand from outside of the chamber using a lever and rotary linkage system.



- | | |
|-----------------------------|--------------------------------------|
| 1. Laser beam | 11. Build cylinder |
| 2. Pressure sensor | 12. Build zone |
| 3. Powder inlet | 13. Base plate |
| 4. Gas inlet | 14. Build plate |
| 5. Build chamber | 15. Viewing window |
| 6. Feed thro' for push rods | 16. Gas outlet |
| 7. Powder Hopper | 17. Control handle for powder hopper |
| 8. Push Rods | |
| 9. Deposition blade | |
| 10. Parallel runners | |

Figure 2.8: Schematic diagram of the process chamber.



1. Zinc/Selenium laser window
2. Pressure sensor
3. Argon gas inlet
4. Build plate
5. Piston head
6. Connecting rod
7. Linear bearing
8. Air outlet

- Inert gas flow
- Air flow
- Build areas

Figure 2.9: Schematic diagram showing the passage of gas flow through the process chamber.

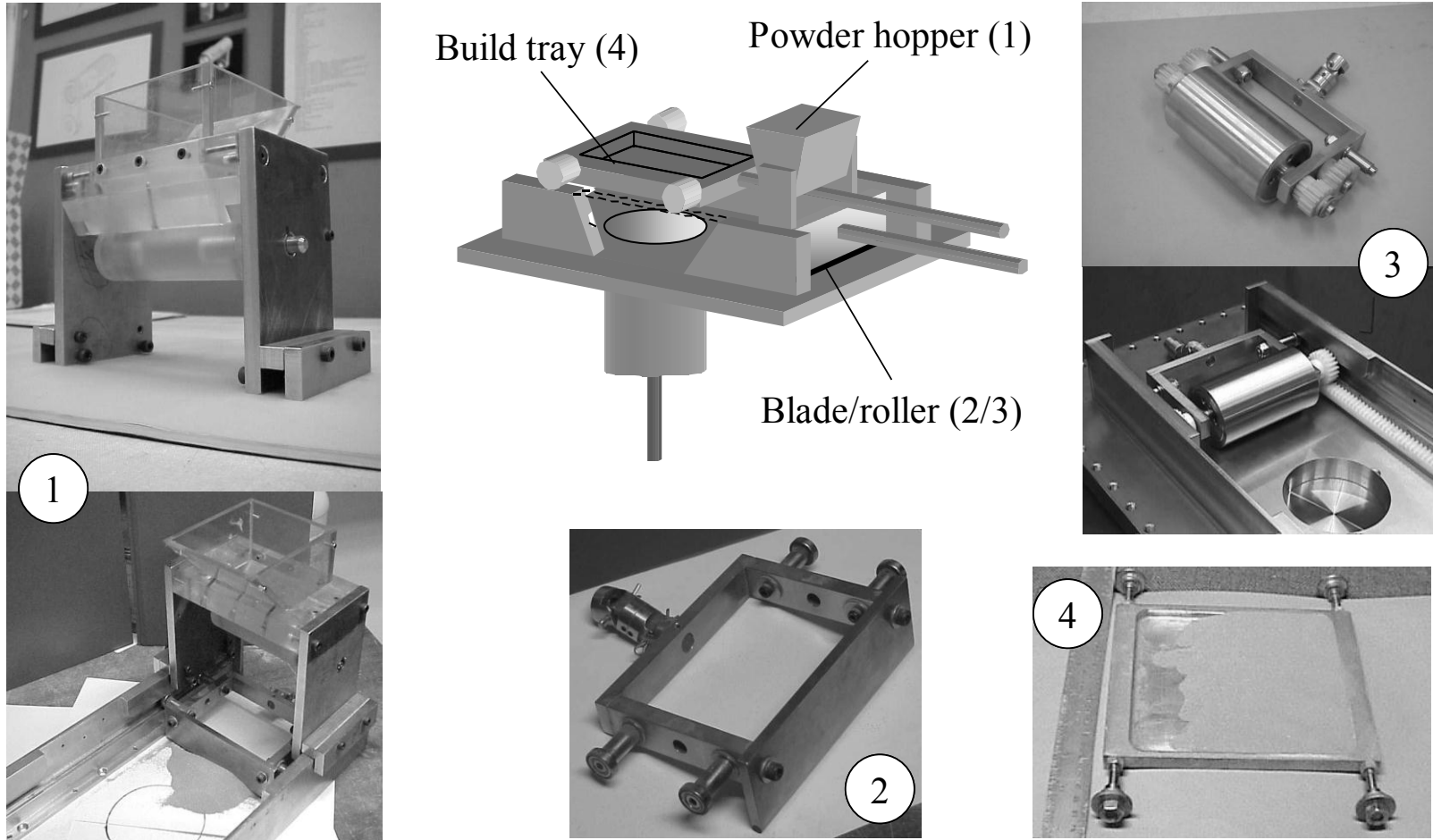


Figure 2.10: Schematic diagram and photographs of the power handling apparatus.

Build Tray

To maximise productivity during a build cycle a tray was used for all single line and single layer experiments which did not require gas percolation. The tray consisted of a 170mm x 140mm x 10.0mm thick stainless steel plate with a machined pocket of dimensions 140mm x 130mm x 7.0mm deep, into which the powder was deposited and levelled prior to the plates insertion into the build chamber. Four flanged wheels fixed to the plate located the tray onto the upper level of the parallel runners housed within the build chamber (see Figure 2.8). Once environmental conditions were established inside the chamber the plate could be traversed across the exposure range to maximise the effective powder layer area (see Section 2.4). The linear movement of the tray was achieved by a push rod which exited through the wall of the build chamber via a vacuum sealed brass fitting.

2.1.4.4 Motion Control Table

The depth change of the powder bed within the process chamber was controlled by a single axis positioning system supplied by Naples Coombe Ltd (Chaddleworth, UK). The equipment was centred around an NC2000 series linear translation stage capable of indexing a load of 150kg over a vertical distance of 250mm while maintaining a guaranteed accuracy of 0.1mm per 50mm of travel. The stage was driven by a servo motor and gearbox (5:1 reduction) while an encoder (accuracy 0.01mm) tracked the position of the stage. Attached to the stage was a 400mm x 400mm mounting platform with an array of M6 inserts onto which was mounted the connecting rod which formed a rigid link between the stage and the piston head (see Figures 2.2 and 2.3). The table was driven by a PC based single axis DMC 1010 motion control card and a Galil DMC 1010 rack mountable enclosure housing an AMC 12A8 brushed servo amplifier. A DOS based software programme, called talk2bus, was used to control the table.

2.1.5 Pin fixture Array

The design and use of a fixture to anchor the first layer of a multiple layer build was found to be successful for reducing layer movements during a multi layer build operation (see Figure 2.11). The fixture consisted of a circular stainless steel block machined to hold an array of pins (standard dressmaker pins), onto which the first layer of a build could be bonded. The block slide fitted into a sleeve forming an adjustable recess into which powder could be deposited. The assembly was then located on top of the piston head where additional holes machined through the pin block still allowed air to percolate through the powder bed.

The design allowed for minimal interaction between the pins and the melt volume so that the behaviour of the melt pool would not be affected by the fixture. An engineering drawing of the pin fixture is given in Appendix A.

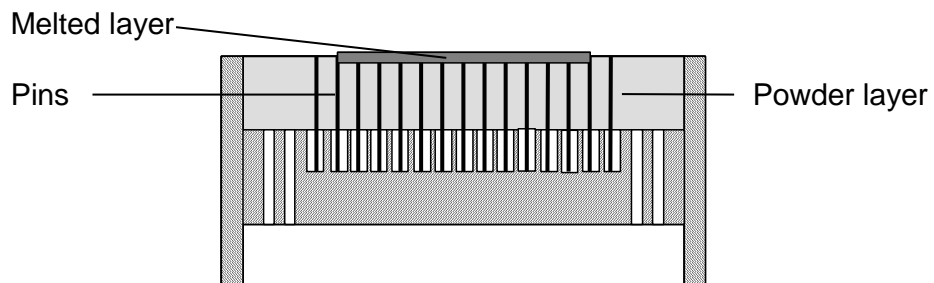
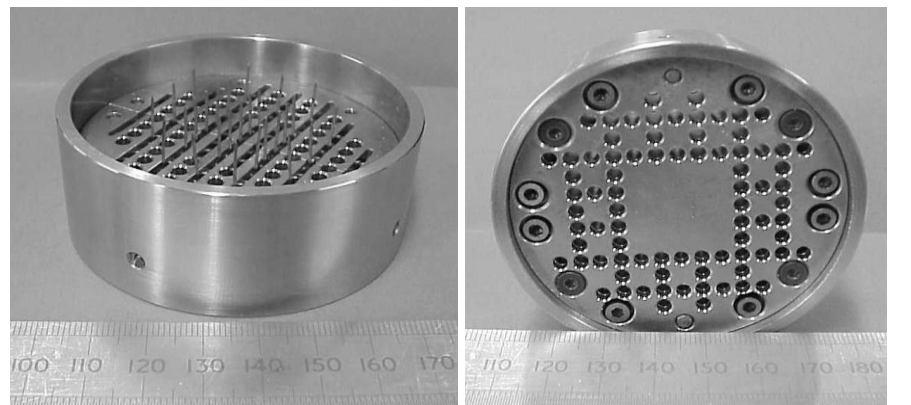


Figure 2.11: Stainless steel pin fixture used for securing the first layer of a multi layer build.

2.1.6 Powder Mixing Equipment

Powder mixing was carried out using a cascade of five v-cone or twin shell mixers designed and built specifically for this study (see Figure 2.12). The design allowed for several different samples of powder or an entire storage container to be mixed simultaneously. Each individual mixer consisted of two stainless steel tubes, cut and welded together to form a 60° V. The open end of each tube was used to load the powder into the mixer cavity before being sealed using a threaded end cap fitted with a rubber o-ring.

Each v-cone mixer was fitted to a central shaft at 72° rotation between each V-cone to minimise vibration during use. The mixer assembly was then turned by placing the shaft between centres of a Harrison lathe; a single v-cone mixer, capable of mixing similar quantities of powder would have been too large to rotate using the Harrison lathe, thereby compromising safety within the laboratory. An engineering drawing detailing the mixer assembly can be seen in Appendix A.

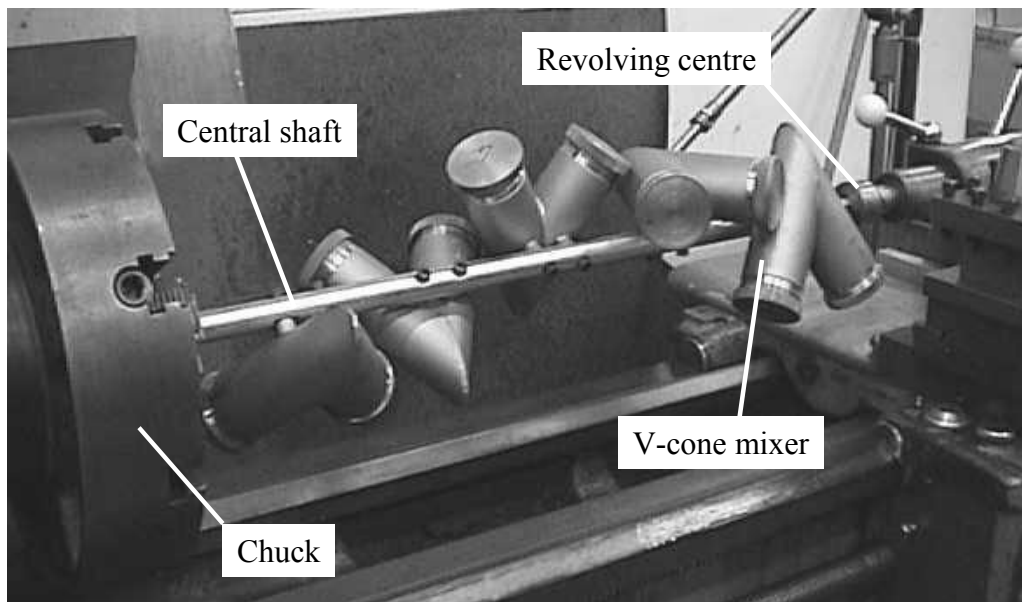


Figure 2.12: V-cone mixer assembly used for mixing of powders.

2.1.7 Microscopy and Materials Preparation Equipment

Two instruments were used for observing solidification microstructure. Firstly, a CAMSCAN CS44EX Scanning Electron Microscope (SEM) with link Systems EDX for image capture was used to observed powder particle shape and particle microstructure. The second was a Leitz Laborlux 12ME ST optical microscope fitted with a micrometer adjustable stage. A JVC digital camera fitted to the optical microscope and linked to a Pentium II PC was used for image capture. The software used for image capture was Image Pro Plus V3.0.

All samples prepared for inspection were cut using a Struers Actum 5 circular cutting machine equipped with a 356CA circular cutting wheel (HV 500 grit). Samples were lapped using a Metaserve 2000 grinding wheel using progressively finer grinding papers (P800 and P1200). Samples were polished using Metalo polishing wheels; firstly using a wheel containing 6 μ m diamond compound, then a final stage wheel containing 1 μ m diamond compound.

Cross sectional images of melt tracks were obtained using a Nikon Shadow graph at x10 and x30 magnification. The smaller magnification being used for the larger melt tracks. The projected image was captured using a Sony digital Mavica camera. Low background lighting during image capture was found to dramatically increase the contrast of the image. A 2mm square graduated grid, placed over the projected image, was used to calibrate the size of the captured image.

2.1.8 Measurement Equipment

The optical microscope with micrometer adjusted stage and a digital vernier calliper was used for dimensional measurement. Both had an accuracy of 0.01mm. An electronic balance with 0.001 grams accuracy was used for all mass measurements.

Scanning and Scanning Software

In this research two scanning techniques were used. The first was a unidirectional traverse to create single tracks (see Figure 2.15a). The second was raster scanning and was used to scan areas of the powder bed to build up layers (see Figure 2.15b). The basic approach to raster scanning and the scanning co-ordinate system adopted in this thesis has been described elsewhere (see Chapter 1, Section 1.2). However, to limit the build up of heat at the start and end of each scanned line, the laser was automatically switched to tickle mode during crossover (see Figure 2.15b). This switching mechanism during scanning is implemented in the commercial DTM SinterStation 2000TM. The size and shape of the raster geometries used in the experimental works are described in Section 2.5.1.1.

PC-Mark MT is the software hub for scanning control. It uses Printer Command Language (PCL) as the control structure. The PCL structure controls all of the scan head features except those used for vector graphics, which are controlled by HPGL (Hewlett Packard Graphics Language) commands. HPGL commands are based on a vector graphics architecture, which comes in the form of points and lines that are geometrically and mathematically associated. Points are stored using the coordinates, for example, a two-dimensional point is stored as (x, y). Lines are stored as a series of point pairs, where each pair represents a straight line segment, for example, (x1, y1) and (x2, y2) indicating a line from (x1, y1) to (x2, y2). Each line can be either active or non active i.e. the mirrors can follow the path of the vector with the laser on or off.

A software programme, referred to in this thesis as L-SCAN, was written at the onset of this research to compile a list of HPGL commands based on dimensional parameters inputted by the user. A programme flow chart detailing the steps used to generate the HPGL code is given in Figures 2.13 and 2.14. Examples of raster scanning routines generated using L-Scan are shown in Figure 2.15. The dashed lines in Figure 2.15 describe the route taken by the laser spot when in tickle mode. An example HPGL data file can be seen in Appendix B.

2.1.8.1 Scan Length and Laser Beam Offset

Dimensional accuracy was not considered nor investigated in this work. However, scan length accuracy was important for scan speed calibration procedures (see Section 2.6.1). As the beam scans using its centre as the reference point, excess material at the ends of each scanned line will melt and affect the dimensional accuracy. To compensate for this error, twice the beam offset needs to be subtracted from the scan length. The offset is equal to the radius, $2a$, of the laser beam i.e. an equal offset, a , from both ends. Figure 2.16 shows an intended size and the excess dimension due to the beam offset. L-Scan automatically configured the HPGL file(s) to compensate for this over sizing effect. Scan speed calibration procedures are given in Section 2.6.1.

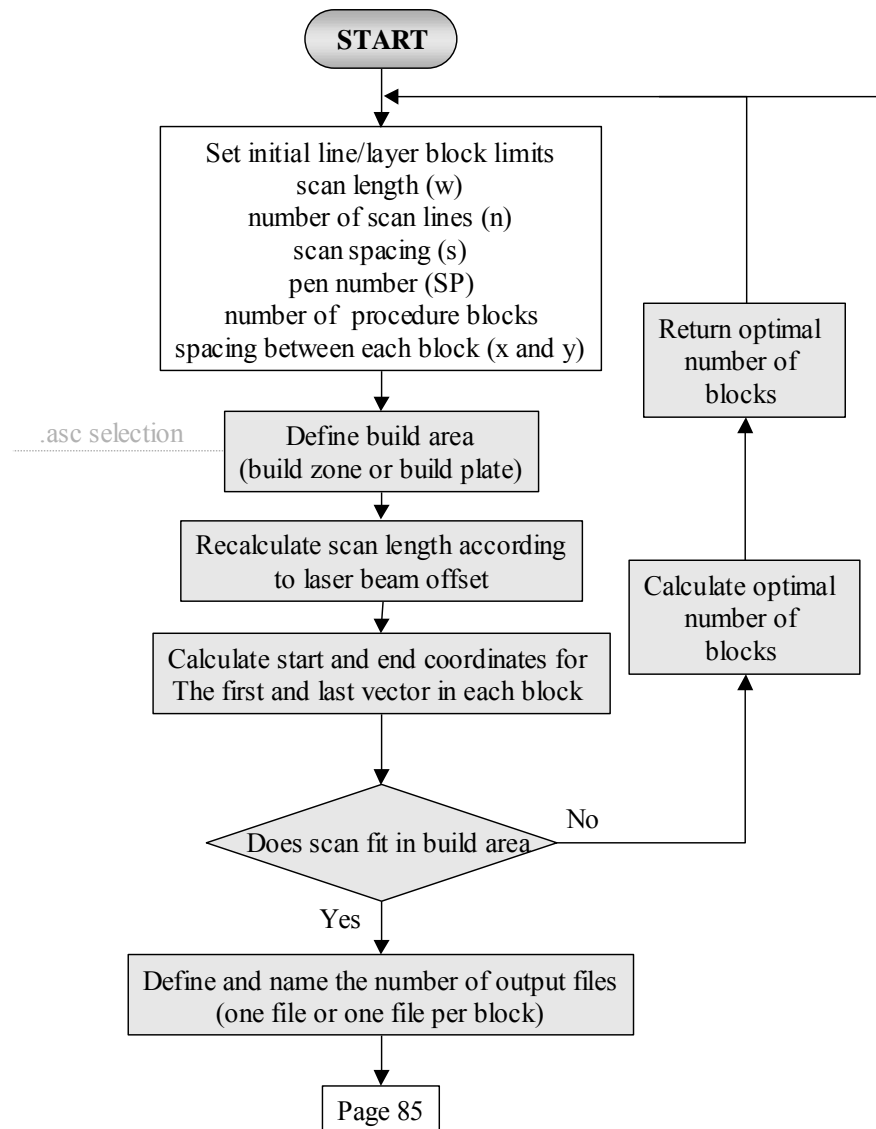


Figure 2.13: Programme flow chart for HPGl file generation (Part A).

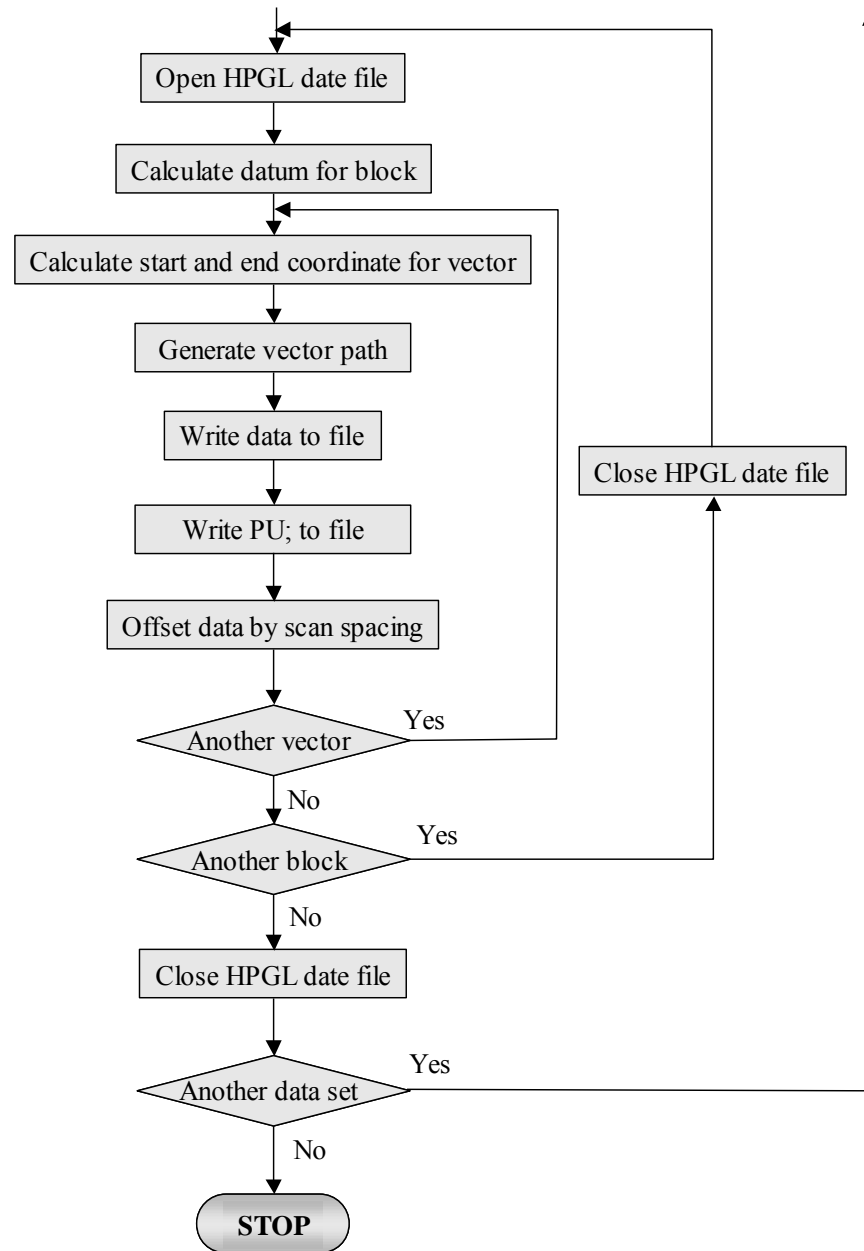


Figure 2.14: Programme flow chart for HPGL file generation (Part B).

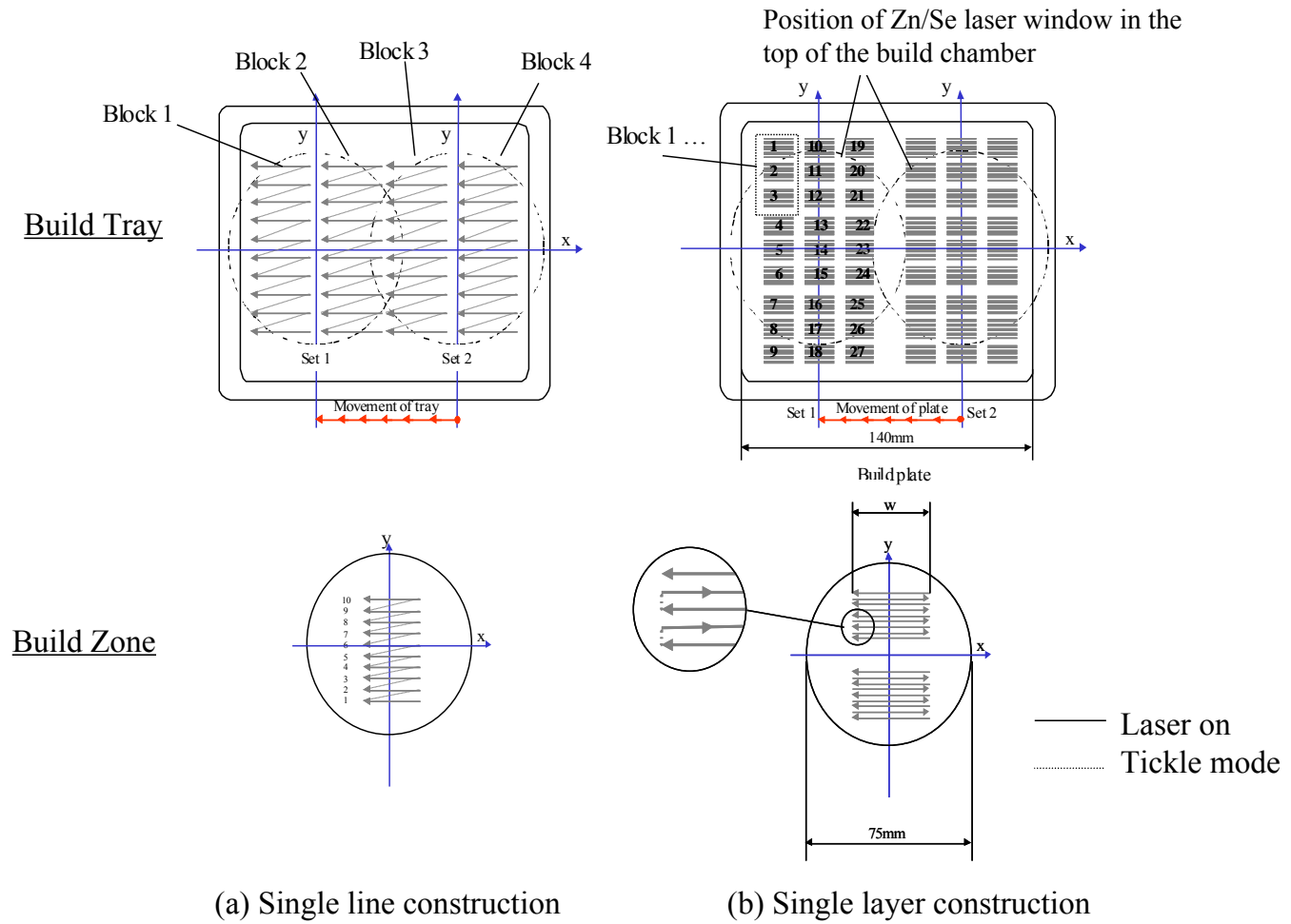


Figure 2.15: Example scanning routines (a) single lines and (b) single layers.

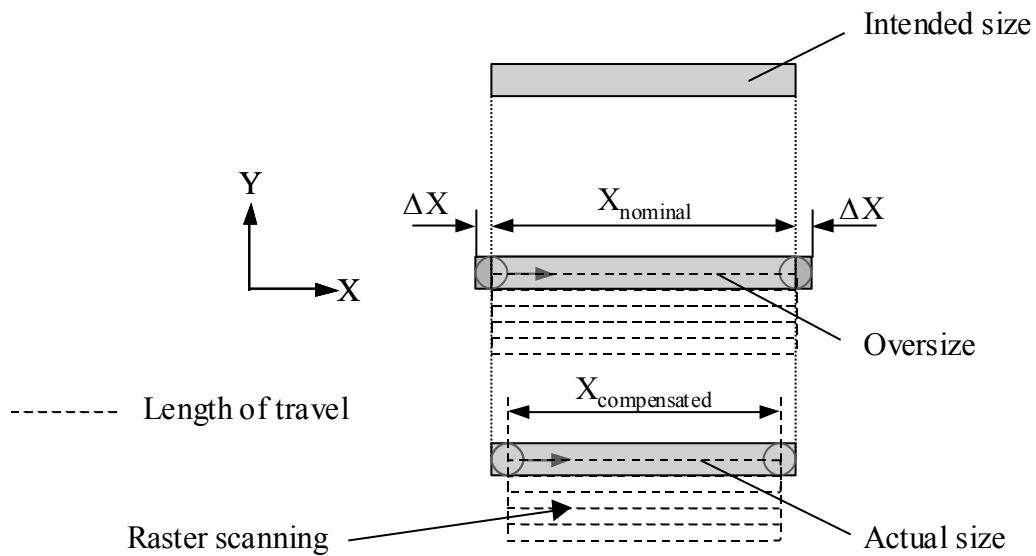


Figure 2.16: Intended size and excess dimension due to beam offset.

Experimental Procedure

All test conditions were carried out using three different environmental conditions, four batches of stainless steel powder (environmental conditions are described in Section 2.5.2 and the powder characteristics and composition for each batch is described in Section 2.1) and a range of laser scanning conditions (see Section 2.5.1.).

2.1.9 Scanning Conditions

A simple unidirectional traverse was used to mark a series of tracks in the deposited powder layer (see Figure 2.15). The scan speed was varied from 0.5mm/s to 50mm/s and the laser power was varied from 8W to 190W. The specific conditions are charted in Figure 2.17. In Figure 2.17 the laser power conditions appear arbitrary in nature. However, they have been selected based on results from the laser power calibration procedures described in Section 2.6.2. The other scanning conditions and mirror parameters, which remained constant for all tests, are listed in Appendix C.

The length of the tracks were also varied from 5mm to 100mm (in steps of 10mm), in order to observe the effects of scan length on melt behaviour. The spacing between each track (centre to centre) was assigned a value of 8mm throughout all

testing to ensure no interaction between neighbouring melt tracks. A one minute cooling down period was also enforced between the laser off command at the end of one track to the laser on command at the start of another to minimise the potential effects of changes in powder bed temperature caused by a localised heat affected zone. Finally, a minimum powder layer thickness of 7mm was also employed during all single layer experiments to ensure that the melt volume was not influenced by or interacted with the top of the piston head or the base plate material of the build tray.

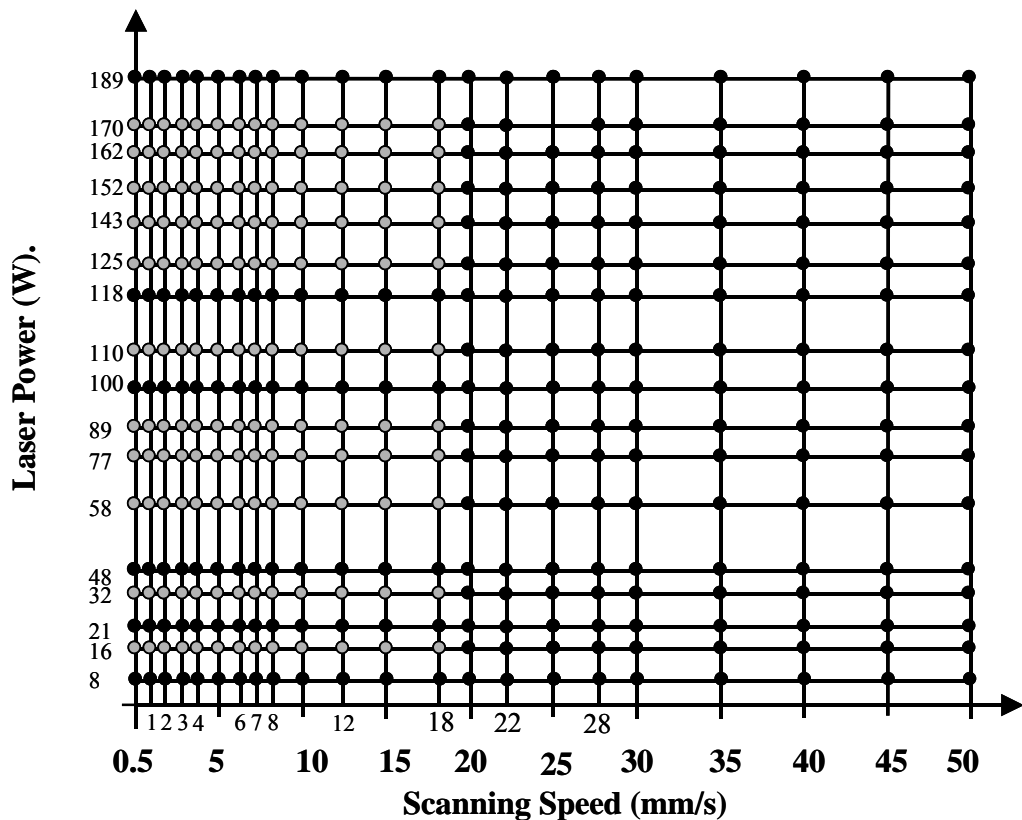


Figure 2.17: Chart showing the scanning conditions used during the experimental works. Each node represents 1 of 374 different conditions.

Tracks produced at conditions represented by grey nodes were also used for dimensional and mass measurement and for testing the repeatability and reproducibility of results (particle size dependant).

2.1.9.1 Single Layer Test Conditions

All single layer experiments were carried out using scanning conditions selected based on the results from single track experiments described in Section 2.5.1. In addition to these conditions, scan spacing's of 0.75, 0.5, 0.25 and 0.1 were used together with scan lengths ranging from 5mm to 100mm and the number of rastered tracks ranging from 2 to 50 (depending on space within the build area). The values of scan spacing represent the fraction of melt pool overlap; hence, the scan spacing was measured with reference to the width of the melt track produced for a given set of conditions rather than with reference to the beam diameter. This method was thought necessary since the width of the melt track was highly variable and in most cases was larger than the spot diameter.

When using the build tray, a large number of samples could be constructed within one environmental purge cycle, during which, the build tray would heat up to temperatures which would require careful handling of the plate after processing. Therefore, to maintain good repeatability of results and impose safe handling, the number of coupons produced on the build tray was restricted to a maximum of 10 when the scan speed was less than 10mm/s and the laser power was greater than 80W.

2.1.9.2 Multiple Layer Test Conditions

Multiple layer tests were conducted in three stages. The first stage was the construction of multiple layer objects using the roller mechanisms (see Section 2.3.1.3) and the build zone. The second stage tests were conducted using the wiper blade and build zone. The final series of tests were conducted using the wiper blade and pin fixture (see Section 2.3.2). All multiple layer experiments were carried out using scanning conditions selected based on the results from single layer experiments described in Section 2.5.1.2. In addition to these conditions several values of layer thickness were chosen, 0.25mm, 0.5mm, 0.6mm, 1.0mm and 1.5mm and each remained fixed for the duration of a build. The number of layers within a build was also varied between 2 and 16.

2.1.10 Environmental Conditions

2.1.10.1 Air Atmosphere

The air atmosphere was typical of a laboratory atmosphere and was achieved by removing the door of the process chamber during scanning. For safety reasons a polycarbonate screen was slid across the build chamber opening to scatter any reflected laser light (see Figure 2.2).

2.1.10.2 Argon Rich Atmosphere

An Argon rich atmosphere was achieved by a combination of build chamber evacuation (to approximately 50mbar gauge pressure) followed by an argon gas purge until local atmospheric pressure was re-established. This procedure was repeated twice before balancing the flow rate of argon through the build chamber at a slight overpressure (50mbar). Since no flow gauges were available, to maintain consistency the flow rate was balanced at the maximum pumping speed of the vacuum pump (see Section 2.3.1.3). The inlet flow from the gas bottle was regulated using the LV10K flow control valve connected to the outlet flow of the build chamber (see Figure 2.2). The flow control valve which controlled the out gas flow from the build cylinder remained closed at all times.

Once the flow rate through the build chamber was balanced the build chamber was left for a 10 minute settling period before laser exposure. These conditions were maintained throughout the duration of each experimental test and during a 5 minute cooling down period at the end. The total cycle time for build chamber conditioning prior to laser exposure was 25 minutes. The argon was supplied by BOC and was bottled with a 99.9% purity. Trace elements of other gases, particularly oxygen, are still likely to reside within the build chamber. However, it was thought that the three environmental conditions chosen for this work were sufficiently diverse to warrant evading the measurement of trace gasses. Evacuation was found to be essential to increase cycle time and to improve the consistency of results.

2.1.10.3 Argon Rich Atmosphere with Argon Percolation

An argon rich atmosphere with argon percolation was achieved using the same procedures outlined in Section 2.5.2.2. However, the flow of argon through the chamber was balanced using the flow control valve connected to the outflow of the build cylinder; allowing purged argon to be drawn through the powder layer and expelled through the gas outlet in the build cylinder. The flow control valve connected to the out flow of the build chamber was closed at all times.

During the deposition and spreading of each fresh powder layer the build cylinder flow control valve was momentarily closed. If the bed remained fluidised during the recoating cycle, the deposited powder layer was found to have reduced surface quality with large areas of open porosity. Between each recoating cycle the system was left for a 10 minute settling period before laser exposure to maintain consistency between the first deposit layer and all subsequent layers.

2.1.11 Repeatability of Results

The repeatability of results is defined in this work as the consistency of the melted tracks for any given powder deposit and at any given point in time within the purge cycle. The reliability of data from testing is important when comparisons between different tests are required. Therefore it was important at the onset of this study to establish and maintain a sufficient level of consistency in the melting results.

To test the repeatability of the data three tracks were produced on the same powder sample using the same scanning conditions and over a three minute time frame within the purge cycle. The tests were carried out as outlined in Section 2.5.1.1. Each track was then measured, weighed and any surface irregularities recorded. The range of conditions used for repeatability testing are represented by grey nodes in the scanning parameter chart of Figure 2.17. However, not all conditions displayed in this chart created tracks suitable for measurement. The range of conditions available for measurement fluctuated depending of the powder batch being used.. These tests were repeated for all four powder batches and all three atmospheric conditions.

2.1.12 Reproducibility of Results

The reproducibility of the data is defined in this work as the consistency of the melted tracks produced using different powder deposits from the same batch and after prolonged atmospheric conditioning. Reasons for the importance of the reproducibility of the data are as follows:

1. Testing was carried out over many atmospheric conditioning cycles.
2. Gas purging was often continuous for up to 2 hours when using the build plate.
3. Many powder samples were used, and
4. Testing was performed over a period of two years (for all melting experiments presented in this thesis).

To examine the reproducibility of data the results from tests described in Section 2.5.3 were repeated for different powder deposits; once after a 15 minute purge and once after a 90 minute purge. The tests were also conducted using the air atmosphere to ensure powder and environmental comparisons were being made between reproducible results. To monitor the reproducibility of data, control data was taken at three intervals over the two year period. The results are presented in Chapter 3.

2.1.13 Dimensional Measurement

Dimensional measurement was carried out in the y and z directions of single tracks, when on their own and within single and multiple layers. These parameter settings have been described in Section 2.5.1. The equipment used for dimensional measurement was a digital vernier calliper and optical microscope. Both pieces of equipment have been described previously in Section 2.3.4.

2.1.13.1 Single Tracks

Dimensional measurement of melt tracks was carried out in two steps. The first step was measurement of track width and depth in the y and z directions using the digital vernier calliper. Three positions were selected to be measured for each direction, at the middle and at the ends. The positions of each, shown in Figure 2.18, are numbered Y_1 , Y_2 and Y_3 and Z_1 , Z_2 and Z_3 . The variance between each measurement was calculated and used to evaluate melt track uniformity. The second step was to

section and mount each track in a direction perpendicular to the direction of scan and measure the y and z directions using the optical microscope. Specimen preparation procedures are outlined in Section 2.5.6. The prepared samples were placed onto the microscope stage and secured using plasticine. Crosshairs superimposed onto the eyepiece of the microscope were used to reference the position of the sample as the stage was traversed using the x and y stage micrometers. The second measurement step allowed for a more precise measurement and could take into account any powder particles attached to the core melt volume.

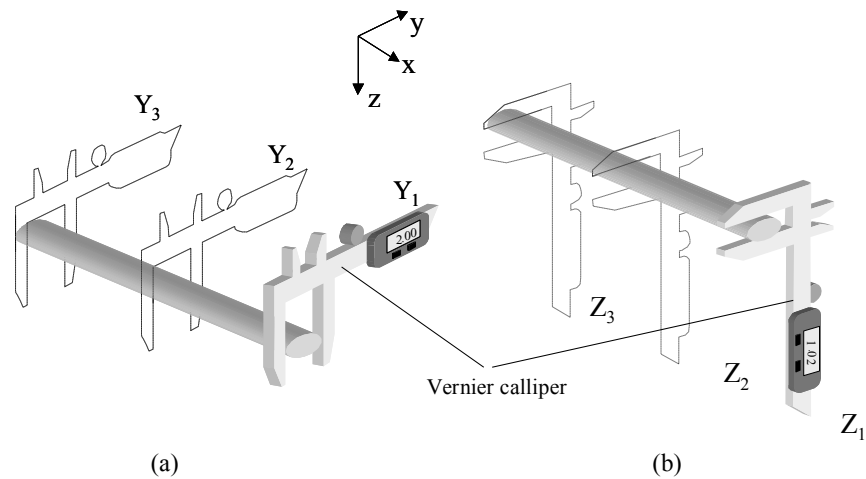


Figure 2.18: Position of measurement for single tracks.

2.1.13.2 Single and Multiple Layers

Dimensional measurement of single tracks within layers and multiple layers was carried out by sectioning and measuring using the optical microscope. The procedure has been previously outlined in Section 2.5.5.1.

2.1.14 Sample Preparation for Microscopy Inspection

2.1.14.1 Powder

In preparation of specimens for the SEM, a small sample of powder from each of the powder batches was taken and independently mounted by suspending the particles in a solution of Epofix resin and Hardener (Struers). Left overnight the resin hardened to a clear translucent solid. The surface of the resin was then ground until the suspended powder particles became exposed. Polishing of the sample then took place as outlined in Section 2.3.4. The epoxy mount was then glued to a conductive fixture. A track of graphite paste was then applied between the polished surface and the conductive fixture before placing the sample into the SEM.

Specimens containing samples selected from the 300/150 and 150/75 powder batches were etched by placing the specimens face down in Marbles Reagent (10g copper sulphate, 50ml HCL and 50ml distilled water) for a period of 30 seconds. Specimens containing powder samples from the 75/38 and 38 batches proved difficult to etch due to differences in cooling rate between small and large particles.

2.1.14.2 Melt Tracks

Single line scan tracks were sectioned parallel to the direction of scan and in a direction normal to the direction of scan (see Figure 2.19). The tracks were cut using a Actum 5 (Struers) equipped with a 356CA cutting wheel containing HV 500 grit. The cut specimens were mounted in Bakelite then lapped with progressively finer grit papers. The specimens were then polished then etched as outlined in Sections 2.3.4. and 2.7.7.1 respectively.

2.1.15 Measurement of Grain Size

The grain size was measured by the mean linear intercept method (MLI) as outlined by Pickering, (1975). In this, the MLI was measured from a linear traverse by counting the number of boundaries which intercept the traverse of known length, L . This was achieved by capturing the area of interest using the microscope and image capture software. The image was then blown up and a line of known length, relative to the image, was arbitrarily drawn across the image. The MLI is given by:

$$\bar{d} = \frac{L}{N} \quad (2.1)$$

where N is the number of intercepting boundaries.

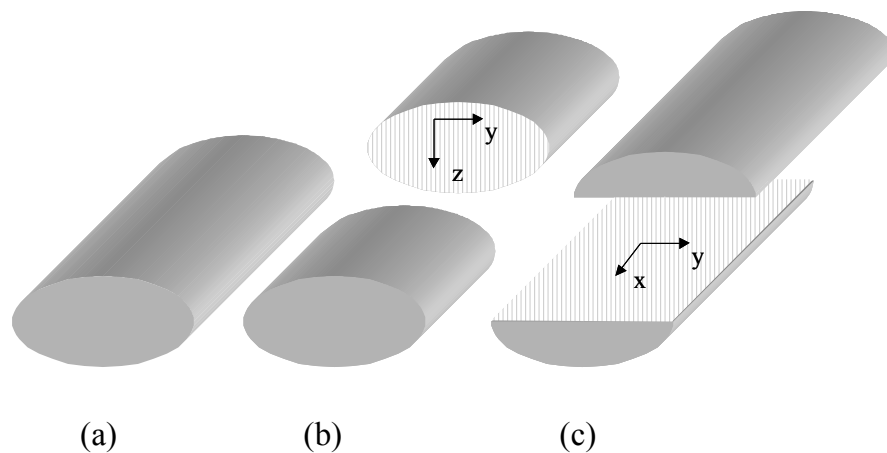


Figure 2.19: Area cross-sections of single lines for microscopic inspection.

2.1.16 Powder Mixing Procedure

Powder was poured from its storage container into a glass beaker until a pre-marked limit line was reached. The limit line corresponded to a 25% fill capacity when the contents were transferred to one of the v-cone mixers. German, (1994) suggests that a powder volume between 20% and 40% of the mixer's total capacity is usually optimal. The powder was then mixed for a period of 15 minutes at a rotational speed of 120rpm. The time period was chosen based on results from the powder mixing calibration results (see Section 2.5.9.1 and Chapter 3, Section 3.2) and the rotational speed was calculated using equations given in Appendix A.

2.1.16.1 Mixing Time Calibration

Powder mixing time was investigated by comparing the powder density variance with mixing time for sixteen randomly selected storage containers from a possible forty (four from each batch giving a total of four sets of experiments - A, B, C, D). Each of the sixteen containers had their contents equally split into five smaller samples, giving a total of 80 samples. Each of the five samples were taken from different heights in the container so that the effects of particle segregation could also be monitored (see Figure 2.20). Before mixing, a small shot of powder was removed from each of the 80 samples and used for control purposes.

Each of the five samples were placed into separate v-cone mixers and mixed for 7.5, 15, 30, 45, and 60 minutes and at a fixed rotational speed of 120rpm (see Appendix A). The mixing times were cumulative, and so at the close of each time segment, rotation of the mixer was paused and a small shot of powder was removed for density measurements. At the end of 60 minutes the volume of powder remaining in each of the five mixers was still greater than the lower mixing efficiency limit of 20% of the total mixing volume.

After mixing each shot of powder was deposited into a machined nylon cup; 10mm deep and 70mm in diameter (inner). Deposition occurred by placing the nylon cup on top of the piston assembly in the process chamber (see Section 2.3.1.3). The shot of powder was placed in front of the wiper blade then spread across the build zone, filling the cup from right to left (see Figure 2.21). The weight of the powder, w , was measured using an electronic balance with 0.001 grams accuracy. The volume, V , of the cup was measured using a digital vernier calliper. The density of each shot was calculated according to equation 2.2;

$$\rho = \frac{w - w_c}{V} \quad (2.2)$$

Where w_c is the weight of the cup. The average density of the powder contained within one storage cylinder was then obtained by applying equation 2.3 with $n=5$.

$$\bar{\rho} = \frac{1}{n} \sum_i^n \frac{w_i}{v_i} \quad (2.3)$$

where $\bar{\rho}$ is the average density and the index i is the number of the part, 1 to n . The results from the calibration tests are given in Chapter 3, Section 3.2.

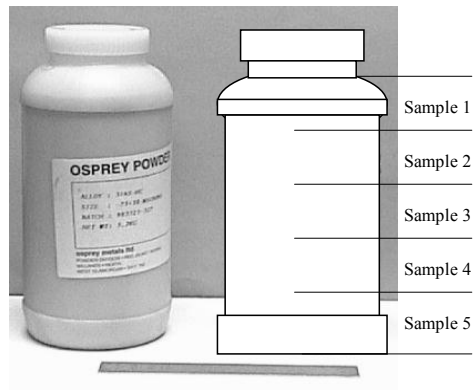


Figure 2.20: Showing relative position and sample identity numbers of powder samples taken for mixing calibration.

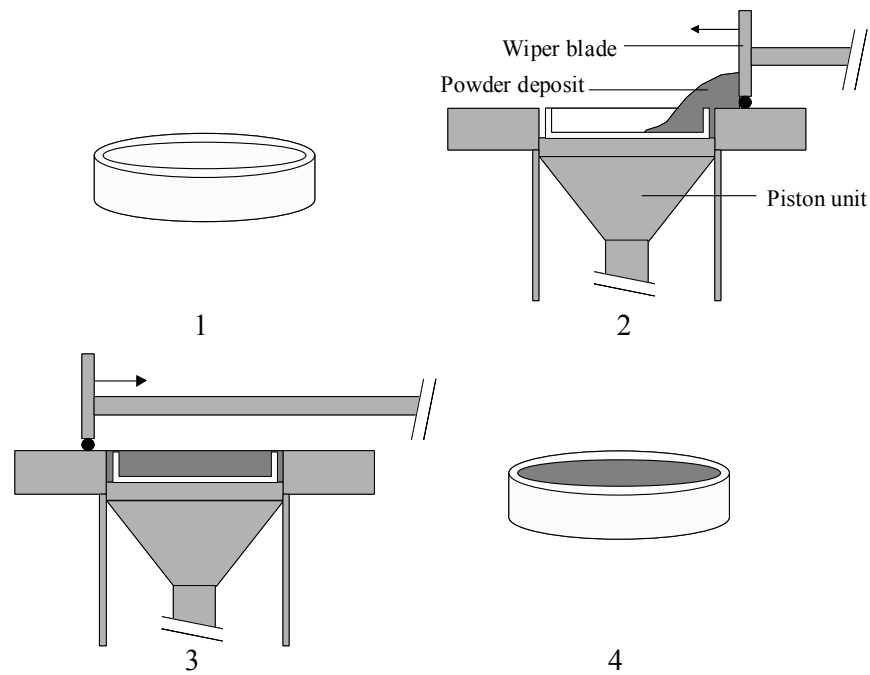


Figure 2.21: Filling of nylon cup during powder density calibration.

Machine Calibration Procedures and Results

2.1.17 Galvanometer and Beam Velocity

The velocity of the beam over the powder bed surface (for both build areas) was calculated using the procedure and equations given in Appendix C. The equations were used to generate look-up tables (see Appendix C) containing data to allow easy configuration of the mark parameter settings in the PC-Mark MT software (see Section 2.4).

The accuracy of the calculated results were compared with experimental values. The experimental values were obtained by measuring the time taken for the laser spot to pass between two fixed points located on the powder bed surface. Both the build zone and the build tray were used in the experimental testing. The distance between the points remained fixed at 70mm, but the test run was carried out at different locations within the powder bed.

Although a small variation did occur between the experimental and calculated results (see Figure 2.22), the differences were thought not to be significant for two main reasons. Firstly, it was evident that the greatest variance occurred when the scan speeds were high, suggesting that the increase was caused by discrepancies in the hand-eye reaction time when required to start/stop the digital timer at the start/end of each scan. Secondly, the experimental testing discussed previously in Section 2.5 was centred around scan speeds no greater than 20mm/s, an area showing less than 1% deviation in the experimental results. Finally, no speed variations, other than those accountable through experimental error, were recorded in experiments carried out at different locations within the powder bed.

2.1.18 Laser Power

The laser power output was calibrated using a laser power probe with a $\pm 5\%$ accuracy over 500W. The probe was supplied by L.G. Products Ltd (Slough, UK) and was calibrated by them prior to dispatch. The power of the laser was measured by placing the heat sink of the power probe into the path of the laser beam at a position approximately 150mm above the build zone. This position was not critical provided it was at a location sufficiently away from the focal point of the laser. At the focal point

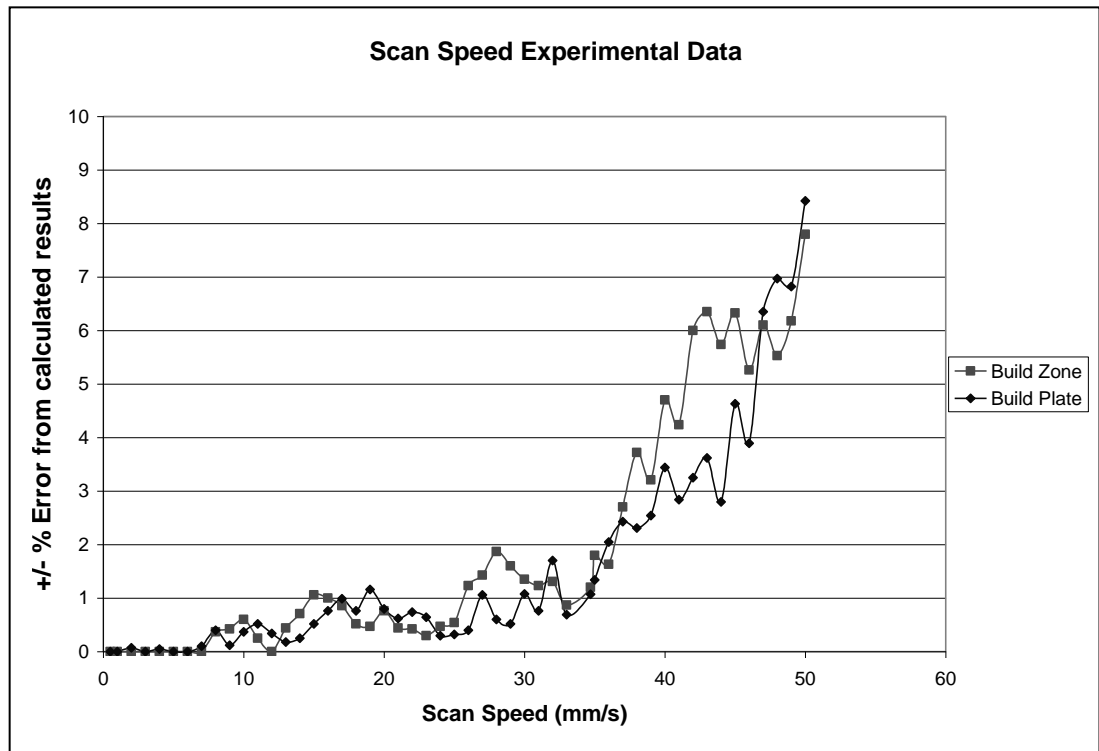


Figure 2.22: Deviation of scan speed experimental results from calculated results.

the high heat intensities could damage the surface coating on the heat sink, compromising the accuracy of the probe.

The probe was exposed to the stationary beam for a period of 20 seconds, removed, then left for a further 15 seconds before taking the reading. The reading was then multiplied by a factory set calibration factor of 1.032 to ensure a $\pm 5\%$ accuracy. Between all measurements, the UC-1000 controller was left in „standby“ mode. This mode supplied a tickle or pulse (every 1μ sec) below the lasing threshold to maintain the plasma in the lasing tubes in an ionised state, allowing positive laser switching; therefore eliminating the need for a warm up period.

The laser power was measured for every 50th unit recorded on the numerical counter. The graph in Figure 2.23 shows the relationship between changes in the values of the numerical power control counter and the power output from the laser head. The error bars in Figure 2.23 represent a 3% error recorded over three consecutive tests

when the laser power was greater than 20W. At 16W the error increased to 6% and at 8W the error was 15%. To maintain consistency between experimental results the calibration procedure was repeated several times over the duration of the research. This was important as the research was performed over a period of approximately 2 years. Figure 2.24 shows the results from these trials. It illustrates that all results fall within the error values recorded in Figure 2.23, implying the laser output power remained stable throughout the duration of the research.

Summary

Methods of handling, storing and preparing powder for melting were established, and melt test protocols and environmental conditioning cycles were developed. The results in Chapter 3 suggest good reproducibility and repeatability of each. The design of integral and auxiliary SLS equipment has also been demonstrated together with the compilation of a successful computer programme to generate HPGL source code and control the switching of system level commands. Furthermore, other SLS equipment has been introduced and described in such detail to aid discussions in Chapter 5 concerning equipment design and its use during processing. Finally, machine calibration procedures were also successfully developed showing good reliability of the equipment. These techniques procedures were used to identify factors influencing the melting behaviour of a stainless steel powder during melting by SLS.

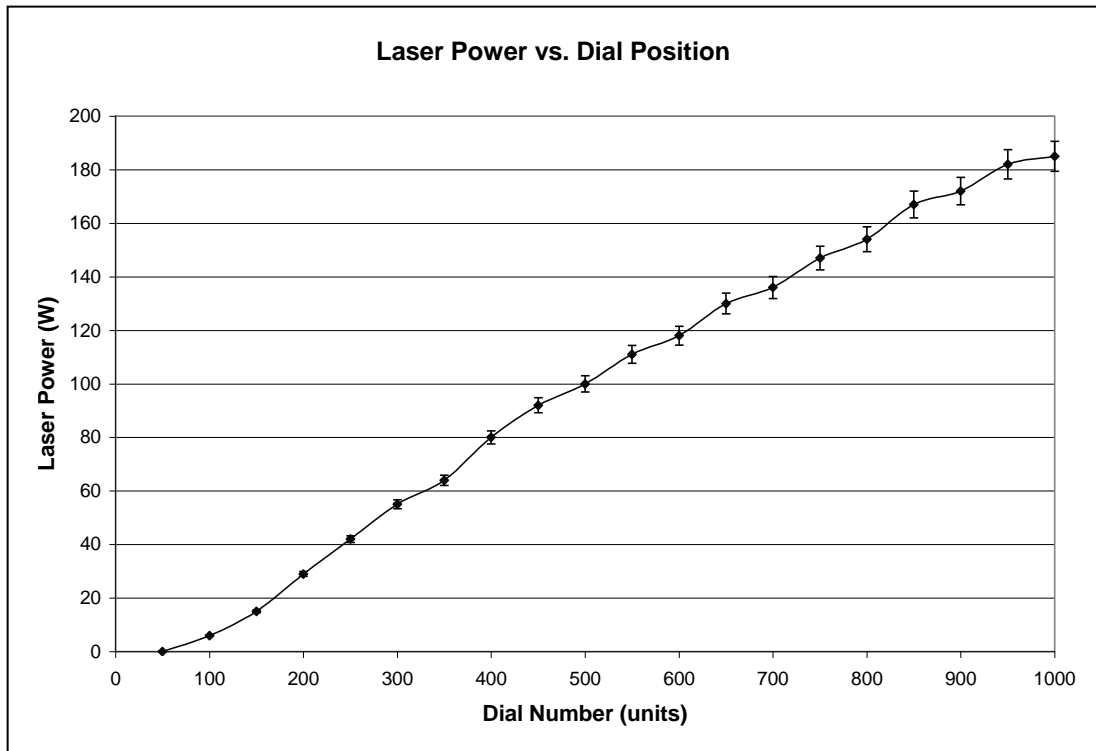


Figure 2.23: Calibration graph for manual laser power modulation. Error bars show 97% confidence limits.

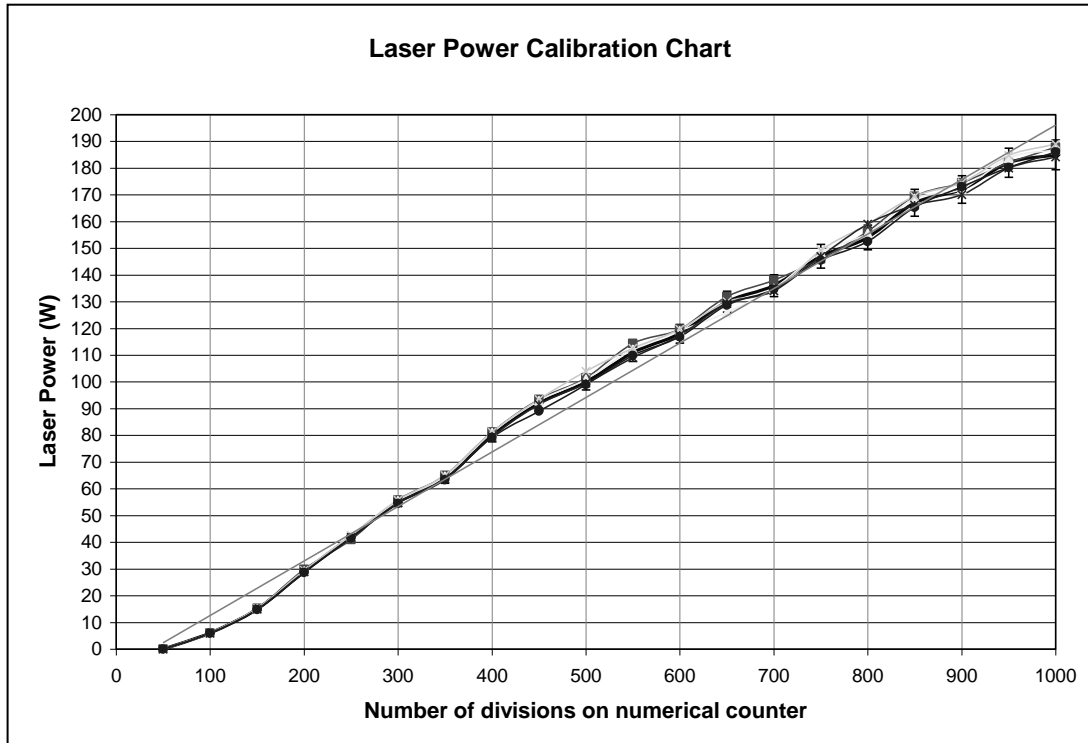


Figure 2.24: Calibration graph showing laser power deviance during manual power modulation over an 18 month period.

CHAPTER THREE

RESULTS OF SINGLE TRACK MELT TESTS USING DIFFERENT ENVIRONMENTAL CONDITIONS, SCANNING CONDITIONS AND POWDERS

Introduction

This chapter firstly sets out the results and a brief discussion concerning the work on powder mixing and powder mixing calibration (see Section 3.2). This is followed by the results of the microscopy studies observing powder particle structure and shape (Section 3.3). The main body of work then follows which reports on the observations made and measurements taken during the construction of single tracks. The literature review in Chapter 2 showed that a single track melt pool can experience large changes in shape, volume and flowability. It was also clear in the literature that surface tensions forces, scanning conditions, laser-material interactions, powder characteristics and atmosphere play a decisive role in affecting these changes. However, the importance and effects of these parameters, both as a single entity and when in combination with each other, is less clear. Therefore, the purpose of the work presented in this Chapter is geared towards increasing the understanding of these parameters for melt pools created in deep powder beds. Results from this work has also allowed for the development of mathematical models to model a number of process aspects such as melt fragmentation and laser-material interactions. The models are presented in Chapter 5 of this thesis.

Each of the four powder batches, described previously in Chapter 2, Section 2.2, has been melted using the scanning conditions reported in Chapter 2, Section 2.5.1 and all three environmental conditions reported in Chapter 2, Section 2.5.2. The results fall into separate sections, with the air atmosphere results first (Section 3.4), followed by the argon atmosphere results (Section 3.5) and finally, the argon atmosphere with argon

percolation results (Section 3.6). In each section the 150/75 powder batch, selected at random, forms the foundation of the research to which all other powder batches are compared. Included in these results are observations and measurements of melt track dimensional changes; including width, depth and area cross section together with measurements of mass changes of good quality melt tracks. Good quality in this case, refers to a continuous un-rastered melt pool. Microstructural examinations of the melt tracks and observations of powder displacements and trenching during laser exposure and their influence over melt behaviour have also been recorded here.

A number of experimental tests were also conducted to assess the role of scan length on melt pool behaviour, experimental repeatability and experimental reproducibility. The experimental conditions are given in Chapter 2, Sections 2.5.1, 2.5.3 and 2.5.4 respectively. Results examining the role of scan length demonstrated that changes in scan length had few noticeable effects on many melt pool characteristics, including dimensional and volume changes, mass changes, track deformations and changes in oxidation behaviour. Experiments to prove the repeatability and reproducibility of results also had a similar outcome, where any recorded changes fell within acceptable limits. Importantly, the results also emphasised that a 10-15 minute purge of argon gas into the process chamber prior to melting stopped all visible signs of oxidation progression. A purge time of less than 10 minutes caused severe oxidation and purge times greater than 15 minutes were considered to be unnecessary and imparted no noticeable improvements over oxidation control and melt pool quality and growth. No further reporting on this subject matter is deemed necessary. Finally, all track data, which can also be used to compare track repeatability, can be seen in Appendix D.

Powder Mixing Calibration Results

The experimental apparatus used in the powder mixing trials is given in Chapter 2, Section 2.3.3, the mixing and density measurement procedures have been discussed in Chapter 2, Section 2.5.8 and all calibration data accumulated during the experimental works has been tabulated in Appendix E. Figure 3.1 displays the results of changes in the average packing density with mixing time for each of the four batches of powder. The figure emphasises the importance of powder mixing for both the attainment of higher packing densities and as a method to ensure a high reproducibility between packing density data. Reproducibility is presented as error bars in the figure and includes the density variation between all samples investigated including samples taken at different depths within the storage container.

The results of the 300/150, 150/75 and 75/38 batches were similar, showing a peak in average packing density after 15 minutes of mixing. Furthermore, at this time period the density variation between all samples measured was at a minimum. Above 15 minutes of mixing there was an initial decrease in packing density, but not as abruptly as the initial increase observed between 0 and 15 minutes, followed by a period of little change. It is also interesting to note that the greatest density variation in each of the three powder batches occurred in samples taken from the unmixed powder and powder that was mixed for 60 minutes. This first observation is likely to be due to particle segregation caused by transportation and prolonged storage. The second observation can often be triggered by over mixing causing particle re-segregation. It is well documented that if the mobility and density of the particles differ as a result of their forms and sizes, the effect of external forces may cause segregation (German, 1998).

It is also evident when comparing Figures 3.1a-c, that the average packing density recorded at each mixing time interval generally decreased with decreasing particle size and the average packing density variation was shown to increase. These two observations are likely to be both caused by a change in the flow properties of the powder samples, where powder flow is known to reduce with reducing particle size (German, 1998).

The results for the -38 powder batch followed a different trend, although the average powder packing density recorded at each mixing time interval remained lower than values recorded at similar time intervals in the other three powder batches. As a general rule, an increase in mixing time caused the packing density to decrease and the packing density variance to increase; hence this was the only powder batch to have its highest packing density recorded in its unmixed state. This suggests that the mixing process acted only to cause re-segregation. These differences are again likely to be connected to the poor flow properties which were observed when handling samples taken from this powder batch. It is reasonable to assume that the poor flow properties restricted the mixing efficiency of the V-cone mixers and the filling efficiency of the plastic cup during the density measurements.

The change in density of powder samples taken from different heights within each of the storage containers was also investigated. The data points were compared for mixing times of 0, 7.5, 15, 30 and 45 minutes and none of the differences were found to be statistically significant. However, after 60 minutes of mixing and due to reasons described above, the drop in density was considered significant, especially in samples taken from the bottom of the storage containers.

Given the results obtained from the powder mixing trials, powder samples taken from the 300/150, 150/75 and 75/38 powder batches were mixed for 15 minutes prior to their deposition and melting in the research SLS machine. This time period was chosen to ensure the highest reproducibility between all deposited powder layers and was not chosen on the basis of a high packing density; the latter factor being largely indeterminate during SLM (see Chapter 1, Section 1.7.1.2). For the -38 powder batch, the highest reproducibility occurred in the unmixed samples and so no further mixing was carried out on this powder.

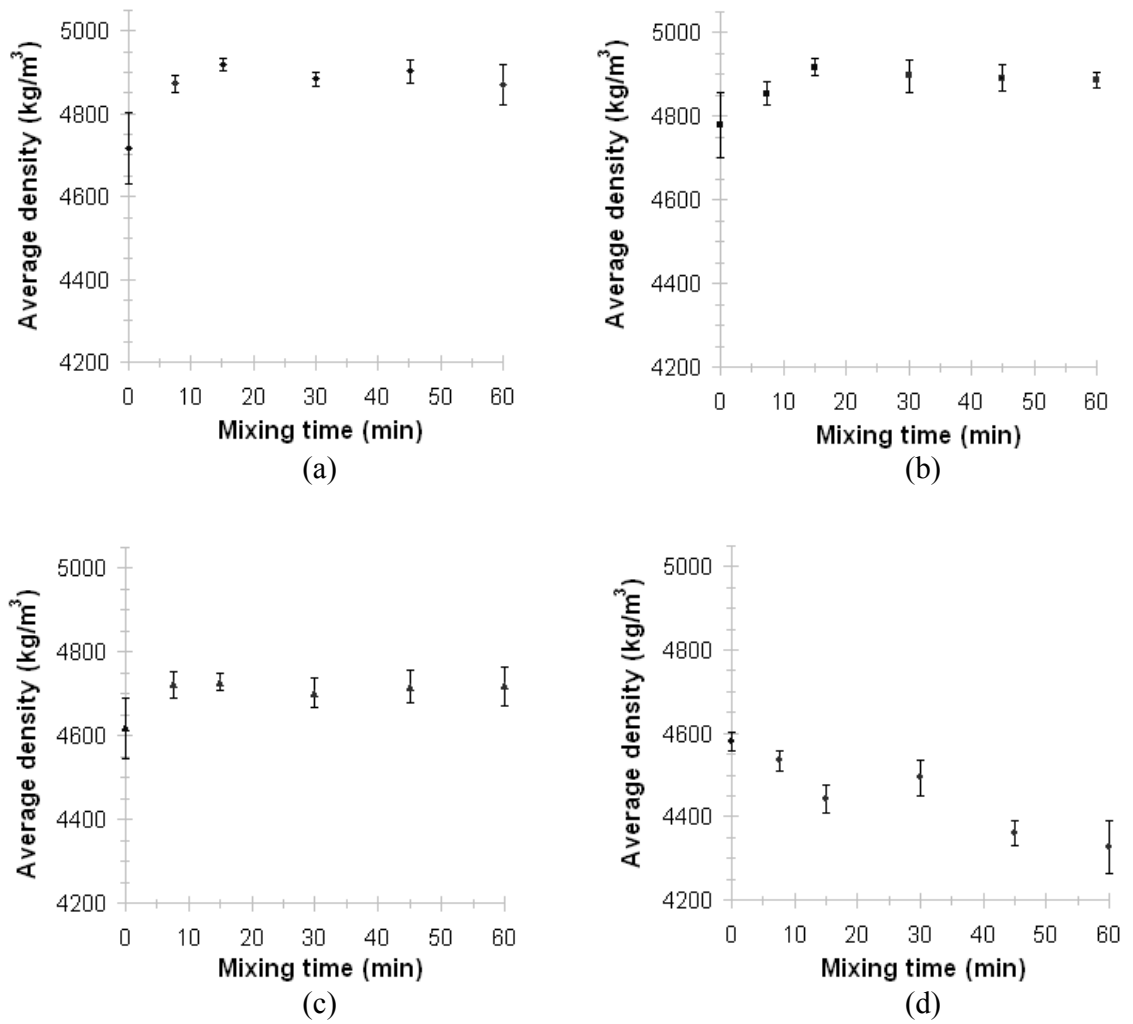


Figure 3.1: Density variation with mixing time for (a) 300/150 powder batch, (b) 150/75 powder batch, (c) 75/38 powder batch and (c) 38 powder batch.

Powder Microscopy Results

SEM micrographs showing typical particle grain structures observed in this study are shown in Figure 3.2. From the figure it can be seen that the solidified structure was almost always equiaxed and generally uniform in size and shape. This can be expected since this type of structure is characteristic of a rapidly solidified alloy.

Figure 3.3, charts the results of the changes in grain size with particle size for particles taken from the 300/150, 150/75 and 75/38 powder batches. The grain size was measured using pictures similar to those shown in Figure 3.2 and the method outlined in Chapter 2, Section 2.5.7. The grain structure of particles within the –38 powder batch could not be obtained because the particles were too small to mount and etch correctly with the available equipment. The powder particle grain size measurement data obtained during the experimental works has been tabulated in Appendix E.

The variation of particle grain size, \bar{d} , with particle diameter approximately follows the relationship:

$$\bar{d} \propto \sqrt{r} \quad (3.1)$$

where, r , is the particle radius, as can be seen from the plot on the same figure of grain size $\propto \sqrt{\text{powdersize}}$, with the constant of proportionality of 1.0. The dependence on particle grain size may be related to the cooling rate during gas atomisation manufacture of the powder. The cooling rate of a particle can be found from a heat balance on the particle i.e. equating the sensible heat loss of a particle to the heat loss through the particle surface, such that:

$$\rho C_p V \frac{\partial T}{\partial t} = h 4\pi r^2 (\Delta T) \quad (3.2)$$

where

h = surface heat transfer coefficient ($\text{W}/\text{m}^2 \cdot \text{K}$)

V = volume of powder particle (m^3)

ΔT = $T_{\text{particle}} - T_{\text{ambient}}$ (K)

ρ = density of particle (kg/m^3)

C_p = specific heat $\text{J}/\text{kg} \cdot \text{K}$

r = radius of spherical particle (m)

assuming, h , is constant during the period of solidification, then:

$$\frac{\partial T}{\partial t} \rho C_p \frac{4}{3} \pi r^3 = h 4 \pi r^2 (\Delta T) \quad (3.3)$$

$$\therefore \frac{\partial T}{\partial t} = \left[\frac{3h}{\rho C_p} \Delta T \right] \frac{1}{r} \quad (3.4)$$

Thus cooling rate is proportional to $1/r$ and cooling time is proportional to r . Previous studies discussed in Chapter 1, Section 1.8.2 suggest that microstructure depends on the square root of cooling time with equiaxed structures occurring at very low values of $\sqrt{\text{time}}$. Equation 3.1 is in line with this observation.

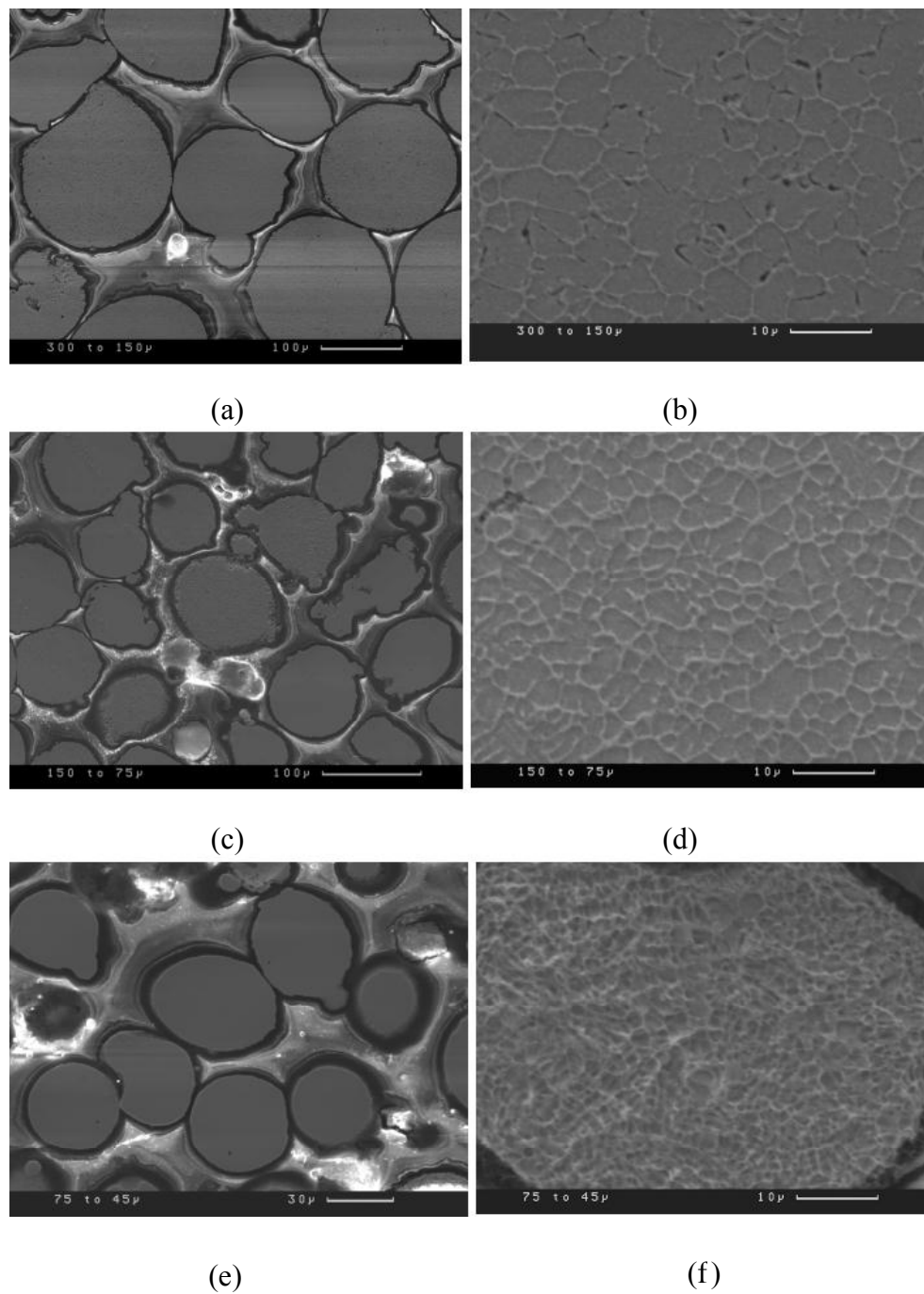


Figure 3.2: Particle shape and grain structure in powder batches (a/b) 300/150, (c/d) 150/75 and (e/f) 75/38.

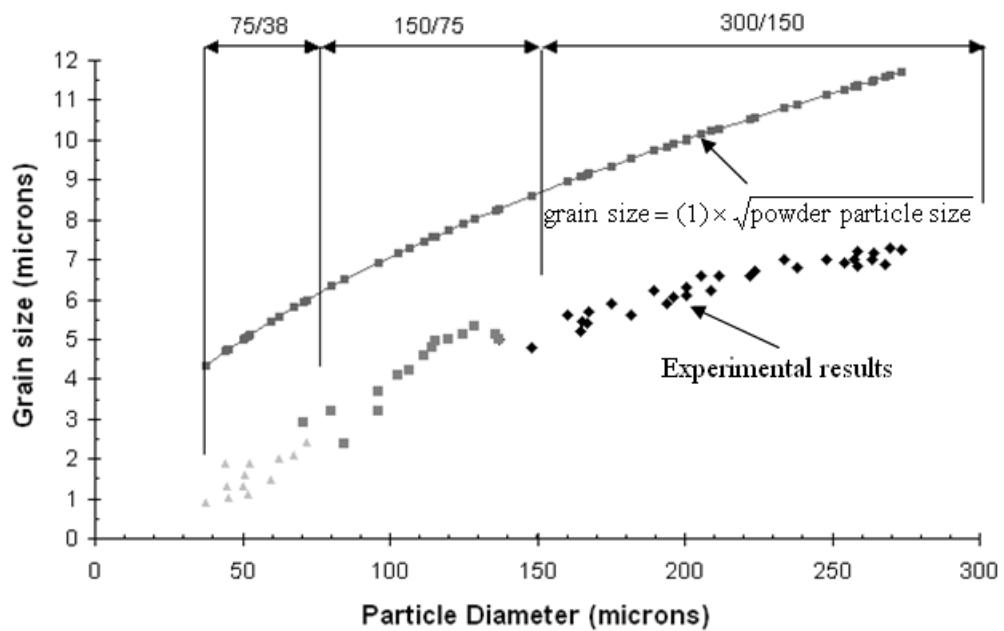


Figure 3.3: Variation of grain size with particle diameter for particles contained within the 300/150, 150/75 and 75/38 powder batches. The calculated curve has been plotted with a constant of proportionality of 1.0.

Selective Laser Sintering of Single Tracks Scanned in an Air Atmosphere

The purpose of carrying out single track melting tests within an oxygen based atmosphere (laboratory air) was to establish a benchmark study to help determine the role of oxygen and the effects of oxidation on melt pool behaviour. Particular attention was given to the type of melt front growth and oxide scales that form during laser scanning.

3.1.1 Qualitative Observations

Figures 3.4 – 3.7 show pictures of typical melt tracks produced by scanning a series of unidirectional traverses of the laser beam. In the figures, a number of tracks have been intentionally slanted to indicate melt solidity; a procedure carried out after the melt had cooled. All four powder batches are represented in the figures.

Due to the complexity of characterising all of the discrete changes observed in the powder during exposure a number of changes of a qualitative classification have been chosen to be representative of each powder's total heating and melting response.

Oxidation, particle bonding and melt pool growth and quality were all taken into account during their selection. It is important to note here that powder particles located within the heat affected zone (HAZ), but which lie outside of the beam spot, are not considered by the process maps unless those particles have directly interacted with the melt volume. The classifications are listed below.

Powder heating but no marking: A focussed, moving Gaussian beam impinging on the surface of a powder layer causes no physical changes, including, no discolorations of particle surfaces, no melt formation and no bonding between neighbouring particles (See Figure 3.4: Part A). Due to the short heating times inherent in SLM, it was assumed that a melt phase was required to initiate particle bonding. Therefore, melt formation (or the lack of it) was determined by observing, then comparing with virgin powder, the movements of individual particles and the interactions between neighbouring particles whilst disturbing the irradiated powder layer with a knife edge.

Temper Colorations but no melting: A focussed, moving Gaussian beam impinging on the surface of a powder layer causes temper colorations on the surfaces of irradiated particles and on particles situated within a localised HAZ (See Figures 3.4: Part A, 3.8: Part A and 3.9: Part A). During exposure, particles with the smallest size fraction may be melting causing some liquid action. However, due to a combination of a small liquid volume and an imbalance of surface energies caused by the oxide scale, the liquid does not wet, and therefore does not form bonds between larger unmelted particles. This produces tempered tracks with a powdery surface finish which fall to a loose powder when disturbed. The temper colorations are a consequence of a thickening oxide layer which changes colour with increasing temperature. For a visual comparison, Table 3.1 summarises the colour changes inherent in a stainless steel block heated over a range of temperatures from 300°C to 750°C (Monypenny, 1954). In Table 3.1, the colours and name representations follow closely the colorations observed in the experimental works. For example, pale straw colorations were found to occur on all

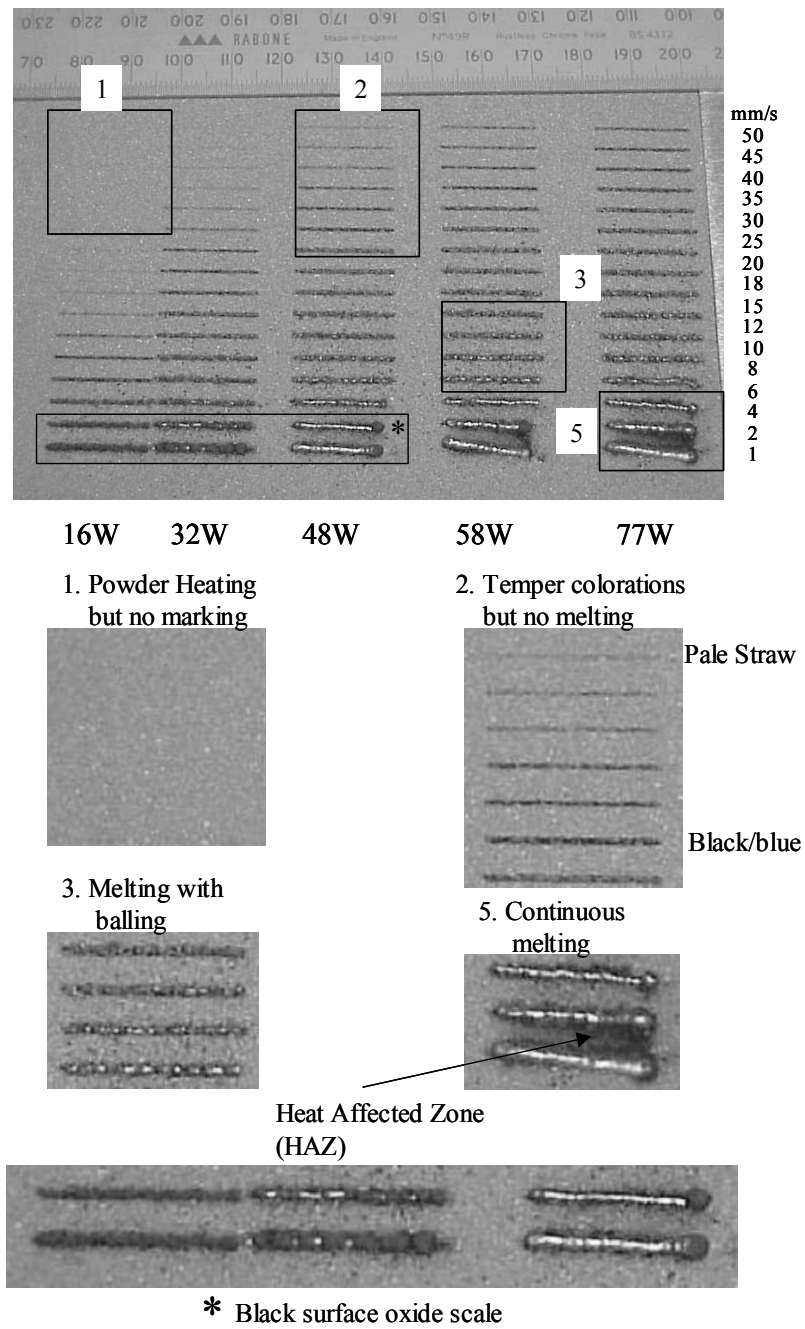


Figure 3.4: Part A: Tracks melted in air atmosphere using 300/150µm powder batch at different scanning conditions.

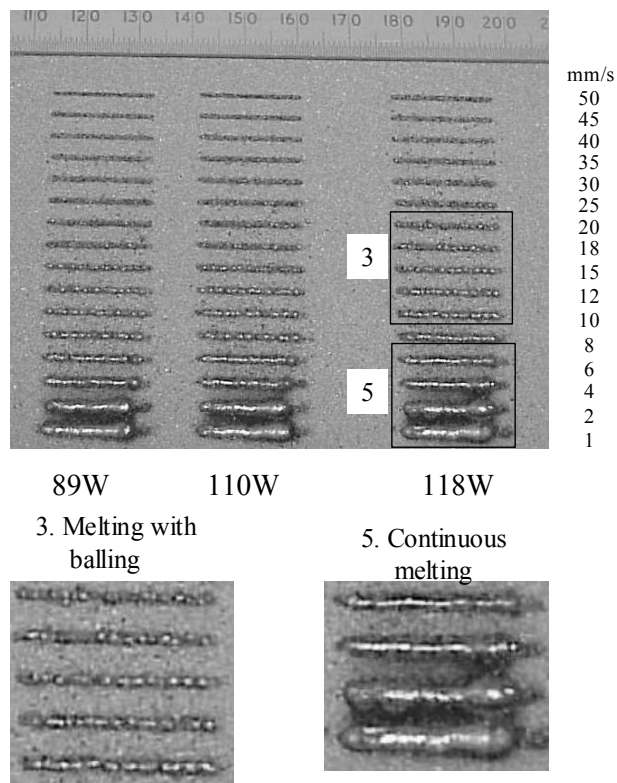


Figure 3.4: Part B: Tracks melted in air atmosphere using 300/150 μ m powder batch at different scanning conditions.

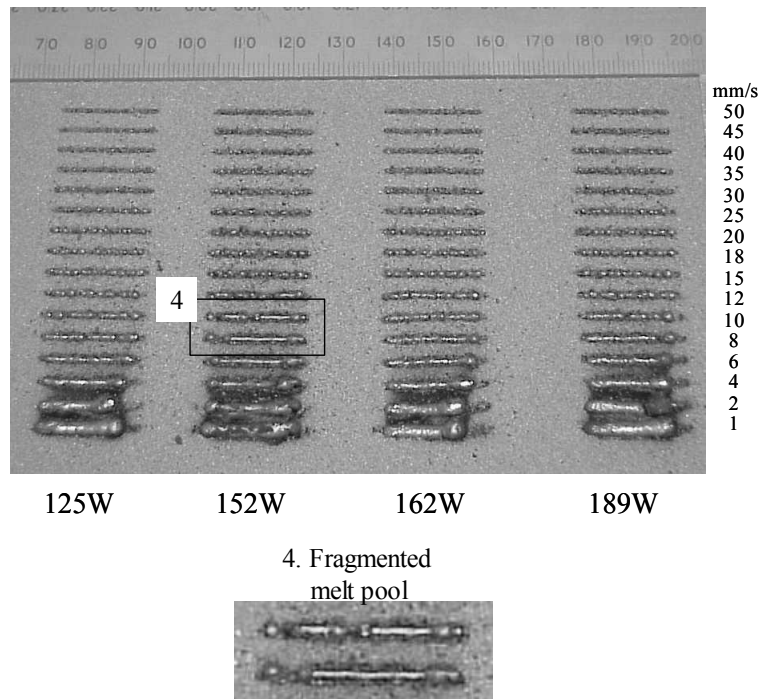


Figure 3.4: Part C: Tracks melted in air atmosphere using 300/150 μ m powder batch at different scanning conditions.

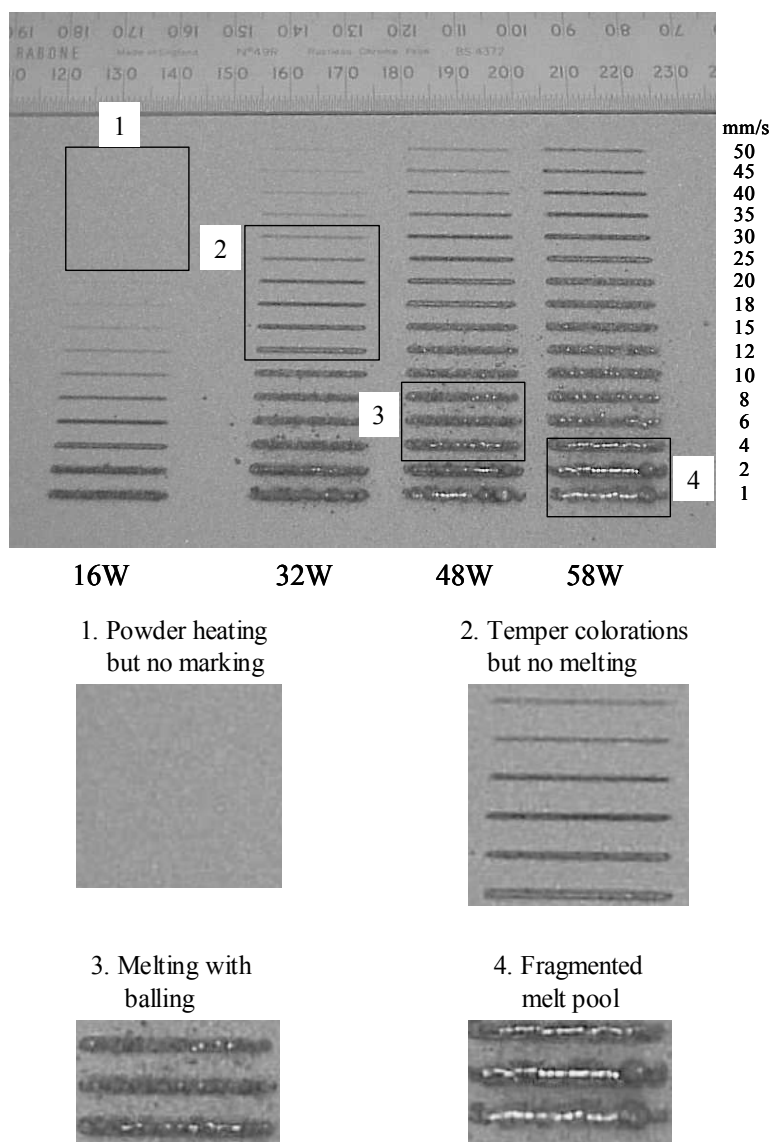


Figure 3.5: Part A: Tracks melted in air atmosphere using 150/75µm powder batch at different scanning conditions.

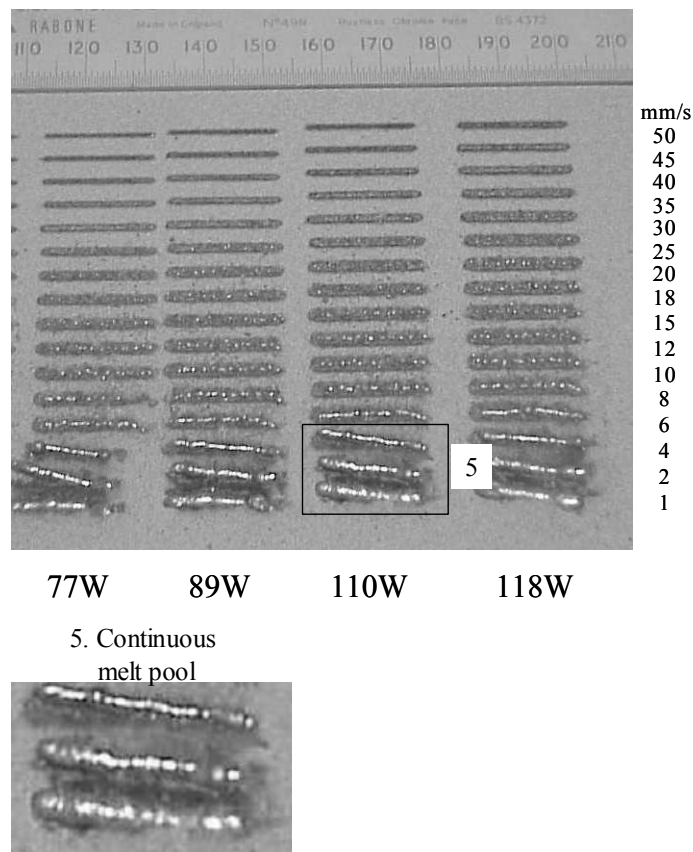


Figure 3.5: Part B: Tracks melted in air atmosphere using 150/75µm powder batch at different scanning conditions

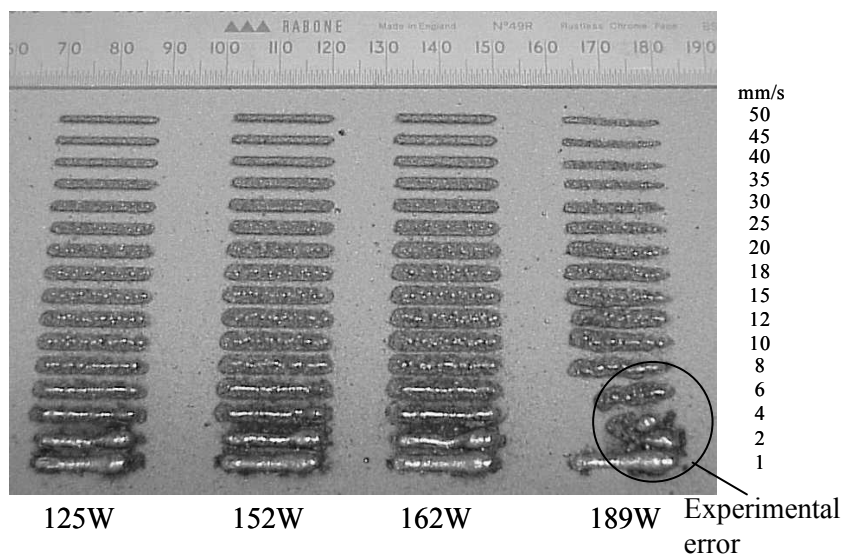


Figure 3.5: Part C: Tracks melted in air atmosphere using 150/75µm powder batch at different scanning conditions

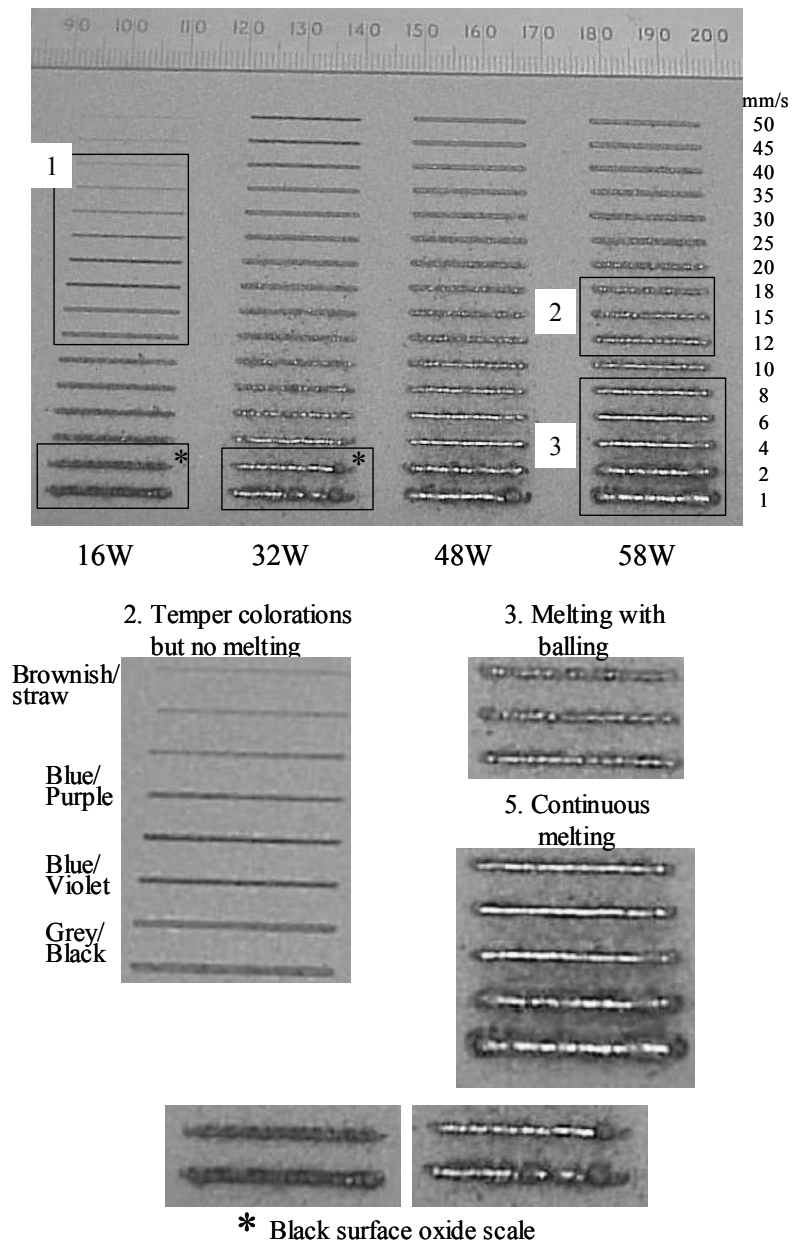


Figure 3.6: Part A: Tracks melted in air atmosphere using 75/38µm powder batch at different scanning conditions

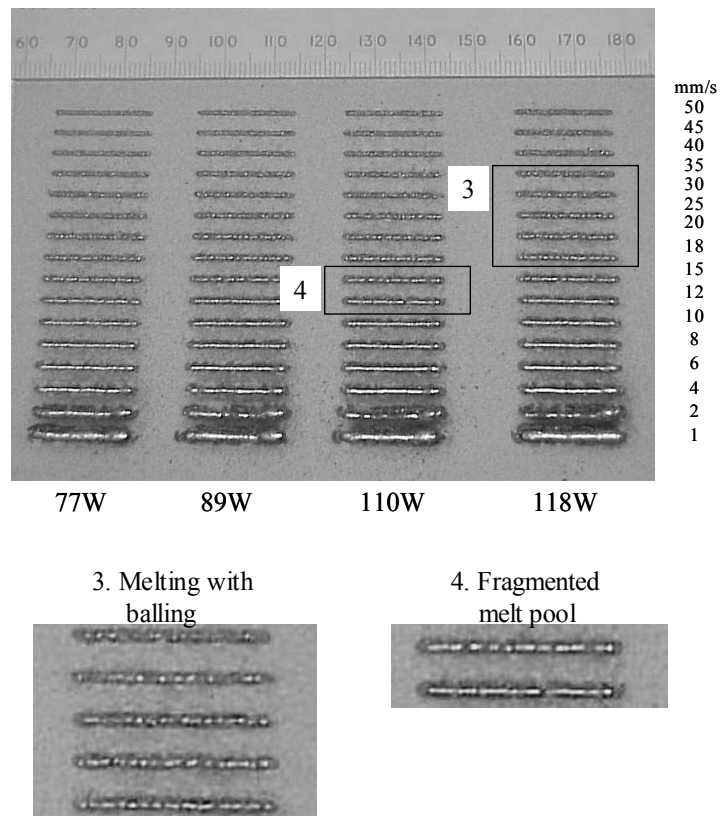


Figure 3.6: Part B: Tracks melted in air atmosphere using 75/38 μ m powder batch at different scanning conditions

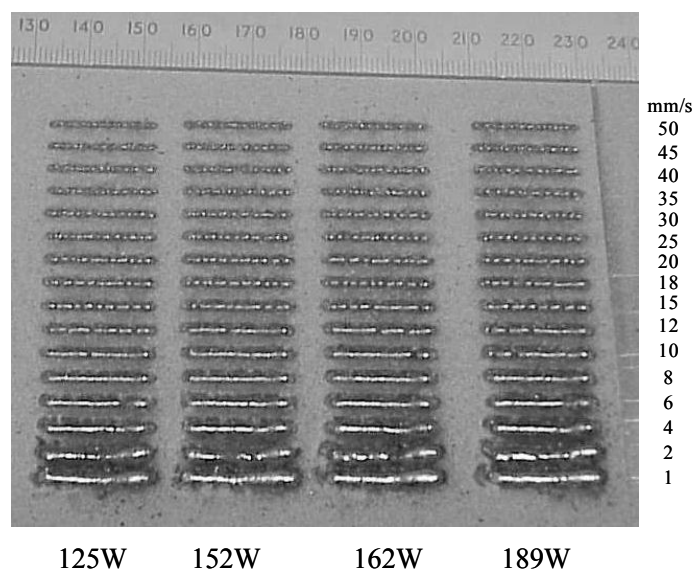


Figure 3.6: Part C: Tracks melted in air atmosphere using 75/38 μ m powder batch at different scanning conditions

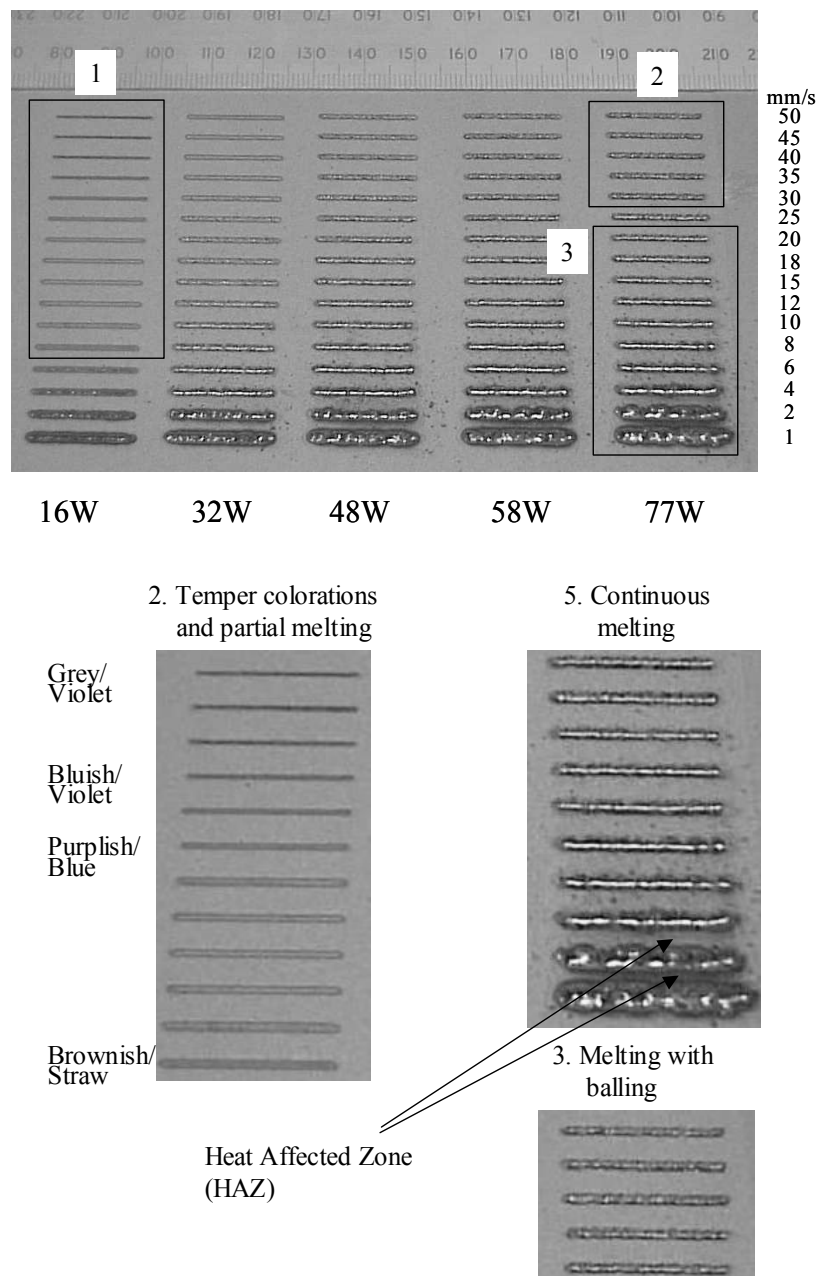


Figure 3.7: Part A: Tracks melted in air atmosphere using $-38\mu\text{m}$ powder batch at different scanning conditions

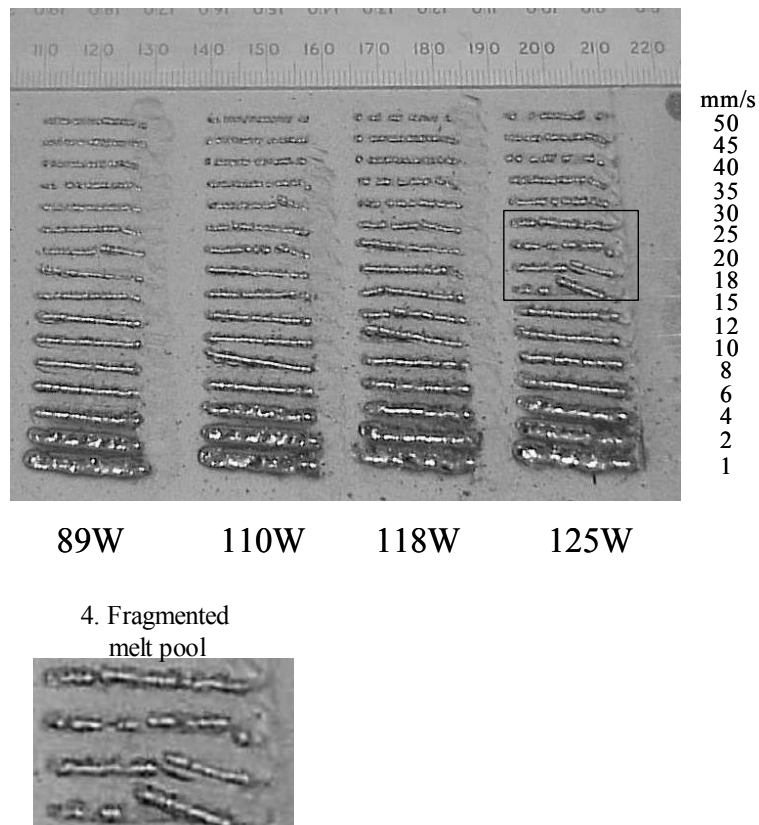


Figure 3.7: Part B: Tracks melted in air atmosphere using $-38\mu\text{m}$ powder batch at different scanning conditions

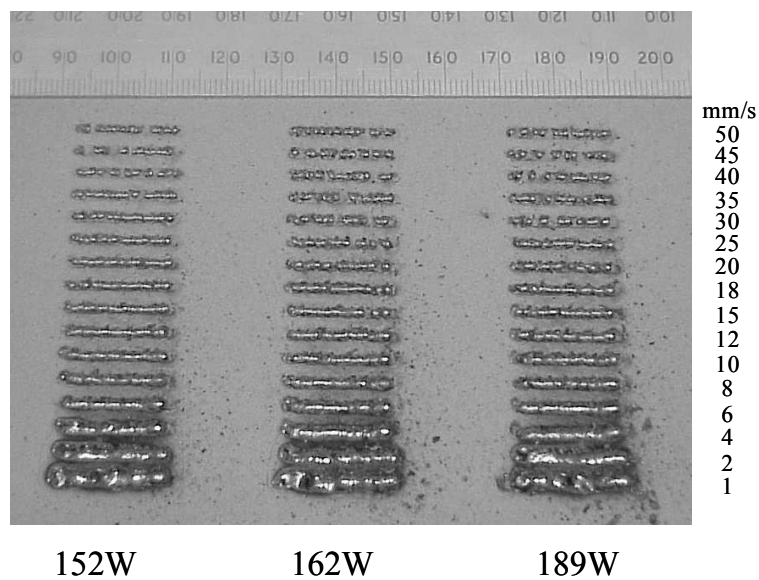


Figure 3.7: Part C: Tracks melted in air atmosphere using $-38\mu\text{m}$ powder batch at different scanning conditions

directly irradiated particles exposed to the lowest values of energy density recorded within the limits of this regime (see Figures 3.4: Part A and 3.6: Part A and process maps in Figures 3.8 to 3.10 for boundary locations). These colorations were also often found on particles located within the periphery of many HAZ's caused by much higher energy density exposure (see Figures 3.4: Part A and 3.7: Part A).

On the other hand, grey/black colorations were found to occur on all directly irradiated particles exposed to the highest values of energy density recorded within the limits of this regime (see Figures 3.4: Part A and 3.6: Part A). A grey/black surface scale was also observed on the surfaces of fully molten powder at the onset of balling (see Figures 3.4: Part A and 3.6: Part A). Due to the difficulty in measuring the surface temperature of the irradiated powder, a more detailed analysis was not obtained nor deemed necessary for the purposes of this work.

Table 3.1: Temper colorations observed during the heating of the powder (Monypenny, 1954).

Temperature °C ⁺	Temper Coloration*
300	Pale Straw
350	Brownish Straw
400	Brownish Purple
450	Bluish Purple
500	Reddish Purple
550	Purplish Blue
600	Light Blue
650	Bluish Violet
700	Greyish Violet
750	Grey/Black

⁺ Temperatures are for reference only and were obtained by heating a stainless steel block (Monypenny, 1954).

* The printed colours should be treated as a guide only.

Temper Colorations and partial melting: A focussed, moving Gaussian beam impinging on the surface of a powder layer (75/38 and 38 powder batches only) causes temper colorations on the surfaces of irradiated particles and on particles situated within a localised HAZ. During exposure, particles with the smallest size fraction are melting causing some liquid action. Because of the greater number of smaller particles in the 75/38 and 38 powder batches, the liquid volume is sufficient in quantity to wick into the neck region between neighbouring unmelted larger particles, creating a network of re-solidified melt and suspended particles. This produces tempered tracks with a powdery surface finish. However, since wetting is still impeded by the oxide scale, the tracks are very fragile, but do remain intact with careful handling (see Figure 3.7: Part A). The oxide colour scale presented in Table 3.1 is again applicable here as a colour comparator. However, the order in which the oxide scales occur, particularly in the -38 powder batch, appear random in nature (see Figure 3.7: Part A). For example, it is shown in Table 3.1 that grey/black colorations will occur when cooling from a high temperature ($\sim 750^{\circ}\text{C}$) and brownish/straw colorations occur when cooling from a much lower temperature ($\sim 350^{\circ}\text{C}$). In comparison, Figure 3.7: Part A shows grey black temper colorations occurring on particle surfaces after being irradiated with lower values of energy density than those particles that have cooled and formed a surface scale showing brownish/straw colorations. The reason for these differences is likely to be linked to the complexity of surface scale control and the cleanliness of the powder layer; oxygen and other contaminants such as water vapour can greatly affect oxide thickness.

Full Particle Melting with Temper Colorations A focussed, moving Gaussian beam impinging on the surface of the powder layer causes full particle melting, forming a conduction limited melt pool. The amount of powder directly under the line source of energy is small in comparison to the actual amount melted. All except the very smallest of tracks produced at low energy densities are visibly larger in cross section than the nominal amount of powder available for melting (see Section 3.4.3 and 3.4.5). This occurs because powder on each side of the melt pool collapses into it. This is especially noticeable when the melt width contracts and forms a cylindrical cross section, leaving behind an unstable wall of powder. The admission of this extra powder allows for increased melt volume, but also leaves denuded areas (or a trench) around all sides of the melt (see Figures 3.4: Part C and 3.9: Part C). The extent of this gathering of

surrounding powder is affected by the speed and power of processing which governs the width and average temperature of the melt as well as its vertical position within the powder layer (see Section 3.4.8). Upon removal of the solidified melt pool from the surrounding powder layer, the underlying powder was almost always blue/violet in colour. Powder within the wall of the denuded area was unaffected by surface coloration suggesting that powder in this area was subjected to only very small temperature rises.

The melt had a yellowish silver appearance that is attributed to the oxide scale forming on the surface of the melt pool. Due to its colour, it is likely that the slag is rich in chromium (Cr_2O_3).

The aspect ratio of the melt was almost always close to unity (circular aspect ratio creating cylindrical melt tracks). This occurrence might also have been caused by the slag covering. In Section 3.4.5, microstructural observations show distinct regions of re-solidification, suggesting little or no melt pool stirring i.e. no surface tension driven fluid flows. Work reported in Chapter 1, Section 1.4, clearly show that such forces would otherwise dictate melt geometry.

There were also very few particles attached to the solidified melt, even on the underside, giving it a smooth surface finish. As the laser spot travels over the surface of the powder layer, three different types of melt pool growth were observed (see Figure 3.8):

Growth Type I (Melting with Balling): At generally higher scan speeds, a molten pool, approximately circular in cross section, is produced whose growth type is strongly influenced by surface tension forces. A struggle appears to exist between interaction time, power density and surface tension forces. Because the interaction time is short, and the power density is therefore small in comparison, the high surface to volume ratio of the melt means that the major effect controlling the morphology of the melt is surface tension. To reduce the surface free energy, the melt pool fragments, forming a series of equi-sized, equi-spaced melt balls. Furthermore, because the interaction times are generally small, the melt volume is very small and short lived, and therefore has a low average temperature in comparison with other melts to be discussed. This explains the low interaction observed with surrounding powder causing only a small denuded area (see Figure 3.6: Part B as one example). Nevertheless, the

admission of even small amounts of powder will help to cool the surface of the melt still further.

Growth Type II (Melting with Breakages or Fragmentation): As processing speeds are decreased, the increased laser interaction melts even more material resulting in a melt pool with an approximately circular cross section and a reduced surface to volume ratio. The outcome is a more continuous melt pool, but which still exhibits random fragmentation along its length (see Figure 3.7: Part C as one example). This hotter more extensive melt pool incorporates an increased proportion of incoming powder through trenching, until the combination of laser removal and incoming powder solidify the melt. However, the coalescence of neighbouring particles does not sufficiently denude the surrounding area of powder completely, leading to a build up of loosely bonded material at the sides of the melt pool (see Section 3.4.5).

Growth Type III (Continuous Melting): At even slower processing speeds, the increased laser interaction melts even more material resulting in a melt pool with an approximately circular cross section and a much reduced surface to volume ratio. The outcome is a continuous melt pool surrounded by large denuded areas. Due to more excessive trenching, the melt volume has a greater number of attached powder particles and agglomerates. On a large number of tracks there is also a highly noticeable „bobble“ or build up of melt at the start of each track. It is believed this bobble is linked to the trenching phenomena and is discussed in detail in Section 3.4.5.

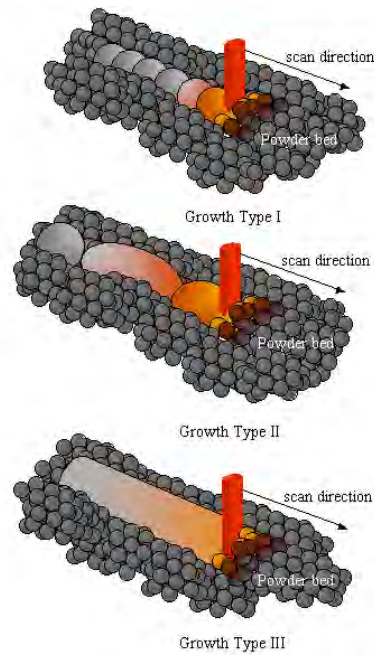


Figure 3.8: Qualitative classification of the three types of solidification observed in the experimental works.

Growth Type I: Balling, Growth Type II: Melting with Breakages, Growth Type III: Continuous melting.

3.1.2 Process Maps

Process maps plotting the heating and melting response of the powders have been constructed to help increase the understanding of melt front progression as laser powers, scan speeds and particle size distribution change.

The maps, given in Figures 3.9 to 3.12, have similar regions or regimes. Each regime is based on the qualitative classifications presented in Section 3.4.1. They are in most part well defined and the regimes in the 300/150, 150/75 and 75/38 process maps are closely associated. The nodal array displayed on each map indicates the number and value of experimental points used in the construction of the maps and the coloured nodes located along region boundaries help communicate boundary accuracy by indicating the degree of regime crossover.

In all four maps a diagonal boundary line a-a separates the regimes of powder heating but no marking below from the regime of temper colorations but no melting above. The boundary is linear, suggesting that a critical value of energy density must be reached before the powder will oxidise under the incident radiation. The values range between 0.2J/mm and 0.5J/mm and increase with increasing powder particle size. It is also clear from all four process maps that this boundary line cuts the laser power axis at approximately 8W, suggesting that at least 8W of laser power is required before the powder will react to the incident radiation.

A boundary line b-b separates the temper colorations but no melting regime to the right from a melting with balling regime to the left. In the 75/38 and -38 process maps this boundary is again distinct and linear. However, the distinction is less clear in the 300/150 and 150/75 process maps, particularly at higher laser powers and scan speeds. These regions are highlighted by the closed boundaries WXYZ and XYZ in Figures 3.9 and 3.10 respectively. Irradiating the powder at conditions within these regions, as both the maps and Figures 3.4 and 3.5 suggest, would cause temper colorations to form on particle surfaces. However, there were also a small number of sporadic groups of what appeared to be agglomerated particles forming along the length of the irradiated track. Although melting was visually inconclusive, it is highly likely that the agglomeration of particles was caused by capillary forces triggered by the presence of a melt volume. If melting is indeed occurring in these regions, then the shape of the boundary line b-b in the 300/150 and 150/75 process maps would change and become close to linear, continuing the trend observed in the 75/38 and -38 process maps. This trend is a reasonable assumption since it is also reasonable to assume that some critical value of energy density is required to promote melting of the irradiated powder; providing that a thickening surface oxide layer does not affect radiation absorptivity. Hence, the argument concerning melt formation in the regions bounded by WXYZ and XYZ is strengthened. Assuming the boundary line b-b is linear for all four process maps, then the values of energy density along the boundary line would range between 1.4J/mm and 2.5J/mm, again steadily increasing with increasing powder particle size. However, because these maps are based on visual interpretations, the regions bounded by WXYZ and XYZ will remain as regions portraying temper colorations but no melting.

A line c-c separates the melting with balling regime to the right from a fragmented melt pool regime to the left. Finally, a line d-d separates the fragmented melting regime to the right from a continuous melting regime to the left. The phenomenon of melt pool balling and fragmentation was widespread during air sintering. In the 300/150, 150/75 and 75/38 powder batches balling was found to occur from the point of first melting and could only be controlled, whilst maintaining a melt volume, by reducing the scan speed. Hence, a continuous melt pool could only be maintained at scan speeds typically less than 10.0mm/s (boundary line d-d). If the laser power was very low (<32W although this value is dependant on the powder batch), then melting with balling could not be controlled at any value of scan speed. It was also noted that each re-solidified melt ball was uniform in shape, equi-spaced between its neighbours and grew in diameter and reduced in number as the energy density increased; melting with breakages also followed a similar relationship, except that the broken melt was obviously more elongated in shape.

The dashed line in all four process maps indicate the range of scanning conditions over which the collapse of powder can be expected. Obviously, due to the unpredictable nature of the powder bed, the collapse of powder to reveal significant denude areas around the melt cannot always be predicted. Nevertheless, there is a general trend emerging. For the 300/150, 150/75 and 75/38 powder beds, significant collapse of powder generally occurs over all scanning conditions suitable for the creation of a continuous or fragmented melt pool. Powder collapse also occurs when the melt pool balls. However, due to reasons given above, the denude areas are very small and difficult to distinguish because of the highly disconnected melt bead and because of surface oxidation of surrounding particles which cast artificial shadows. For the -38 powder batch, powder collapse generally occurs over similar regions to the other three powder batches providing there are no sinter bonded particles attached to the core melt volume i.e. at scan speeds greater than 3mm/s at high laser powers (>125W) and at higher scan speeds when the laser power is low. The cause and effects of sinter bonded particles is discussed in greater detail in Section 3.4.3.2.

The main difference between the four process maps was the arrangement of the boundaries in the -38 process map once melting took place. The map shows that melting with balling and a fragmented melt pool only occur at high laser powers and high scan

speeds. This allows for two important differences. Firstly, a continuous melt pool can be produced from the point of first significant melting providing the scan speeds remains low (<30mm/s). Secondly, it allowed for a much larger process window at low powers in which to irradiate the powder bed whilst maintaining a continuous melt pool.

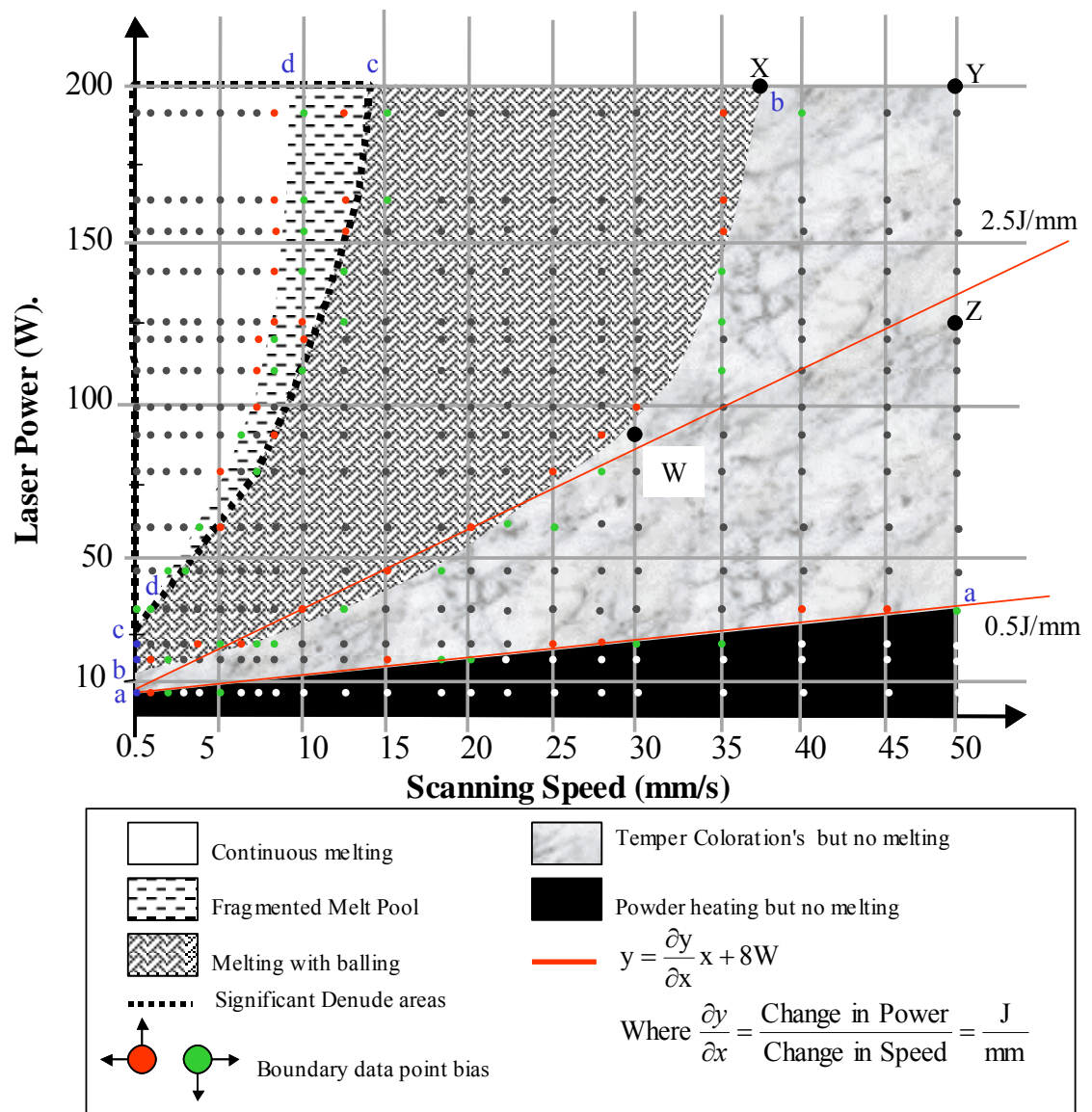


Figure 3.9: Process map for the 300/150 powder batch processed within a laboratory „air“ atmosphere.

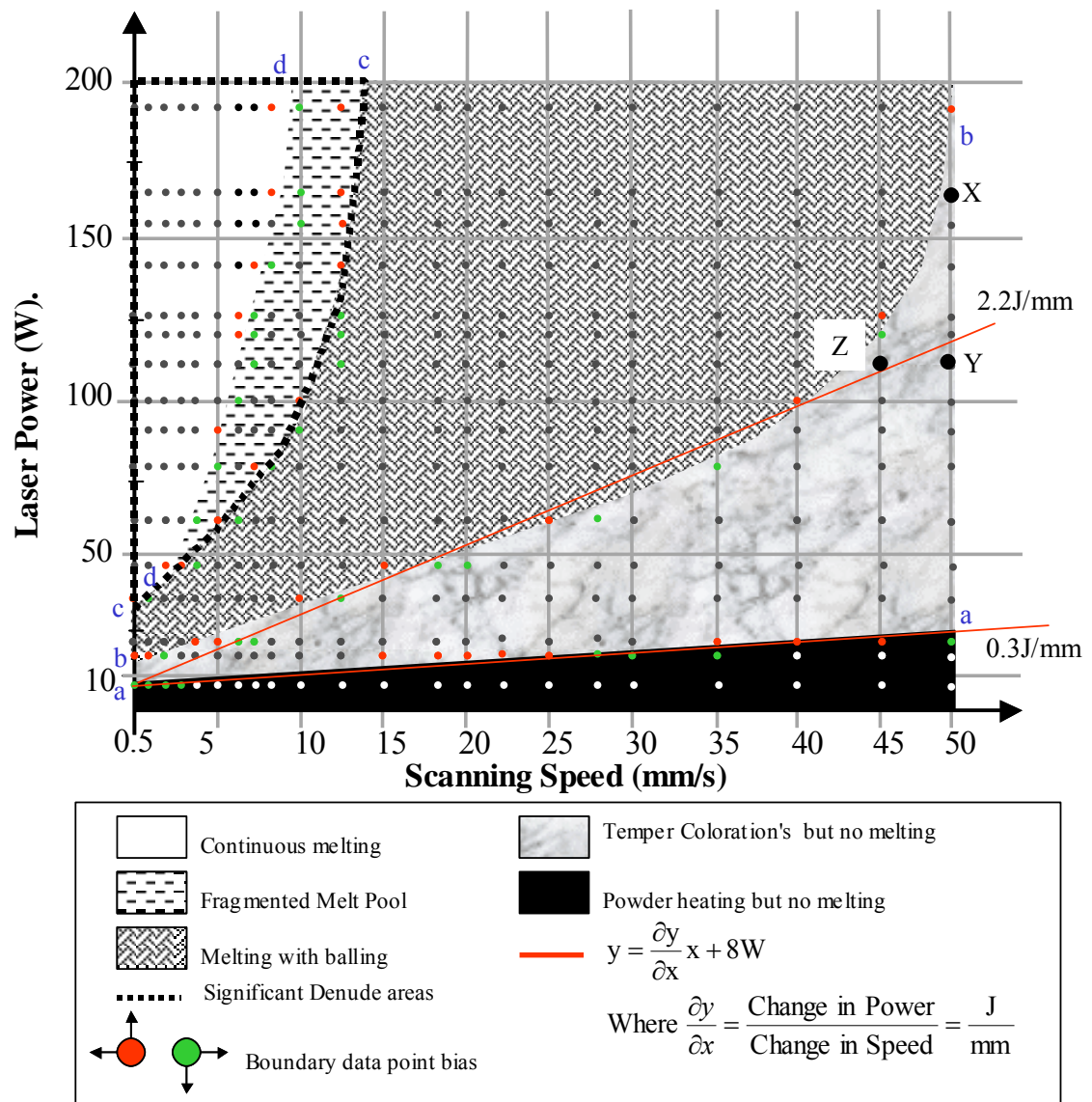


Figure 3.10: Process map for the 150/75 powder batch processed within a laboratory „air“ atmosphere.

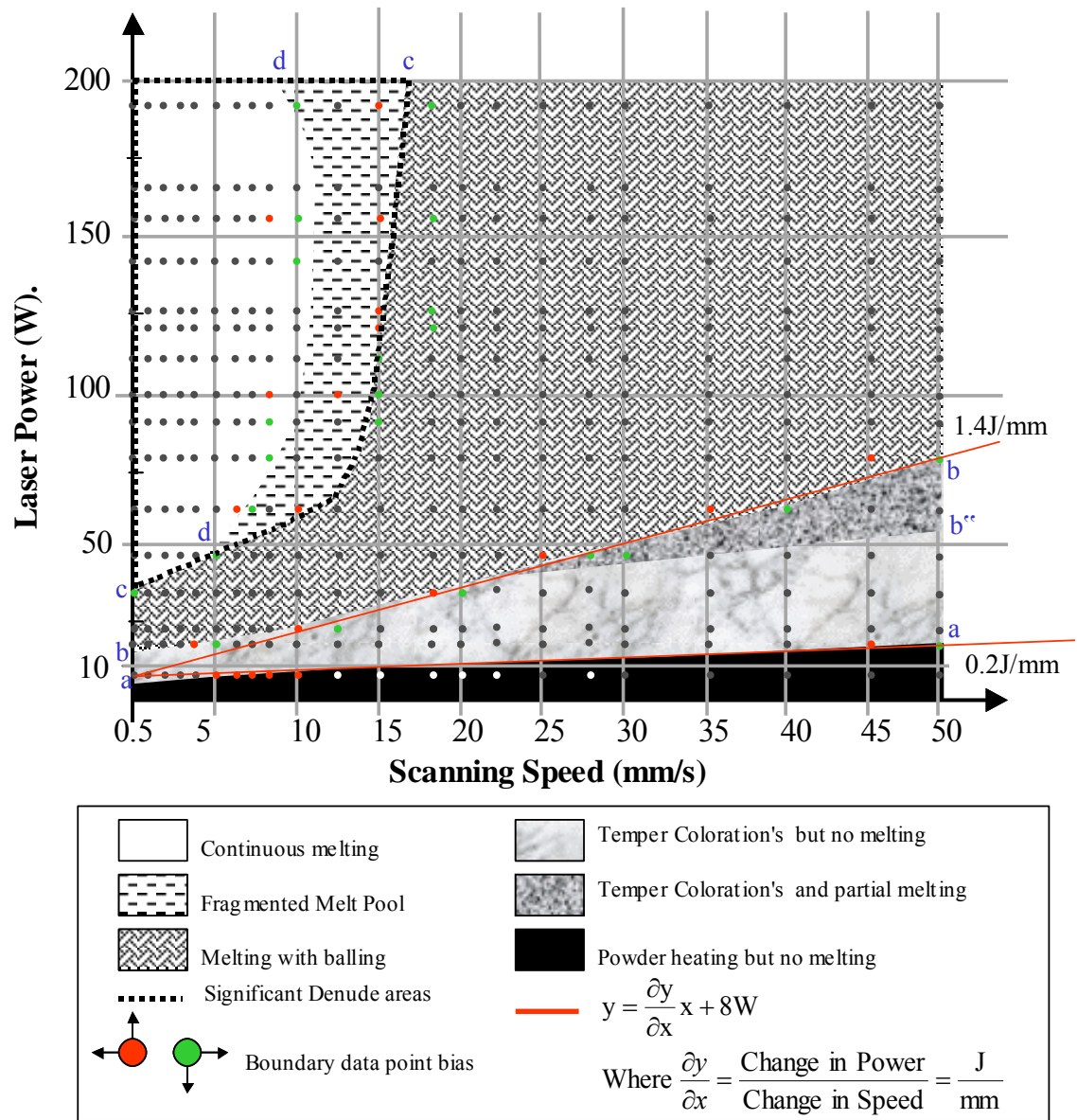


Figure 3.11: Process map for the 75/38 powder batch processed within a laboratory „air“ atmosphere.

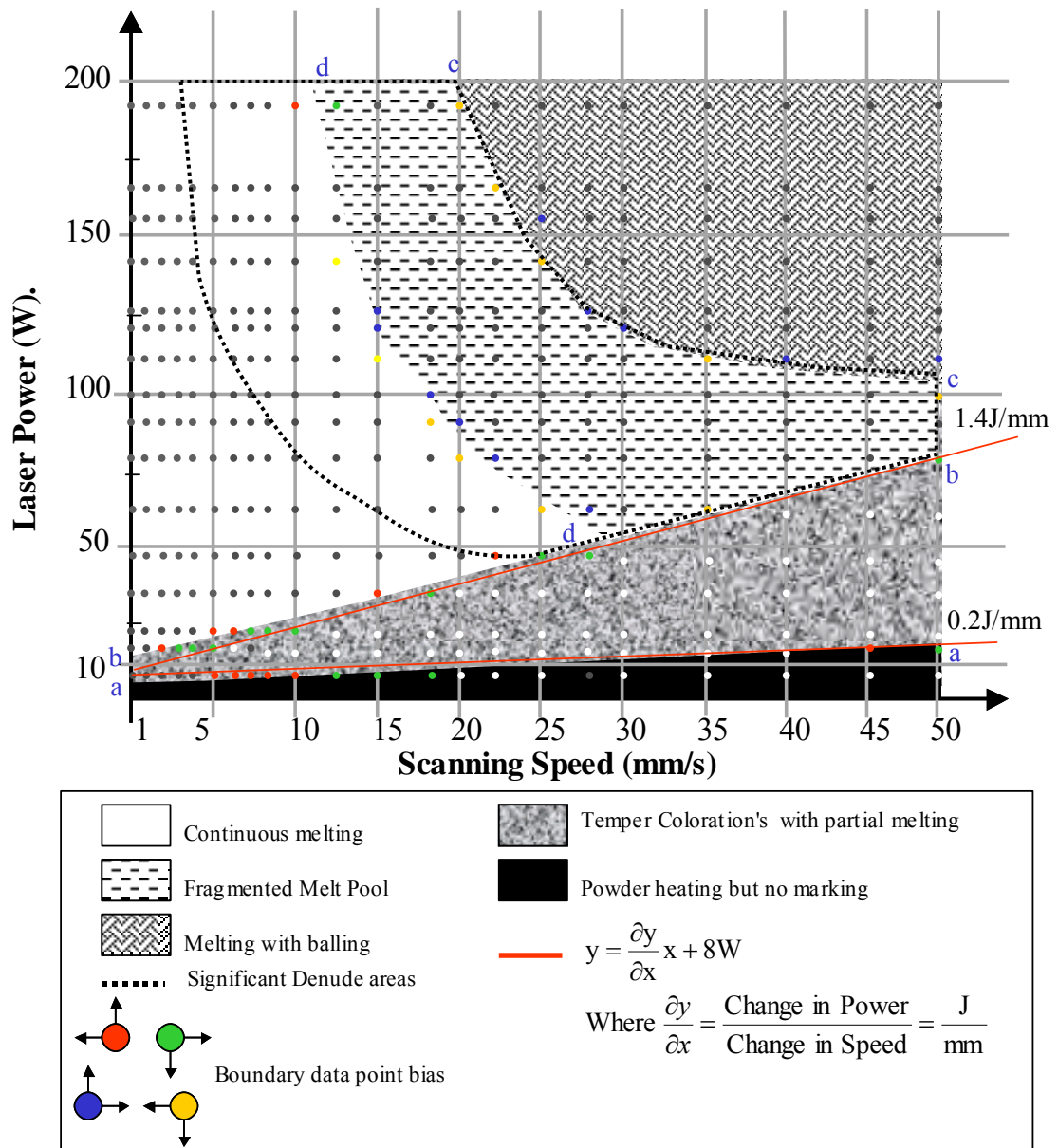


Figure 3.12: Process map for the -38 powder batch processed within a laboratory „air“ atmosphere.

3.1.3 Characteristics of the Melt Pool

3.1.3.1 Melt Pool Form

The pictures of melt tracks in Figures 3.4 – 3.7, the process maps displayed in Figures 3.9 – 3.12 and the measured results in Appendix D show, for the 300/150, 150/75 and 75/38 powder batches, that a variation of laser power from 30W to 200W and scan speeds from 0.5mm/s to 10mm/s (speed range increasing with increasing laser power) produced melt tracks that are largely continuous, have uniform width and depth along their entire length and are smooth in shape. The underside of the melt tracks (side facing the powder bed) was generally covered in sinter bonded powder at high energy densities (J/mm). However, as the energy density reduced the sintered bonded powder diminished leaving tracks with a reasonable smooth underside at high scan speeds (see Section 3.4.3.2). Some irregularities or melt pool „bulges“ were recorded, but these are generally more prolific at low scan speeds and limited to the very start of the scan track.. The occurrence of these bulges is believed to be caused by a combination of melt pool balling at the point of first melting and a large volume collapse of powder (see Section 3.4.4). However, it is difficult to be precise on this matter due to the speed of formation and solidification of the melt tracks, even at such low speeds.

Melt tracks produced from the -38 powder batch were largely similar in shape and form to tracks produced from the other three powder batches. There are however, some important differences. Firstly, combinations of low scan speeds (<3mm/s) and mid to high laser powers (>70W) produced tracks with large voids that looked analogous to blowholes or keyholes. Since such phenomena are associated with over heating, it is speculated that increased laser absorptivity, trigger by perhaps oxidation (see Chapter 1, Section 1.6 and 1.73) or an increase in apparent surface area due to finer particles, is the likely cause. Secondly, again at low scan speeds (<3mm/s) the melt was surrounded by a large amount of loosely bonded powder, caused by a probable increase in thermal conductivity due to a greater number of contacting spheres per unit volume, creating melt tracks with a much higher aspect ratio (depth/width). Finally, due to a combination of the „key hole“ effect and sinter bonding of powder to the melt core, tracks produced at low scan speeds were very irregular in shape, rough and often fragile or broken in the

vicinity of a keyhole. For this reason, melt tracks produced below 3mm/s were not measured or weighed.

3.1.3.2 Width and Depth Changes

The single tracks described in Section 3.4.1 were removed, where possible, from their powder beds and their dimensions (width, depth and length) were measured and an average value was recorded. The width and depth of each track was measured to assess changes in melt pool shape (aspect ratio) and size as scanning conditions and powder particle size distribution change. In all cases the initial melt bobble that occurs at the start of many of the tracks was not taken into account during measurement (see Section 3.4.4). The track length was also obtained in conjunction with track mass to enable mass per unit length data to be calculated. These latter results are described in Section 3.4.3.3.

The equipment used to obtain the dimensional data is described in Chapter 2, Section 2.3.5 and data accumulated during measurement can be seen in Appendix D. Before each measurement was taken each track was lightly brushed to remove any loose debris i.e. excess powder and loosely bonded particles, to enable accurate measurement of the core re-solidified melt volume. As a final note, in Appendix D tabulated data showing track length can change significantly if the melt pool fragments (the process maps displayed in Figures 3.9 – 3.12 can be used to reference this phenomena).

As outlined in Section 3.4.1 and discussed in greater detail in Section 3.4.5, the collapse of powder into the melt causes the melt pool width to grow and become very much greater than the beam width (beam width = 1.1mm). Hence, for the 300/150, 150/75 and 75/38 powder batches the melt width reached a maximum value of 3.5mm and reduced steadily with decreasing scan speed and decreasing power. The minimum melt pool width generally ranged between 1.0mm and 2.0mm before balling and fragmentation commenced (see Figures 3.13 – 3.15). The curve d-d in the figures corresponds to the fragmented melt pool boundary line d-d in the process maps.

There are however, a couple of exceptions to the general observations discussed above. Firstly, all melt pools produced from the 150/75 powder batch reached a minimum value of approximately 1.0mm before fragmentation and balling commenced, suggesting perhaps some link between melt pool width and beam width as a trigger for

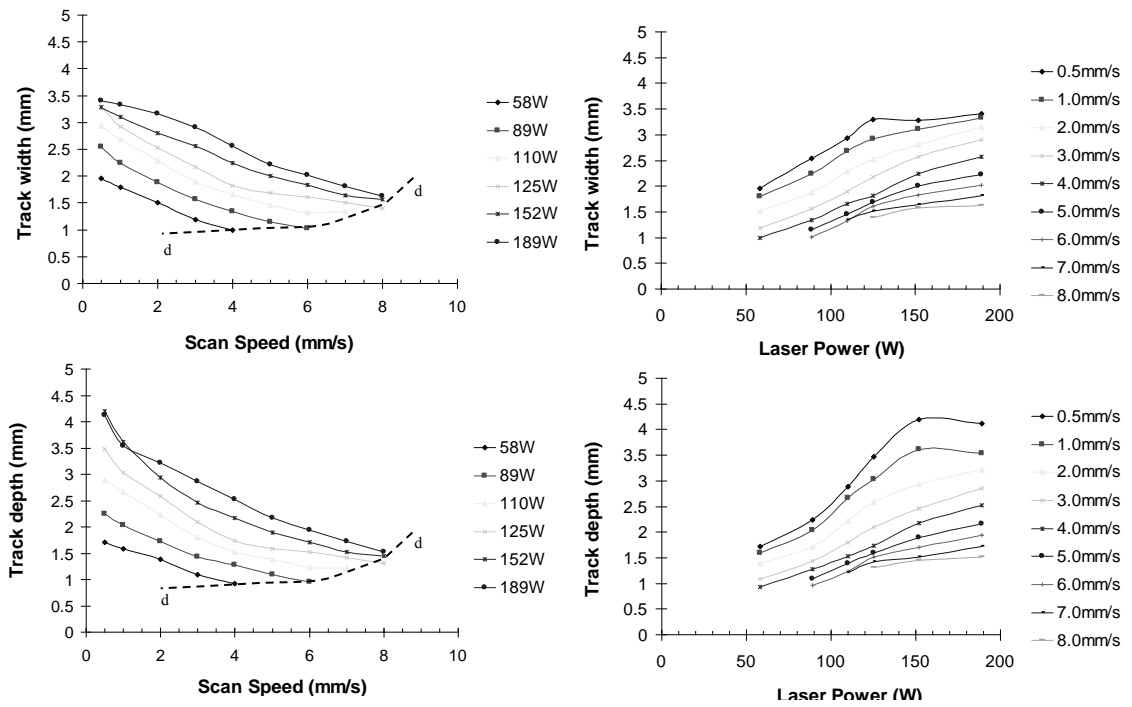


Figure 3.13: Melt pool dimensions as a function of scan speed and laser powder. Results for the 300/150 powder batch are shown.

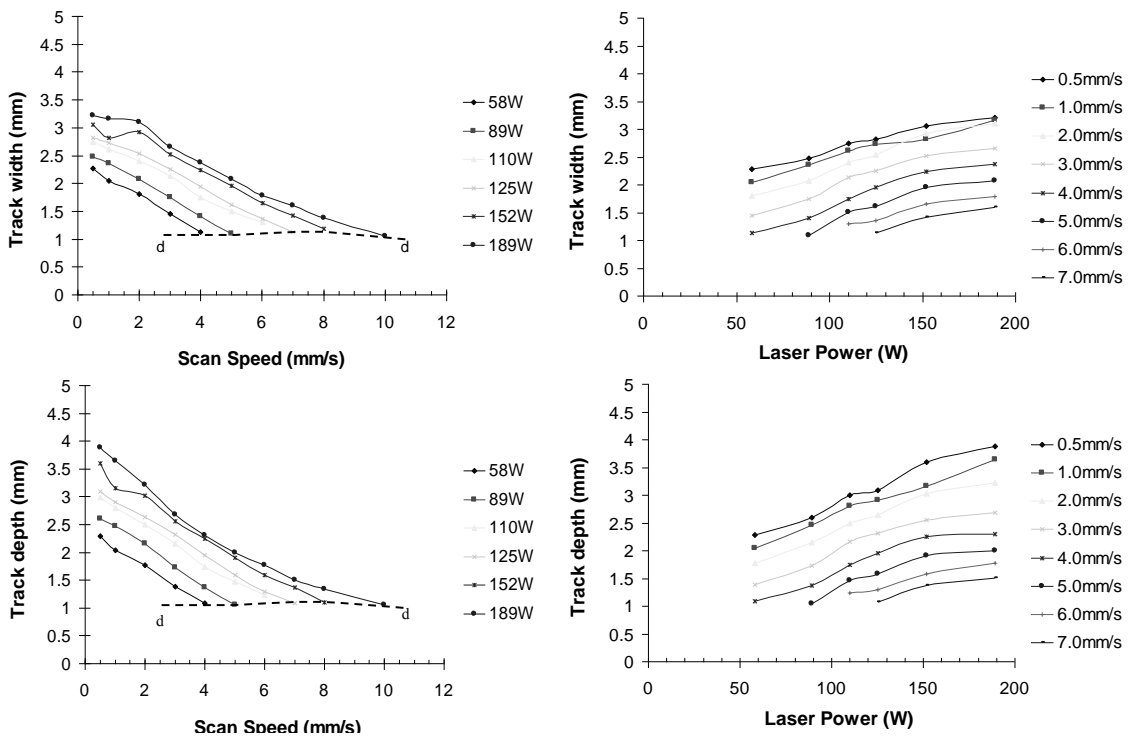


Figure 3.14: Melt pool dimensions as a function of scan speed and laser power. Results for the 150/75 powder batch are shown.

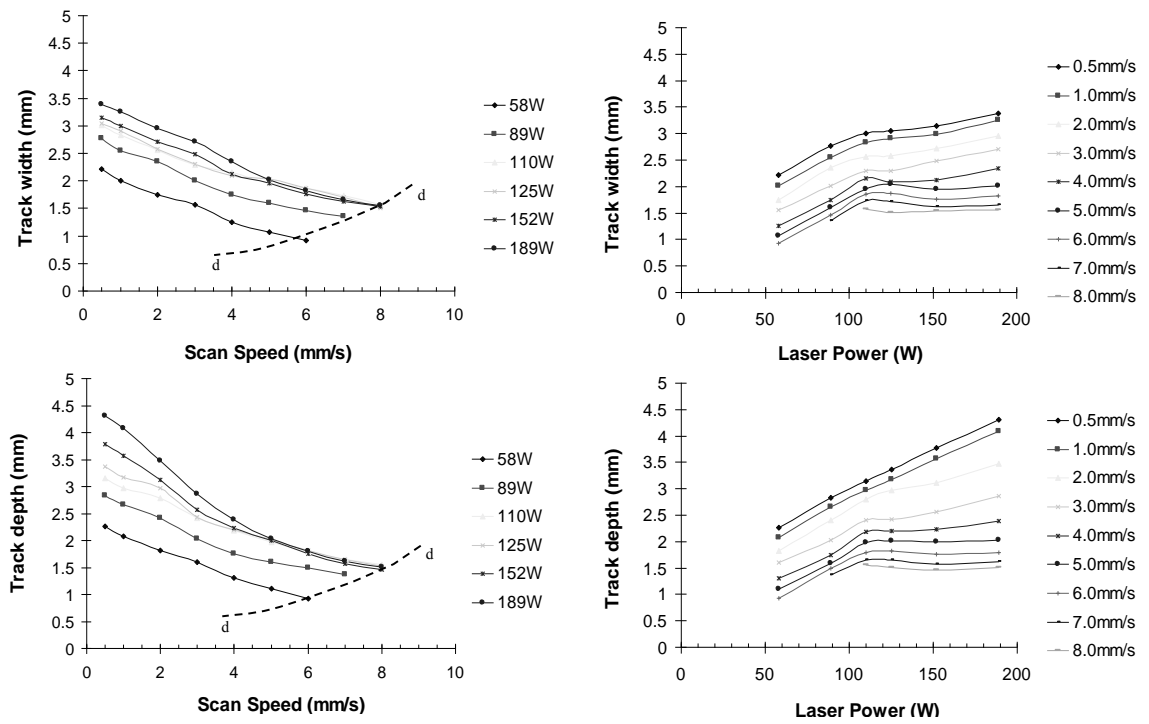


Figure 3.15: Melt pool dimensions as a function of scan speed and laser power. Results for the 75/38 powder batch are shown.

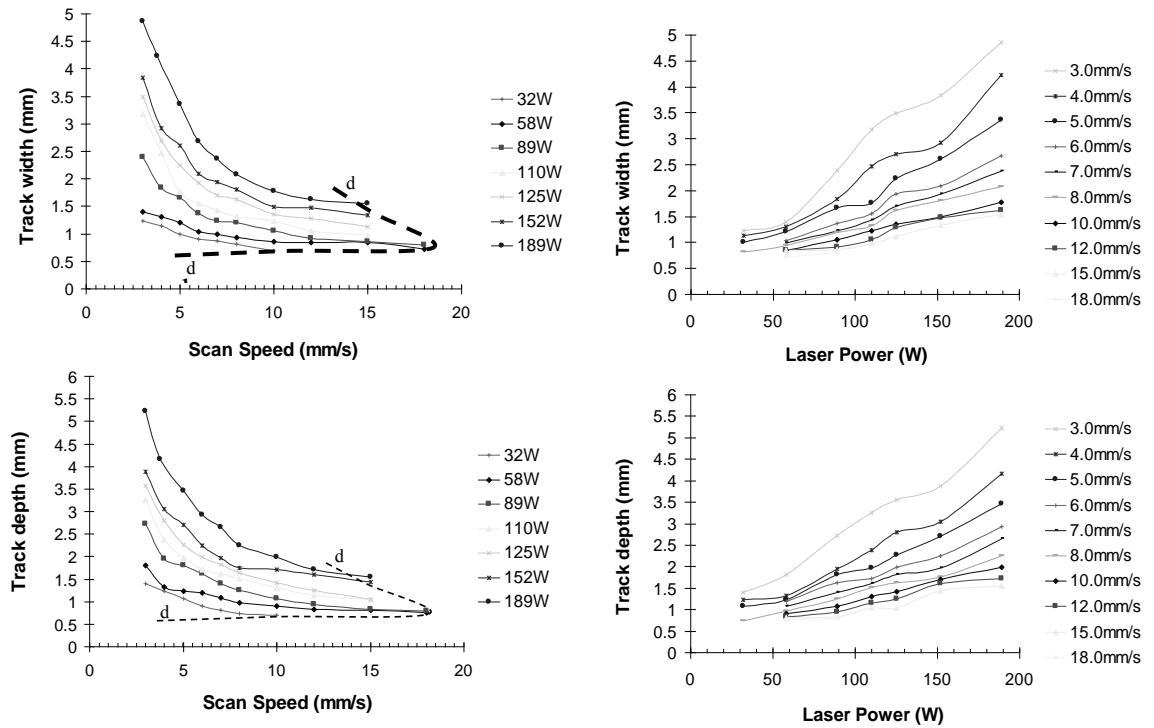


Figure 3.16: Melt pool dimensions as a function of scan speed and laser power. Results for the -38 powder batch are shown.

balling. Secondly, at high laser powers ($>125\text{W}$) there is a drop off in width progression with all further increases in power. An immediate response to this observation might be to associate the observation with the formation of a small vapour cloud above the melt front which might be occurring at high energy densities (J/mm). This vapour cloud would act to obscure the laser radiation. However, it is apparent in Figures 3.13 – 3.15, that this width reduction phenomenon is not consistent between powder batches. For the 300/150 powder batch, it only occurs at the high powers reported above and at low scan speeds, i.e. supporting the claim of a vapour cloud. However, the phenomenon does not occur in the 150/75 powder batch and only occurs at high scan speeds in the 75/38 powder batch, thus dismissing the vapour cloud theory. As an alternative solution, it might perhaps be better to consider the effects of the collapsing powder since this is known to affect melt dimension and be affected by powder fluidity i.e. powder particle size distribution. This argument is perhaps further strengthened if we now consider the relationships between width and depth and power and speed of melt tracks produced using the -38 powder batch (see Figure 3.16).

The effects of speed and power on track width for the -38 powder batch are given in Figure 3.16. At low scan speeds and/or high laser powers the melt width reached a maximum value of 5.0mm. Because the melt pool was subjected to only small amounts of collapsing powder, the increased width of the tracks, when comparing with tracks from the other three powder batches, was instead caused by large amounts of powder sinter bonding to the melt core through increased powder bed thermal conductivity. Hence, tracks produced at low speeds and high powers consisted of a fully melted core edged by liquid phase sintered powder within the heat affect zone. Because of limited powder collapse, the melt pool width reduced more rapidly in the speed range 3.0mm/s to 6.0mm/s compared to the other three powder batches. Between 6.0mm/s and 12.0mm/s the melt width began to level out reaching values, again between 1.0mm and 2.0mm, and continued to remain at these values until much higher scan speeds once again triggered melt pool balling (15mm/s – 18mm/s). These steady state values are reached because the laser-material interaction time reduces with increasing speed and so the melt volume becomes more short lived and therefore the sinter bonding of surrounding powder particles reduce. This omission of extra powder, both from

conduction and collapse, creates track widths which remain smaller and at the lowest energy densities, they remain similar in width to the diameter of the laser spot.

The effect of scan speed and laser power on melt pool depth is also shown in Figures 3.13 – 3.16. Because the melt pools are generally cylindrical in shape and governed by surface tension forces, the melt depth follows a similar relationship to that of width.

The ratio, depth/width, known here as the melt aspect ratio, has been calculated for all melt tracks and the relationship as a function of scan speed has been plotted and given in Figure 3.17. Images showing the change in melt cross section as a function of change in incident energy source for an un rastered line (i.e. showing melt pools in a direction normal to the direction of scan) are given in Figure 3.18. The width (b) and depth (d) dimensions are marked on the figure adjacent to the relevant cross section together with the values of the scanning parameters. For the 300/150, 150/75 and 75/38 powder batches, at low scan speeds (<4mm/s) and/or high laser powers (>110W) the melt aspect ratio was generally high. This again can be attributed to the sinter bonding of loose powder on the underside of the melt and is clearly visible on the images of melt aspect ratio in Figure 3.18. As the speed increases when irradiating at high power, or when the power remains low (<110W) the melt aspect ratio approaches values in the range 0.9 – 1.0, irrespective of particle size distribution. In contrast, the aspect ratio of melt pools taken from -38 powder beds shows a more chaotic relationship as scan speeds increased. Most results falls between values of 0.9 and 1.2, but because of the large amount of sinter bonded powder around the underside, the aspect ratio of the melt core is somewhat disguised. Also shown on Figure 3.17 are two curves; (1) a curve representing the path taken of the d-d melt fragmentation boundary and (2) a curve which passes through the minimum points of all the d/b versus scan speed curves. In the figure it can be seen that both curves follow each other reasonably closely, are both reasonably horizontal and have average values of aspect ratio between 0.92 and 0.96. This suggests that for all scanning conditions and for all powder batches (excluding -38) the melt aspect ratio approaches a similar value when the transition boundary between continuous melting and melting with fragmentation is reached. If an average of all results is calculated (see Figure 3.17), then the melt aspect ratio is seen to reduce with

reducing powder particle size. An observation again linked to the amount of powder sinter bonded to the underside of the melt track.

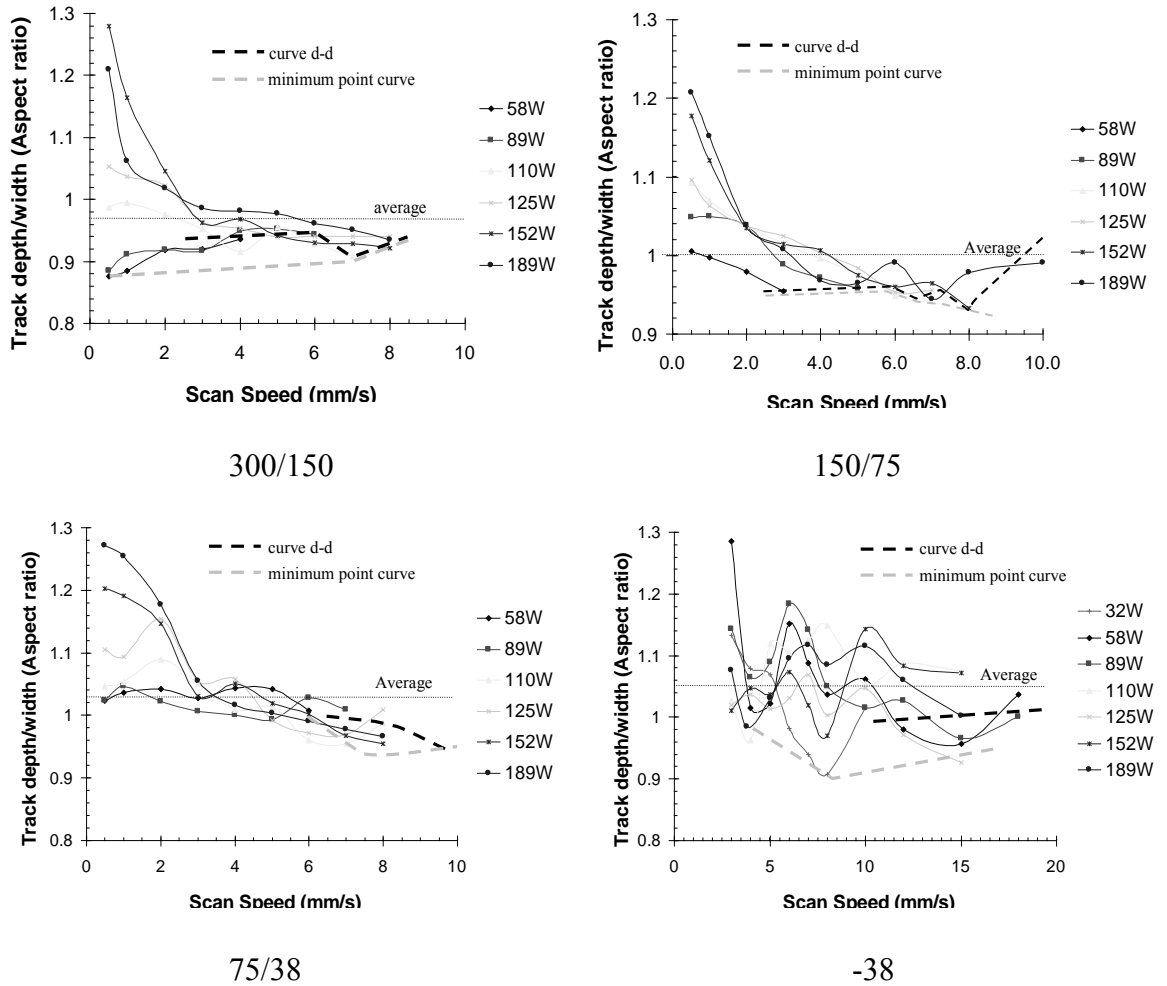


Figure 3.17: Melt pool aspect ratio as a function of scan speed for the 300/150, 150/75, 75/38 and -38 powder batches.

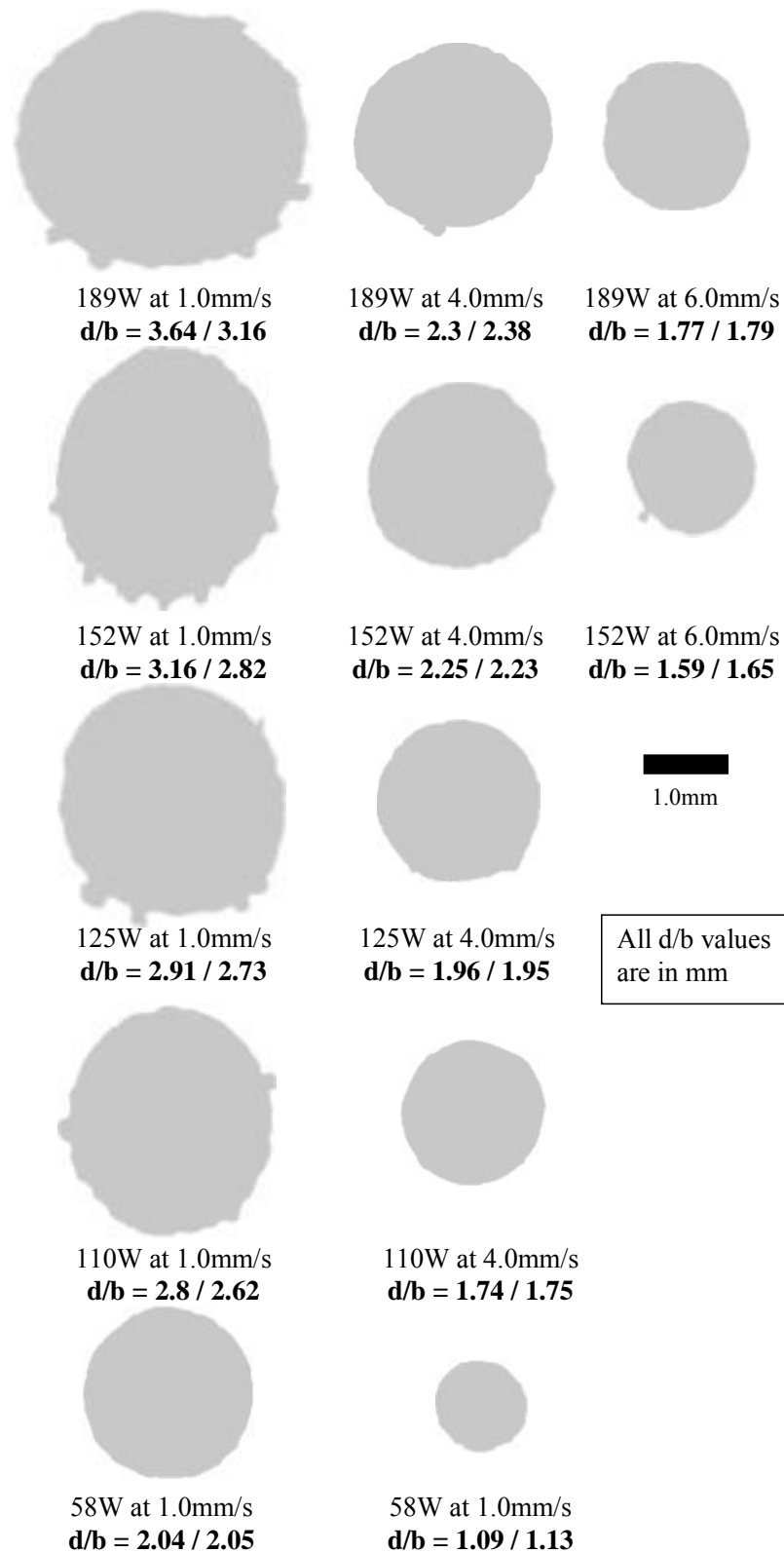


Figure 3.18: Images showing melt track aspect ratio. All tracks were removed from powder beds containing the 150/75 powder size distribution. The Images are approximately at X8 magnification.

Finally, Figure 3.19 shows contours of constant track width which have been superimposed onto duplicates of the process maps which were originally given in Figures 3.9 – 3.12. The purpose of this figure is to outline the change in dimensions of the melt tracks relative to the continuous melting – fragmented melt pool boundary. Once again a similar pattern is emerging where in all but the -38 powder batch, the contours of constant track width follows similar directions and changes in direction at the boundary line. Once again emphasising a possible link between melt pool shape and balling. These results will be discussed further in Chapter 5.

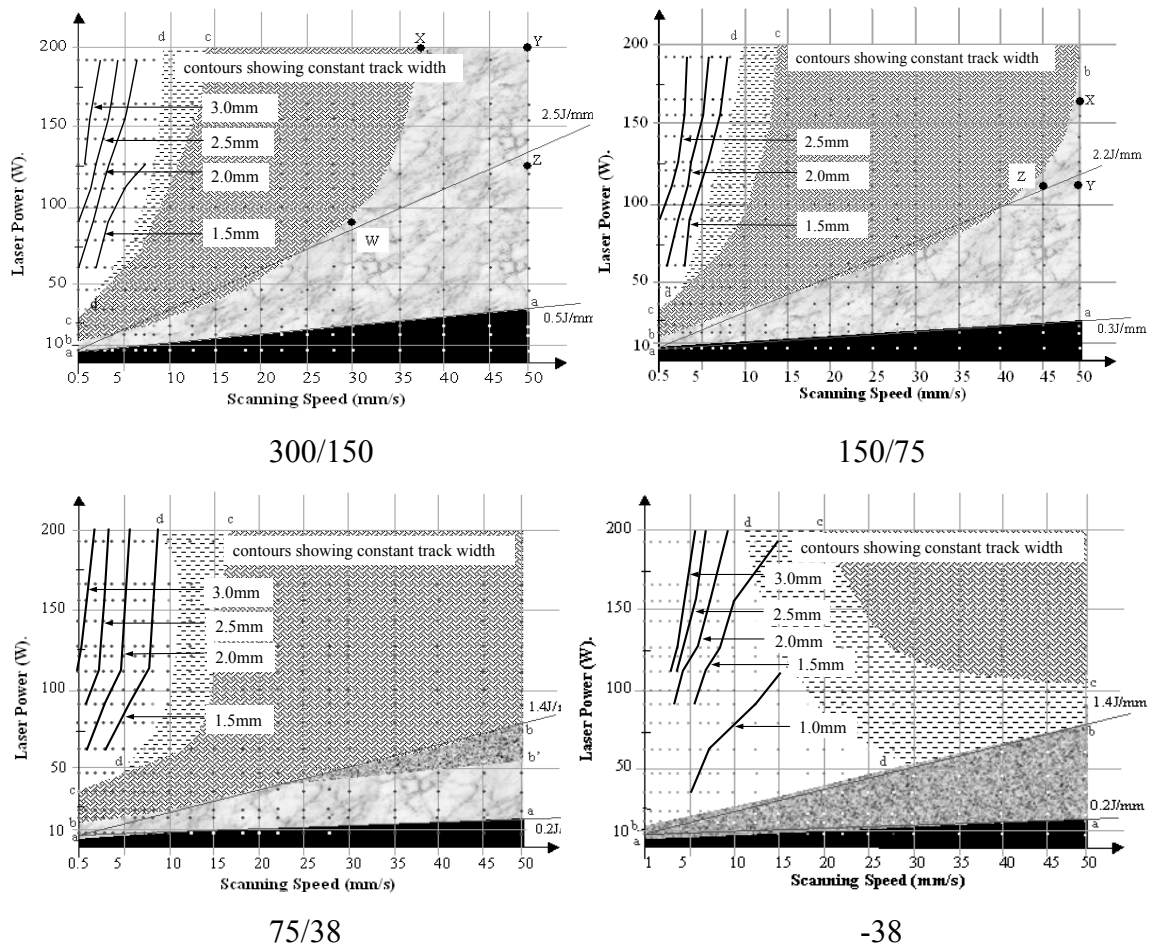


Figure 3.19: A plot showing contours of constant track width superimposed onto the process maps for the 300/150, 150/75, 75/38 and -38 powder batches.

3.1.3.3 Mass Changes

As well as measuring melt pool dimensions, tracks removed from the 150/75 and 75/38 powder beds were also weighed and plots of track mass per unit length (grams/mm) as a function of laser energy density (J/mm) were created. These plots can be seen in Figure 3.20. Most of the results again fall within one region bounded by two straight line slopes labelled High Speed (HS = >4mm/s) and Low Speed (LS = 0.5mm/s). Data points that lie outside of this zone are generally associated with low laser powers. However, for the 150/75 powder batch, results of track mass per unit length for tracks produced at the very highest laser power (189W) have a much lower value than all of the other tracks produced at much lower laser powers. A reason for this anomaly cannot be determined and therefore the results at this particular power level are considered to be the effect of some unknown experimental error. Values for laser absorptivity can be estimated from these plots. This will be considered further in the discussion in Chapter 5.

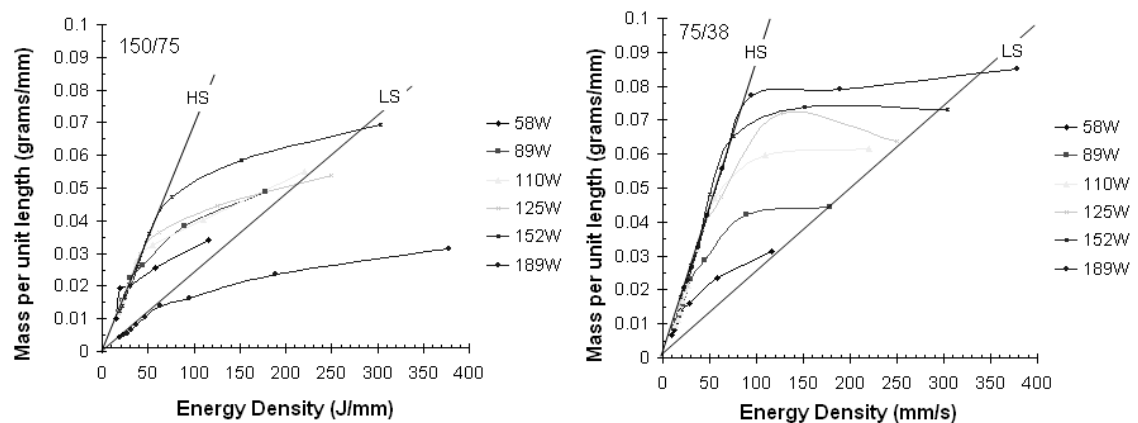


Figure 3.20: Melt pool mass per unit length plotted as a function of laser energy density for the 150/75 and 75/38 powder batches. LS represents the Low Speed slope (0.5mm/s) and HS represents the High speed slope (>4mm/s).

3.1.4 Powder Trenching and Melt Pool Irregularities

A number of melt pool irregularities, such as depth changes within the powder bed and the „bobble“ that forms at the start of the melt track, are thought to be linked to the effects of suppressed surface tension driven fluid flows and powder displacements during melt formation, both of which cause a trench or denude area to form around the periphery of the melt volume. Before these irregularities are discussed, the mechanisms which cause trenching will be considered.

3.1.4.1 Powder Trenching

Due to the cylindrical shape of the melt volume, powder displacements leading to denude areas around the periphery of the melt pool were frequently observed. Typical examples of these observations are given in Figure 3.21. Due to the difficulty in photographing this phenomenon, the reader is urged to look at the shaded region under the ruler in the figure to gauge the degree of trenching around each melt pool.

Trenching is triggered by the changing shape of the melt pool. Immediately upon melting, surface tension forces pull the melt into a cylindrical form (see Figure 3.22). This leaves a denude area all around the periphery of the melt volume (see Figure 3.22b). Hence, due to the cylindrical shape of the majority of melt tracks, melting within an air atmosphere often causes this phenomenon; this is emphasised by the process maps in Figures 3.9 – 3.12.

Immediately after the change of shape of the melt pool, the walls of the trench become unstable and so collapses, causing movement of particles from the trench walls to the melt volume (see Figure 3.23). This causes both the trench and the melt volume to increase in size as well as affecting the solidification rate of the melt (see Section 3.4.5). Hence, trenching appears to be a two stage process.

Although not measured, the angle „ θ “ of the stable trench wall is likely to be closely associated with a powder characteristic known as the angle of repose. The repose angle „ ϕ “ (see Figure 3.22d) is the angle made between the slanted surface of a powder pile and the horizontal plane, and is a measure frequently used to quantify the flowability of a powder (German, 1998). Since flowability is governed by particle size, the angle of repose and therefore the size of the trench, is affected by powder particle

size. The experimental results are in line with this assumption, where reductions in the size of the denude area are especially noticeable when irradiating the -38 powder batch (see Figure 3.7). Furthermore, because the angle of the trench wall is presumably constant for a particular power batch, the trench will therefore increase in size as the melt volume, or more specifically the melt depth, increases. Again, based on visual interpretations, the experimental results agree with this assumption.

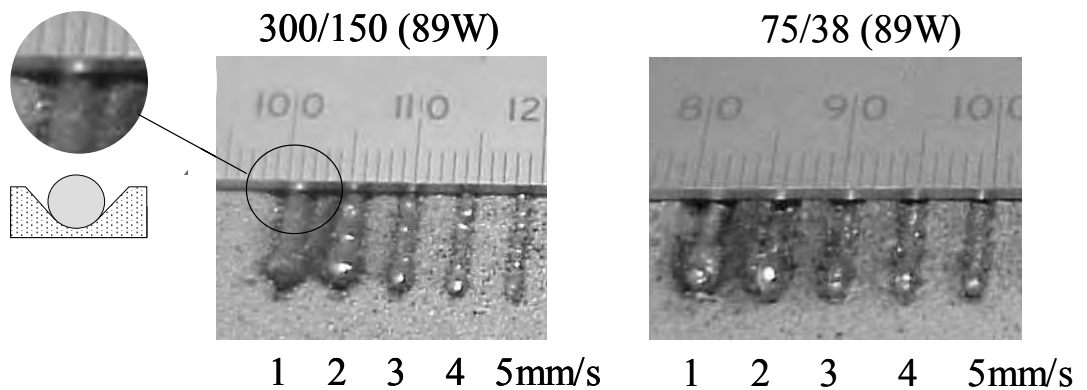


Figure 3.21: Trench formation during SLS.

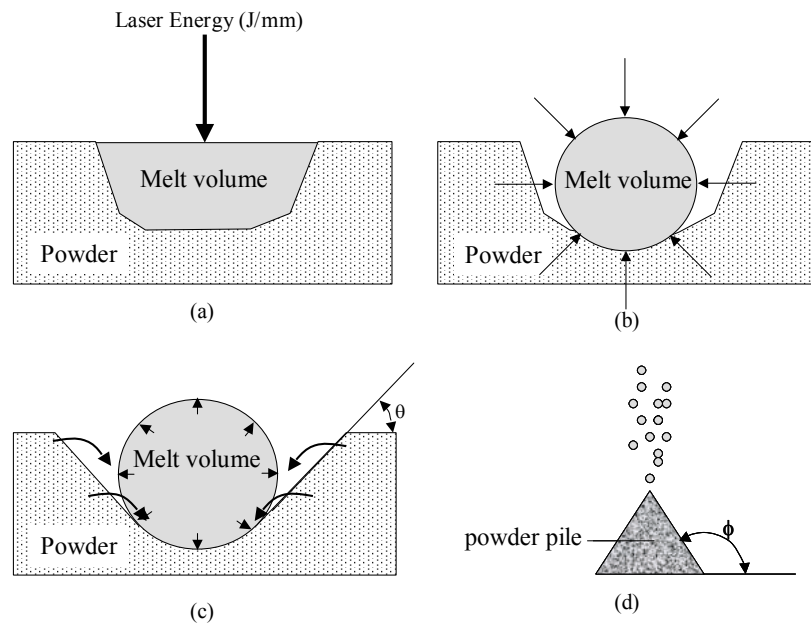


Figure 3.22: Stages of powder collapse and trench formation during SLS.

3.1.4.2 Melt Pool Irregularities

During melting a large melt bobble was often found securely attached to the melt tracks at the point of first melting. Figure 3.23 shows a typical example of a series of solidified tracks lifted from their powder bed, placed on their side and photographed. In the figure, at high scan speeds (and low laser powers) the bobble is clearly visible. As the speed reduces (or the laser power increases) the bobble clear increases in size and exhibits a change in shape from spherical to more elliptical. At very low scan speeds (approx. $< 5\text{mm/s}$) the bobble is often followed by a downwards shift of the melt front, before a final period of horizontal growth. This causes the remainder of the melt volume to be situated significantly below the powder surface. It is also worth noting that at very low scan speeds (1mm/s) the underside of the melt is often distorted by a large number of sintered bonded particles. Schematic diagrams given in Figures 3.24-3.26 show the „bobble“ effect and ensuing melt growth more clearly as scanning conditions and powder particle sizes change. The figures emphasise that in all cases the melt bobble sticks up above the powder surface, that the magnitude of the downwards shifting melt front is higher in the 75/38 powder batch, that the cross sectional area of the melt remains fairly constant throughout (excluding bobble) and that the size of the bobble reduces with reducing powder particle size.

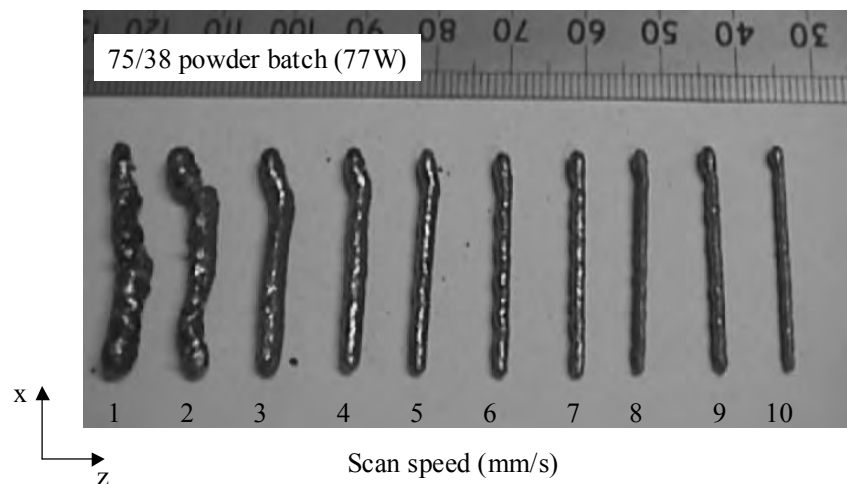


Figure 3.23: Melt pool irregularities during air melting.

When the laser first hits the powder layer, a melt pool will be created which, due to surface tension forces, will take up the shape of a sphere. This will be followed almost immediately by the formation of a trench as outlined in Section 3.1.1.1. Due to the large amount of displaced powder falling into the melt (from all sides), the sphere will quickly freeze and remain intact (see Figure 3.27). As the laser scans the powder surface the subsequent melt is much smaller in volume because of fewer displaced particles (from the side and front only). Furthermore, as the beam scans the powder surface it is highly feasible that the beam will be irradiating powder particles located within the trench rather than at the powder bed surface. This might explain the downwards shift of the melt front, although it does not explain why this shift recedes after a short period of melt front growth.

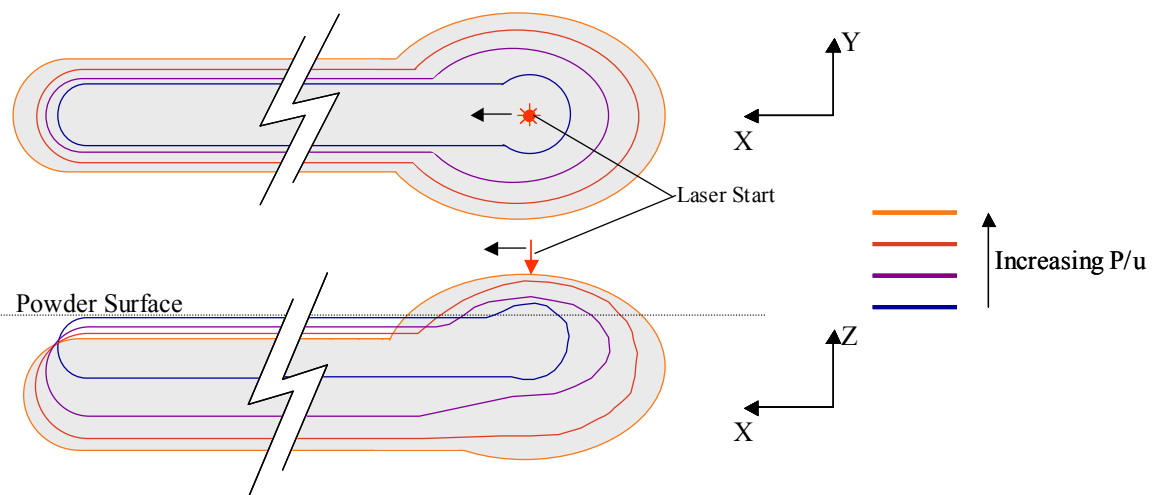


Figure 3.24: Bobble formation in melt tracks produced using the 300/150 and 150/75 powder batches.

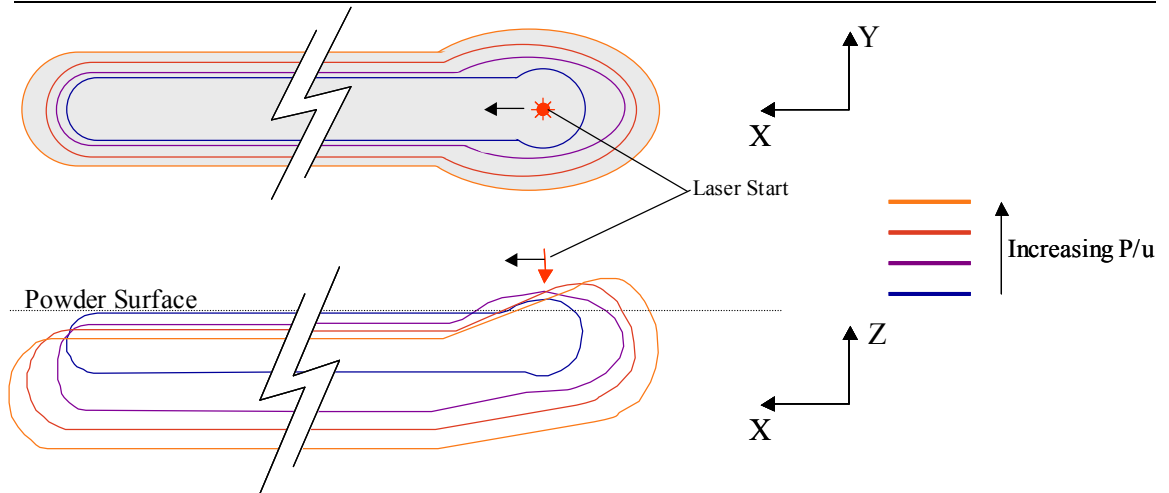


Figure 3.25: Bobble formation in melt tracks produced using the 75/38 powder batch.

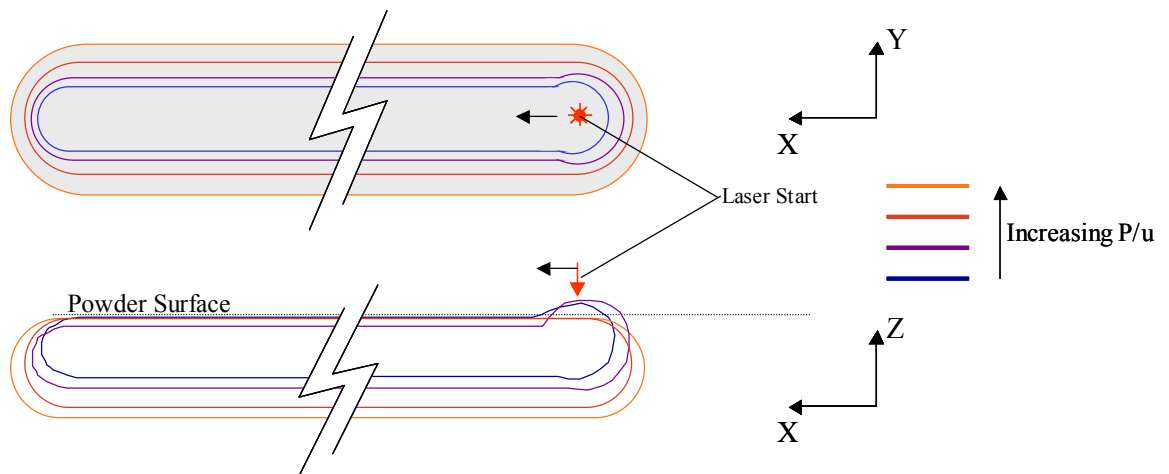


Figure 3.26: Bobble formation in melt tracks produced using the -38 powder batch.

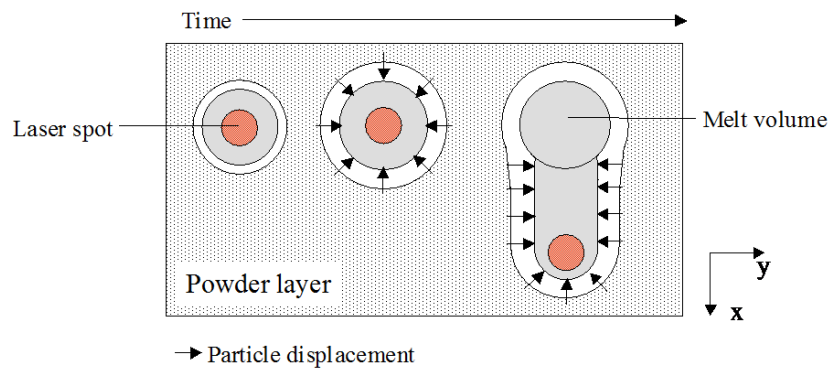


Figure 3.27: Bobble formation in melt tracks.

3.1.5 Microscopy studies

The single tracks described in Section 3.4.1 were removed, where possible, from their powder beds and sectioned in a direction normal to the direction of scan. The samples were then prepared for inspection by mounting, polishing and etching as outlined in the procedures given in Chapter 2, Section 2.5.6.

In Section 3.3, it was shown that the microstructure of the starting powder was predominantly equiaxed dendritic. As the laser scans the surface of the powder (low power) the particles will heat up (still in the solid phase) and the microstructure will coarsen a little bit. The speed of heating and cooling is so rapid that solid phase bonding through atom migration will not occur and the powder particles can still be considered singular. As the laser power is increased further, the temperature of the particles increases and liquid action begins to occur. This can occur over a wide range of scanning conditions as outlines in the process maps in Figures 3.9 – 3.12.

From a powder consolidation point of view, the existence of the liquid phase occurs at the outer shell of the particles forming necks between neighbouring particles (see Figure 3.28). From a microstructural point of view, the presence of some liquid action will start to cause regions between the dendrites to become liquid. As the power increases further and the temperature is raised, more and more liquid becomes available. Because mass transfer is much faster in a liquid the coarsening rate increases dramatically. Therefore, the dendritic skeleton that was once present will coarsen and spheradise. With further heating, remelting and coarsening continues until the temperature of the melt, T_m , gets sufficiently high above the liquidus temperature, T_L , such that the melt becomes fully liquid. T_L is approximately 1350°C for stainless steel 314s HC.

If partial remelting is only achieved before the laser power is removed ($T_m < T_L$), such as conditions depicted by the partial melting region of the 75/38 or -38 process maps (see Figures 3.11 and 3.12), then the solid phase will begin to re-grow from solid fragments that are present in the melt, since these are ideal nucleation points. If there is full remelting ($T_m > T_L$), such as in the continuous melting regime, then no sites are available to nucleate the solid from within the melt pool. Instead, and ignoring the possibility of nucleation from impurities, the crystals that form are nucleated by the

particles attached to the underside of the melt volume. This will be referred to as the powder-liquid interface in this thesis. These particles originate from the underlying and surrounding powder layer and attach either through association or through entrapment as powder particles collapse into the melt from the walls of the surrounding trench (see Section 3.4.4).

This type of crystal growth is known as epitaxial. Hence each crystal in the melt pool is forming initially as a continuation of one of the dendritic grains in the original powder particle. This is clearly shown in the micrographs given in Figures 3.29-3.31. Hence, the results of this work are in agreement with earlier work by Smugeresky et al., (1997) (see Chapter 1, Section 1.8).

As the solid phase grows back into the liquid the temperature is sufficiently low to drive growth but not sufficiently low to cause further nucleation. Therefore, fully liquid nucleated particles at the bottom grow up, liquid closest to the laser beam (top of the melt track) never gets cold enough to have any other nucleation and so the crystals will re-grow unhindered all the way out creating a cellular or columnar structure i.e. growing in one direction and panning out in a direction opposite to the heat flux. This structure is often seen in cast or welded alloys. Once again, Figures 3.29 and 3.30 clearly demonstrates epitaxial growth of the cellular structure from the equiaxed dendritic crystals located at the interface between the two growth regimes.

The size of the dendritic grains within the melt pool are strongly dependant on the grain size of the initial powder particle, hence grain refinement could theoretically be achieved by careful selection of particle size, since particle size dictates particle grain size (see Section 3.3). The effects of particle grain size on the growth of the cellular structure is however less clear. Since the cellular structure grows epitaxially from the dendritic microstructure, the results do suggest a link. However, because the dendritic structure coarsens as it progresses up through the melt, the differences clearly observed at the particle-liquid boundary were found to be less distinguishable at the dendritic/cellular interface.

This interface between the equiaxed dendritic zone and the columnar zone is very distinct i.e. not highly diffusive, and this is a good indication of very little convective stirring occurring within the melt pool. Furthermore, it is likely that the boundary

between the two zones shows the position at which the melt volume reached the liquidus temperature of the material, T_L . In the majority of cases this boundary was close to the bottom of the melt pool. It followed closely the contours of the melt and covered an area up to 180° about the vertical centre line of the melt. However, the boundary was found to move up marginally through the melt as the laser power density reduced (see 3.32). Hence, at the highest values of energy density the elevated temperature of the melt caused cellular crystals to grow directly from nucleation sites at the powder-liquid interface (see Figure 3.31). Interestingly, this structure was also found to occur at very low power densities in the 300/150, 150/75 and 75/38 powder batches, suggesting that perhaps nucleation is primarily initiated by displaced powder from trenching rather than underlying particles. In Section 3.4.4.1, it was discussed that trenching was less severe when the melt volume was small.

It was thought that the above statement might perhaps be strengthened by observing the structure of melt pools produced using the -38 powder batch since trenching was less severe when melting this powder. However, a far greater number of particles were found attached to the melt volume when processing this powder, and so these must of acted as effective nucleation sites, since the interface between equiaxed dendritic and the columnar microstructure was marginally higher (by approximately 10%) up the melt volume (see Figure 3.32).

Finally, ignoring the small changes discussed above, in general powder particle size appeared to have little bearing on the location of the dendritic/cellular interface.

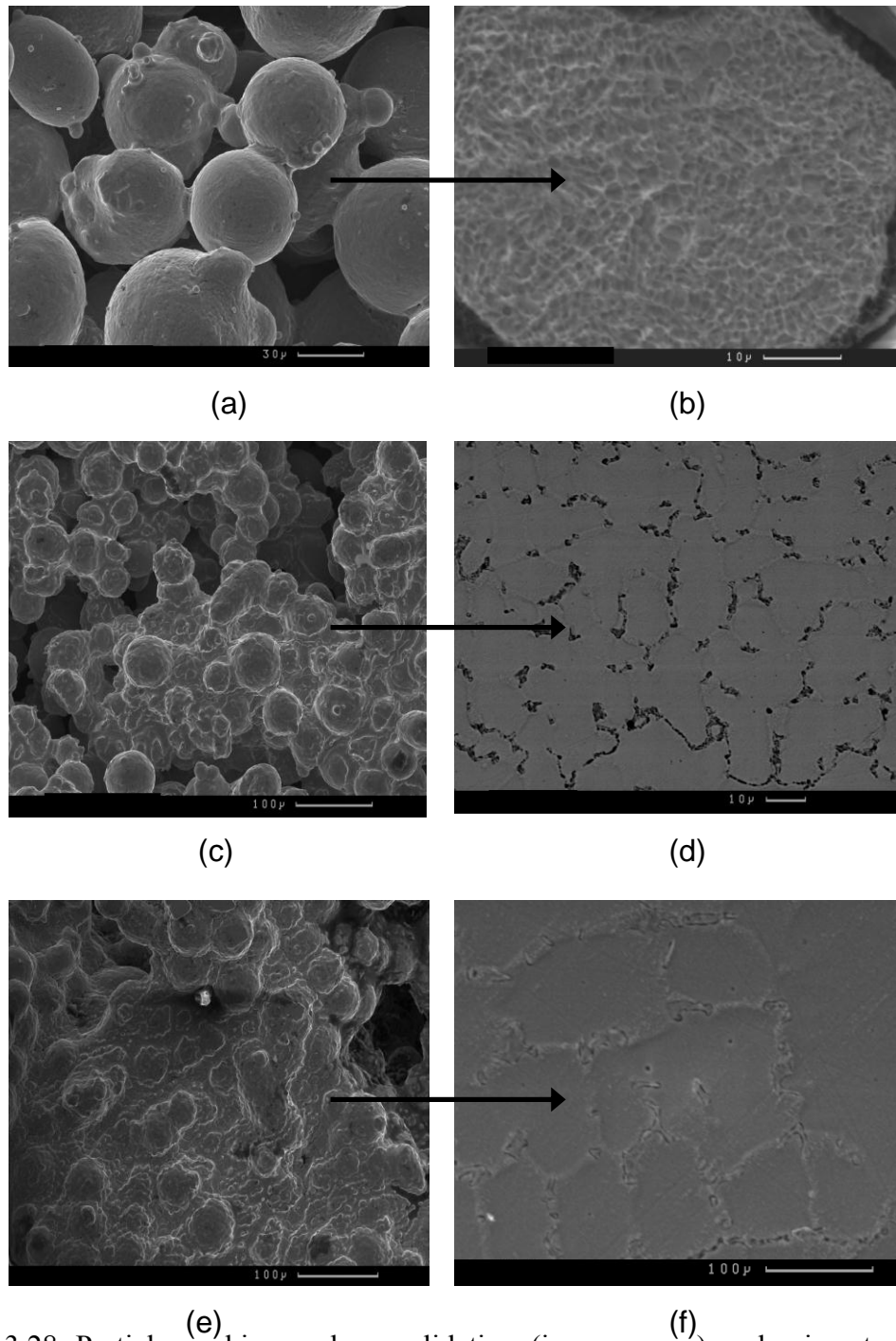


Figure 3.28: Particle necking and consolidation (images a,c,e) and microstructure coarsening (images b,d,f) during melting of the 75/38 powder batch in air. The laser power was fixed at 50W and the scan speed changed from (a/b) 35mm/s, (c/d) 30mm/s and (e/f) 25mm/s.

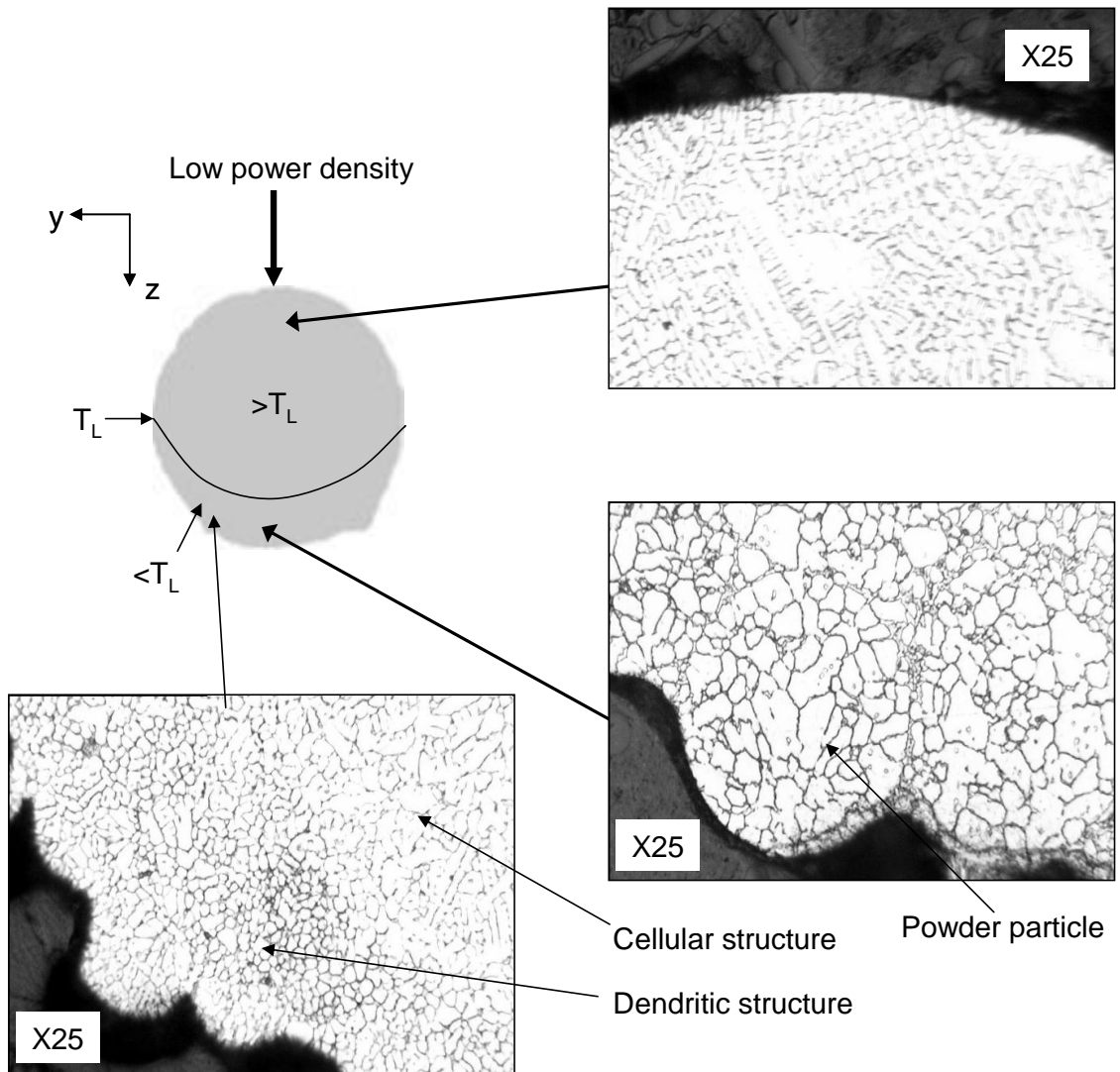


Figure 3.29: Microstructure of melt tracks scanned at low power densities (typically 110W at 4mm/s)

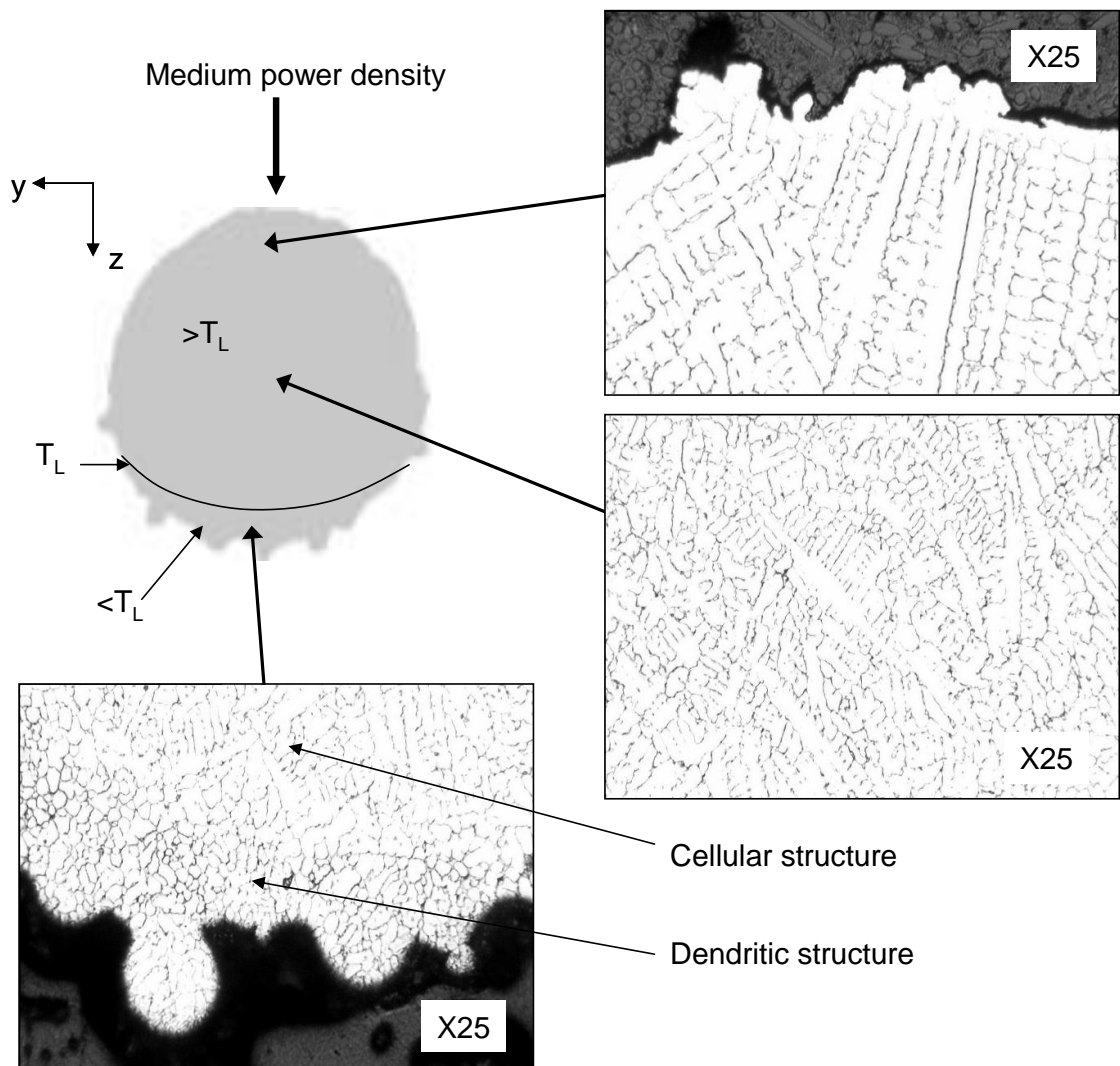


Figure 3.30: Microstructure of melt tracks scanned at medium power densities (typically 125W at 1mm/s).

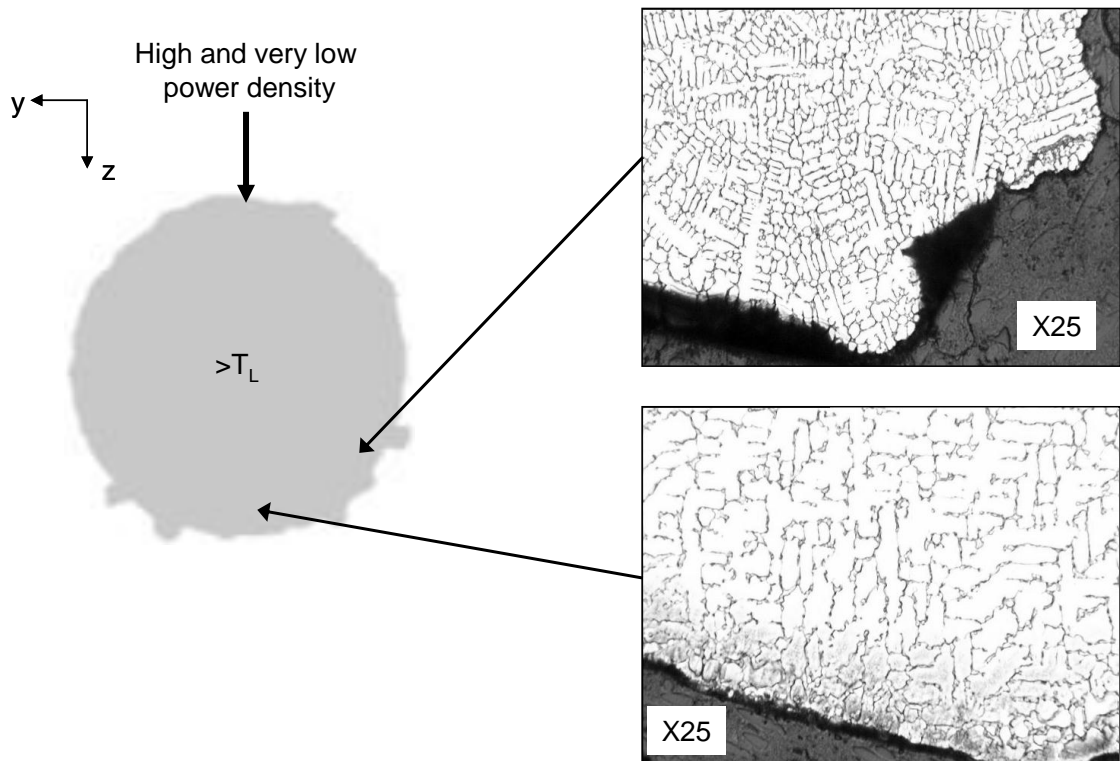


Figure 3.31: Microstructure of melt tracks scanned at high and very low power densities (typically 189W at 1mm/s).

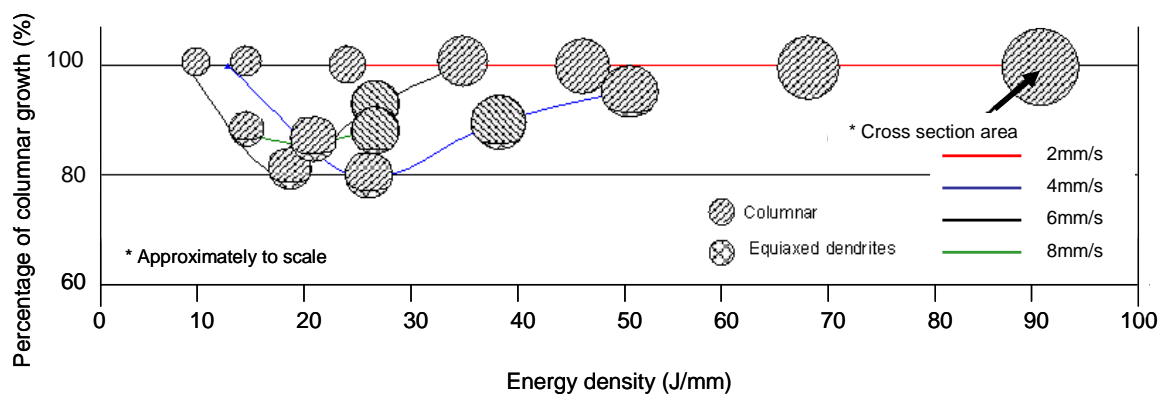


Figure 3.32: Percentage of columnar growth in melt tracks produced using the 300/150, 150/75 and 75/38 powder batches as scanning conditions change.

Selective Laser Sintering of Single Tracks Scanned in an Argon Atmosphere

The purpose of carrying out single track melting tests within an argon based atmosphere was to primarily observe and establish the effects of scanning conditions on melt behaviour patterns from within a controlled environment. The information gained from these experiments was then compared with results from experiments carried out within a non-controlled environment i.e. under oxidising conditions (see Section 3.4). These comparisons are discussed in Chapter 5 of this thesis.

The second objective of this study was the investigation of scanning strategies to produce good quality single tracks which yield good quality single and multiple layers. Good quality in the first instance, refers to a continuous uniform melt bead. Good quality, in the case of single layers, refers to a smooth uniform surface with minimal porosity, and in the case of multiple layers, a good interfacial weld or bond between layers. It will also become clear in Chapter 4, that melt pool aspect ratio has some additional importance on these quality characteristics. The results of the single and multiple layer tests are given in Chapter 4 of this thesis.

3.1.6 Qualitative Observations

Figures 3.33 – 3.36 show pictures of typical melt tracks produced by scanning a series of unidirectional traverses of the laser beam in an argon atmosphere. In the figures, there are a number of tracks scanned at 0.2mm/s and 0.8mm/s. These scan speeds are not given as experimental data points in Chapter 2: Experimental Methods. The reason for this is due to an unexpected phenomenon occurring in the melt pools at low scan speeds (see Section 3.5.2). This phenomenon, which affected the melt depth, required further investigation and so these extra data points have been included.

All four powder batches are represented in the figures. Once again, due to the complexity of characterising all of the discrete changes observed in the powder during exposure a number of changes of a qualitative classification have been chosen to be representative of each powder's total heating and melting response. Due to a great number of similarities in melting behaviour between air and argon processing some of the classifications have already been described in detail elsewhere in this thesis.

Therefore, to minimise repetition, suitable cross-references will be given in the text where appropriate. The classifications are listed below.

Powder heating but no marking (See Section 3.4.1): Scanning conditions over which this regime occurs during argon processing are generally limited to very low values of energy density (J/mm). An accurate summation of the extent of this regime over the scanning conditions covered in this work can be seen in the process maps of Figures 3.37 – 3.40.

Partial Melting (Liquid Phase Sintering): A focussed, moving Gaussian beam impinging on the surface of the powder layer has sufficient intensity to only causes melting of those particles located within a finite depth of the powder bed. The melt front will locally penetrate surrounding porosity and solidify, causing neighbouring particles to bond together in a manner similar to conventional liquid phase sintering (German, 1998). Because the penetrating melt front is short lived, the width of the tracks are often comparable in size to the laser spot diameter. Furthermore, because the viscosity of the track is high (melt volume + solid particles) the track is always greater in width than depth. Due to the protective argon atmosphere there are no visible signs of oxidation on the surface of the track or in the surrounding area influenced by a heat affected zone. Examples of this regime can be seen in Figure 3.33 at a laser power of 32W and scan speeds greater than 5mm/s.

Full Particle Melting (See Section 3.4.1): The behaviour of fully melted tracks produced within an argon atmosphere follow closely the behaviour of melt tracks produced within an oxidising atmosphere. There are however, some notable differences which will be discussed in the following text. Firstly, a continuous melt pool is not necessarily always cylindrical in shape. Due to surface tension driven fluid flows (see Chapter 1, Section 1.4.1) and increased melt viscosity due to the increase in sinter bonded particles on the underside of the melt, the melt track can assume a form where its width is very much greater than its depth. This is discussed in greater detail in Section 3.5.3. Secondly, all visible signs of oxidation are now largely diminished leaving the melt with a silver-metallic finish and all surrounding powder looking and behaving no differently to virgin powder. Thirdly, the highly visible „bobble“ frequently recorded at the start of tracks produced within an oxidising atmosphere rarely occurs in

tracks produced within an argon atmosphere. Finally, when comparing the extent of powder collapse between the two sets of results, it has become clear that trenching is not only dependant on powder properties, but it appears to be also dependant on melt aspect ratio. Therefore, when tracks exhibit a low aspect ratio (depth/width), irrespective of scanning conditions, the amount of collapsing powder reduces. This has been discussed in detail previously in Section 3.4.3.2. As the laser spot travels over the surface of the powder layer, again three different types of melt pool growth are observed (see Section 3.4.1 for a more in depth explanation):

Growth Type I (Melting with Balling): Typical examples of melting within this regime can be seen in Figure 3.35 at a laser power of 143W and a scan speed of 10mm/s and in Figure 3.36 at a laser power of 170W and scan speeds in the range of 30mm/s – 50mm/s.

Growth Type II (Melting with Breakages or Fragmentation): Typical examples of melting within this regime can be seen in Figure 3.34 at a laser power of 170W and a scan speed of 2mm/s and 5mm/s and in Figure 3.35 at a laser power of 110W and scan speeds in the range of 5mm/s – 10mm/s.

Growth Type III (Continuous Melting): Typical examples of melting within this regime can be seen in Figure 3.33 at a laser power of 110W and scan speeds in the range of 0.2mm/s – 10mm/s and in Figure 3.34 at a laser power of 70W and scan speeds in the range of 0.2mm/s – 10mm/s.

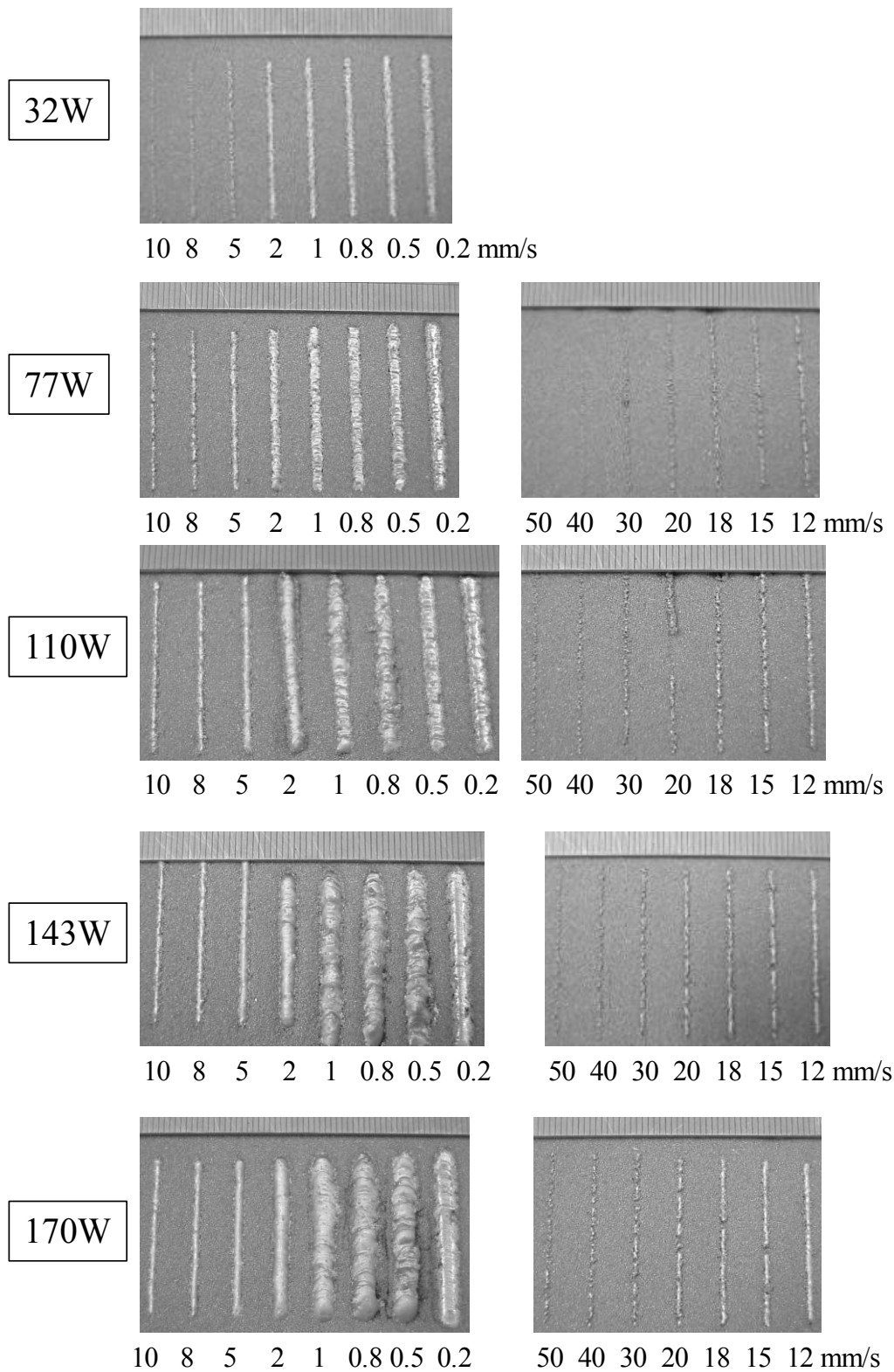


Figure 3.33: Tracks melted in an argon atmosphere using -300+150 μ m powder batch at different scanning conditions

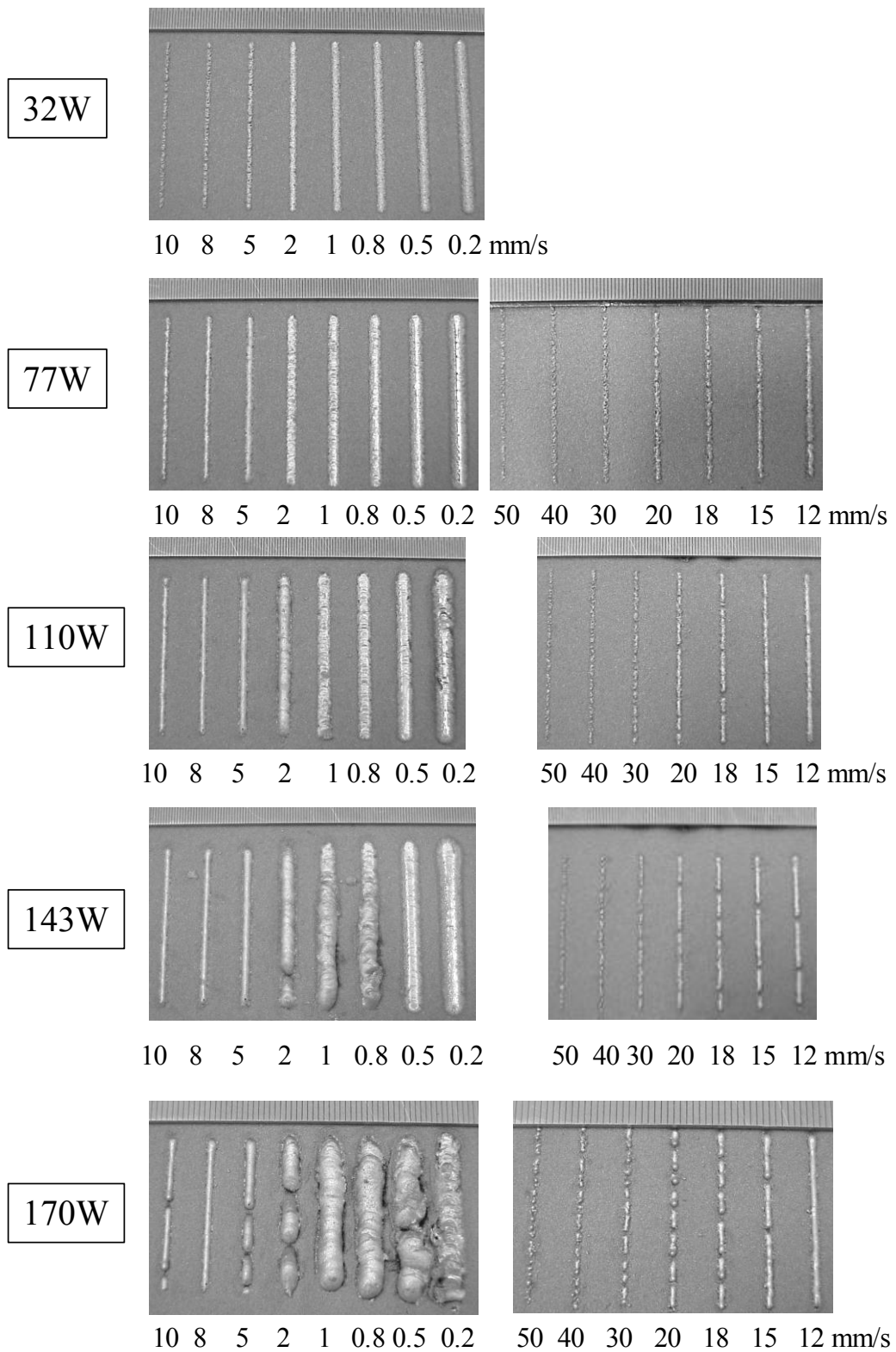


Figure 3.34: Tracks melted in an argon atmosphere using -150+75 μ m powder batch at different scanning conditions

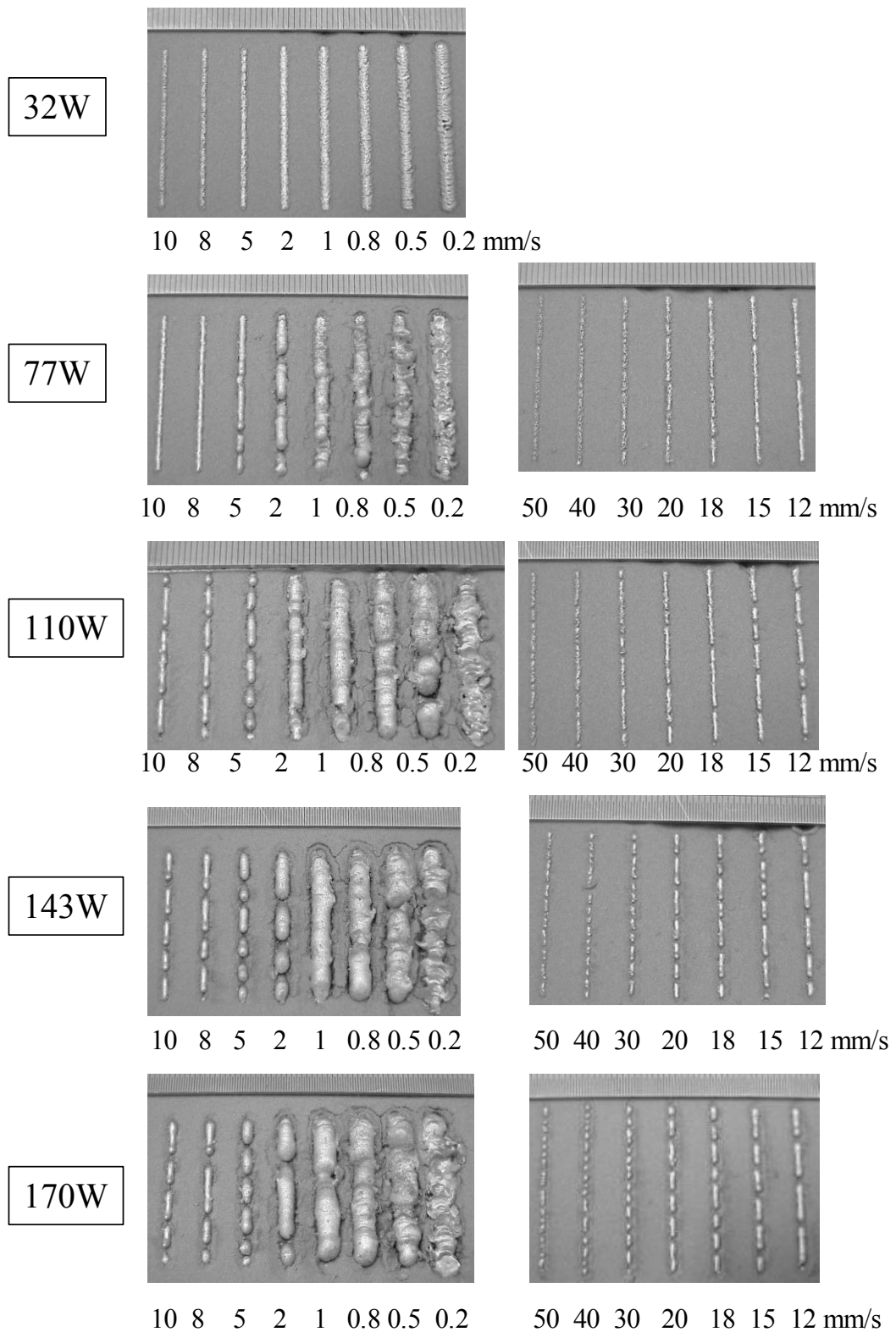


Figure 3.35: Tracks melted in an argon atmosphere using -75+38 μ m powder batch at different scanning conditions

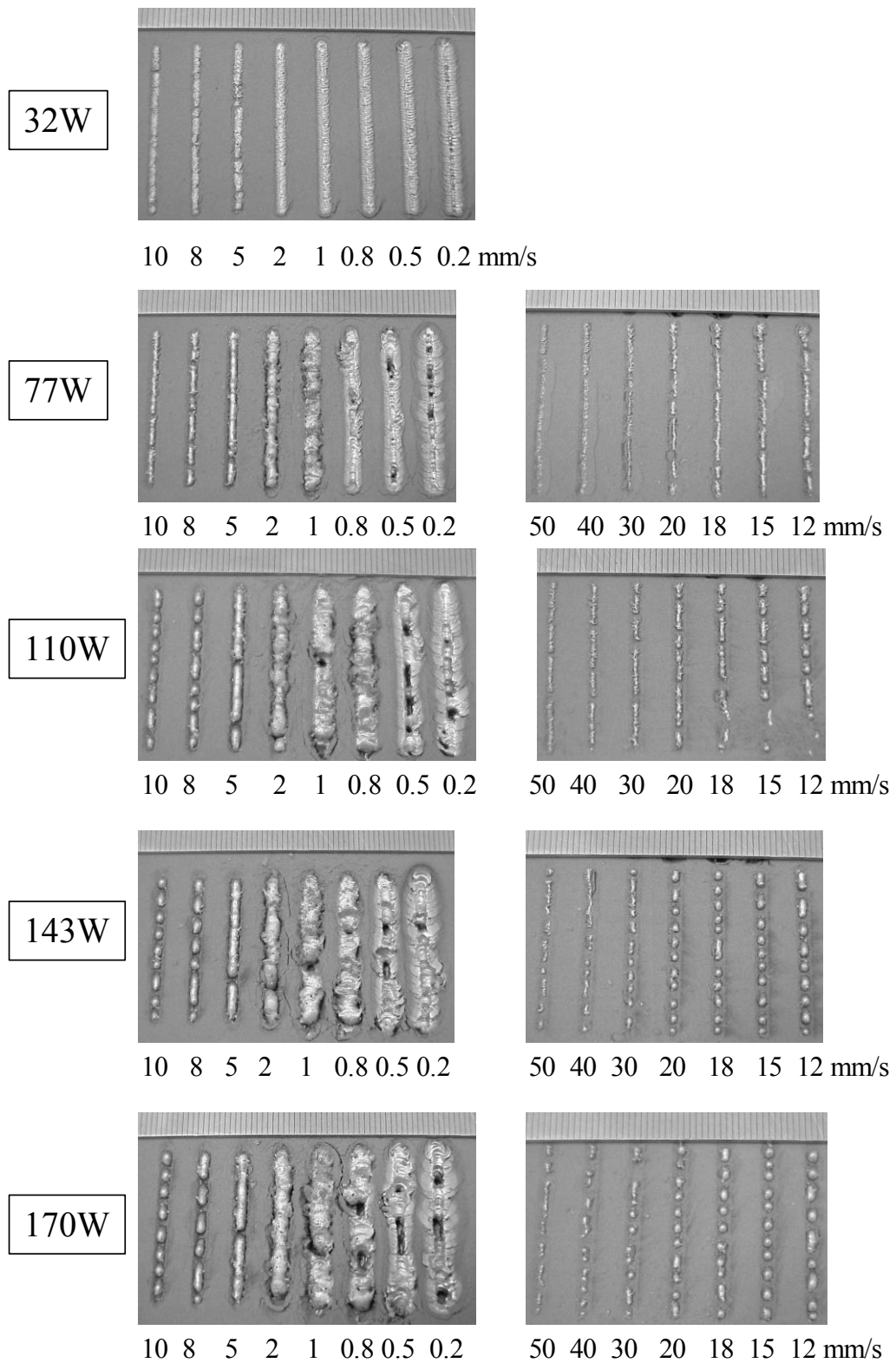


Figure 3.36: Tracks melted in an argon atmosphere using -38 μ m powder batch at different scanning conditions.

3.1.7 Process Maps

Process maps plotting the heating and melting response of the powders have been constructed to help increase the understanding of melt front progression as laser powers, scan speeds and particle size distributions change.

The maps, given in Figures 3.37 to 3.40, have again similar regions or regimes. Each regime is based on the qualitative classifications presented in Section 3.5.1. They are in most part well defined, often very predictable, and the powder heating but no marking and partial melting regimes are closely associated. Once full melting is achieved, the association between powder batches becomes less obvious. These differences will be discussed throughout this section. The nodal array displayed on each map indicates the number and value of experimental points used in the construction of the maps and the coloured nodes located along region boundaries help communicate boundary accuracy by indicating the degree of regime crossover.

In all four maps a diagonal boundary line a-a separates the regimes of powder heating but no marking below from the regime of partial melting (liquid phase sintering) above. The boundary is linear, suggesting that a critical value of energy density must be reached before the powder will melt under the incident radiation. The values range between 0.17J/mm and 0.5J/mm and increase with increasing powder particle size.

A boundary line b-b separates the partial melting regime to the right from a melting with breakages regime to the left. One significant difference observed between air and argon atmospheres is the break up kinetics of the melt. Section 3.4.2 demonstrates that an unstable melt pool within an air atmosphere will initially fragment creating a series of shortened, capsule shaped melt pools. As the scan speed increases, the melt pool capsules will quickly shorten and increase in number until finally, the irradiated area contains a number of equi-sized spheres. This occurs over a very small scan speed increase, typically 5mm/s-10mm/s. On the other hand, an unstable melt pool created within an argon atmosphere will also fragment, but will remain fragmented over a greater scan speed range. As the speed increases, the length of the melt capsules was found to reduce while their number was found to increase.

In the 300/150 and 150/75 powder batches, balling was found not to occur at all for scan speeds up to 50mm/s. In the 75/38 powder batch, balling was observed only at

high scan speeds, but since the melt volume was very small, processing conditions were difficult to define. Therefore, the melting with balling regime for this powder batch can only be approximated on the process map by an area to the left of the boundary line X-Y. For the -38 powder batch melt pool balling was more wide spread and therefore easier to distinguish. The regime was generally limited to laser powers above 90W and scan speeds greater than 10mm/s and was not too dissimilar to the process conditions depicted in the same process map for air melting.

A line c-c separates the fragmented melt pool regime to the right from a continuous melting regime to the left. For the 300/150 powder batch, the continuous melting regime covers a similar process window to that of air melting, hence the regime is still limited to a maximum scan speed of 10.0mm/s – 12.0mm/s before fragmentation commences. For the 150/75 powder batch the process window increases marginally along the scan speed axis, reaching a maximum value of approximately 15mm/s. However, this maximum value was found to peak around 100W, before reducing and falling back to 8.0mm/s-10.0mm/s at high laser powers. Within this regime there was also an isolated pocket where fragmentation took place. This occurred at laser powers above 150W and scan speeds below 5mm/s, where the behaviour of the melt was often unpredictable (see Figure 3.38). In the 75/38 and -38 powder batches the continuous melting regime was much reduced. Above 100W continuous melting could only be achieved at scan speeds below 2.0mm/s – 3.0mm/s. Below 100W continuous melting could be achieved at speeds up to 10mm/s in the 75/38 powder batch and up to 5.0mm/s in the -38 powder batch. However, in these two powders the melt volume was often extremely rough and not very uniform, especially at high laser powers (see Figures 3.35 and 3.37). Furthermore, melt pools produced in the -38 powder batch had a number of slots or keyholes forming along the centre line of the melt track.

In almost all cases the continuous melt pool was close to cylindrical in shape and so once again a denude area surrounding the melt pool could be observed. The dashed line in all four process maps indicates the range of scanning conditions over which a significant collapse of powder takes place. Again denude areas can be observed around fragmented and balled melt pools but since the melt volume is often much smaller, denude areas are also very small and difficult to distinguish. Powder collapse and trenching will be discussed in greater detail in Section 3.5.4. Finally, at low scans

speeds a region existed in the continuous melting regime where the melt pools had a low aspect ratio (depth/width). This and other observations concerning melt pool form will be discussed in greater detail in Sections 3.5.3.

The main differences between the four process maps was the shape and arrangement of the boundary line c-c which separates the fragmented melt pool regime and the continuous melting regime and the amount of melt pool balling that takes place. The change in position of the boundary line c-c did cause the continuous melting regime to reduce in area as the powder particle size reduced, but the shape of the boundary proved difficult to predict. This is discussed in greater detail in Chapter 5.

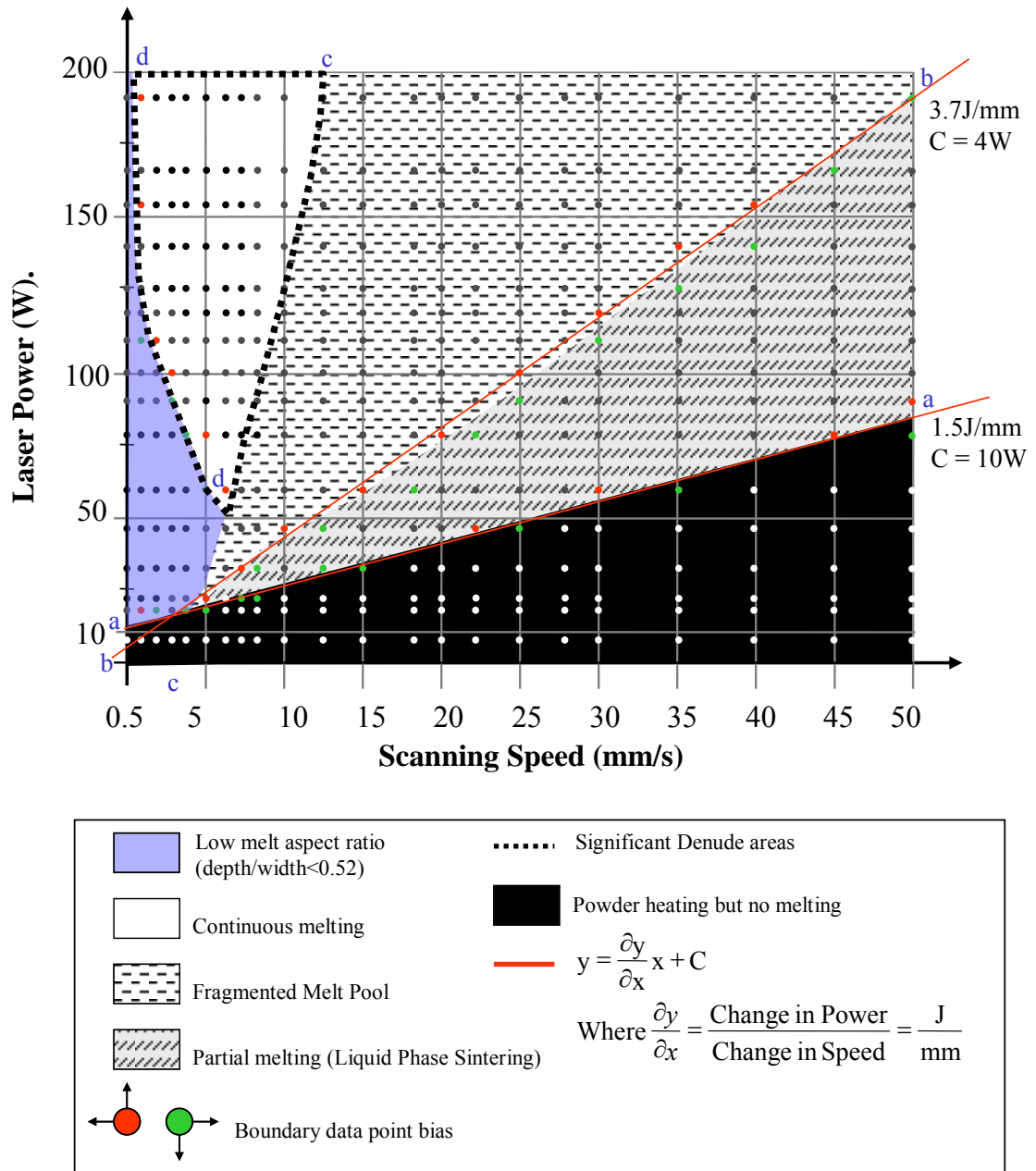


Figure 3.37: Process map for the 300/150 powder batch processed within a argon atmosphere.

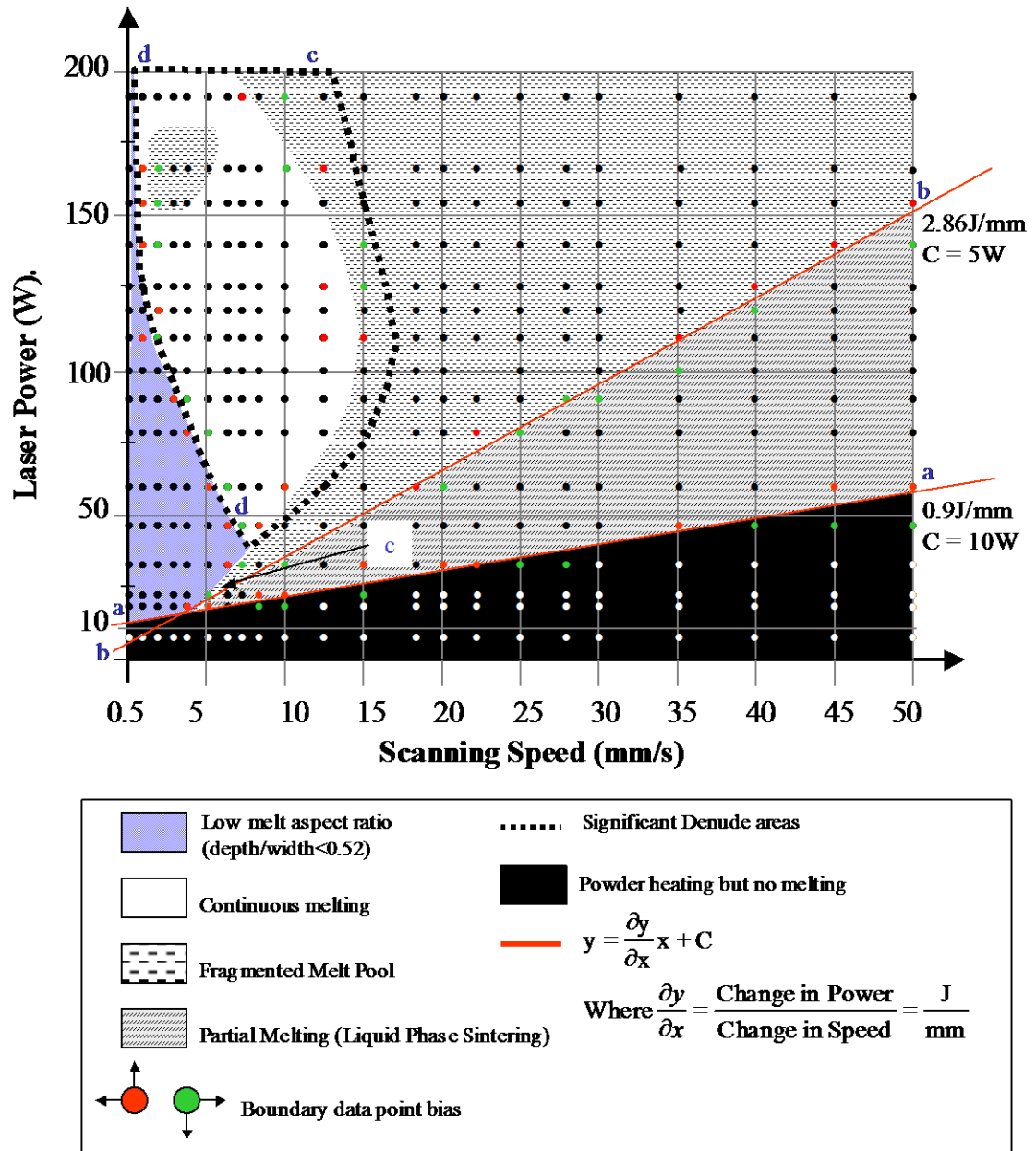


Figure 3.38: Process map for the 150/75 powder batch processed within a argon atmosphere.

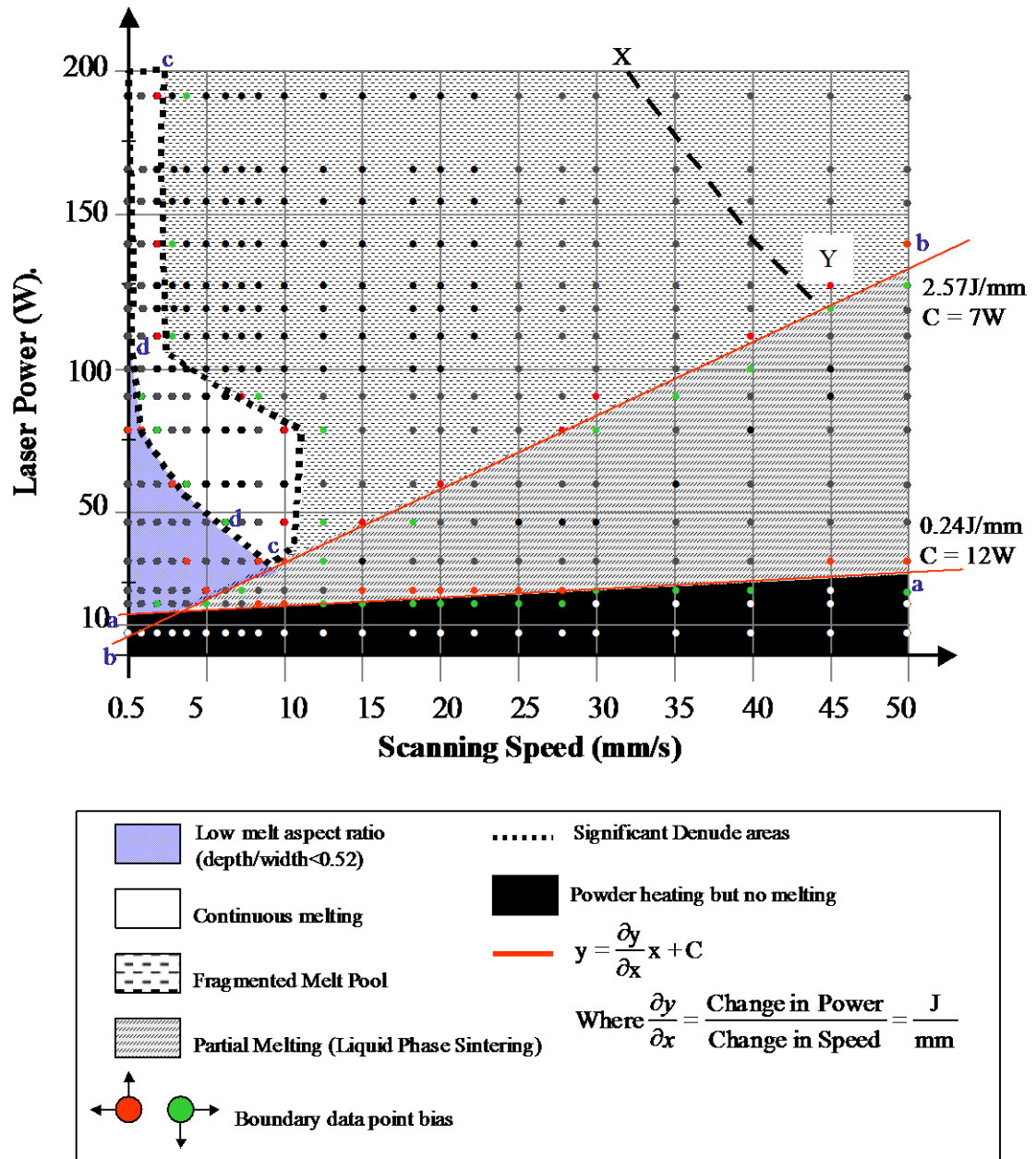


Figure 3.39: Process map for the 75/38 powder batch processed within a argon atmosphere.

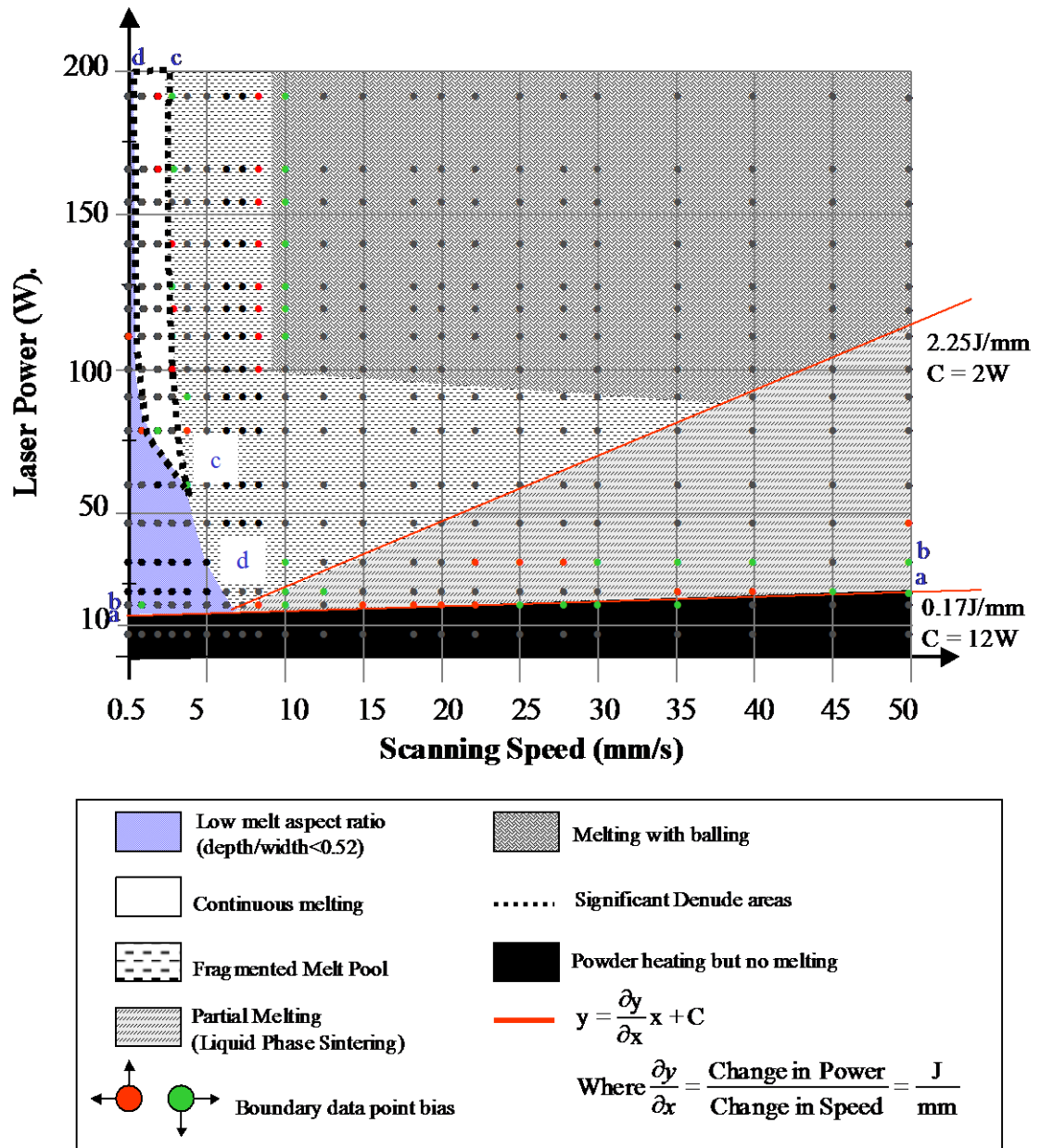


Figure 3.40: Process map for the 75/38 powder batch processed within a argon atmosphere.

3.1.8 Characteristics of the Melt Pool

3.1.8.1 Melt Pool Form

The pictures of melt tracks in Figures 3.33 – 3.36 and the process maps displayed in Figures 3.37 – 3.40 show that melt tracks produced within an argon atmosphere are highly variable in both form and surface quality and that these attributes change considerably with scan speed, laser power and powder batch. When considering the effects of the powder particle size, the 300/150 and 150/75 powder batches were the most closely associated. At laser powers below 50W and scans up to 5mm/s-6mm/s the melt tracks were continuous, highly repeatable, had a uniform width and depth along their entire length and had a low melt aspect ratio (see Section 3.5.3.2). The repeatability of results can be studied by looking at the experimental results tabulated in Appendix D. A theoretical and mathematical approach to the study of the various boundaries between the melting regimes is presented and discussed in Chapter 5. The section centres on visual interpretations of the melt volume while in the continuous state.

Between 50W and 100W the continuous melting regime increased over the scan speed range reaching values of 8mm/s in the 300/150 powder batch and 15mm/s in the 150/75 powder batch. In this region the melt tracks were again continuous, showed good repeatability between experimental results and were uniform in both width and depth. However, there was a distinct boundary emerging throughout this region that, once crossed, the melt tracks changed from being flat with a low melt aspect ratio to cylindrical with a high melt aspect ratio. The positions of this boundary through the continuous melting regime was dependant on both power and speed at low laser powers (<125W) (see Figures 3.37 and 3.38). Above 125W, the low melt aspect ratio region reduced dramatically and was only found to occur at a scan speed of 0.5mm/s. Additional experimental testing (see Section 3.5.1), showed that this low melt aspect ratio also occurred at 0.2mm/s and 0.8mm/s, although the latter was less frequent.

As the scan speed increased above 1.0mm/s the melt aspect ratio was again circular in cross section, remained continuous to the c-c boundary and was found to improve in both uniformity and repeatability as scan speeds increased. Above 140W, and excluding tracks produced at 0.2mm/s and to some extent 0.5mm/s, the solidified

melt pool, though still continuous, became extremely irregular in shape and had extremely poor repeatability. This is clearly shown in Figures 3.33 and 3.34 where the melt tracks at high powers have a far rougher surface quality and fluctuate considerably in width and depth along their length. However, melt tracks produced at 0.2mm/s were much more predictable and maintained a more uniform shape up to higher laser powers (<160W).

Melt tracks produced from the 75/38 and -38 powder batches were generally extremely irregular in shape and therefore the dimension, uniformity and behaviour of the melt pool was extremely difficult to predict. This perhaps explains the more irregular shape of the c-c boundary and the greatly reduced continuous melting regime, all of which are clearly visible on the process maps in Figure 3.39 and 3.40. At laser powers below 50W the majority of solidified melt tracks created within the continuous melting regime had a low melt aspect ratio. These tracks were also highly repeatable and uniform in width and depth along their entire length. The position of the flat track regime boundary followed a similar line to the boundaries on the 300/150 and 150/75 process maps. However, above 50W, the tracks, though predominantly larger in width, were highly irregular in shape and their melt behaviour was extremely unpredictable. Furthermore, melt tracks produced using the -38 powder batch exhibited a key-hole phenomena occurring along their centre line, this was especially noticeable at low scan speeds (0.2mm/s and 0.8m/s) suggesting that the powder is being over melted.

In the majority of cases the solidified melt tracks had a large number of loosely bonded particles attached to their underside. This had a marginal effect on causing fluctuations in melt depth (see Section 3.5.3.2) but had no significant effect over melt irregularity; this was predominantly affected by melt pool behaviour and powder displacement (see Section 3.5.4). There was also no significant increase in the number of particles attached to the melt pool as the laser power increased, although the opposite was true for increases in scan speed, where numbers were found to reduce.

Finally, the melt tracks produced in an argon atmosphere were largely more irregular than tracks produced within an air atmosphere. Furthermore, these irregularities were consistent throughout the length of the track and so there were no isolated regions of irregularity i.e. no melt pool bobble at the start of the scan. There

was also no significant out of plane movements of the melt pool. (plane of reference being the powder surface).

3.1.8.2 Width and Depth Changes

The single tracks described in Section 3.5.1 were removed, where possible, from their powder beds and their dimensions (width, depth and length) were measured and an average value was recorded. The width and depth of each track was measured to assess changes in melt pool shape (aspect ratio) and size as scanning conditions and powder particle size distribution change. The track length was also obtained in conjunction with track mass to enable mass per unit length data to be calculated and evaluated. These latter results are described in Section 3.5.3.3.

The equipment used to obtain the dimensional data is described in Chapter 2, Section 2.3.5 and data accumulated during measurement can be seen in Appendix D. Before each measurement was taken each track was lightly brushed to remove any loose debris i.e. excess powder and loosely bonded particles, to enable accurate measurement of the core re-solidified melt volume.

As outlined previously in Section 3.4.1 and discussed in greater detail in Section 3.4.5, the collapse of powder into the melt causes the melt pool width to grow and become very much greater than the beam width (beam width = 1.1mm). For this reason, melt tracks produced using the 300/150, and 150/75 powder batches reached maximum width values of 4.5mm. This upper value was found to reduce steadily with decreasing scan speed and/or decreasing laser power (see Figures 3.41 and 3.42). At the very lowest values of energy density for each power increment the minimum melt pool width generally ranged between 1.0 and 1.5mm and this was found to remain fairly static at the c-c regime boundary, suggesting an emerging relationship between melt width and melt pool fragmentation (this will be discussed in greater detail in Chapter 5). However, there appears to be obvious correlation between melt width and its value as a trigger for melt aspect ratio changes.

The effects of speed and power on track width for the 75/38 and -38 powder batches are given in Figures 3.43 and 3.44. Again the changes in width with changes in speed and power follow a similar trend to that observed in the other two powder batches, although there are some minor differences. Firstly, the maximum

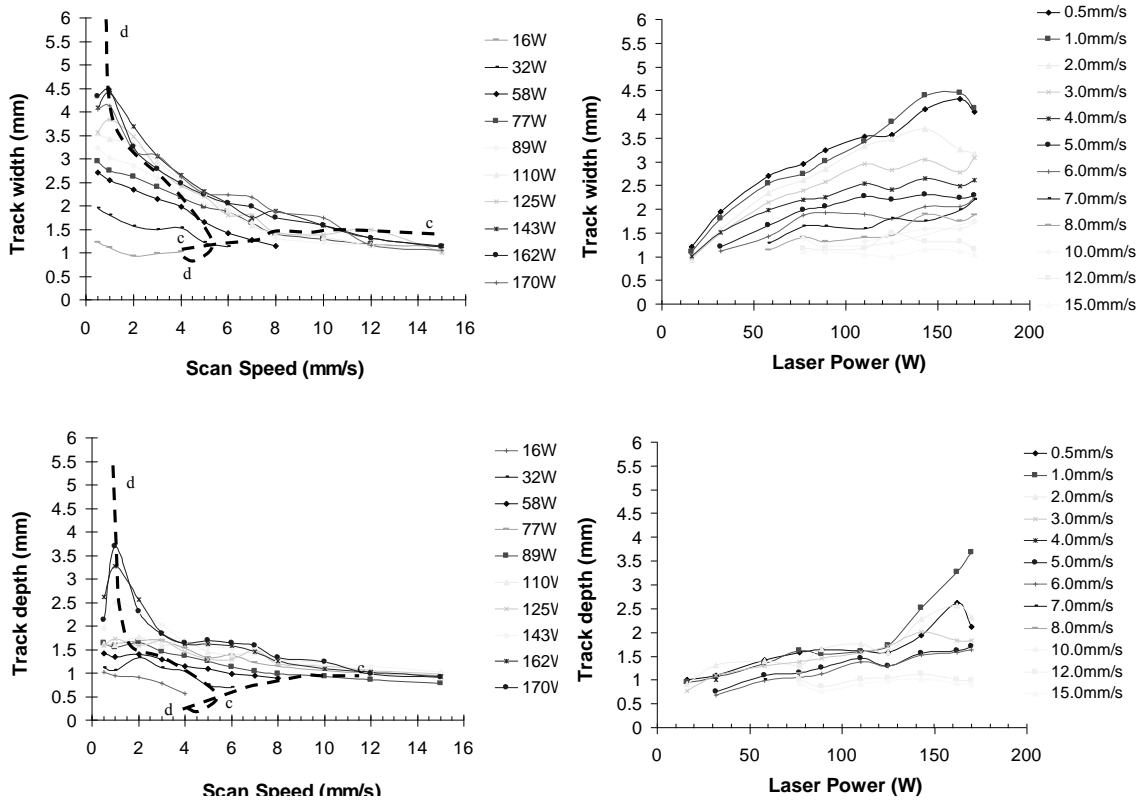


Figure 3.41: Melt pool dimensions as a function of scan speed and laser powder. Results for the 300/150 powder batch are shown.

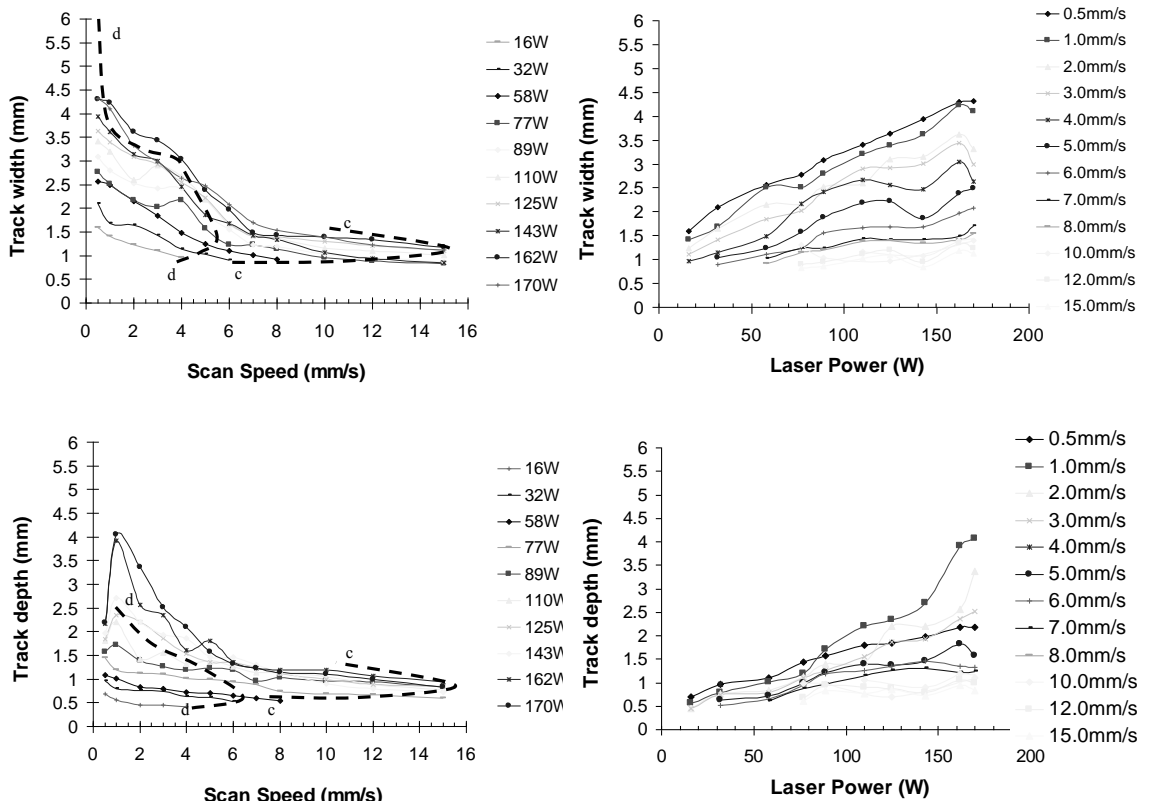


Figure 3.42: Melt pool dimensions as a function of scan speed and laser powder. Results for the 150/75 powder batch are shown.

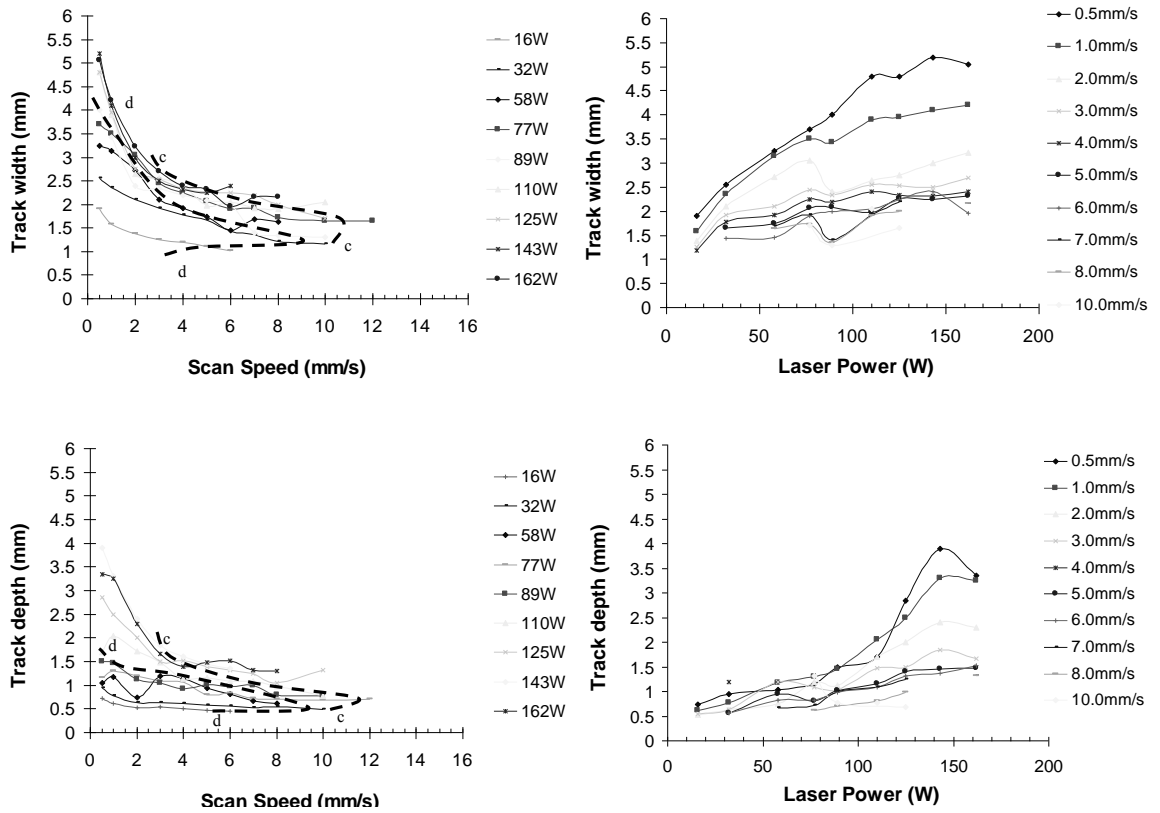


Figure 3.43: Melt pool dimensions as a function of scan speed and laser powder. Results for the 75/38 powder batch are shown.

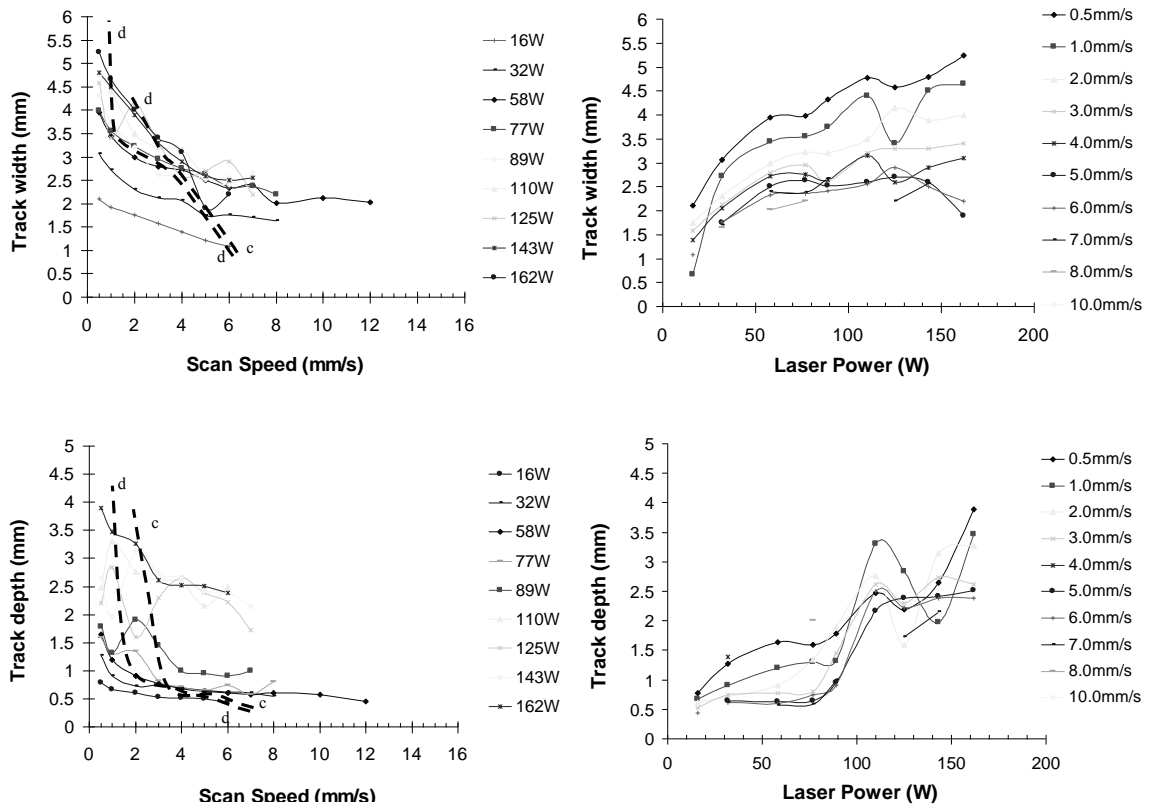


Figure 3.44: Melt pool dimensions as a function of scan speed and laser powder. Results for the -38 powder batch are shown.

melt pool width increased marginally to a range between 5mm – 5.3mm. However, the data obtained from these two powder batches must be treated with some care since the irregularity of the melt tracks made accurate measurement recording more difficult. Secondly, at low values of energy density the minimum melt pool width for each power increment ranged between much higher values (1.0mm and 2.5mm). This caused the change in width to be highly variable at the c-c boundary, suggesting no obvious link between melt fragmentation and width for these two powder batches.

Finally, there were no significant differences in melt pool width across the boundary between flat tracks and cylindrical tracks. Since trenching was more severe around cylindrical tracks, the results suggest that the trenching phenomena has little controlling effect over melt pool width.

The effect of scan speed and laser power on melt pool depth is also shown in Figures 3.41 to 3.44. From the figures it is clear that changes in both power and speed have a different affect on melt depth than they do on melt width. This is certainly evident in the 300/150, 150/75 and 75/38 powder batches. At high scan speeds (>4mm/s) and for laser powers up to 100W the melt depth remains fairly static for each power increment and typically ranges between 0.5mm and 2mm; the range is greatest in the 150/75 powder batch and generally takes a little longer to settle as the power is reduced. As scan speeds reduce below 4mm/s the melt depth begins to rise steadily, reaching maximum values in the range of 3.5mm to 4mm; a phenomena particularly noticeable at higher laser powers (>120W). However, in the 300/150 and 150/75 powder batches there is a sudden reduction in melt depth as the speeds falls below 1mm/s. This decline is also noticeable in the 75/38 powder batch but only at higher laser powers. This sudden change in melt depth ties in with the boundary line d-d on the process maps i.e. the point at which the melt volume changes from a cylindrical to a flat cross section. Hence this change appears to be governed by depth changes and not by changes in width.

Depth changes of solidified melt pools produced using the -38 powder batch show a general depreciating with increasing power or decreasing speed (see Figure 3.44). However, due to the extreme irregularity of the solidified melt track and the greater number of sinter bonded particles to the underside, these changes are difficult to record accurately; this is accentuated by the large fluctuations in the results in Figure 3.44.

The ratio, depth/width, known here as the melt aspect ratio, has been calculated for all melt tracks and the relationship as a function of scan speed has been plotted and given in Figure 3.45. Figure 3.46 shows image manipulation of melt cross sections and Figures 3.47 – 3.50 shows the changes in melt cross section as power and scan speeds change. The width (b) and depth (d) dimensions are marked on the figure adjacent to the relevant cross section together with the values of the scanning parameters.

For the 300/150 and 150/75 powder batches the melt aspect ratio typically falls between 0.4 and 1.0, with average values reaching 0.68 and 0.67 respectively. Generally, the aspect ratio increased with increasing scan speed, although at very high laser powers (>140W) the aspect ratio reached values close to 1.0 in the 1mm/s to

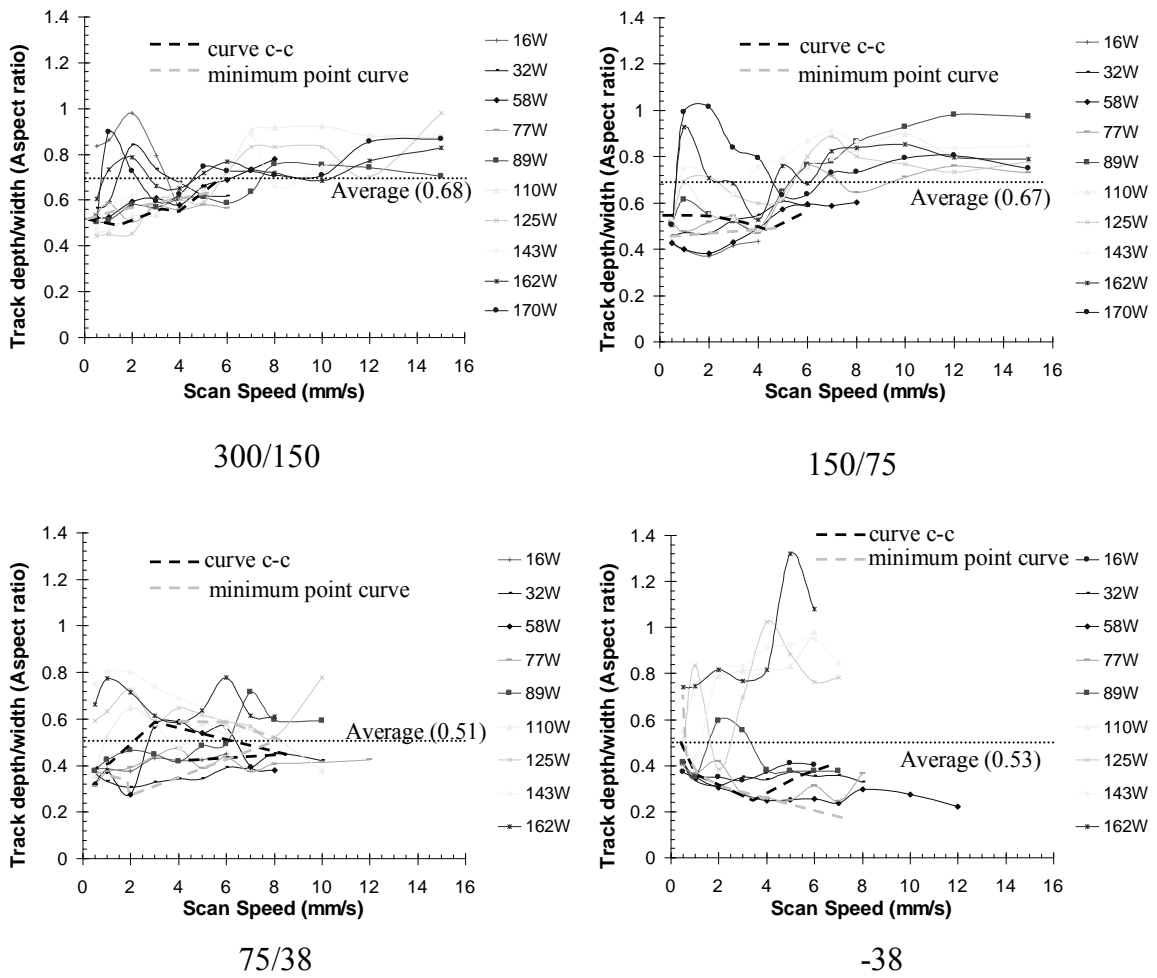


Figure 3.45: Melt pool aspect ratio as a function of scan speed for the 300/150, 150/75, 75/38 and -38 powder batches.

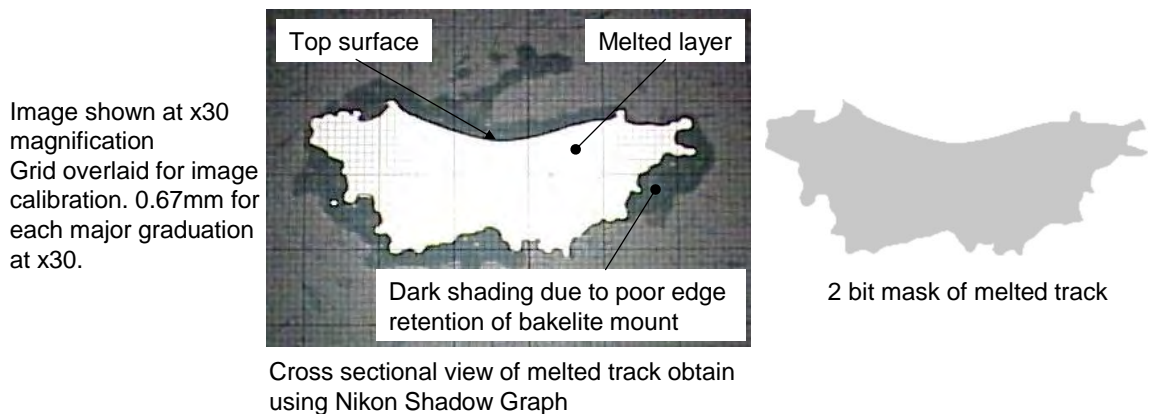


Figure 3.46: Track cross sections: before and after image processing.

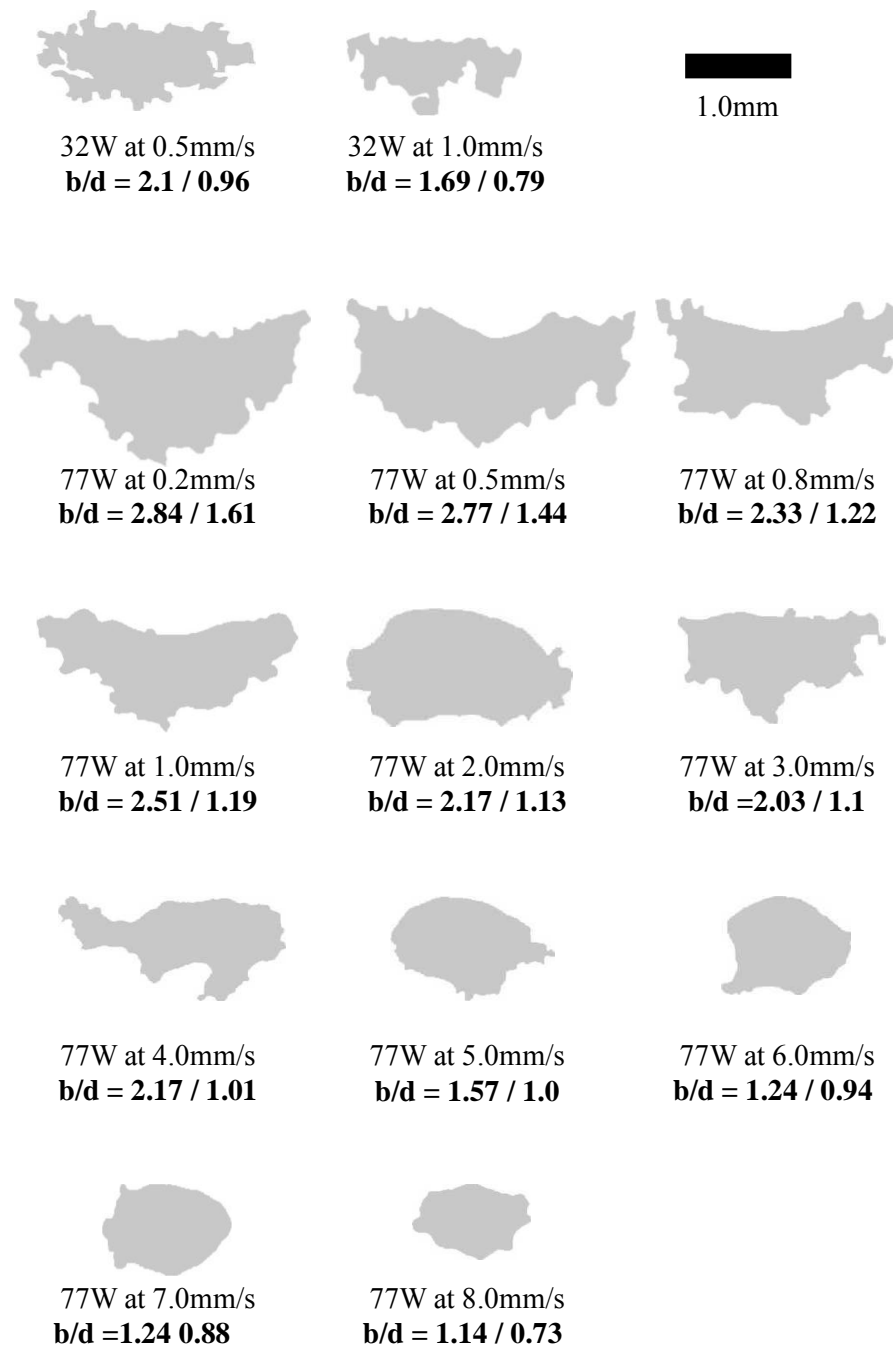


Figure 3.47: Images showing melt track aspect ratio. All tracks were removed from powder beds containing the 150/75 powder size distribution.

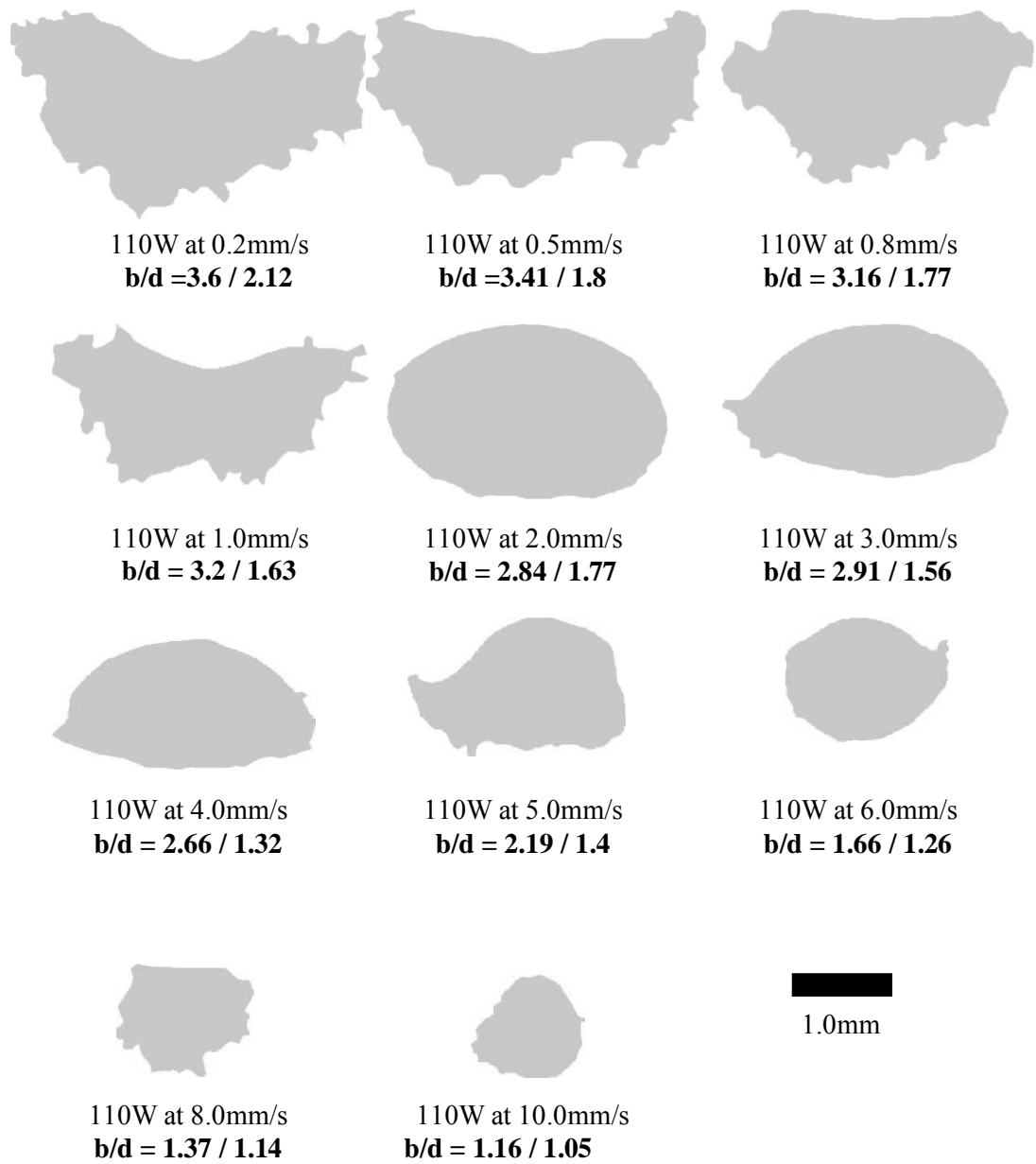


Figure 3.48: Images showing melt track aspect ratio. All tracks were removed from powder beds containing the 150/75 powder size distribution.

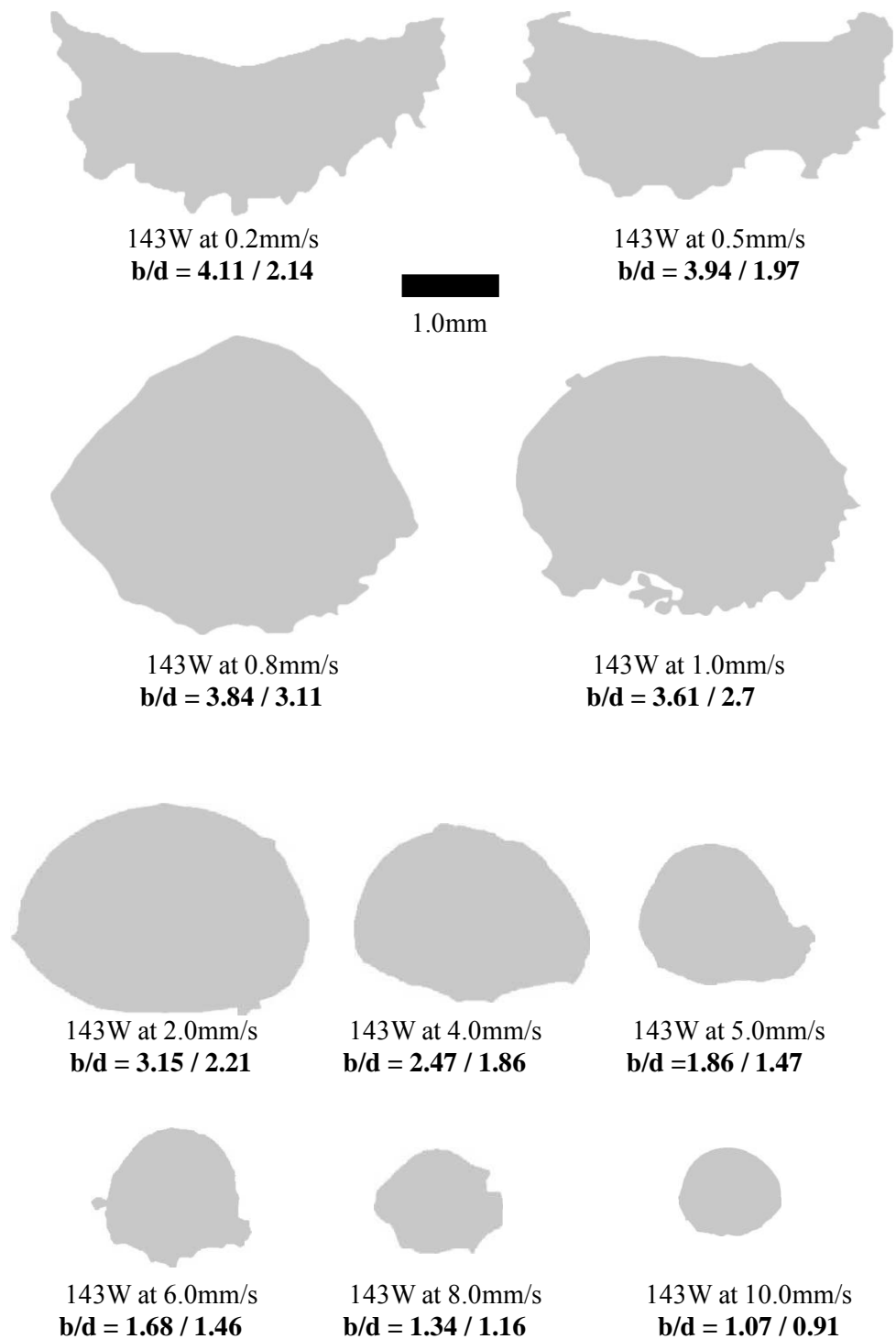


Figure 3.49: Images showing melt track aspect ratio. All tracks were removed from powder beds containing the 150/75 powder size distribution.

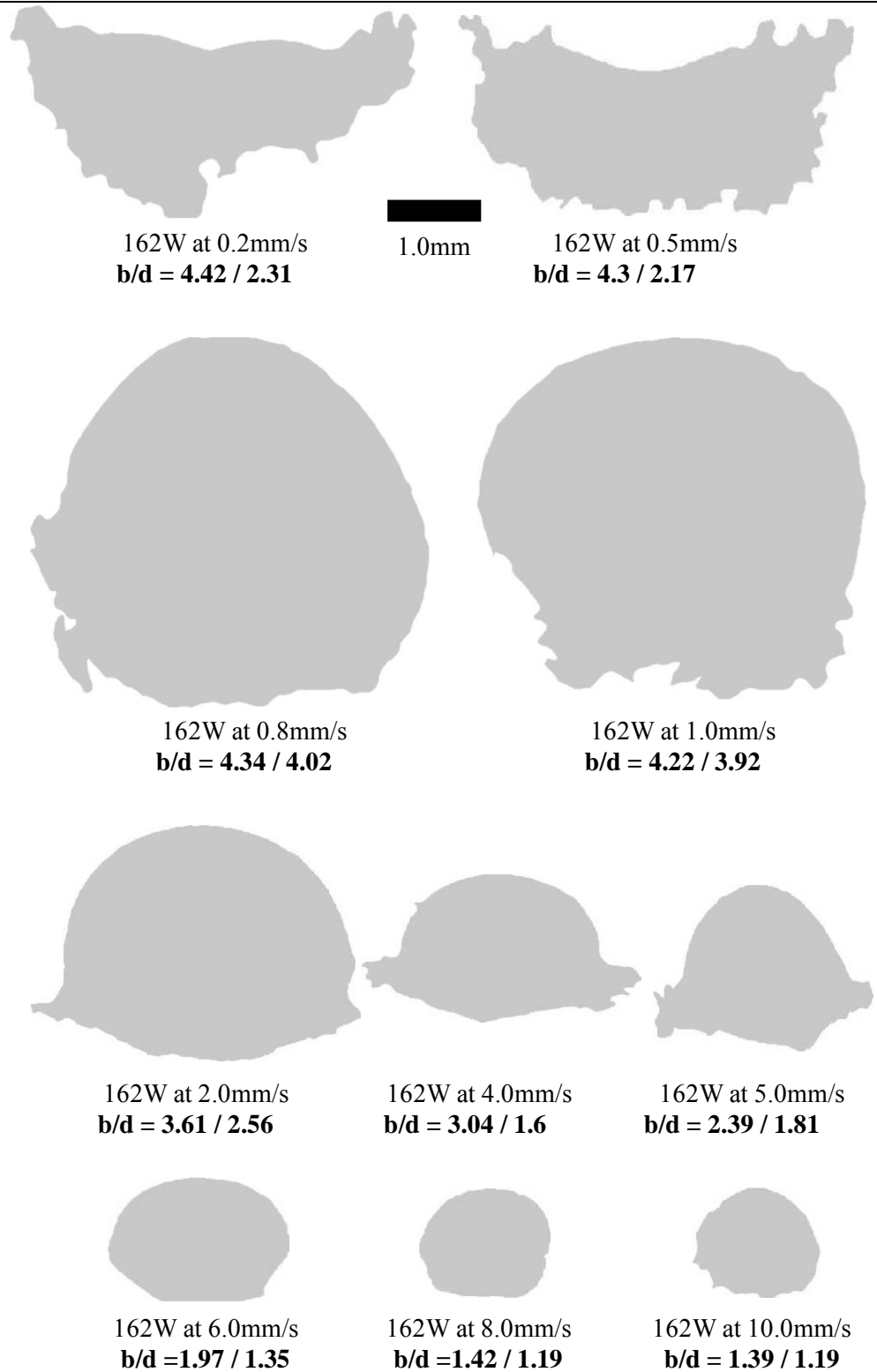


Figure 3.50: Images showing melt track aspect ratio. All tracks were removed from powder beds containing the 150/75 powder size distribution.

4mm/s scan speed range. The effects of changes in laser power on melt aspect ratio is less clear. The results clearly show an overall size increase in the melt volume as the power increases, but the change in melt aspect ratio appears fairly static for each scan speed increment.

For the 75/38 powder batch the change in melt aspect ratio typically falls between 0.3 and 0.8, with an average value of 0.51. However, there are a large number of fluctuations in the results, making it extremely difficult to gauge the relationships between changes in melt aspect ratio and changes in power and speed.

For the -38 powder batch the average value of melt aspect ratio was calculated to be 0.53. However, two distinct groups of results were emerging. For values of laser power up to and including 89W, the melt aspect ratio was found to steadily reduce with increasing scan speed with all values falling below the average value line. For laser powers above and including 110W, the melt aspect ratio was found to increase with increasing laser power with all values falling above the average value line.

Also shown on Figure 3.45 are two curves; (1) a curve representing the path taken of the c-c melt fragmentation boundary and (2) a curve which passes through the minimum points of all the d/b versus scan speed curves. In the figure it can be seen that both curves follow each other reasonably closely, are both reasonably horizontal in the 300/150 and 150/75 powder batches, showing that the melt aspect ratio lies within a small range (0.5 - 0.7 for the 300/150 and 0.5 - 0.6 for the 150/75 powder batch) when the transition boundary between continuous melting and melting with fragmentation is reached. If an average of all results is calculated (see Figure 3.17), then the melt aspect ratio is seen to reduce with reducing powder particle size.

When comparing the shape of the melt aspect ratio in Figures 3.47 - 3.50, one can clearly see a third melt cross section shape emerging. The shape can best be described as bell shaped, a shape with a smooth and almost circular form except for two regions in the low left and right edges which protrude out in a horizontal manner away from the melt. microscopy studies in Section 3.5.5 reveal that these regions contain a great number of prior particle contacts, furthermore, these particles are clearly seen within the melt volume. It is interesting to note at this point, that melt tracks of this shape are often associated with very rough and irregular melt tracks. Suggesting perhaps that these

entrapped particles, through powder displacements, are increasing the viscosity of the melt and therefore not allowing the melt to assume a more regular form. This observation has also been observed in the other three powder batches. This argument is further strengthened when considered the -38 powder batch, whose cross sectional microstructures reveal a greater number of prior particle contacts (see Section 3.5.5).

Figure 3.51, again shows the changes in melt aspect ratio observed in the 150/75 powder batch. However, the images have now been superimposed onto the 150/75 process map. The figure clearly shows the increase in melt depth, and therefore overall melt volume, as scan speeds increase and cross the d-d boundary. The experimental results suggests that the absorptivity of the laser is changing at this point. A discussion and theoretical analysis of behaviours at this boundary is discussed in detail in Chapter 5. Finally, it is also interesting to note that within the power range 100W to 143W and scan speed range 2mm/s to 4mm/s i.e. cylindrical track regime, the aspect ratio of the melt reduces marginally, causing the melt to change from near circular to oval. At higher scan speeds the melt reverts back to a more circular aspect ratio. This perhaps suggests that fluid flow phenomena is indeed acting within the melt volume and causing these changes. However, such phenomena is usually associated with changes in soluble oxygen. It is difficult to visualise where such changes might be occurring (see Chapter 1, Section 1.4).

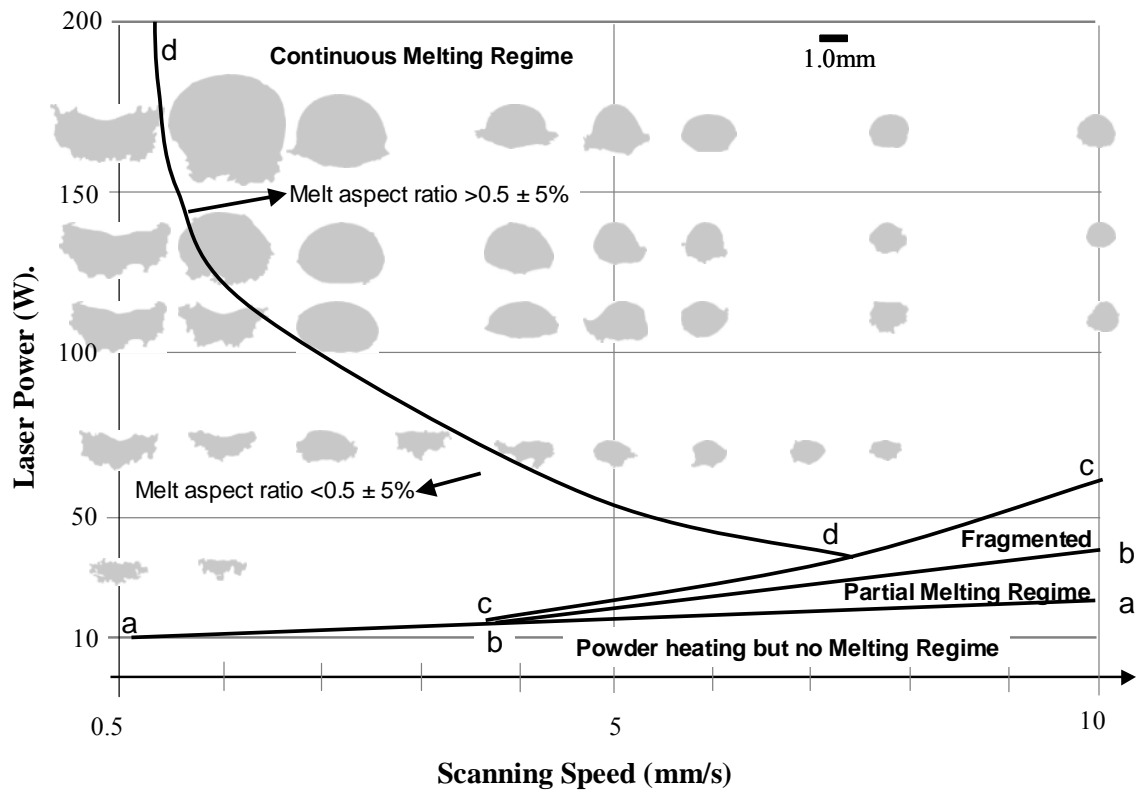


Figure 3.51: Images showing melt track aspect ratio superimposed onto the 150/75 process map.

3.1.8.3 Mass Changes

As well as measuring melt pool dimensions, tracks removed from the powder beds were also weighed and plots of track mass per unit length (grams/mm) as a function of laser energy density (J/mm) were created. These plots can be seen in Figure 3.52. Most of the results again fall within one region bounded by two straight line slopes labelled High Speed (HS = >4mm/s) and Low Speed (LS = 0.5mm/s). Data points that lie outside of these zone are generally associated with very high laser powers. These graphs will be discussed further in Chapter 5.

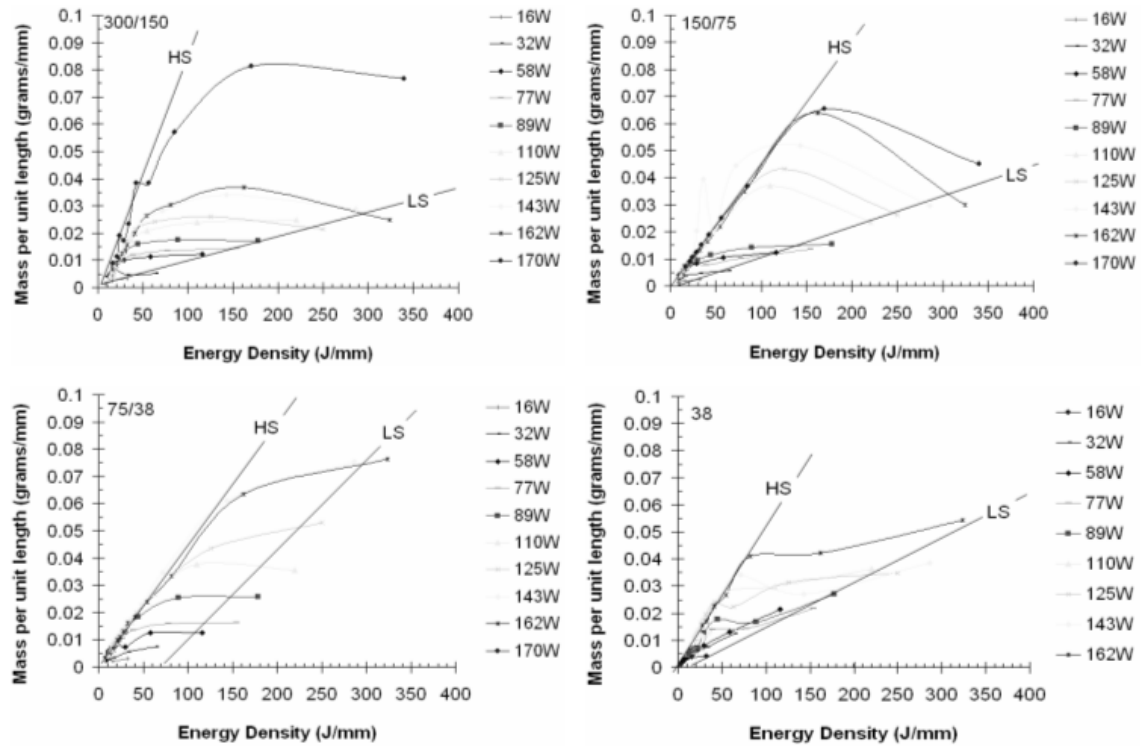


Figure 3.52: Melt pool mass per unit length plotted as a function of laser energy density. LS represents the Low Speed slope (0.5mm/s) and HS represents the High speed slope (>4mm/s).

3.1.9 Powder Trenching and Melt Pool Irregularities

Very few isolated melt pool irregularities were found to occur in melt pools created within an argon atmosphere. Those that do, have already been discussed in Sections 3.5.3.1 and 3.5.3.2. Conversely, melt pool trenching is again wide spread during argon processing and occurs predominantly around melt pools with a circular cross section. The reasons for this are given in Section 3.4.4. As well as creating a denude area around the periphery of the melt volume, it has also been observed that powder entrapment caused by displaced powder from the trench walls is likely to be increasing melt viscosity and could perhaps be linked to a more irregular melt volume thought reduced surface tension trigger fluid flows.

3.1.10 Microscopy Studies

The single tracks described in Section 3.4.1 were removed, where possible, from their powder beds and sectioned in a direction normal to the direction of scan. The samples were then prepared for inspection by mounting, polishing and etching as outlined in the procedures given in Chapter 2, Section 2.5.6.

In Section 3.4.5, it was discussed that the microstructure of melt tracks produced within an air atmosphere are both dendritic at locations farthest from the laser heat source and columnar in regions closest to the laser heat source. Hence a boundary is clearly visible running from left to right through melt track cross sections. This observation is also apparent in melt pools created with an argon atmosphere. Especially when the melt pools are cylindrical in shape. Therefore, the discussion given in Section 3.4.5 is also relevant here.

When the melt has a low aspect ratio, the melt volume is predominantly fully dendritic (see Figure 3.53). Grain coarsening also occurs but this is only within a finite layer in the upper region of the melt volume i.e. at a point closest to the beam, suggesting a vast number of nucleation sites within the melt. However, melt pools with a low aspect ratio are often created at very high values of incident energy density i.e. very low scan speeds. It would therefore stand to reason that the microstructure could be expected as being fully columnar, due to the high heat input. Because this is clearly not the case, these results strengthen the discussion in 3.5.3.2 that a drop in absorbed

energy density maybe occurring across the boundary between flat and cylindrical tracks. Reasons for this change are still not clear. However, a number of theories have been generated and are discussed in Chapter 5.

The microstructure of „bell“ shape tracks (see Section 3.5.3.2) have also been examined and an overview of the observations are given in Figure 3.54. In figure 3.54, it is clear that the microstructure exists as a combination of the microstructures observed in both cylindrical and flat melt pools. The core melt volume is both equiaxed dendritic and cellular and the boundary between them, which runs from left to right, moves up through the melt as the absorbed energy density increases. Within the catchment area in the lower corners of the melt volume there is clearly a number of prior particle contacts. The original particle shape is easily distinguishable and there is clearly no evidence of full particle melting within these regions, though there is some evidence of a melt phase forming between the particles. The presence of these particle catchment regions causes the liquidus boundary to be much higher up the melt, proving that a greater number of nucleation sizes are occurring in the lower region of the melt volume. Hence, one again strengthen the theory that bell shape melt pools have an increased melt viscosity.

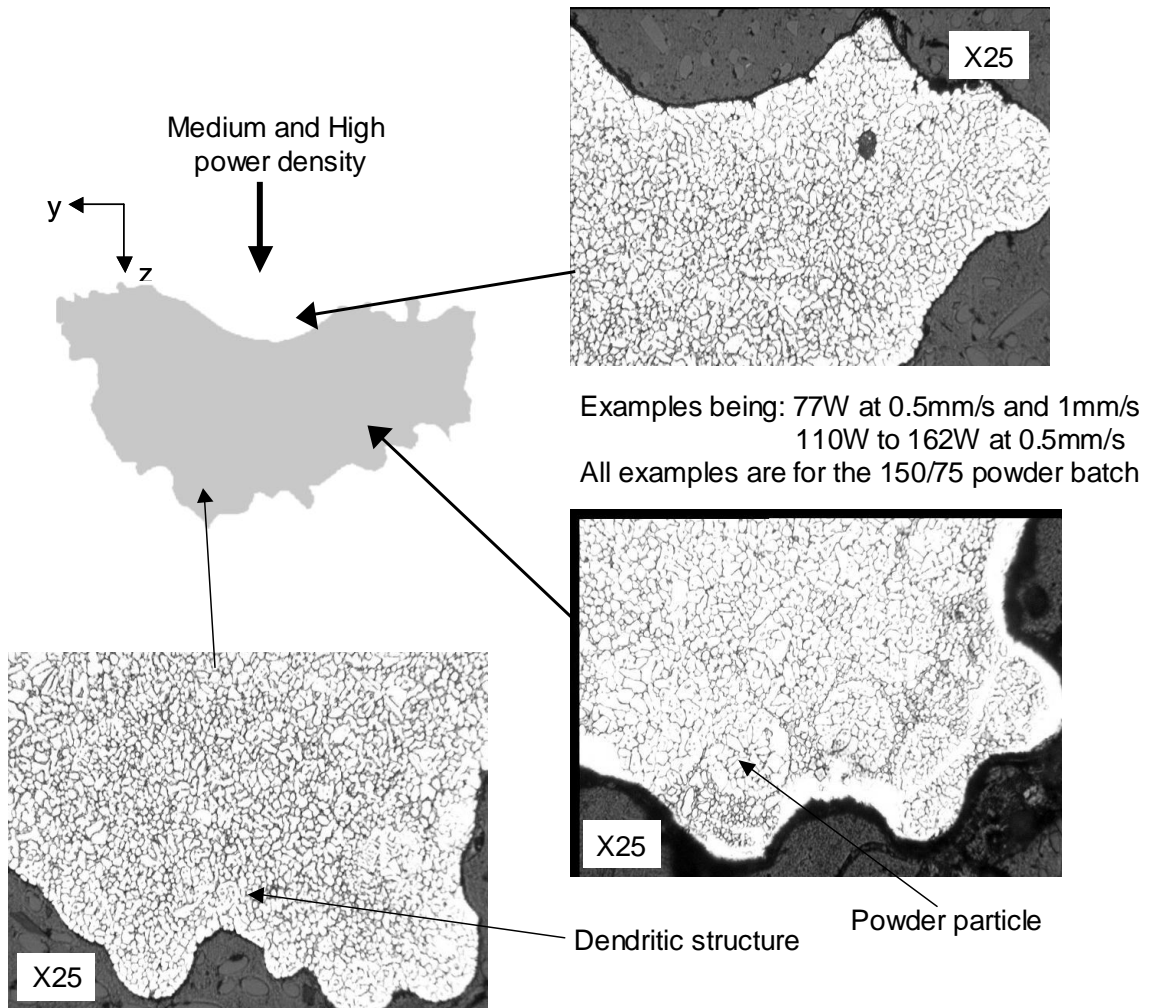


Figure 3.53: Typical examples of microstructure found in melt pools that exhibit a low melt aspect ratio.

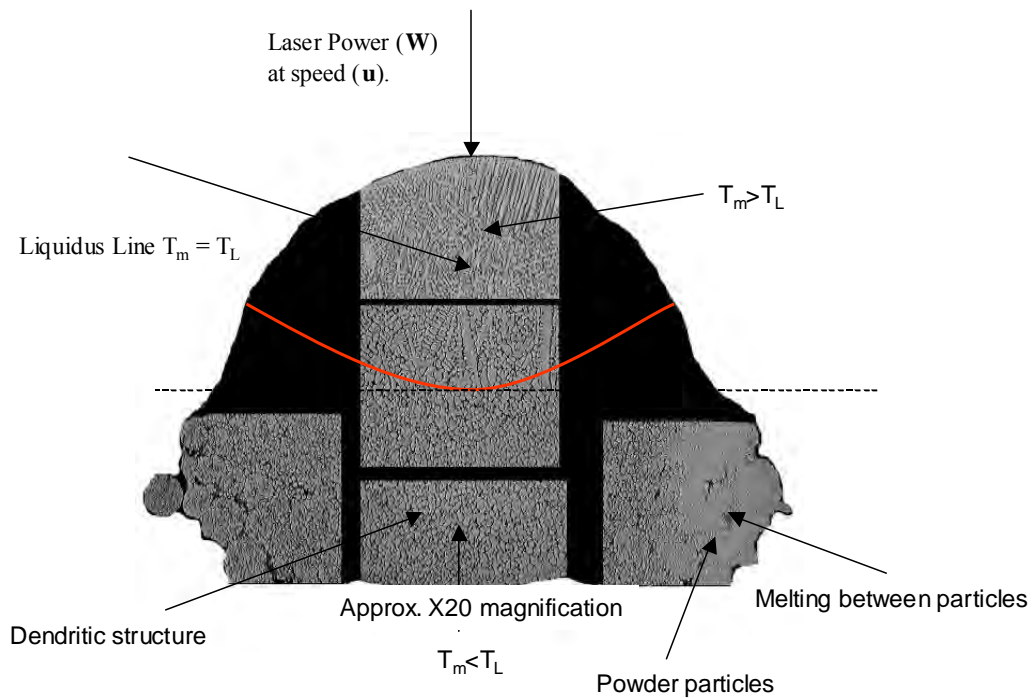


Figure 3.54: An overview of typical microstructures found in melt pools that exhibit a „bell“ shaped cross section i.e. 110W to 143W at 4mm/s to 5mm/s in the 150/75 powder batch.

Selective Laser Sintering of Single Tracks Scanned in an Argon Percolated Atmosphere

Percolating argon gas through the powder bed as outlined in Chapter 2, Section 2.5.2 resulted in virtually no differences in melt pool behaviour, dimensional and mass changes and solidification microstructure. There was some evidence of reduced melt pool irregularities at higher laser powers, and some improvements in the repeatability of melt pools created as scan speeds of 0.8mm/s. However, these differences are only small and therefore the results do not warrant a more detailed explanation in this thesis.

CHAPTER FOUR

SINGLE AND MULTIPLE LAYER CONSTRUCTION

4.1 Introduction

This chapter discusses the observational results from the experimental work on single and multiple layer construction. Preliminary studies highlighted that understanding the interactions between the laser and the powder bed, the behaviour of the melt pool and its dimensional variations as laser power and scan speed change allows for process refinement, leading to improvements in the quality of melted layers and multiple layers. Therefore, much of the work presented in this chapter is an extension of the work in Chapter 3, examining the similarities and distinctions between rastered and unrastered melt pools. The focus then shifted onto methods to improve layer surface quality and density. Layer dimensional accuracy was not investigated in this work.

The powder selected for this investigation was the 150/75 powder batch. This was the powder batch of choice due to its heightened performance during single track scanning: including increased surface quality, form and reduced irregularity over a wide range of scanning conditions. Experiments were performed on a loose powder bed of arbitrary depth, 7mm. The scanning conditions used in the experimental works have, in part, been reported previously in Chapter 2, Section 2.5.1. However, the laser power and scan speed range was not confirmed until all single track experiments were complete. This decision allowed for a balanced account of the melting behaviour of single layers, allowing direct comparisons to be made between tracks, layers and multiple layers. The chosen experimental values are given throughout this chapter.

The operation of the two spreading mechanisms detailed in Chapter 2, Section 2.3.1.3 will also be discussed in this chapter. Their functionality will be assessed and their strong influence governing the choice of layer thickness and overall build strategy

will be reported. The design, testing and manufacture of each mechanism was the focus of a parallel research project.

A number of experimental tests were also conducted to assess the importance of scan strategy, in particular scan length, in controlling layer warping and solidification cracking. These results will be discussed along with the implications of irradiating room temperature (cold) powder layers.

4.2 Single Layer Build Strategy

4.2.1 Layer Distortions and Methods of Reduction

The distortion and warping of layers and the occurrence of solidification tearing between neighbouring tracks increases dramatically with increasing scan length (see Figure 4.1). Apart from affecting the integrity of the layer, the distortions also hinder the free movement of the powder spreading and deposition mechanism, causing the layer to move during deposition (see Section 4.5).

The distortions are a consequence of the local thermal history as the layer is built (Carter et al., 1993). The cyclic heating, caused by the rastering melt front, creates a temperature gradient across neighbouring tracks. Consequently, the neighbouring tracks cool at different rates causing differential solidification and shrinkage. The differential shrinkage causes residual stresses which are relieved by shape change in the form of distortions and tearing. Hence, as the scan spacing reduces, residual stresses increase causing an increase in layer distortions; this is in agreement with the experimental observations.

Carter et al., (1993) also suggested that the temperature gradient between the upper and lower surfaces of individual melt tracks were also responsible for layer distortions. However, this is likely to also lead to distortions in single tracks, but this was not observed in the experimental works described in Chapter 3.

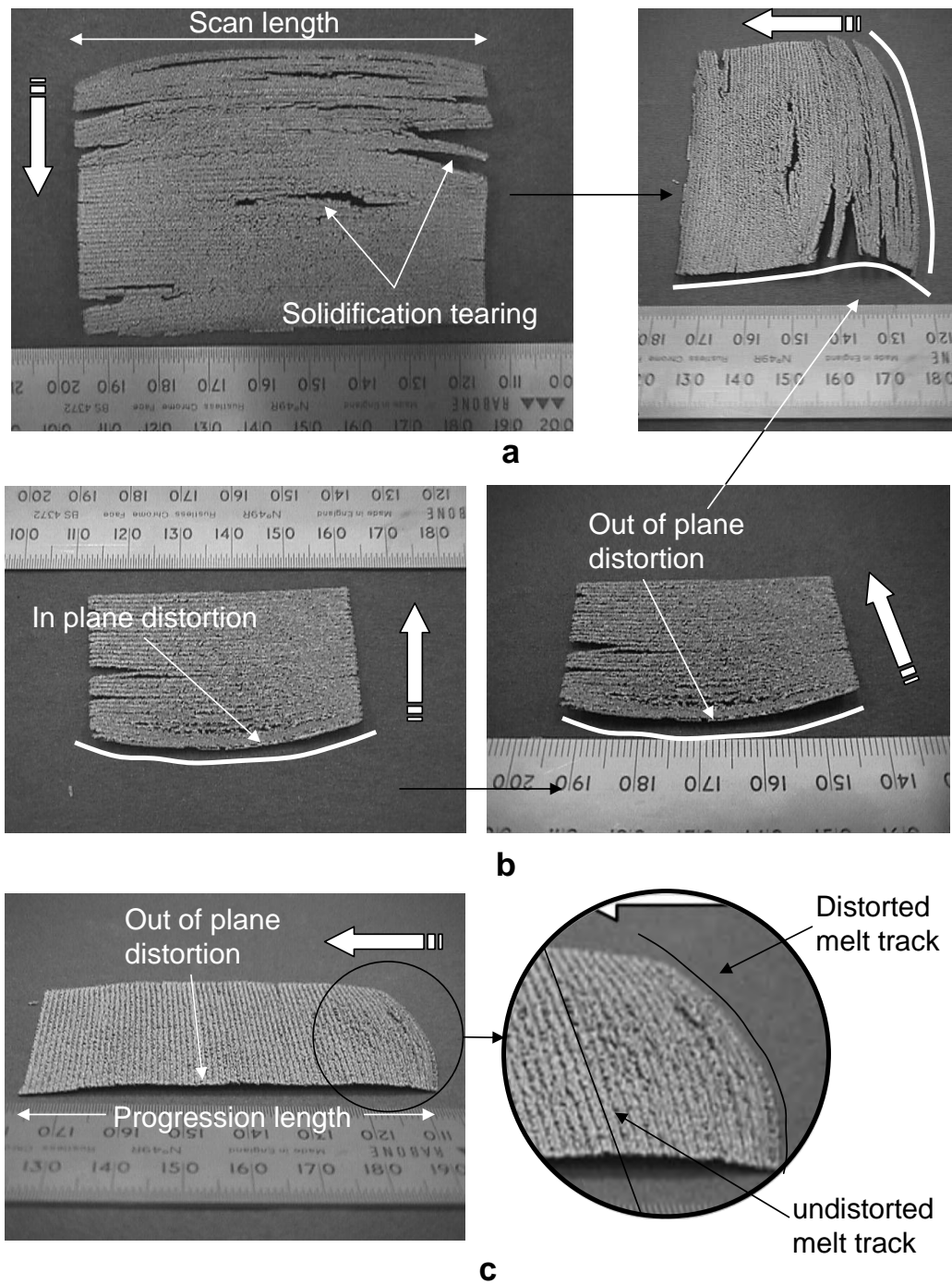


Figure 4.1: Layer distortions and solidification tearing in (a) a layer with a scan length of 80mm, (b) a layer with a scan length of 50mm and (c) a layer with a longer progression length of 60mm. All layers were produced with a scan spacing ratio, s_b , of 0.5, a laser power of 77W and a scan speed of 5mm/s. The atmosphere was argon.

The movement of the rastering melt front across the powder surface causes two types of distortion, in-plane distortions and out-of-plane distortions (see Figure 4.1a/b). The in-plane distortions occur within the plane of the powder bed, causing the tracks to bend in a direction opposing the direction of the rastering melt front. They occur in the first 10 – 20 scanned tracks only (the number increased with increasing scan length) and the magnitude of the distortion in the preceding tracks gradually increased as more tracks were created. Solidification tearing was also very severe at this stage of the developing layer (see Figure 4.1a). The majority of the tearing occurred around the edges of the layer, where temperature gradients between neighbouring tracks are lower, suggesting that tearing was perhaps a consequence of layer distortions and not a direct consequence of temperature differences.

After the first 10 to 20 tracks, the in-plane distortions diminished (see Figure 4.1 c). However, they were followed by out-of-plane distortions which became very severe at longer scan lengths (>70mm), causing the layer to bulge up from the powder surface by several mm. Their severity often caused the in-plane distorted tracks at the beginning of the layer to lift away from the powder surface. Shortening the scan length to ~40mm prevented all out-of-plane distortions when the scan spacing (in mm) was 75% of the beam diameter. This reduced to ~20mm when the scan spacing was 25%. On the other hand, the in-plane distortions diminished at scan lengths shorter than ~30mm, a value which had less dependence on scan spacing.

The effect of the progression length (or layer length) on layer distortion was also investigated (see Figure 4.2). It was found that an increasing layer length had only a marginal effect on increasing the magnitude of the out-of-plane distortion. The magnitude of the in-plane distortions was not affected and did not re-occur further down the layer, suggesting that the magnitude of all distortions peaked in the early stages of layer growth. Solidification tearing was however found to occur repeatedly throughout the progression length of a long layer, even when the scan length was short, and particularly when the scan spacing was 75% of the beam diameter.

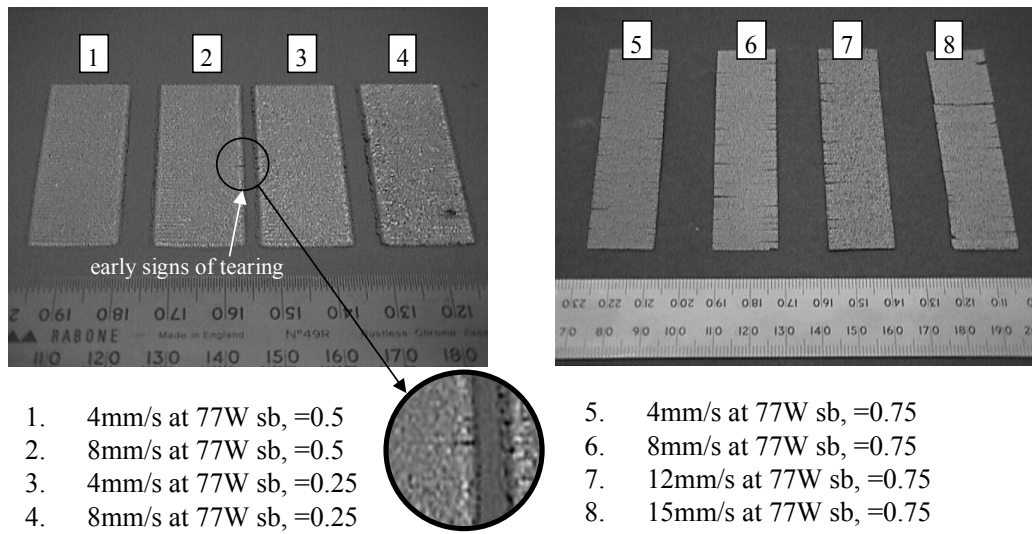


Figure 4.2: Layers produced with a short scan length and a long progression length.

Deeper layers, caused by increased energy density, were also found to resist layer distortions due to their increased efficiency to resist bending; though tearing was still noticeable at a larger scan spacing. The effect was difficult to illustrate using layers produced within the argon atmosphere because the melt track dimensions were less responsive to changes in energy density (this will be discussed in greater detail in Section 4.4). However, melt tracks produced within the air atmosphere were often much larger, particularly in depth (see Figure 4.3). The outcome was the occurrence of in-plane distortions only, again in the first part of layer growth, and receding in the first 5-10 scanned tracks. In this region solidification tearing still persisted. However, shortening the scan length to $\sim 45\text{mm}$ stopped all distortions, a value again having less dependence on scan spacing.

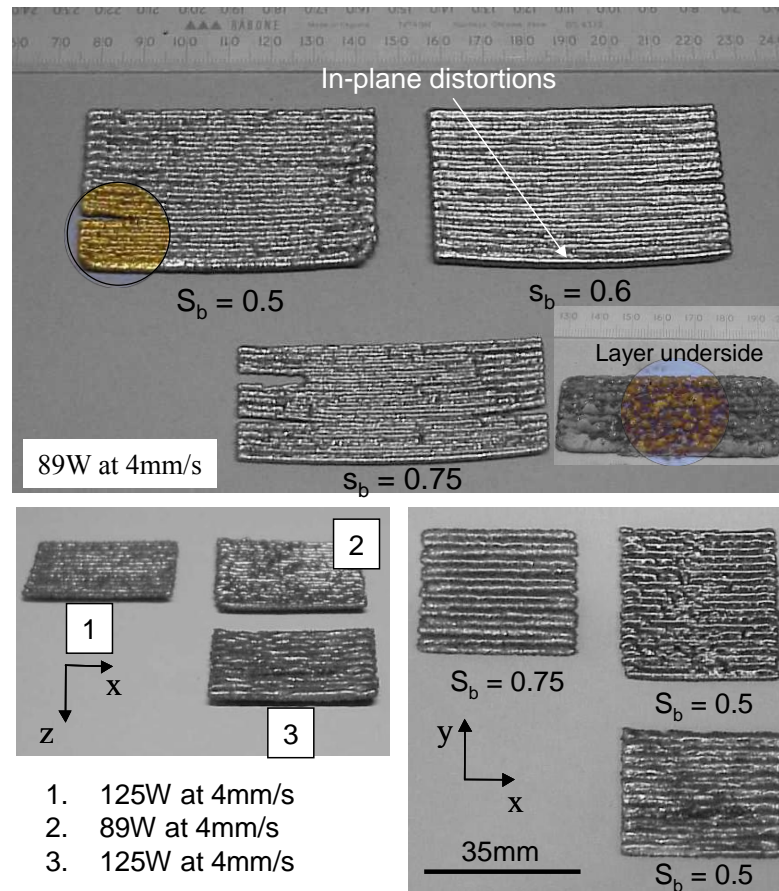
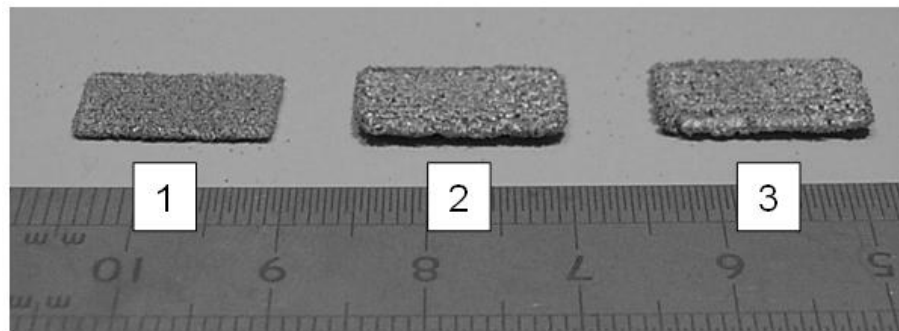


Figure 4.3: Distortions in layers created within an air atmosphere.

There are several established methods available to reduce layer distortions including pre-heating the powder to reduce thermal gradients, bonding the layer to an underlying substrate to physically anchor the layer and careful planning of scanning conditions i.e. high energy densities. Observations from results presented here also show that limiting the scan length, and to some extent the progression length, also alleviates thermal distortions and solidification tearing. It is this latter solution that has been adopted in this work. This approach, however, limits the size of the layers that can be produced; further investigations revealed a distortion free layer only occurs if its dimensions are no greater than 15mm x 15mm. An example is given in Figure 4.4. Nevertheless, this method does permit layers to be produced, undistorted, for all

scanning conditions covered in this work; an unlikely outcome if scan condition planning was chosen as a method to alleviate distortions.

From another practical view point, pre-heat temperatures required to reduce thermal gradients for metal powder processing need to approach half the melting temperature of the material to have any significant affect (Benda, 1994). Such a high temperature would be very difficult to achieve and would require specialist equipment to generate and retain the heat safely. Also, bonding layers to an underlying substrate was found unreliable because the laser energy density was insufficient to promote a sufficient fusion bond between the melt and the underlying solid substrate. This is discussed in detail in Section 4.5.



Scan spacing ratio, s_b , =0.25

1. 4mm/s at 58W
2. 4mm/s at 110W
3. 4mm/s at 143W

Figure 4.4: Layers with a short scan length, created within a argon atmosphere.

4.3 Single Layer Air Atmosphere Results

Constructing good quality layers within an air atmosphere proved almost impossible due to frequent balling and/or over melting causing deep globular layers. Figures 4.5 - 4.7 show three maps, each displaying the 150/75 single track process map for air which has been updated to include information on single layer melting behaviour for a scan spacing of 25%, 50% and 75% of the beam diameter respectively (or scan spacing ratio, s_b , of 0.25, 0.5 and 0.75). The nodal array displayed on each map shows the number and frequency of the experimental conditions. Included on the maps are a number of superimposed regions, defined by thick boundary lines, which indicate the power and speed combinations over which several different heating and melting behaviours were observed. In the Figures, the qualitative regions are supported visually by several single layer images. Furthermore, a selected number of these images also display a cross sectional image of the melted layer taken in a direction perpendicular to the direction of the rastering melt front. Five regions (or behaviours) were recognised:

1. Temper Colorations without bonding;
2. Temper colorations with bonding;
3. Significant melting with balling;
4. Uncontrolled melting; and
5. Continuous melting.

When comparing the single track boundary lines with the superimposed single layer boundary lines, there are clearly some significant differences. Firstly, due to repeat heating during the raster scanning procedure, layers produced at conditions which fall in the temper colorations but no melting regime of single tracks were found to be loosely bonded, particularly when irradiating the powder at power and speed combinations which fall in region 2 on the process maps. This, depending on the type of consolidation taking place (see following text), might suggest that little cooling takes place between consecutive passes of the laser spot, allowing individual particles to reach higher temperatures. However, it might also suggest that the individual particles are simply maintaining elevated temperatures for longer periods of time. These two possible temperature-time history changes allow for one of two different consolidation routes

(German, 1998). The first route might be by solid state sintering, triggered by the increased period at elevated temperature, causing necks to form between particles by atom migration; a route which is thought not to occur during single track production. The second route might be by liquid phase sintering where the potentially higher temperatures are triggering some „early“ liquid action, where early is defined here as first significant melting at energy densities lower than those recorded during single track production. Neither route was examined in detail because it was deemed unnecessary for the purposes of this work. However, it is important to note that the bond strength between the neighbouring particles was only just sufficient to facilitate careful layer removal from the powder bed.

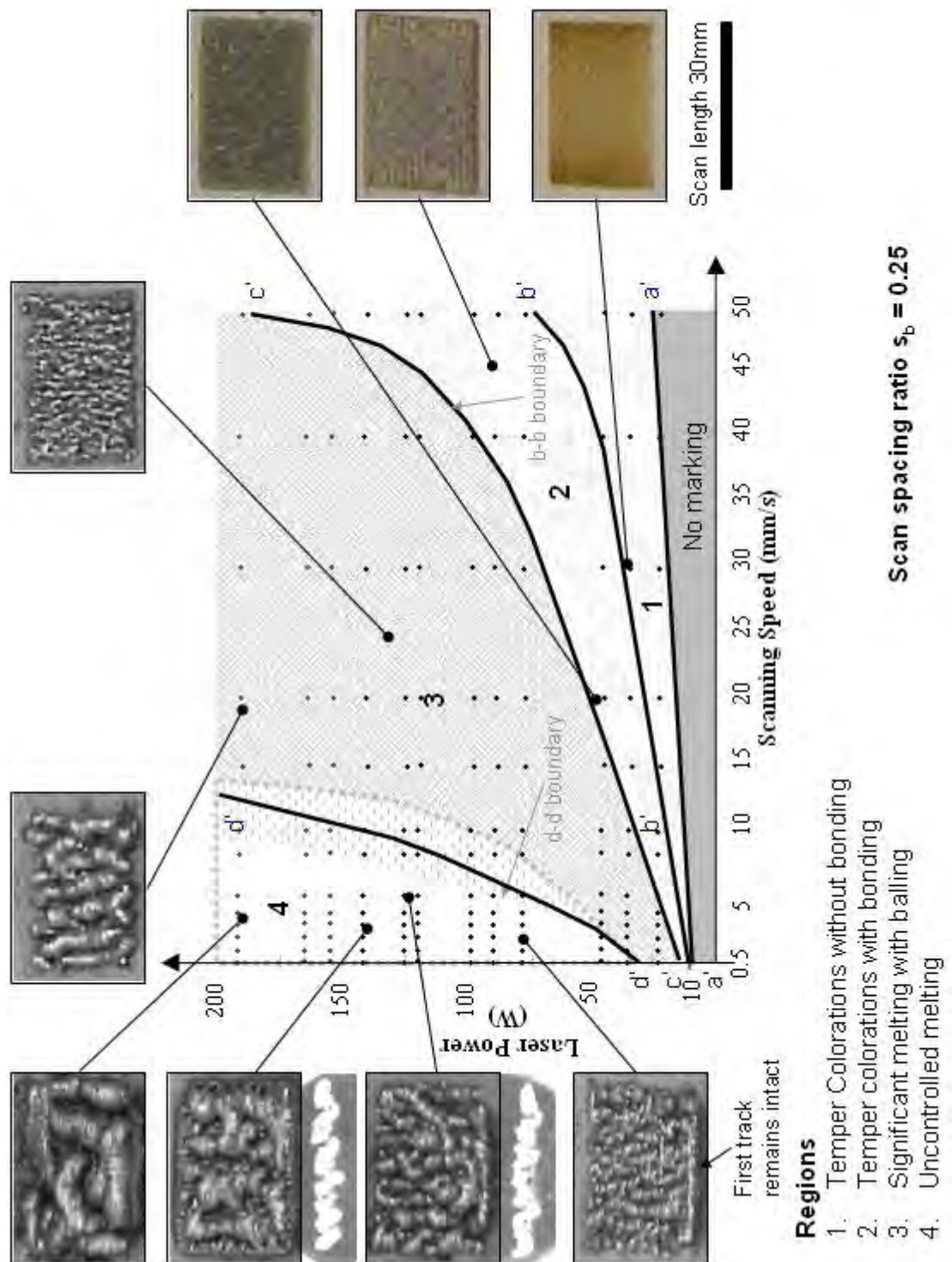


Figure 4.5: 150/75 single track process map showing superimposed regions of differing single layer melting behaviour. The map has been produced using a scan spacing ratio, s_b , of 0.25.

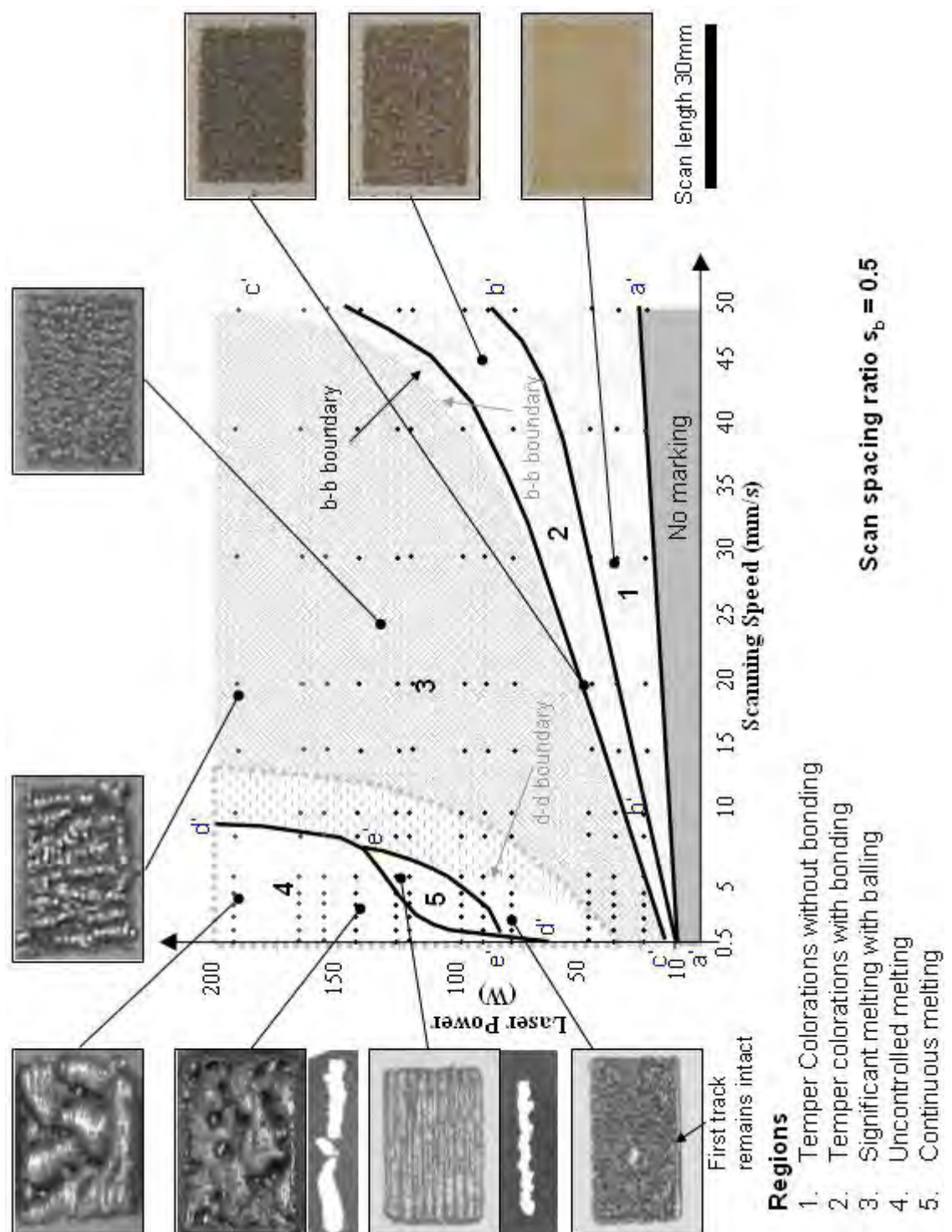


Figure 4.6: 150/75 single track process map showing superimposed regions of differing single layer melting behaviour. The map has been produced using a scan spacing ratio, s_b , of 0.5.

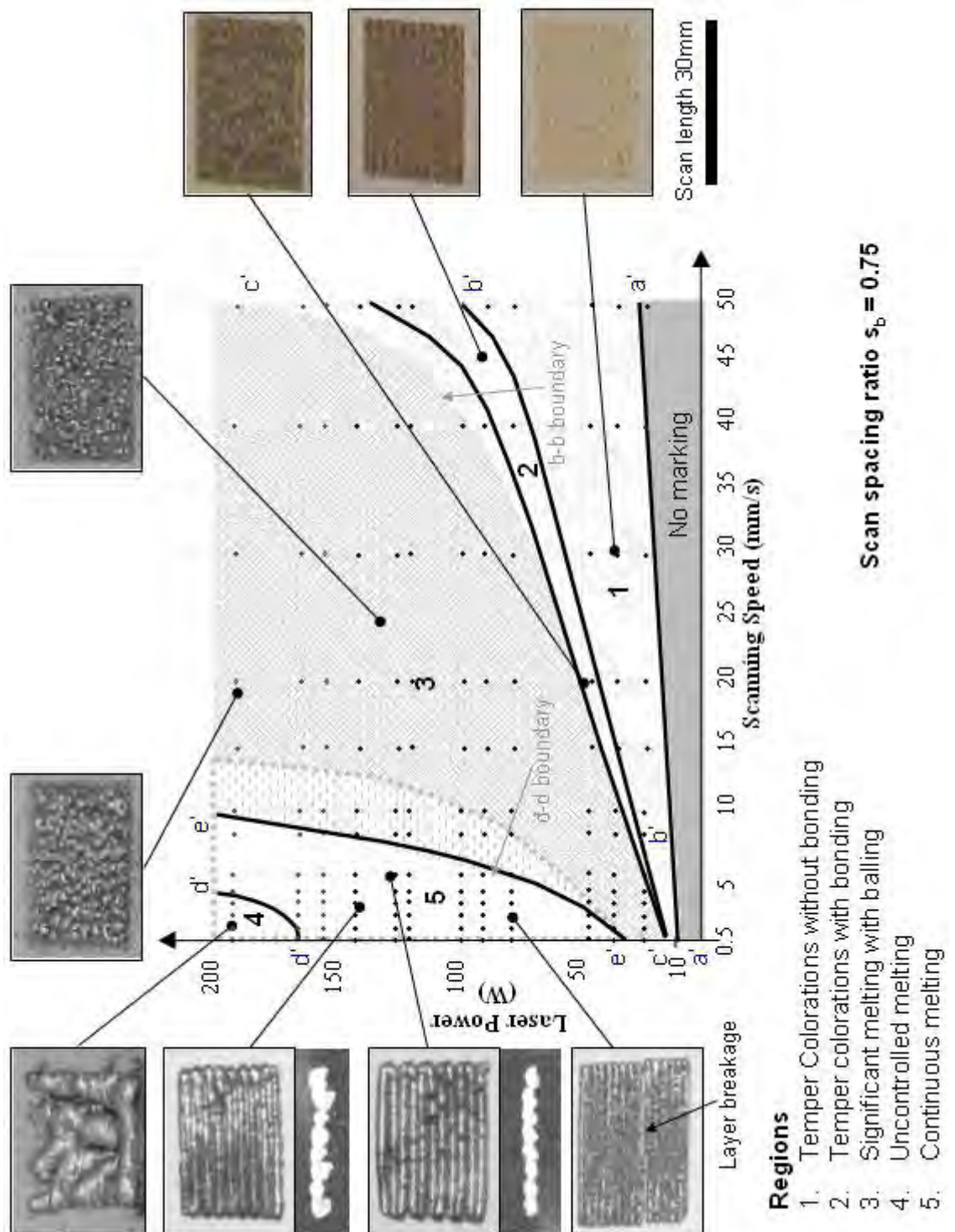


Figure 4.7: 150/75 single track process map showing superimposed regions of differing single layer melting behaviour. The map has been produced using a scan spacing ratio, s_b , of 0.75.

As the number of repeat scans increases, from, $s_b = 0.75$ to $s_b = 0.25$, the surface oxide layer darkens and particle bonding increases marginally, causing a downwards shift of the b''-b'' boundary.

The boundary line c''-c'' which separates the temper colorations region to the left with the significant melting with balling region to the right, follows a similar path to the boundary line, b-b which separates similar behaviours during single track production. This suggests that repeat scanning, up to a maximum of 4 times per exposed area, ($s_b = 0.25$), has little affect on the temperature change of the molten powder causing only a marginal change in the power-speed combinations at which melting with balling can first occur. The reason for such a small change, which only occurs at high power and speed combinations and larger scan spacing ratios, is likely to be associated with reductions in incident energy caused by increased reflectivity of the laser radiation when melting powder local to a solidified melt volume. This argument is perhaps strengthened when considering that the shift in the c''-c'' boundary is greater at larger scan spacing's.

At laser powers below 100W, the melting with balling region of single layers was found to extend into lower power-speed combinations where single tracks were found to remain continuous. This was particularly apparent at scan spacing ratios, s_b , of 0.25 and 0.5. At these conditions, and in the majority of cases, only the first scanned line of the layer remained continuous; as predicted by the underlying single track process map (see Figures 4.5 and 4.6). However, all subsequent rastered tracks balled. This phenomenon is likely to be caused by poor wetting properties of the chromium rich oxide slag, which as the experimental results suggest, becomes more significant as the scan spacing ratio reduces.

The boundary line e''-e'' which separates the melting with balling region to the right with the continuous melting region to the left defines a region where low scan speeds allow for the rastering melt front to maintain a continuous melt pool (region 5). At a scan spacing ratio, s_b , of 0.75, this region extends over a large power range where the boundary follows an identical path to the boundary line d-d which separates similar melt pool behaviours during single track production (see Figure 4.7). At a scan spacing ratio, s_b , of 0.5, a continuous rastering melt front again occurs but over a much smaller

power range; bounded by the melting with balling region at powers lower than 90W and the over melted layer region at laser powers greater than ~125W. Again this region terminates at scan speeds which fall along the d-d boundary, suggesting that a larger scan spacing (>50% of the beam diameter) allows tracks within the layer to behave in a manner similar to single tracks. The melt pool size between the two scanning conditions is also comparable.

The boundary line d''-d'' which separates the melting with balling region to the right with the uncontrolled melting region to the left defines a region where high laser power and low scan speed combinations cause layers to become over melted, forming large globular layers. Interestingly, the distinctiveness of individual tracks within the layers are now lost. Instead, layers contain a number of melt globules which appear to have a random orientation. Observations during the experimental works suggest that the forming melt globules, which are likely to exist due to the presence of the oxide slag, appear to move around, increase in size and continually changing orientation (or perhaps simply changing shape) as the laser heat source passes back and forth over them.

One factor contributing to the cause of these over melted layers might be realised if a scan spacing, as a percentage of single track width (s_t) is considered instead of as a percentage of beam diameter. If for example we have a laser power of 152W and a scan speed of 2.0mm/s, the resultant single track width is 2.92mm (Appendix D, Table D11). Using results from Figure 4.2 in this example, the scan spacing, s , is 0.55mm (1.1 x 0.5). Hence, the beam will need to pass back and forth over five times before it clears the first melt tack (2.92/0.55).

Figure 4.8 reproduces the maps shown previously in Figures 4.6 and 4.7, but instead shows single layer images produced using a scan spacing relative to the melt track width of 50% and 75%. This change eliminates large globular layers at higher energy densities. However, it does not change the speed and power range over which tracks remain continuous.

Tables 4.1 to 4.3 tabulate calculated values of the scan spacing ratio, s_t , for a number of power-speed combinations which fall in regions 3-5 in Figures 4.6 and 4.7. The ratio has been calculated using values of melt track width recorded in Appendix D,

Tables D7-D12. The tabulated results suggest (assuming the rastered melt track width is the same as the unrastered melt track width) that a scan spacing ratio, s_t , lower than ~ 0.25 , will create globular layers.

Finally, it is also interesting to note that the number of passes of the laser equals the number of melt tracks produced when the scan spacing is 50% and 75% of the beam diameter. This would at first seem an impossible situation given the size and size consistency of the melt tracks. However, closer inspection of the rastering melt front reveals powder displacement along the leading edge of the layer (see Figure 4.15). This must play a key role in providing the admission of extra powder which is clearly being melted on each pass of the laser beam.

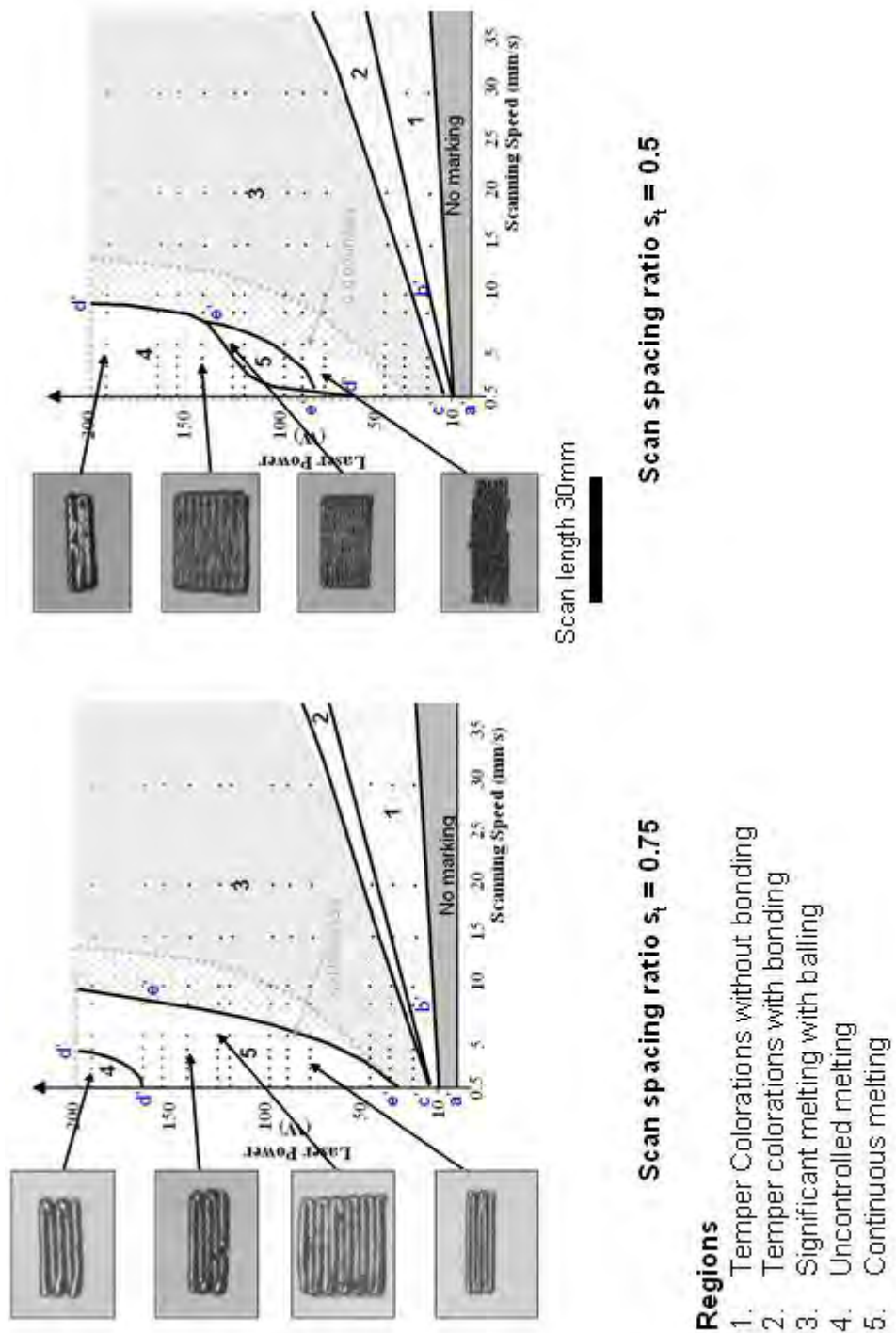


Figure 4.8: 150/75 single track process maps showing superimposed regions of differing single layer melting behaviour. The map has been produced using a scan spacing ratio, s_t , of 0.75 and 0.5.

Table 4.1: Values of $s_t=0.25$, calculated from $s_t = \frac{s}{b} = 1.1 \times 0.25 / b$

Scan Speed \ Laser power	0.5mm/s	1.0mm/s	2.0mm/s	3.0mm/s	4.0mm/s
58W	0.12	0.13	0.15	0.19	0.24
89W	0.11	0.12	0.13	0.16	0.20
125W	0.10	0.10	0.11	0.12	0.14
152W	0.09	0.10	0.09	0.11	0.12
189W	0.09	0.08	0.09	0.10	0.12

Region 4
Region 3
Region 5

Table 4.2: Values of $s_t = 0.5$, calculated from $s_t = \frac{s}{b} = 1.1 \times 0.5 / b$

Scan Speed \ Laser power	0.5mm/s	1.0mm/s	2.0mm/s	3.0mm/s	4.0mm/s
58W	0.24	0.27	0.30	0.38	0.49
89W	0.22	0.23	0.27	0.32	0.39
125W	0.20	0.20	0.22	0.24	0.28
152W	0.18	0.20	0.19	0.22	0.25
189W	0.17	0.17	0.18	0.21	0.23

Region 4
Region 3
Region 5

Table 4.3: Values of $s_t=0.75$ calculated from $s_t = \frac{s}{b} = 1.1 \times 0.75 / b$

Scan Speed \ Laser power	0.5mm/s	1.0mm/s	2.0mm/s	3.0mm/s	4.0mm/s
58W	0.36	0.40	0.46	0.57	0.73
89W	0.33	0.35	0.40	0.47	0.59
125W	0.29	0.30	0.32	0.37	0.42
152W	0.27	0.29	0.28	0.33	0.37
189W	0.26	0.25	0.27	0.31	0.35

Region 4
Region 3
Region 5

4.4 Single Layer Argon Atmosphere Results

This section details all the single layer build results obtained by melting layers within an Argon based atmosphere. The experimental apparatus used in these trials is given in Chapter 2, Section 2.3. The scanning conditions ranged from 32W to 162W and 0.5mm/s up to 10mm/s. Over this range the behaviour of the melt was fairly consistent, though layer density, surface quality and strength was found to vary significantly.

Figures 4.9 to 4.14 show the surface morphology of a mixture of 15mm x 12mm and 12mm x 12mm single layers, produced using a scan spacing of 25%, 50% and 75% of the beam diameter. A number of different qualitative observations can be seen, particularly concerning layer roughness and density. At a scan spacing of 75%, surface roughness and inter-run porosity was high, leading to fragile layers, particularly at low laser powers (see Figure 4.9). The high surface roughness occurred due to the cylindrical nature of the melt tracks, which were similar in size and dimension to the unrastered melt pools (see Figures 3.46 – 3.49, Chapter 3), causing a number of undulations running parallel to the rastering direction.

At low energy densities ($32 < P(W) < 89$ and $2 < U(\text{mm/s}) < 10$), the conduction limited melt pool was insufficient in width to attain strong fusion bonds between neighbouring tracks causing layers to crumble when handled. Layers produced at higher energy densities ($125 < P(W) < 162$ and $1 < U(\text{mm/s}) < 2$), were significantly stronger, but isolated pockets of inter-run porosity was still a significant problem and surface undulations still persisted. Within this band of conditions, layers were found to have an overall density of approximately 60% of theoretical density; calculated assuming the layer has constant width, depth and height as measured about the central axis of the layer and assuming a solid density of $7,900 \text{ kg/m}^3$. At a scan spacing of 50% and 25%, layers produced at low energy densities ($32 < P(W) < 89$ and $5 < U(\text{mm/s}) < 10$) were still reasonably fragile and exhibited a high inter-run porosity, giving an overall layer density of approximately 50%. However, at high energy densities ($89 < P(W) < 162$ and $1 < U(\text{mm/s}) < 2$) inter-run porosity was low giving an approximate layer density in the region of 70% to 80%; the high density occurring at the smaller scan spacing. The surface morphology was also much flatter, even though the conditions were still in the cylindrical track regime (see Figures 3.46 – 3.49, Chapter 3). The first track within the

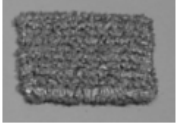
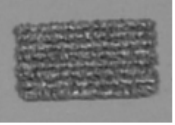
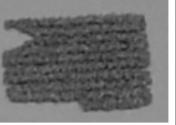
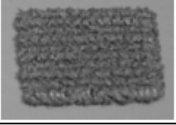
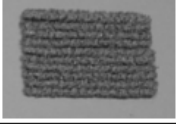
89				too fragile	too fragile
48		too fragile	too fragile	too fragile	too fragile
32		too fragile	too fragile	too fragile	too fragile
P(W) U(mm/s)	1	2	5	8	10

Figure 4.9: Single layers produced at low power, with a 75% scan spacing as a percentage of beam diameter.

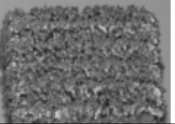
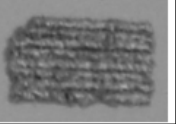

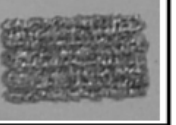
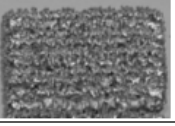
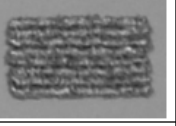
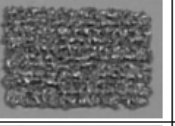
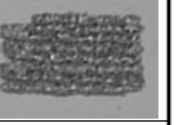
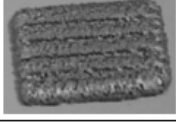
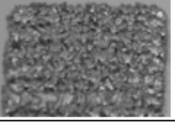
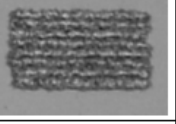
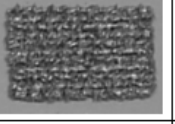
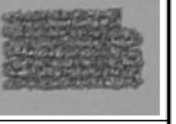
162	Layer too small for accurate comparisons				
143	Layer too small for accurate comparisons				
125					
P(W) U(mm/s)	1	2	5	8	10

Figure 4.10: Single layers produced at high power, with a 75% scan spacing as a percentage of beam diameter.


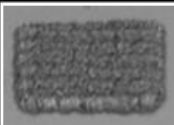
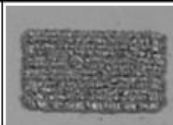
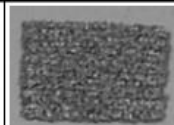
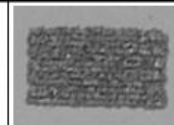
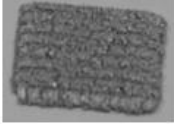



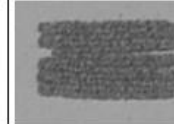

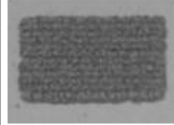
89					
48					
32			too fragile	too fragile	too fragile
P(W) / U(mm/s)	1	2	5	8	10

Figure 4.11: Single layers produced at low power, with a 50% scan spacing as a percentage of beam diameter.

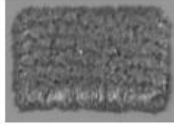



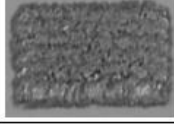
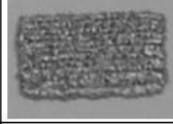
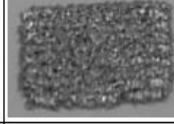
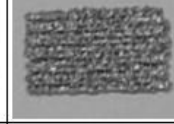
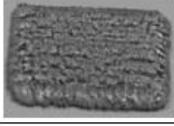
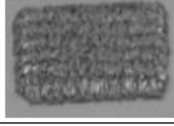
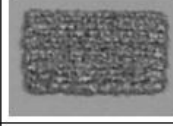
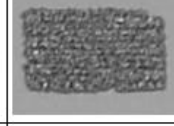
162	Layer too small for accurate comparisons				
143	Layer too small for accurate comparisons				
125					
P(W) / U(mm/s)	1	2	5	8	10

Figure 4.12: Single layers produced at high power, with a 50% scan spacing as a percentage of beam diameter.

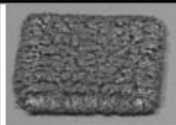
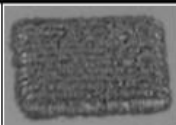



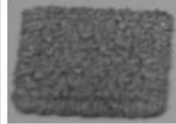


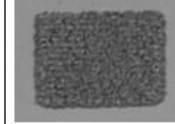
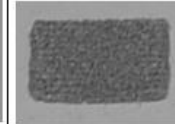
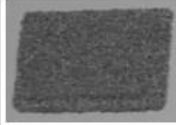
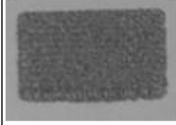
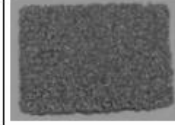
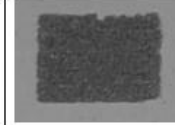

89					
48					
32					
P(W) U(mm/s)	1	2	5	8	10

Figure 4.13: Single layers produced at low power, with a 25% scan spacing as a percentage of beam diameter.

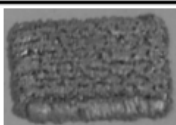
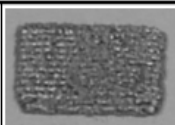
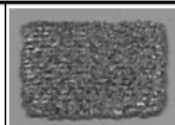
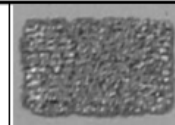
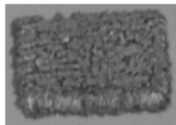
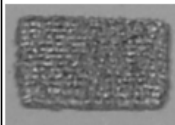
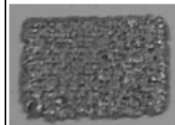


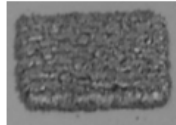
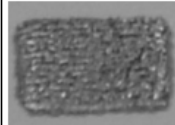
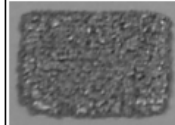

162	Layer to small for accurate comparisons				
143	Layer to small for accurate comparisons				
125					
P(W) U(mm/s)	1	2	5	8	10

Figure 4.14: Single layers produced at high power, with a 75% scan spacing as a percentage of beam diameter.

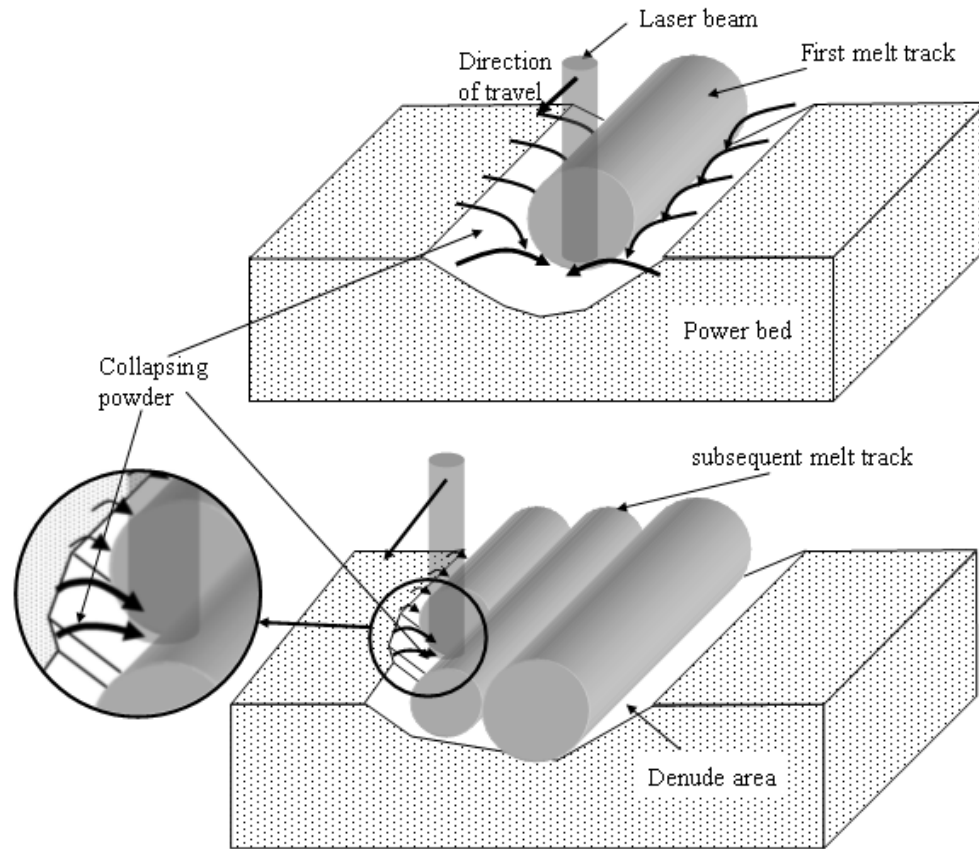


Figure 4.15: Powder displacement during single layer scanning.

layer (as shown in Figure 4.12; 143W at 2mm/s) was often cylindrical, but subsequent ones were much flatter. There are two possible explanations for this. The presence of pre-existing tracks may suppress the rounding behaviour of the melt pool by affecting heat transfer into and through the localised powder bed. Or the admission of additional powder, through trench formation, is much less for subsequent tracks (see Figure 4.15).

Adjusting the laser power and scan speed to create a flat track at the start of the layer i.e. using speeds of 0.5mm/s (see Figures 3.46 – 3.49, Chapter 3), could reduced the size imbalance between the first and all subsequent tracks, improving the overall layer morphology.

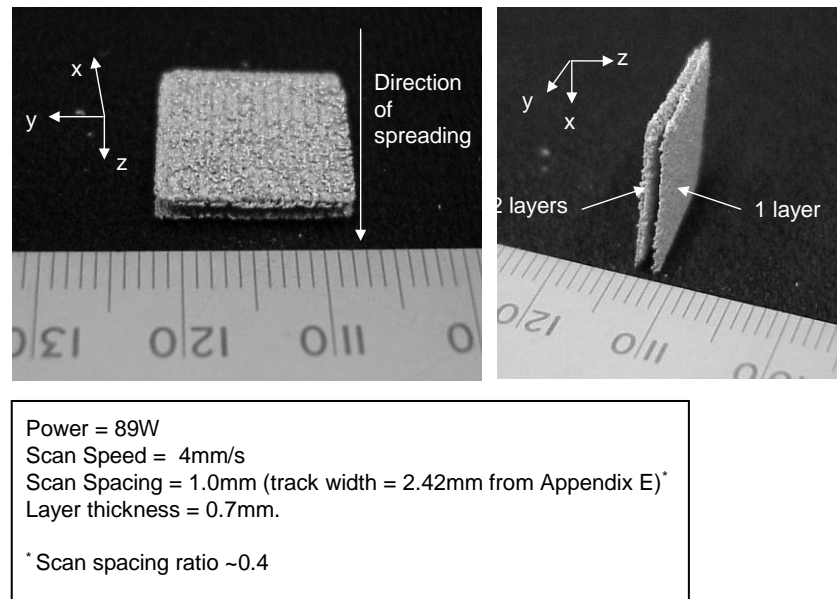


Figure 4.16: Layer delamination caused by oversized melt tracks at the start of each new layer.

From a practical point of view, the presence of a large first track dictated the minimum layer thickness of powder that could be deposited during multiple layer scanning. Hence, when trying to bond layers together it was often found that a good fusion bond could only be achieved at the interface between first scanned lines, causing the layer to delaminate. The delaminating layer would often be hinged about the first scanned line of the current and previous layer as shown in Figure 4.16. The figure shows a three layer build with the final (third) layer detached from the previous two.

Finally, at very high energy densities ($>143\text{W}$ at 1mm/s) the melt volume was too large for the size of the layer being created, making it difficult to judge and compare the outcome accurately.

4.5 Multiple Layer Equipment and Build Strategy

4.5.1 Powder Spreading, Deposition and Layer Displacement

The two spreading mechanisms used in this study included a counter-rotating roller and a simple wiper blade. The design and operation of both is discussed in greater detail in Chapter 2, Section 2.3.1.3. Both mechanisms were moved by hand across the build zone by a push rod that passed through the process chamber wall. A gearing mechanism caused the roller to counter rotate as it was pushed. The wiper blade consisted of a metal plate with a rubber lined working edge. Each mechanism was returned back across the build zone after each deposition and spreading action (home position). If this cycle was not completed the push rod would block the path of the laser beam. A hopper, situated above the spreading mechanism when in the home position, deposited a predetermined heap of powder in front of it which could then be spread and levelled across the build area.

The counter rotating roller mechanism was constructed and used first because it was loosely based on the successful mechanism currently employed in the DTM Sinter StationTM (DTM Corporation, 1996). However, the design of the Leeds system proved to have a significant flaw. The gearing mechanism used to rotate the roller was situated close to both the powder bed surface and the deposition zone of the powder hopper. Hence, the gearing mechanism often became coated in a layer of powder which prevented the smooth running of the roller, causing frequent seizures.

The irregular and jerky motion of the roller caused ridges to form in the spread powder surface. These ridges appeared to have no significant affect on the behaviour of large melt volumes, but when scanning the surface at conditions approaching the fragmented melt pool regime (see Figures 3.37 – 3.40), i.e. when the melt pool was close to becoming unstable, breaks did occur as the melt front passed over the ridges. Furthermore, the ridges were also found mirrored on the surface of irradiated layers when processed at conditions which fall within the partial melting regime of the process maps.

Of greater concern however, was the interactions between the roller and the melted layer as it traversed the build area. These interactions displaced and rotated the

melted layers in the bed and were at first thought to be linked to the erratic motion of the traversing roller (see Figure 4.16). Therefore, the roller was replaced with the less complex and more smoother running wiper blade system. However, the problems were found to still persist.

In Chapter 1, Section 1.7.2, it was discussed that friction between the powder heap and the underlying melted layer caused the shearing and displacement of layers as the powder passed over the build area. However, reducing the weight of the powder shot by reducing the surplus once again proved unsuccessful, suggesting perhaps that protuberances on the melted layer surface were the cause of the interactions. With this in mind, further investigations revealed that an increase in layer thickness ($>0.65\text{mm}$) proved successful at limiting, but not completely reducing, layer displacements. A layer thickness below 0.65mm would cause layer displacement and values below 0.4mm would often cause layers to rotate and skew (see Figure 4.16).

In 4.16a, the degree of displacement can be gauged by comparing the differences in surface roughness between the two facing sides. Furthermore, the displacements were found to occur in two directions, each corresponding to the direction of movement of the wiper blade as it deposited and spread the powder in one direction then returned to the home position in the opposite direction. It should also be made clear that the first layer of the build, which appears to be displaced in a direction perpendicular to the direction of spreading, is due to an error in the scanning procedure.

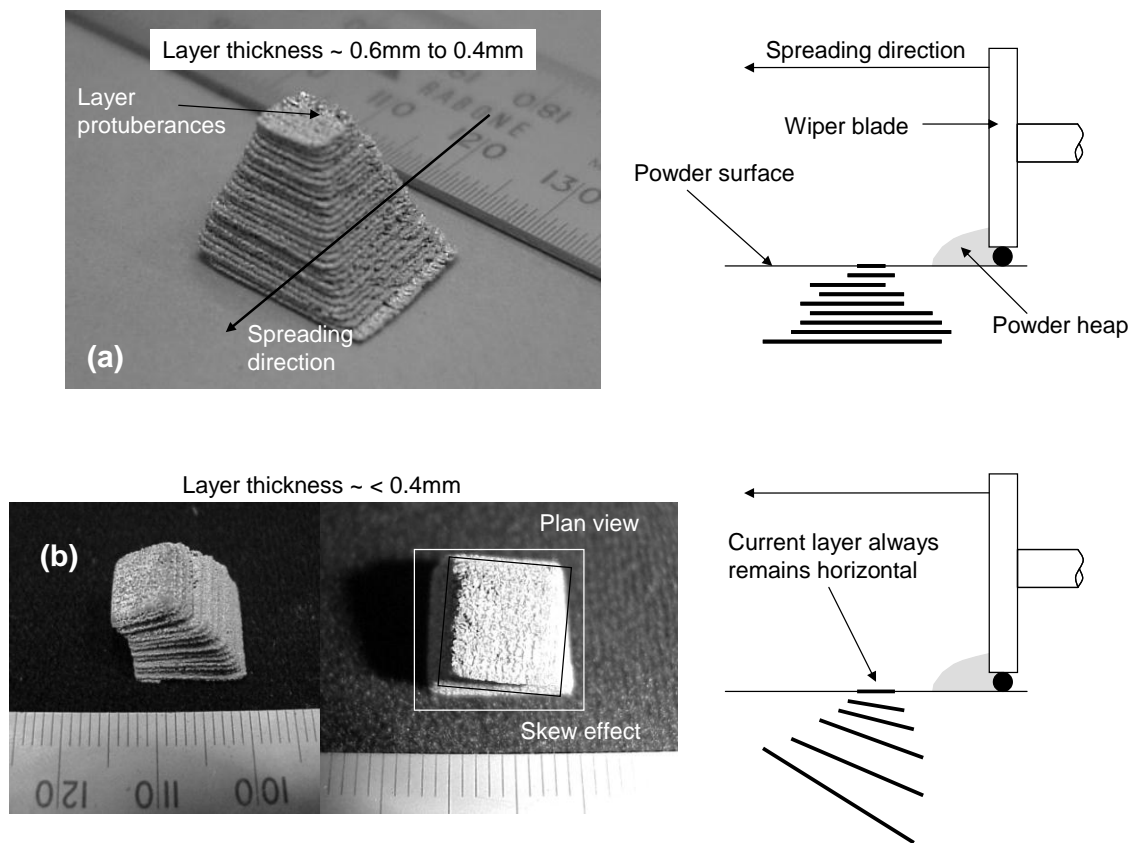


Figure 4.17: (a) Misalignment and (b) rotation and skew of melted layers processed within deep powder beds. The shape should be that of a pyramid.

4.5.2 Build Strategy

The minimum layer thickness of 0.65mm imposed by the deposition and spreading mechanism (see Section 4.5.1) was found to be too large when trying to obtain a strong interfacial bond between layers. This was apparent even at very high energy densities, where weak interfacial bonds caused adjacent layers to delaminate. A number of attempts were made to alleviate layer displacement by bonding or anchoring the first layer of a build to an underlying substrate. It was anticipated that such a route would allow any melt protuberances that would otherwise interact with the passing wiper blade to be broken off, allowing the melted layer to remain in its intended position.

The first attempt involved the bonding of the first layer of a build to a room temperature mild steel or stainless steel solid plate positioned at depths of 0.2mm, 0.4mm, 0.6mm and 0.8mm below the powder surface. However, this technique caused

the melt volume to ball with no or very little adhesion to the substrate. Attempts to increase the temperature of the substrate by approx 100°C-150°C as a method to reduce the thermal load and temperature gradient across the interface, were made but the method was found to be too impractical and not particularly successful. The limited success can probably be linked to the relatively small temperature increase of the substrate, which was restricted to 150°C by the rubber seals located within the piston assembly of the process chamber.

A second attempt involved the bonding of the first layer to a wire mesh which itself was pinned to a mild steel substrate located under the powder surface. The mesh consisted of 0.5mm gauge steel wire with a 3mm grid spacing. This method proved more successful with reasonable attachment being made at the interface between the melt pool and the wire, preventing layer misalignment during powder spreading and deposition. However, the melted surface layer was often very rough, following the undulations of the wire mesh; the melting of several layers was needed before the layer overcame this initial disturbance.

A third approach was to bond the first layer of a build to a series of dress maker pins situated within the powder layer (see Figure 4.17). The method proved successful and appeared to impose no adverse effects on layer melting behaviour. Therefore, this was the „anchoring“ method of choice for multiple layer experiments reported in the following Section. Proving trials conducted to investigate the depth requirement of the pins relative to the powder layer surface, including depths ranging from 0 to 1.5mm, suggested there was no height requirement, providing the pins were situated comfortably within the melt depth of the layer.

Finally, the pins had low stiffness and were free to move vertically in their supports to allow easy removal of the melted layers after solidification. Hence the pins were ineffective as a method to prevent layer distortions. Furthermore, a minimum layer thickness of 0.4mm was still necessary because layers still had a tendency to move around at lower values, though less frequently.

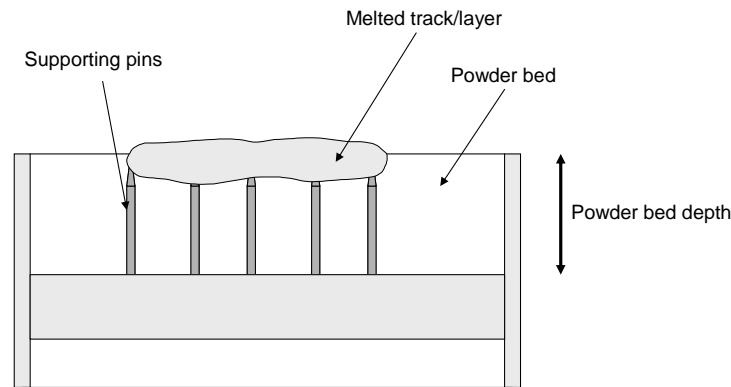


Figure 4.18: Layer building using supporting pins

4.6 Multiple Layer Results

Producing multiple layers, using equipment and methods described in Chapter 2, Section 2.5.1.2 and Sections 4.4 and 4.5 of this Chapter, proved to be very difficult, primarily due to limited time being available to fully evaluate the powder spreading and deposition equipment. With the current set-up, a minimum powder layer thickness of 0.4mm, imposed by the equipment, still proved to be too large, preventing strong fusion bonds being attained between layers, whilst also trying to maintaining a controlled melt front. Figure 4.19 shows a near best attempt at producing a multiple layer block. The cross-section view of the block shows that all layers are still easily distinguishable, suggesting little interlayer remelting. The density of the block was approximately 55% when compared to a theoretical density of 7900Kg/m^3 . However, it is clear from figure 4.19 that the majority of the porosity is present between layers and between melt tracks, the tracks themselves are close to full density.

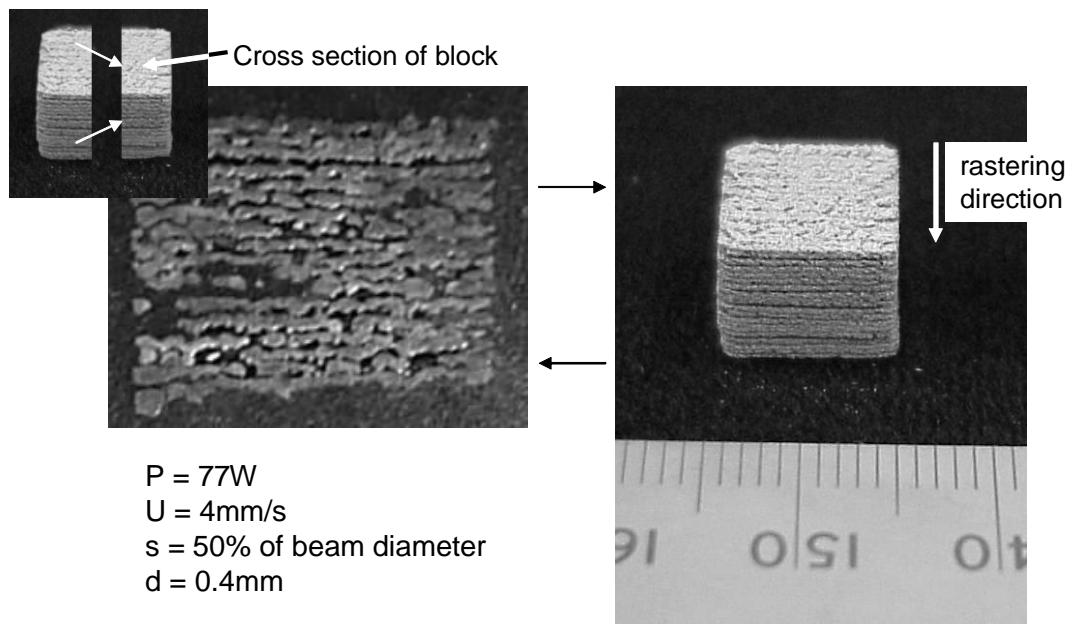


Figure 4.19: Multiple layer block consisting of 18 layers.

CHAPTER FIVE

DISCUSSION AND CONCLUSIONS

5.1 Introduction

The aim of the work presented in this thesis was to develop current understanding of the sintering and melting behaviour of metal powders during SLS. The distinguishing aspect being the melting of tracks and layers in absence of an underlying substrate. To achieve this end, results and observations of melting behaviour, mainly of single tracks, but also of single and multiple layers were successfully reported for both air and argon atmospheres, though multiple layer experiments were limited by the partial success of the powder deposition and spreading equipment. The powder used in this study was an argon atomised austenitic stainless steel of type 314s HC. It was supplied in four batches, each differentiated by particle size distribution; $-300+150\mu\text{m}$, $-150+75\mu\text{m}$, $-75+38\mu\text{m}$ and $-38\mu\text{m}$ (referred to in this work as 300/150, 150/75, 75/38 and -38).

After a discussion on preliminary studies, this chapter will summarise the air and argon atmosphere results for single tracks presented in Chapter 3. The focus being on the changing characteristics of the melt pool (mass, volume, aspect ratio, stability) as the laser power and scan speed change. Mathematical models are also introduced to obtain estimates of laser absorptivity based on experimental mass per unit length data and to support discussions by developing theories on melt track break up. This will be followed by a summary of single layer and multi-layer construction, including the development of powder spreading and deposition equipment. The effects of melt behaviour on features such as density and surface quality will be compared and the changing behaviour of the melt pool during raster scanning will be discussed. This section will also discuss aspects of the work that would have significant implications when considering technology scale up. The chapter will close with conclusions and a final section on future work considerations.

5.2 Preliminary Studies

Mixing of powders for 7.5, 15, 30, 45 and 60 minutes, as outlined in Chapter 3, Section 3.2, changed the packing density of the deposited powder layer and the density variation between samples tested. The packing density of the 300/150, 150/75 and 75/38 powder batches peaked after a 15 minute mixing period, reaching values of 62%, 62% and 60% respectively. Mixing of the -38 powder batch had no improvement over its unmixed density of 58%.

In Chapter 1, Section 1.7.1 it was suggested that the packing density of the loose powder layer often affected the final density of the irradiated or consolidated powder. Because of the closeness of the powder density values recorded in this work this association proved impossible to evaluate. However, a number of qualitative observations may be relevant here. Firstly, once full melting takes place, there is a substantial movement of powder, relative to the size of the melt volume, so the packing behaviour and density of powder local to the progressing melt front would differ to that of the starting powder. Furthermore, once full melting was taking place, the majority of tracks were considered fully dense, other than clusters of loosely bonded particles within the catchment area of the collapsing powder, suggesting perhaps that density and melt formation would be strongly influenced by powder flowability. Investigations in this work of melting behaviour of the -38 powder batch showed that this powder behaved very differently to the other powders, though it is inconclusive whether the reduced flowability or the small particle size was the determining factor.

5.3 Single Track Experiments

5.3.1 Track Cross-Section Observations

Within the continuous melting regime track cross-sections were either flattened, rounded or bell shaped. In an argon atmosphere all three cross-sections were observed. Flat tracks formed predominantly at low power (<100W), and/or low scan speed (<1.0mm/s) and more frequently in the 300/150 and 150/75 powder batches, bell shaped tracks formed at high speed (>4mm/s) and rounded tracks occurred in the transition region between the other two. In an air atmosphere only rounded track cross-sections were observed. The formation of a surface oxide slag in the air atmosphere is strongly

thought to be the cause of the differences in melt behaviour between the two atmospheres.

Figure 3.51, Chapter 3 shows track cross-sections in argon for the 150/75 powder superimposed onto its process map. The boundary between the flattened and rounded tracks is indicated by the solid line. As the boundary is crossed a noticeable increase in track cross-section area with increasing speed is observed. This increase is associated with the sudden increase in melt depth and was unexpected, assuming a constant rate of power absorption as the energy density reduces. Interestingly, the melt width, as perhaps expected, reduced steadily with increasing speed and showed little variation in this trend at the boundary between flat and rounded tracks. Because of the large increase in melt volume, surface tension driven fluid flows (see Chapter 1, Section 1.4) were thought not to be involved with the occurrence of these shape changes. A number of qualitative observations leading to possible explanations for this behaviour are relevant here.

A common observation in the rounded track regime is the admission of extra powder into the melt pool (defined by the region bounded by the dashed line in the process maps of Chapter 3). Tracks often sink into the powder bed and power from either side collapses in, leaving a trench around the track. The admission of extra powder is likely to feed track growth, and maybe a reason for increased melt volume in the rounded track regime and of tracks processed within an air atmosphere.

At low scan speed and high power ($110 < P(W) < 162$ and $1.0 < U(\text{mm/s}) < 2$) the collapsing powder is almost fully enveloped leaving track profiles smooth with only a few groups of satellite particles visible around the lower fringe (powder side) of the solidified track. At low power and high speeds ($32 < P(W) < 77$ and $5.0 < U(\text{mm/s}) < 10$ and $110 < P(W) < 162$ and $2.0 < U(\text{mm/s}) < 10$) the take-up of additional powder into the melt volume appears to be lower, leaving large clusters of sintered bonded particles around the lower edges of the track, giving rise to 'bell' shaped track cross-sections. This situation is likely to arise from the time available for tracks to remain molten; longer at lower speeds.

The one question that remains is what triggers the change from flat to rounded tracks. Currently this cannot be answered by observations alone, though one clue might be found in the shape of the temperature field surrounding the laser beam. At low scan speeds ($< 0.5 \text{mm/s}$), the temperature field might take on a shape more reminiscent of a temperature field around a stationary heat source i.e. a more even heat distribution

rather than a higher concentrated behind the beam, perhaps changing the fluid flow within the molten pool. This however is only speculative.

5.3.2 Track Masses per Unit Length

Examination of track cross-sections clearly shows an increase of area with increasing scan speed at the boundary between flattened and rounded tracks. However, due to the variability in track shape, the exact areas will vary along the length of the track. To obtain an average measure of track size, tracks were removed from their powder beds, weighed and their lengths measured. The results were plotted as mass per unit length against energy density for all four powder batches (see Figure 3.52 Chapter 3). In each case data falls between two limits, an upper and a lower. All data for $U > 4\text{mm/s}$ fall on the upper limit, labelled HS and all data for $U = 0.5\text{mm/s}$ fall on the lower limit, labelled LS. However, at high laser powers ($>110\text{W}$), a large number of melt tracks produced between $1.0 < U(\text{mm/s}) < 4.0$ also fall on this upper limit, reemphasising the sudden increase in melt volume observed in the track cross-sections.

Powder displacement, being one argument for increased track cross-section, has already been addressed in Section 5.3.1. In this section, changes in laser absorptivity are also considered. If absorptivity is directly responsible for these changes, then the variability in absorptivity during scanning is potential large. Measured track mass per unit length, m_L , can be used to obtain an alternative estimate of absorptivity, α^* . Equation 5.1 as an equality is an expression for the minimum value of α^* , based on a heat balance. $\alpha^*(P/U)$ is the absorbed energy per unit track length while $m_L[C_p(T_m - T_o) + L]$ is the energy to melt a unit track length. Where, L , is the latent heat of melting and, C_p , is the specific heat which is the average specific heat from ambient bed temperature, T_o , to the metal's melting temperature, T_m . All material property data is collected in Table 5.1.

$$\alpha^* \geq [m_L / (P/U)] [C_p (T_M - T_o) + L] \quad (5.1)$$

According to equation 5.1, a constant slope $m_L/(P/U)$ corresponds to a constant effective absorptivity, α^* . Therefore, obtaining the gradient of the HS and LS slopes will allow an estimate for the „effective“ absorptivity to be calculated; assuming all power is available for melting. The HS and LS slope values, for all powder batches including those obtained within an air atmosphere, are collected in Table 5.2, in units of

gram/J. Table 5.2 also gives values of, α^* , calculated from the HS and LS slopes. The variation of, α^* , with powder batch is plotted in Figure 5.1.

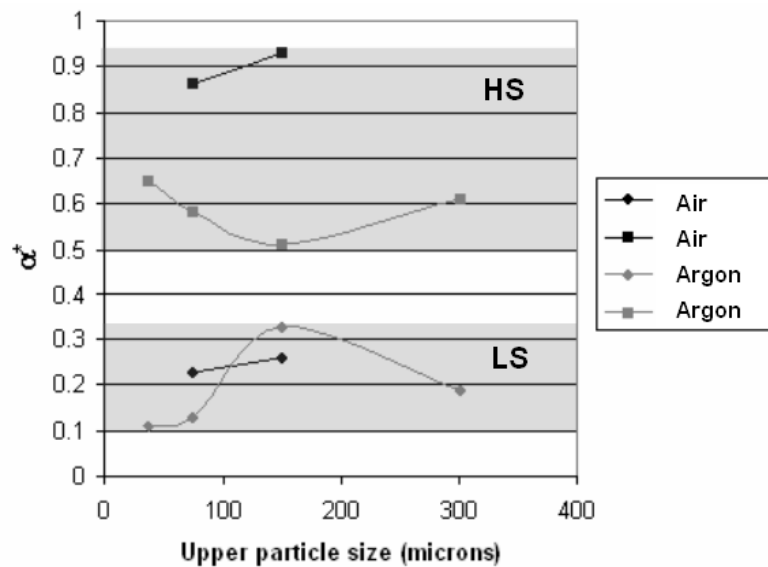
Table 5.2 and Figure 5.1 highlight the significant differences in α^* as scan speeds change. At low speed (0.5mm/s), values fluctuated between 0.1 and 0.33 in argon and 0.2 and 0.3 in air. At high speed (>4mm/s) values were much higher, fluctuating between 0.51 and 0.65 in argon and 0.86 and 0.93 in air. The effects of particle size on α^* is difficult to gauge. The results in Figure 5.1 might suggest an increase in α^* with increasing particle size at low scan speed and perhaps a reduction in α^* with increasing particle size at high speed, though these observations are questionable due to the seemingly out of place values for the 75/38 powder batch. Nevertheless, of greater interest is the enormity of the α^* values, particularly at high speed, suggesting that values of absorptivity for a CO₂ laser into a metal powder bed are far higher than previously thought (See Chapter 1, Section 1.7.3). Discussions on this matter will continue in Section 5.3.4.

Table 5.1: Material property data used in calculations throughout this chapter.

Symbol	Description	Value	Units	Comments
C_p	Specific heat	700	J/kg	This is an average value between 20°C and 1350°C
K_{powder}	Thermal conductivity of powder	0.25	W/mK	Obtained from other research data at Leeds
κ	Thermal Diffusivity of powder	0.074×10^{-6}	m ² /s	$\kappa = \frac{K_{\text{powder}}}{\rho_{\text{powder}} C_p}$
L	Latent heat of melting	280000	J/kg	For stainless steel
ρ	Density of solid	7900	Kg/m ³	Approx. density of stainless Steel 314s HC
ρ_{powder}	Density of powder	4800	Kg/m ³	Average of all four batches after mixing for 15 minutes
T_m	Melt temperature	1340	°C	Melting point of stainless steel 314s HC
T_o	Ambient temperature	20	°C	Estimated to be room temperature

Table 5.2: LS and HS boundary gradients and α^* values calculated from mass/length vs. P/U figures in Chapter 3.

Powder batch	Air Atmosphere				Argon Atmosphere			
	M_L ($\times 10^{-3}$ (g/J))		α^*		M_L ($\times 10^{-3}$ (g/J))		α^*	
	LS	HS	LS	HS	LS	HS	LS	HS
300/150					0.09	0.54	0.11	0.65
150/75	0.19	0.72	0.23	0.86	0.11	0.48	0.13	0.58
75/38	0.22	0.76	0.26	0.93	0.28	0.42	0.33	0.51
-38					0.16	0.51	0.19	0.61

Figure 5.1: Variation of laser effective absorptivity, α^* , with powder particle size.

5.3.3 Process Maps

In the absence of an underlying substrate, tracks formed within an argon atmosphere as either a continuous melt with either a flattened, rounded or bell shape cross-section (see Section 5.3.1), a fragmented or balled melt or as a partially melted track with a flattened cross-section. An generalisation of these behaviours is given in Figure 5.2. The 150/75 process map is used in this example.

Track type observations were recorded for laser powers up to 200W and scan speeds ranging from 0.5mm/s to 50mm/s. The results were plotted on maps as regimes, one for each powder batch, that allow accurate prediction of track type as power and speed combinations change (see Figures 3.37 - 3.40, Chapter 3). A noticeable observation between the maps is the difference in boundary position between regimes as powder particle size changes. The most notable being the increase in the fragmented or balled melt regime as particle size distribution reduced. This caused a notable reduction in the scan speed range, from a maximum of 12mm/s in the 300/150 to >5mm/s in the -38 powder batch, over which a continuous melt pool could be maintain.

Process maps plotting changes in track type for an air atmosphere over the same speed and power range were also created and compared with the argon process maps (see Figures 3.09 – 3.12, Chapter 3). Track types, the distribution of track type regimes and regime boundary changes between powder batches followed a very similar pattern for both sets of maps. The most notable differences were; the absence of a partial melting regime, instead the power tended to agglomerate and oxidise; the melt when unstable tended to form balls rather than melt fragments; and in the continuous melting regime all tracks were rounded, and like the rounded tracks within an argon atmosphere, they all sat within a deep powder trench (see Figure 5.2). The melting boundary and other boundaries depicting melt instability are discussed in more detail in the following sections.

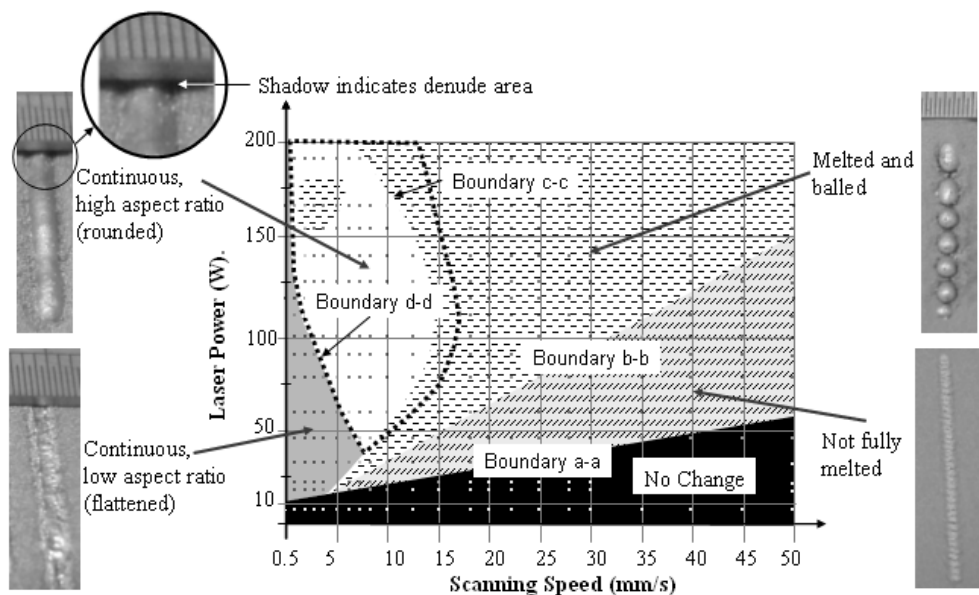


Figure 5.2: Generalisation of melting behaviour within an argon atmosphere.

5.3.4 Melting Boundary

The boundary line b-b on the air process maps and the boundary line a-a on the argon process maps plots the speed and power relationship over which the irradiated powder begins to first form a significant melt volume (observed qualitatively), giving rise to flattened liquid phase sintered tracks in argon and the formation of tiny balls, not much bigger than perhaps several agglomerated particles, in air; though some balls were laid almost side by side. However, tracks similar to those in argon i.e. liquid phase sintered, were also categorised in the -38 powder batch when processed in air. This region was triggered at much lower J/mm (a-a boundary) than the balling region discussed for the other three powders (b-b boundary). Since a melt volume is strongly believed to be required for bonding in this process, the point of first significant melting is deemed to occur at the a-a boundary in the -38 powder.

In each case the relationship was linear, or for the case of the 300/150 and 150/75 powder batches in air, the relationship was judged to be linear after some debate (see Chapter 3, Section 3.4.2), giving rise to a constant slope P/U. Values of the P/U slopes for all powder batches in both atmospheres are collected in Table 5.3, in units of J/mm. From the table it is clear that the energy required to start melting reduces with reducing powder particle size, and is much higher for powders processed in air, the difference being particularly noticeable in the 75/38 and -38 powder batches. This is perhaps surprising since it was discussed in Chapter 1, Section 1.7.3, that surface oxidation often increases absorptivity. However, when a melt volume forms within an air atmosphere it develops a surface slag. This slag is enriched with chromium giving the melt an often shiny appearance, hence forming a potentially very reflective barrier.

Table 5.3: Calculated values of constant energy density along boundary line b-b on the air process maps and the boundary line a-a on the argon process map.

Powder Batch	Slope of first melting boundary (J/mm)	
	Air Processing	Argon Processing
300/150	2.5	1.5
150/75	2.2	0.9
75/38	1.4	0.24
-38	0.2	0.2

Equation 5.2, is another variation of equation 5.1 which is an expression for the value of absorptivity, α , based on a heat balance. The theory being that at the point of first melting the power absorbed extends only to a depth, d , of one particle, forming a melt volume of area, $bd\pi/4$. The width, b , being some fraction of the beam diameter to be determined later. Therefore, $\alpha P/U$ (J/mm) is the absorbed energy per unit width while $\rho_{\text{powder}}bd\pi/4[C_p(T_m-T_o) + L]$ is the energy to melt the powder per unit width. Other material properties have been described elsewhere (see Section 5.3.2).

$$\alpha \frac{P}{U} = \rho_{\text{powder}} \frac{\pi}{4} bd(C_p(T_m - T_o) + L) \quad (5.2)$$

Experimental observations have shown that the width of the melt tracks produced at conditions which fall along the b-b boundary in argon and along the a-a boundary on the -38 map produced from air melting range between 0.3mm and 0.4mm. Table 5.4 gives approximate values of α , derived from P/U values in Table 5.3 and an average track width of 0.35. This value was also a good estimate for the size of the balled tracks in air. The material property values are collected in Table 5.1. An example calculation using data for the 150/75 powder batch processed in argon is given below.

$$\alpha \frac{P}{u} = 4800x[700(1320) + 280000] \times \frac{\pi}{4} 0.35 \times 10^3 \times d \quad (5.3)$$

Therefore:

$$\alpha \frac{P}{u} = 1.59 \times 10^6 d \quad (5.4)$$

If we assume the depth of melting to be equal to the largest particle size in each powder batch, we can therefore estimate the value for α as:

$$\alpha = \frac{1.59 \times 0.15}{0.9} = 0.27 \quad (5.5)$$

Table 5.3 and Figure 5.3 highlight the various α values between powder batches and atmospheres. The formation of a slag in air has already been discussed as one possible means for low α values calculated from the point of first melting. However, these values differ to α^* values calculated from mass per unit length data of larger melt pools, which approached 0.8 in air (see Section 5.3.2). Because the surface slag is

Table 5.3: Values of α calculated from the a-a and b-b boundaries on the process maps in Chapter 3.

Powder Batch	Depth, d (mm)	Absorbivity for air (α)	Absorbivity for argon (α)
300/150	0.3	0.19	0.32
150/75	0.15	0.11	0.27
75/38	0.075	0.085	0.5
-38	0.038	0.3	0.3

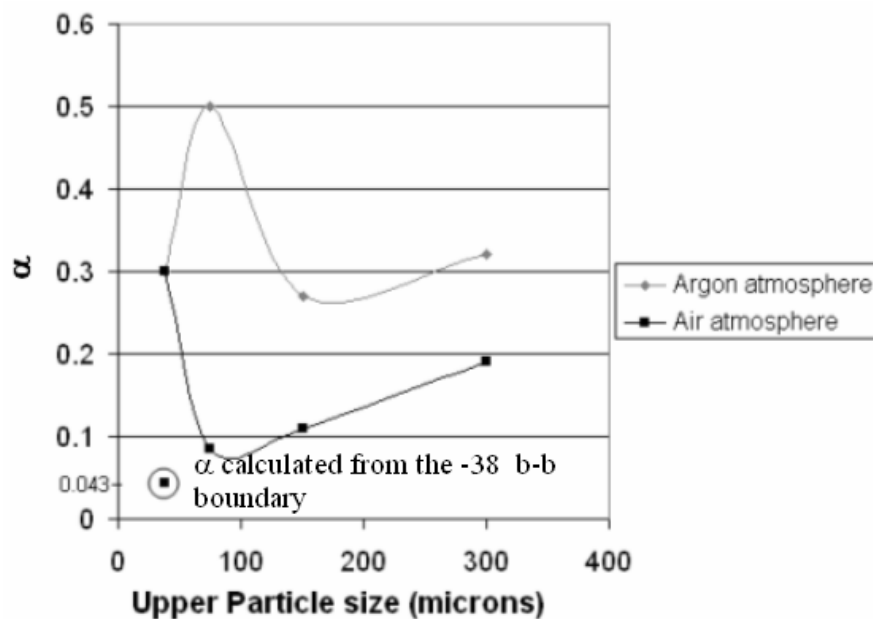


Figure 5.3: Variation of α with powder particle size. Results calculated from slopes of melting boundaries a-a in air and b-b in argon.

present on all melt pools, big or small, the differences in the results leave initial doubt over the function of the slag as a reflector of laser radiation. However, it is also worth considering that reflected radiation, from off the melt pool, maybe irradiating additional

powder either to the front or side of the progressing melt front. This theory, might also explain why rounded tracks are generally larger than flattened tracks, since there is a greater likelihood that any reflected radiation would be contained local to the progressing melt front due to the surrounding trench walls. Hence, even though reflections are likely to be occurring for most of the time, they perhaps only trigger additional melting in rounded tracks that sit within a trench. Since significant trenching does not occur around tracks produced along the boundary of first melting, α values, on the basis of this theory, would be much lower; as shown in the experimental results. This theory is again only speculative and does not explain the cause of the transition from flat to rounded tracks within the continuous melting regime.

The differences in absorptivity when creating tracks in air and rounded tracks in argon is more difficult to resolve. There are two schools of thought, but each are currently lacking a full explanation. Firstly, based on the arguments above, the slag maybe reflecting more radiation onto other areas of the powder bed than the metallic surface of melt pools produced in argon. However, the net energy available for melting would be similar, and so there must have to be some losses during reflection. Secondly, the take-up of displaced powder into the melt is higher when processing in air; a plausible suggestion due to the lack of loosely bonded powder around the periphery of tracks and the lack of nucleation sites within the melt volume. This situation may arise due to the insulating properties of slag's, which in this case might act like a thermal jacket around the melt pool, slowing the rate of solidification.

For the air atmosphere, α values (see Table 5.3) reduced with reducing powder particle size except for the value calculated from the -38 powder batch which was much higher. There was however some doubt as to which boundary on the -38 map to use for these calculations, a-a or b-b, the a-a boundary was chosen (see discussions at the beginning of this section). However, recalculating α for the -38 powder using the b-b boundary continues the downwards trend (see Figure 5.3). It is likely that at the a-a boundary, which depicts the first point at which a track forms, the size of the melt pool has been grossly overestimated. It is likely that only a small melt forms which then wicks into surrounding powder. Using equation 5.4 and assuming an α value of 0.043 (see Figure 5.3), the width of the melt is calculated to be 0.005mm and not 0.35mm as used in the initial calculations.

Finally, values of α calculated using data obtained from the argon atmosphere results appear to remain fairly static with changes in powder batch, though again we see a much higher values for the 75/38 powder. This difference was also found in the α^*

calculations, which either suggests something different is occurring when melting this powder, or more likely that there may be some experimental error.

5.3.4.1 Melt Pool Fragmentation and Balling Boundaries

It is noticeable that the melt front often becomes unstable during scanning leading to fragmentation and balling of the melt pool. In Chapter 1, Section 1.5.2.1, it was suggested that the melt front would remain stable provided the melt length, L , is less than the melt circumference, $b\pi$, where, b , is the melt width. The critical condition being when $L/b = \pi$. Since it is difficult to gauge the length of a tracks molten region, a model has been developed which aims to derive a relationship between P (W) and U (mm/s) and involving the melt pool length, L , which can then be compared to melt instability boundaries on the single track process maps.

$$\alpha P = \dot{q}_{\text{cond}} + \dot{q}_{\text{conv}} \quad (5.6)$$

where (see Figure 5.3):

αP = absorbed incident energy

\dot{q}_{cond} = heat loss by conduction from the pool surfaces.

\dot{q}_{conv} = heat loss by the convection of material through the pool.

There is no heat accumulated term since the melt pool size is constant during a run i.e. quasi steady state assumption. A simplified melt pool will also be used in the model as shown in Figure 5.3b with a cross section area equal to $\pi bd/4$, where b and d are the width and depth of the melt pool respectively. In this model it is also assumed that the beam is stationary and the powder bed, and therefore the melt volume, are moving at a speed, u , with respect to the laser beam. Therefore the convective heat transfer component is:

$$\text{Power out due to convection} = \frac{\pi b d}{4} U [T_m - T_o] \rho C_p \quad (5.7)$$

The latent heat of melting is absorbed at the leading edge of the melt pool and rejected at the rear, hence it does not enter the heat balance. The conduction component is due to the heat loss from the surface when in contact with the surrounding powder

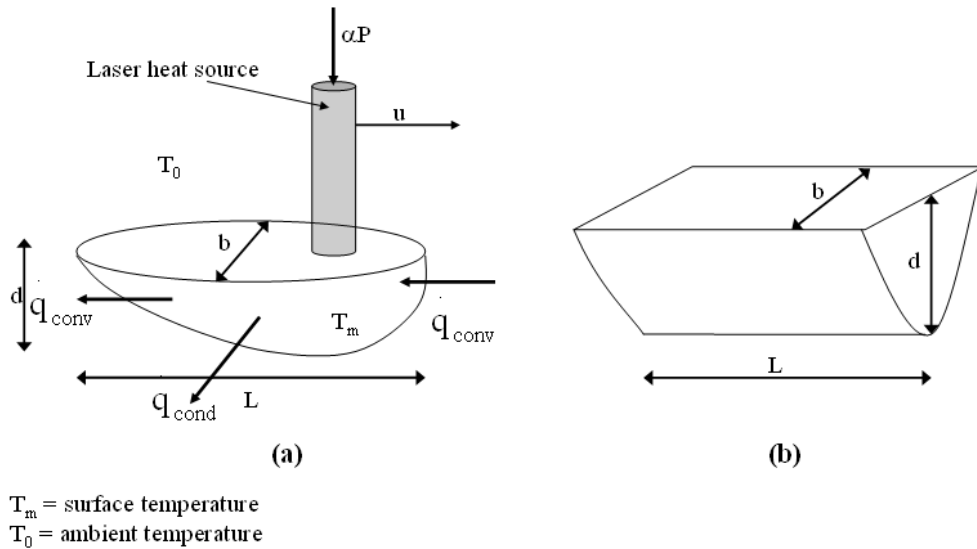


Figure 5.4: (a) temperature field and heat balance around a moving heat source and (b) a simplified melt pool shape.

bed. The temperature of the surface is at the melting point, T_m . The heat will flow according to Fourier's 1st law down a thermal gradient of $(T_m - T_o)/x$. Where, x , from heat diffusion theory, is the distance travelled of the main heat wave in a time, t . Hence $x = \sqrt{4\kappa t}$, where $\kappa = K_{\text{powder}}/\rho C_p$ and is known as the thermal diffusivity of the powder bed. K_{powder} is the thermal conductivity of the powder. The time, t , for the heat to flow is L/U , hence the approximate thermal gradient around the melt pool will be:

$$\text{Thermal gradient around melt pool} = \frac{T_m - T_o}{\sqrt{\frac{4\kappa L}{U}}} \quad (5.8)$$

Hence according to Fourier's 1st law, the conduction loss from the melt pool will be:

$$\dot{q}_{\text{cond}} = K_{\text{powder}} \left[\pi \left(\frac{b+d}{2} \right) L \right] \frac{T_m - T_o}{\sqrt{\frac{4\kappa L}{U}}} \quad (5.9)$$

Therefore, substituting for \dot{q}_{cond} and \dot{q}_{conv} in equation 5.6, the heat balance on the melt pool is:

$$\alpha P = \frac{\pi b d}{4} U [T_m - T_o] \rho C_p + K_{\text{powder}} \left[\pi \left(\frac{b+d}{2} \right) L \right] \frac{T_m - T_o}{\sqrt{\frac{4\kappa L}{U}}} \quad (5.10)$$

rearranging gives:

$$P = \left(\frac{\pi b d \rho C_p}{4\alpha} (T_m - T_o) \right) U + \left(K \frac{\pi(b+d)}{2\alpha} \sqrt{\frac{L}{4\kappa}} (T_m - T_o) \right) U^{1/2} \quad (5.11)$$

Hence, equation 5.11 has the general form (for constant pool length):

$$P = aU + bU^{1/2} \quad (5.12)$$

where, a, and b, and constants. Using the 150/75 process map for air, reasons for which will be given later, the values of a and b can be derived statistically by reading off several power and speed combinations along the melt instability boundary and solving versions of equation 5.8 simultaneously. However, on the maps there are in fact two instability boundaries, one depicting power and speed combinations which trigger melt fragmentation (c-c) and the other depicting power and speed combinations which trigger

melt pool balling (d-d), giving rise to a region of instability between them. It is likely that the melt fragmentation boundary is the more appropriate here since it indicates the first point of melt instability, though for comparative reasons both boundaries will be evaluated. The values of P and U acquired from the process map (see Figure 5.4) and calculated values of constants, a , and, b , are collected in Table 5.4. Figure 5.4 also includes superimposed traces showing the variation of P with U according to equation 5.12 and the calculated values of, a , and, b , given in Table 5.4.

In Figure 5.4, it is clear that the theory described above, accumulating in equation 5.11, appears to not be a too bad a fit with the 150/75 experimental results, particularly if the melt fragmentation boundary is used as a comparator. However, further examinations with different powder batches and the different atmospheric conditions reveal that the model deviates from the experimental results when comparing argon atmosphere results and the -38, and to some extent the 75/38, powder batch within an air atmosphere. Some qualitative observations may be relevant here. When a powder with a large particle size (300/150 and 150/57) is melted within an air atmosphere there are very few satellite particles attached to the periphery of the melt track. There is also little evidence of intact particles present within the solidified melt volume (see Figures 3.29 – 3.31, Chapter 3). This would suggest that the viscosity of the melt is low, further suggesting that the melt volume is governed predominantly by capillary forces i.e. surface tension forces and wetting constraints. As the particle size reduces, or the air atmosphere is changed for argon, a greater number of particles can be observed around the periphery of the melt and within the solidified melt volume. This is likely to have a significant impact on melt behaviour, thus perhaps explaining why the output from the model deviates at these conditions.

Table 5.4: Calculated values for constants, a, and, b, using experimental data obtained from the 150/75 process maps created using an air atmosphere.

Boundary	P(W)	U(mm/s)	$U^{1/2}$ (mm/s)	a	b
c-c	40	2	1.41	9.65	14.68
	100	6.5	2.54		
d-d	40	2	1.41	14.47	7.81
	90	5	2.24		

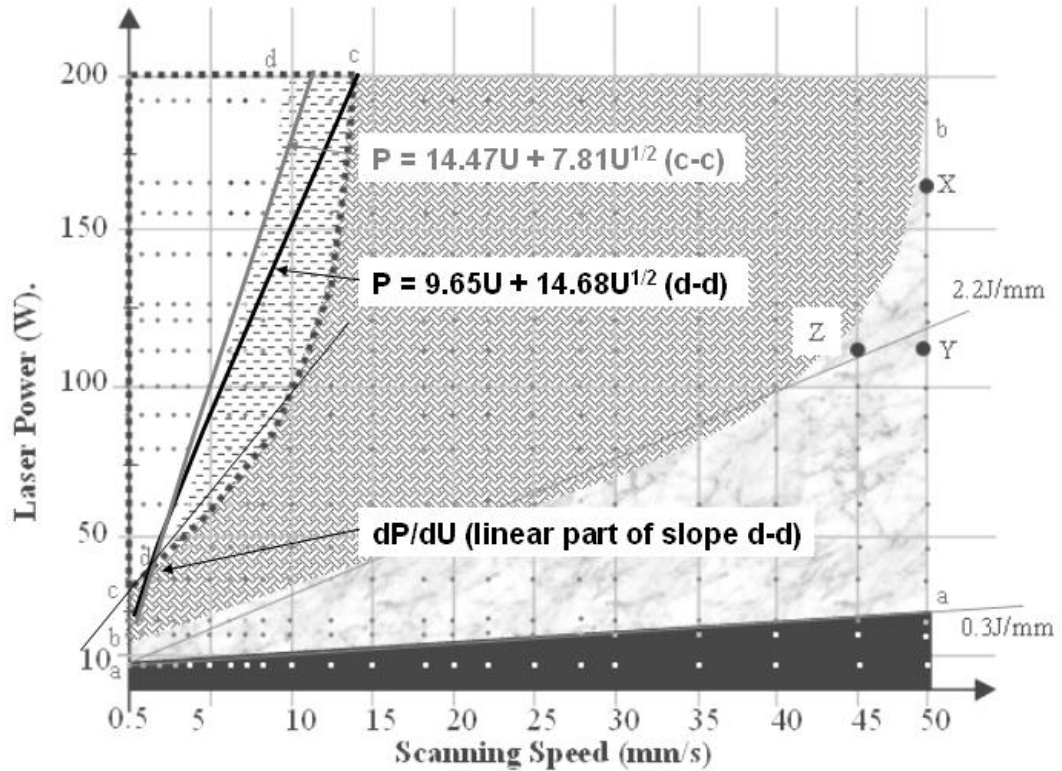


Figure 5.5: Process map for the 150/75 powder batch processed in air showing the calculated boundary when $a = 9.65$ and $b = 14.68$.

Further verification of the model. Using heat loss by convection term in equation 5.11, which describes the slope of the linear component of the model, a direct comparison can be made with the experimental results (see Figure 5.4).

$$\frac{dP}{dU} = \left(\frac{\pi b d \rho C_p}{4\alpha} (T_m - T_o) \right) \quad (5.13)$$

values for, b , and, d , have been obtained from the 150/75 constant width contour plot given in Figure 3.20, Chapter 3. Assuming the melt to be cylindrical, the values of both width and depth, calculated by mathematical interpolation, are 1.1mm at the d - d boundary; a value equal to the beam diameter. Taking reasonable values for all other material property data (collected in Table 5.5), and assuming a value for absorptivity, α , of 0.86 for high speed processing within an air atmosphere (see Table 5.1) the slope dP/dU can be calculated as follows:

$$\frac{dP}{dU} \left(\frac{J}{m} \right) = \frac{\pi 0.0011^2 \times 7900 \times 700}{4 \times 0.86} (1320) \quad (5.14)$$

$$\frac{dP}{dU} \left(\frac{J}{m} \right) = 8066 = 8.1J / mm \quad (5.15)$$

The experimental value of dP/dU taken from the slope of the linear section of the d - d boundary (see Figure 5.4) has a calculated value of 7.14J/mm, a value again not to dissimilar to the predicted value, giving a possible further indication that the theory developed in this thesis is not too far adrift. However, the value of absorptivity is only an estimate from mass per unit length calculations. This value is perhaps higher than expected (see Chapter 1, Section 1.7.3) and so should be treated with a little caution.

5.4 Multi-layers and Scale Up

Single layers were created from the 150/75 powder batch, based on understanding from the single track experiments. This batch was selected because of good dimensional stability and consistency of single tracks produced using it over a wide range of scanning conditions, particularly at high energy densities. However, some single layer qualitative observations for all powers is relevant here. Preliminary trials demonstrated that at low laser energy densities, suitable for partial melting (see Figure 5.2), all powers performed well, particular those with a smaller particle size fraction (75/38 and -38), creating flattened tracks with a high degree of dimensional consistency throughout the length of the track. This consistency transferred through to the single layers giving them a very flat and regular surface morphology. However, producing

layers at these conditions was not perused passed the preliminary stages because of poor interlayer bonding when constructing multi-layer builds (see later).

The surface morphology of fully melted layers produced from the 150/75 powder batch were generally flat at a scan spacing of 25% and 50% (percentage of beam overlap). At a scan spacing of 75%, the track layer surface morphology became undulating, particularly as the energy dropped. If a scan spacing, as a percentage of single track width is considered instead of as a percentage of beam diameter, undulating layers occurred at values greater than ~50%. At these conditions the melt track cross-section dimensions and overall melt behaviour was similar to the unrastered melt pool.

At high laser powers (>100W), the surface morphology of the layer changed slightly at the power and speed condition where single track cross sections changed from flattened to rounded. This change occurred only in the first scanned line of every layer, where the size of the first track was very much greater than all subsequent rastered tracks. This however could be compensated for by modifying the initial scan power and speed combinations to produce a flattened track at the start of each layer.

Multiple layers could only be produced over a limited range of scanning conditions, generally at higher energy densities, so that a fusion bond sufficient to preserve the integrity of a build during its removal from the powder bed could be maintained. The problem was the ineffectiveness of the powder spreading equipment which could only deposit a minimum layer thickness of 0.4mm. This proved to large to enable a good fusion bond between layers with a laser spot size of 1.1mm.

Overall, the behaviour, dimension, form and regularity of the melt pool remained consistent over scan lengths ranging from 15 – 100mm. Issues of size only became important during single layer production. Experiments showed that a scan length greater than 15mm would cause layer distortions, which generally increased in size with increasing scan length. Hence, large scale projects, as intended in the initial aims of the LastForm Program, would be impossible without some method in place to stop these distortions. However, due to the scale of planned tooling (0.5m and up) methods to control distortions would be extremely complex to implicate. Preheating a large power mass to a uniform temperature would be difficult. The processing time would be increased by several hours and there would also be a lengthy pre-heating stage between deposited layers. A more successful route is likely to be the anchoring of the first layer of a build to an underlying substrate, either a solid plate or a pin structure (see Chapter 4, Section 4.5.2). The problem with this method however, would be the anchoring of overhanging features. Either tool shape would have to be modified or

perhaps the PIN structure could be modified so that selected pins pushed their way up through the powder layer to reach overhanging features. It must also be considered that large area layers would have very large residual stresses and so the bonds of the layer to a substrate would have to be strong.

Another consideration would be the design of the powder spreading equipment. Spreading and levelling the powder in one operation requires a large heap of powder to be moves across the build area. If covering a very large area, a large mass of powder would be difficult to spread, and spread evenly.

5.5 Conclusions

In the absence of a constraining solid substrate, continuous fully melted tracks within an argon atmosphere form with a flattened section which sit at the power surface, a rounded section that sinks into the bed or as broken or balled segments which also sink. Behaviour repeatability is also high and so track states can be predicted with good accuracy.

Laser absorptivity changes significantly with scan speed, ranging from 0.1 at low speed (0.5mm/s) to 0.7 at high speed (>4mm/s). The change in absorptivity affects melt pool size considerably and has some bearing on melt pool aspect ratio. The absorptivity between powder batches changes marginally, but are insignificant when compared to the changes observed with speed increases.

Melt pool stability, repeatability and dimensional consistency along the melt reduces as powder bed particle size reduces. Powder falling into the melt volume affects the temperature history and viscosity of the melt making track balling or fragmentation difficult to model. When tracks are made at low energy densities which promote only partial melting then powder beds containing smaller particles produce more consistent tracks.

In the absence of a constraining solid substrate, continuous fully melted tracks within an air atmosphere form with a rounded cross-section that sink into the powder bed. The critical condition for melt instability in air occurred at the point when melt pool length divided by the melt pool width equated to 3 (π).

To avoid layer distortions, all layers produced using a room temperature powder bed required the scan length to be lower than 15mm. The behaviour of the melt during rastering is similar to the unrastered melt pool when the scan spacing (percentage of melt track width) exceeds 60%.

The density of multiple layer components was largely governed by the porosity between layers, which was affected by the layer thickness.

5.6 Future Work

A remaining question to be answered is what causes the change from a flattened to a rounded track cross-section. Work is required to resolve this issue. Examining and/or modelling the temperature profile around the laser beam at different speeds may lead to a more informed explanation.

Further investigations into powder spreading mechanisms are paramount to the success of multi-layer builds. Problems arise when trying to spread and level powder in one operation by pushing a heap of powder over the build area. A hopper mechanism which deposits powder from above while levelling maybe a better option but would need extensive investigation.

The pin structure used to anchor the first layer of a build was proven to work well for reducing layer displacements during powder spreading. However, the pins used (dress maker pins) were quite flexible and often melted. Improving rigidity and heat resisting properties of the pins may also reduce layer distortions at longer scan lengths.

REFERENCES

3D Systems: <http://www.3dsystems.com>

Abe, F. & Osakada, K. (1996a). *Fundamental study of laser rapid prototyping of metallic parts*. Int. J. Japan Soc. Vol. 30, No. 3.

Abe, F. & Osakada, K. (1996b). *A study of laser prototyping for direct manufacturing of dies from metallic powders*. Proc. 5th International Conference on Tech. Plasticity, Columbus. pp. 923 – 926.

Abe, F., Osakada, K. & Kitamura, Y. (2000). *Manufacturing of titanium parts for medical purposes by selective laser sintering*. Proc. International Conference on Rapid Prototyping. Tokyo, Japan. pp. 288-293.

Agarwala, M. K., Bourell, D. L. & Beaman, J. J. (1994). *Densification of selective laser sintered metal parts by hot isostatic pressing*. Proc. Solid Freeform Fabrication Symposium. University of Texas at Austin. Austin Texas. pp. 65-73.

Agarwala, M., Bourell, D., Beaman, J., Marcus, H. & Barlow, J. (1995a). *Direct selective laser sintering of metals*. Rapid Prototyping Journal. Vol.1, No. 1. MCB University Press. pp. 26-36.

Agarwala, M., Bourell, D., Beaman, J., Marcus, H. & Barlow, J. (1995b). *Post processing of selective laser sintered metal parts*. Rapid Prototyping Journal. Vol.1, No. 2. MCB University Press. pp. 36-44.

Barlow, G. (1970). *The flow of liquid metals*. PhD Thesis. The University of Leeds. Leeds, UK. pp.1-25.

Benda, J. A. (1994). *Temperature controlled selective laser sintering*. Proc. Solid Freeform Fabrication Symposium. University of Texas at Austin. Austin Texas. pp. 277-284.

Berjeza, N. A., Velikevitch, S.P., Mazhukin, V. I., Smurov, I. & Flamant, G. (1995). *Influence of temperature gradient to solidification velocity ratio on the structure transformation in pulsed and CW laser surface treatment*. Applied surface science 86. Elsevier Science Ltd. pp. 303-309.

Brody, H. D. (1986). *Segregation and structure in the weld zone*. Proc. Advances in Welding Science and Technology. Gatlinburg, Tennessee, USA. pp.83-91.

- Bunnell, D. E. Bourell, D. L. & Marcus, H. L. (1996). *Solid freeform fabrication of powders using laser processing*. Advances in Powder Metallurgy and Particulate Materials, Volume 4, Part 15. pp. 93-106.
- Burcham, C. L., Sankaran & S. Saville, D. A. (1998). *Electrohydrodynamic stability of a liquid bridge – THE ALEX EXPERIMENT*. 4th Microgravity fluid physics & transport phenomena conference. Cleveland, Ohio. pp579-583.
- Burgardt, P. & Heiple, C. A. (1986). *Interaction between impurities and welding parameters in determining GTA weld shape*. Welding J. 65, 150s-155s.
- Carslaw, H. S. and Jaeger, J. C. (1959). *Conduction of Heat in Solids*. Oxford University Press, UK.
- Carter, W. T. & Jones, M. G. (1993). *Direct Laser sintering of metals*. Proc. Solid Freeform Fabrication Symposium. University of Texas at Austin. Austin Texas. pp. 51-59.
- Childs, T. H. C. Berzins, M. Ryder, G. R. & Tontowi, A. (1998). *Selective laser sintering of an amorphous polymer – simulations and experiments*. Proceedings from the Institution of Mechanical Engineers, Vol. 213, Part B. IMechE. pp. 333-349.
- Cottrell, (Sir) A. (1995). *An introduction to powder metallurgy. Second Edition. The institute of materials*. The University Press Cambridge. UK. Chap 21.
- Crawford, R. H. (1993). *Computer Aspects of solid freeform fabrication: geometry, process control and design*. Proc. Solid Freeform Fabrication Symposium. University of Texas at Austin. Austin Texas. pp. 102-112.
- Das, S., Wohler, M., Beaman, J. J., & Bourell, D. L. (1997a). *Direct selective laser sintering of high performance metals for containerless HIP*. Advances in Powder Metallurgy and Particulate Materials, Volume 3, Part 21. pp. 67-78.
- Das, S., Wohler, M., Beaman, J. J., & Bourell, D. L. (1997b). *Direct selective laser sintering and containerless hot isostatic pressing for high performance metal components*. Proc. Solid Freeform Fabrication Symposium. University of Texas at Austin. Austin Texas. pp. 81-89.
- Das, S. Fuesting, T. P. Danyo, G. Brown, L. E. Beaman, J. J. Bourell, D. L. & Sargent, K. (1998a). *Direct laser fabrication of a gas turbine engine component-microstructure and properties. Part I*. Proc. Solid Freeform Fabrication Symposium. University of Texas at Austin. Austin Texas. pp. 1-9.

- Das, S. Fuesting, T. P. Danyo, G. Brown, L. E. Beaman, J. J. Bourell, D. L. & Sargent, K. (1998b). *Direct laser fabrication of a gas turbine engine component-microstructure and properties. Part II*. Proc. Solid Freeform Fabrication Symposium. University of Texas at Austin. Austin Texas. pp. 10-19.
- Das, S., Beaman, J. J., Wohlert, M. & Bourell, D. L. (1998c). *Direct laser freeform fabrication of high performance metal components*. Rapid Prototyping Journal. Vol. 4, No. 3. MCB University Press. pp. 112-117.
- Das, S., Wohlert, M., Beaman, J. J. & Bourell, D. L. (1998d). *Processing of titanium net shapes by SLS/HIP*. Proc. Solid Freeform Fabrication. Symposium. University of Texas at Austin. Austin Texas. pp. 469-478.
- Das, S. Wohlert, M. Beaman, J. J. Bourell, D. L. (1999). *Processing of titanium net shapes by SLS/HIP*. Materials and Design 20. Elsevier Science Ltd. pp. 115-121.
- Deckard, C. & Miller, D. (1995). *Improved energy delivery for selective laser sintering*. Proc. Solid Freeform Fabrication Symposium. University of Texas at Austin. Austin Texas. pp. 151-158.
- DTM Corporation (1996). The RapidTool LR Process using RapidSteel (LM-6000). DCN: 8001-10004, September.
- El-Batahgy, A. M. (1997). *Effect of laser welding parameters on fusion zone shape and solidification structure of austenitic stainless steel*. Materials letters 32. Elsevier Science. pp 155-163.
- Ergy, I., Langen, M. & Lohöfer, G. (1998). *Measurements of thermophysical properties of liquid metals relevant to Marangoni effects*. Phil. Trans. Royal. Soc. London. UK. pp 845-856.
- Fuesting, T. Brown, L. Das, S. Harlan, N. Lee, G. Beaman, J. J. Bourell, D. L. Barlow, J. W. & Sargent, K. (1996a). *Development of direct SLS processing for production of cermet composite turbine sealing components. Part I*. Proc. Solid Freeform Fabrication Symposium. University of Texas at Austin. Austin Texas. pp. 39-46.
- Fuesting, T. Brown, L. Das, S. Harlan, N. Lee, G. Beaman, J. J. Bourell, D. L. Barlow, J. W. & Sargent, K. (1996b). *Development of direct SLS processing for production of cermet composite turbine sealing components. Part II*. Proc. Solid Freeform Fabrication Symposium. University of Texas at Austin. Austin Texas. pp. 47-56.

- Gedda, H. (2000). *Technical Report: laser surface cladding – a literature review. Department of Materials and Manufacturing Engineering. Division of Materials Processing. Lulea University of Technology. Sweden.*
- German, R. M. (1985). *Liquid phase sintering*. Plenum Press, New York, NY.
- German, R. M. (1994). *Powder metallurgy science. Metal Powder Industries Federation, New Jersey. Chapters 2 and 7.*
- German, R. M. (1998). *Powder metallurgy of iron and steel*. John Wiley & Sons, USA. Chapter 6.
- Goetzel, C. G. (1949). *Treatise on powder metallurgy*. Volume 1. Interscience Publishers.
- Gratzke, U. Kapadia, P.D. Dowden, J. Kroos, J. and Simon, G. (1992). *Theoretical approach to the humping phenomenon in welding processes*. J Phys. D: Appl. Phys., 25 1640-1647.
- Heiple, C. R. & Roper, J. R. (1981). *Effect of minor element effects on GTAW fusion zone shape*. Trends in Welding Research in the US. Ed. David, S. A. ASM Metals Park (OH), USA. pp. 489-520.
- Heiple, C. R. & Roper, J. R. (1982). *Mechanism for minor element effect on GTA fusion zone geometry*. Welding J., 61. PP. 97s-102s.
- Heiple, C. R. & Roper, J. R. (1990). *Geometry of gas tungsten arc, gas metal arc and submerged arc weld beads*. Welding Theory and Practise. Eds. Olson, D.L. Dixon, R. Liby, A. L. Elsevier Science Publishers. pp. 1-33.
- Hu, C. & Baker, T. N. (1999). *A semi empirical model to predict the melt depth developed in overlapping laser tracks on a Ti-6Al-4V alloy*. Journal of Materials Processing Technology 94. Elsevier Science. pp116-122.
- Hügel, H. Dausinger, F. Bloehs, B. & Grunenwald, B. (1994). *Basic coupling mechanisms in laser surface treatment*. Laser Processing: Surface Treatment and Film Deposition. Proceedings of the NATO Advanced Study Institute on Laser Processing: Surface Treatment and Film Deposition. Kluwer Academic Press. Netherlands. pp. 21-46.
- Hügel, H. & Dausinger, F. (1996). *Interaction phenomena and energy coupling in laser surface treatment*. Eurolaser Academy. Institute für Strahlwerkzeuge, University of Stuttgart, Germany.

- Karapatis, N. P., Van Griethuysen, J. P. S & Glardon, R. (1998). *Direct rapid tooling: A review of current research*. Rapid Prototyping Journal, Vol. 4, No. 2. pp 77 – 89.
- Karapatis, N. P., Egger, G., Gyax, P. E. & Glardon, R. (1999). *Optimisation of powder layer density in selective laser sintering*. Proc. Solid Freeform Fabrication Symposium. University of Texas at Austin. Austin Texas. pp. 255-163.
- Kruth, J. P. Lue, M. C. & Nakagawa, T. (1998a). *Progress in additive manufacturing and rapid prototyping*. Annals of CIRP, Vol. 47/2. pp. 525-540.
- Kruth, J. P., Peeters, P., Smolderen, T., Bonse, J., Laoui, T. & Froyen, L (1998b). *The performance of CO₂ and Nd:YAG lasers in the selective laser sintering of steel-copper powders*. Proc. of the 7th Assises Européennes du prototypage Rapide, Paris. pp 15-27.
- Kurz, W. & Fisher, D. J.(1989). *Fundamentals of solidification*. Trans Tech Publications. Switzerland. Chapter 1.
- Lancaster, J. F. (1999). *Metallurgy of Welding*. Sixth Edition. Abingdon Publishing, UK. Chaps. 7 and 8.
- Lauwers, B. Kruth, J. P. Froyen, L. Bonse, J. & Morren, B. (1998). *Hard metal parts by SLS*. Prototyping Technology International. pp. 124-126.
- Li, Y & Ma, J. (1997). *Study on overlapping in the laser cladding process*. Journal of Surface Coatings Technology 90. Elsevier Science. pp1-5.
- Longtin, J. P. Kunio, H. & Ogawa, K. (1999). *Laser induced surface-tension-driven flows in liquids*. International Journal of Heat and Mass Transfer. Vol. 42. Elsevier Science Ltd. pp. 85-93.
- Manriquez-Fayre, A. & Bourell, D. L. (1990). *Selective laser sintering of binary metallic powder*. Proc. Solid Freeform Fabrication Symposium. University of Texas at Austin. Austin Texas. pp. 99-106.
- Manriquez-Fayre, A. & Bourell, D. L. (1991). *Selective laser sintering of Cu-Pd/Sn solder powders*. Proc. Solid Freeform Fabrication Symposium. University of Texas at Austin. Austin Texas. pp. 236-244.
- Marr-Lyon, M. J., Thiessen, D. B., Blonigen, F. J. & Marston, P. L. (1998). *Radiation and Maxwell stress stabilization of liquid bridges*. 4th Microgravity fluid physics & transport phenomena conference. Cleveland, Ohio. pp570-574.
- Marcus, H. L., Bourell, D. L., Manthiram, A., Beaman, J. J., Barlow, J. W. & Crawford, R. H. (1994). *Laser processed solid freeform fabrication*. Proc. of the 3rd

- European Conference on Rapid Prototyping and Manufacturing, University of Nottingham, UK. pp. 231-244.
- McLean, M. A. Shannon, G. J. & Steen, W. M. (1997). *Laser direct casting high nickel alloy components*. Advances in powder metallurgy and particulate materials. Vol. 3, part 21. pp. 3-15.
- Meiners, W., Over, C., Wissenbach, K. & Poprawe, R. (1999). *Direct generation of metal parts and tools by Selective Laser Powder Remelting (SLPR)*. Proc. Solid Freeform Fabrication Symposium. University of Texas at Austin. Austin Texas. pp. 655-661.
- Miller, D. Deckard, C. & Williams, J. (1997). *Variable beam size SLS workstation and enhanced SLS modelling*. Rapid Prototyping Journal, Vol. 3, No. 1. MCB University Press. pp. 4-11.
- Mills, K. C. and Keene, B. J. (1990). *Factors affecting variable weld penetration*. International Materials Review 35: 185–216.
- Mills, K. C., Keene, B. J., Brooks, R. F. and Shirali, A. (1998). *Marangoni effects in welding*. Marangoni and Interfacial Phenomena in Materials Processing. IOM Communications in association with The Royal Society. pp. 97-112.
- Minkoff, I. (1986). *Solidification and cast structure*. John Wiley & Sons Ltd. UK. Chaps. 9 and 10.
- Monypenny, J. H. G. (1954) *Stainless Iron and Steel*. Chapman and Hall, 3rd Edition, London. Chap 3.
- Niu, H. J. & Chang, I. T. H. (1998). *Liquid phase sintering of M3/S high speed steel by selective laser sintering*. Scripta Materialia, Vol. 39, No. 1. Elsevier Science Ltd. pp. 67-72.
- Niu, H. J. & Chang, I. T. H. (1999a). *Selective laser sintering of gas and water atomised high speed steel powders*. Scripta Materialia, Vol. 41, No. 1. Elsevier Science Ltd. pp. 25-30.
- Niu, H. J. & Chang, I. T. H. (1999b). *Instability of scan tracks of Selective Laser Sintering of high speed steel powder*. Scripta Materialia, Vol. 41, No. 11. Elsevier Science Ltd. pp. 1229-1234.
- Niu, H. J. & Chang, I. T. H. (2000). *Selective laser sintering of gas atomised M2 high speed steel powder*. Journal of Materials Science, No. 35. Kluwer Academic Publishers. pp. 31-38.

- O'Neill, W. Sutcliffe, C. J. Morgan, R. & Hon, K. K. B. (1998). *Investigation of short pulsed Nd:YAG laser interaction with stainless steel powder beds*. Proc. Solid Freeform Fabrication Symposium. University of Texas at Austin. pp. 147-159.
- O'Neill, W. Sutcliffe, C. J. Morgan, R. Landsborough, A. & Hon, K. K. B. (1999). *Investigation on multi-layer direct metal laser sintering of 316L stainless steel powder beds*. CIRP Annals, 48/1. pp. 151-154.
- Radstok, E. (1999). *Rapid tooling*. Rapid Prototyping Journal, Vol. 5, No. 4. MCB University Press. pp. 164-168.
- Ricci, E., Nanni, L. & Passerone, A. (1998). *Oxygen transport and dynamic surface tension of liquid metals*. Phil. Trans. Royal Soc. London. UK. pp857-870.
- Schiaffino, S. & Sonin, A. A. (1997). *Formation and Stability of Liquid Molten Beads on a Solid Surface*. J. Fluid Mech. Cambridge University Press. Vol 343, pp. 95-110.
- Sih, S. S., & Barlow, J. W. (1995). *Emissivity of Powder Beds*. Proc. Solid Freeform Fabrication Symposium. University of Texas at Austin. Austin Texas. pp. 402-408.
- Singer, O. (1997). *Singer's Lock*. Singer press, US. Chap. 8 (available online at www.singer.com/book.html).
- Steen, W. M. (1996). *Laser surface treatment. Laser Processing: Surface Treatment and Film Deposition*. Proceedings of the NATO Advanced Study Institute on Laser Processing. Kluwer Academic Press. Netherlands. pp. 1-19.
- Steen, W. M. (1998). *Laser material processing*. Second Edition. Springer- Verlag, London.
- Smugeresky, J. E. Keicher, D. M. & Romero, J. A. (1997). *Laser Engineered Net Shaping (LENS™) Process: Optimisation of Surface Finish and Microstructural Properties*. Advances in Powder Metallurgy and Particulate Materials, Volume 3, Part 21, 1997, pp 33 – 42.
- Stewart, T. D., Dalgarno, K W., Childs, T. H. C. & Perkins, J. (1998). *Strength of the DTM RapidSteel 1.0 Material*. Proc. Solid Freeform Fabrication Symposium. University of Texas at Austin. Austin Texas. pp. 443-449.
- Thummler, F. & Oberacker, R. (1993). *Introduction to powder metallurgy*. The Institute of Materials. London. Chap. 3.

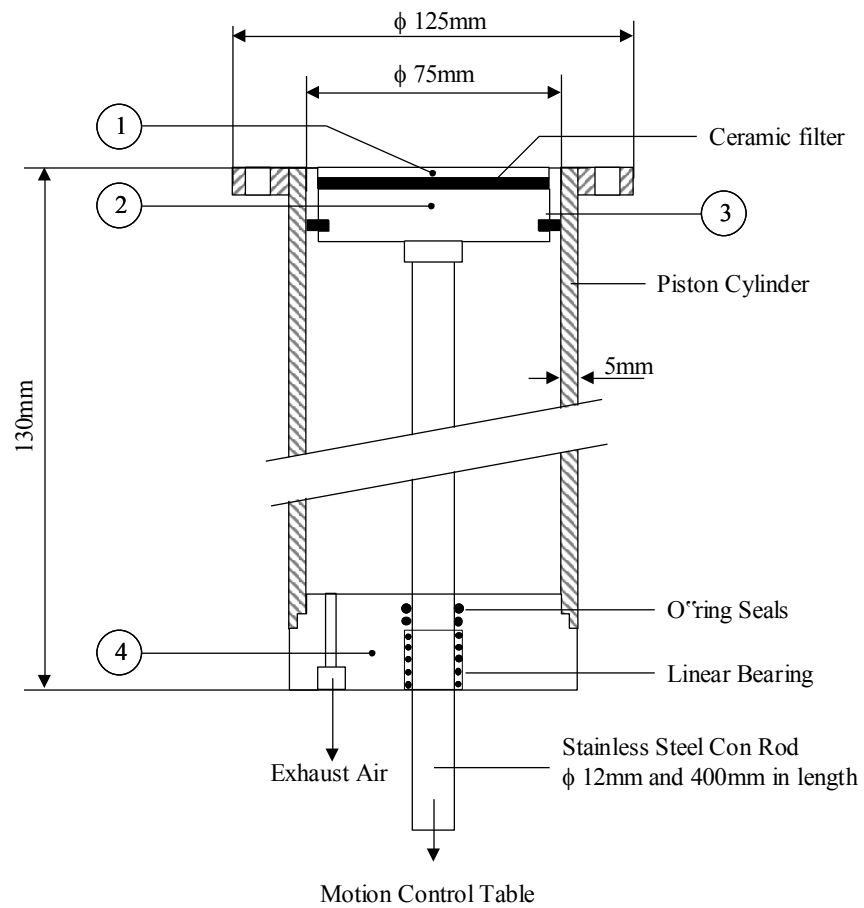
- Tolochko, N. K., Laoui, T., Khlopkov, Y. V., Mozzharov, S. E., Titov, V. I. & Ignatiev, M. B. (2000). *Absorptance of powder materials suitable for laser sintering*. Rapid Prototyping Journal, Vol. 6, No. 3. MCB University Press. pp. 155-160.
- Tsukerman, S. A. (1965). *Powder metallurgy*. Pergamon Press.
- Van der Schueren, B. & Kruth, J. P. (1995). *Powder deposition in selective metal powder sintering*. Rapid Prototyping Journal, Vol. 1, No. 3. MCB University Press. pp. 23-31.
- Wang, X. & Kruth, J.P. (2000). *Simulation of the Selective Laser Sintering Process*. Proc. of 5th Belgian National Congress on Theoretical and Applied Mechanics, Louvain-la-Neuve, Belgium, May 23-24.
- Welch, M. A. (1997). *Modelling of single-pass bead-on-plate steel welds*. PhD Thesis, The University of Leeds, UK.
- Wahab, M. A., Painter, M. J. & Davies, M. H. (1998). *The prediction of the temperature distribution and weld pool geometry in the gas metal arc welding process*. Journal of Materials Processing Technology 77. Elsevier Science. pp233-239.
- Wieters, K. P. Kieback, B. & Loschau, W. (1996). *Laser sintering of composite metal powders*. Advances in Powder Metallurgy and Particulate Materials, Volume 4, Part 15. pp. 77 – 91.
- Williams, J. D. & Deckard, C. R. (1998). *Advances in modelling the effects of selected parameters of the SLS process*. Rapid Prototyping Journal, Vol. 4, No. 2. MCB University Press. pp. 90-100.
- Wohlert, M., Das, S., Beaman, J. J. & Bourell, D. L. (1999). *Direct laser fabrication of high performance metal components via SLS/HIP*. Proc. Solid Freeform Fabrication Symposium. University of Texas at Austin. Austin Texas. pp. 281-288.
- Yevko, V., Park, C. B., Zak, G., Coyle, T. W. & Benhabib, B. (1998). *Cladding formation in laser-beam fusion of metal powder*. Rapid Prototyping Journal, Vol. 4, No. 4. MCB University Press. pp. 168-184.
- Zacharia, T. & David, S. A. (1993). *Heat and fluid flow in welding*. Mathematically modelling of weld phenomena. Ed. Cerjak, H. & Easterling, K. E. The Institute of Materials. pp. 3-23.
- Zong, G. Wu, Y. Tran, N. Lee, I. Bourell, D. L. Beaman, J. J. & Marcus, H. L. (1992). *Direct selective laser sintering of high temperature materials*. Proc. Solid

Freeform Fabrication Symposium. University of Texas at Austin. Austin Texas. pp.72-85.

Appendix A

Engineering Drawings and Powder Mixing Calculations

A1 Piston Head Assembly



Assembly Diagram

Figure A1: Assembly diagram for piston head and build cylinder.

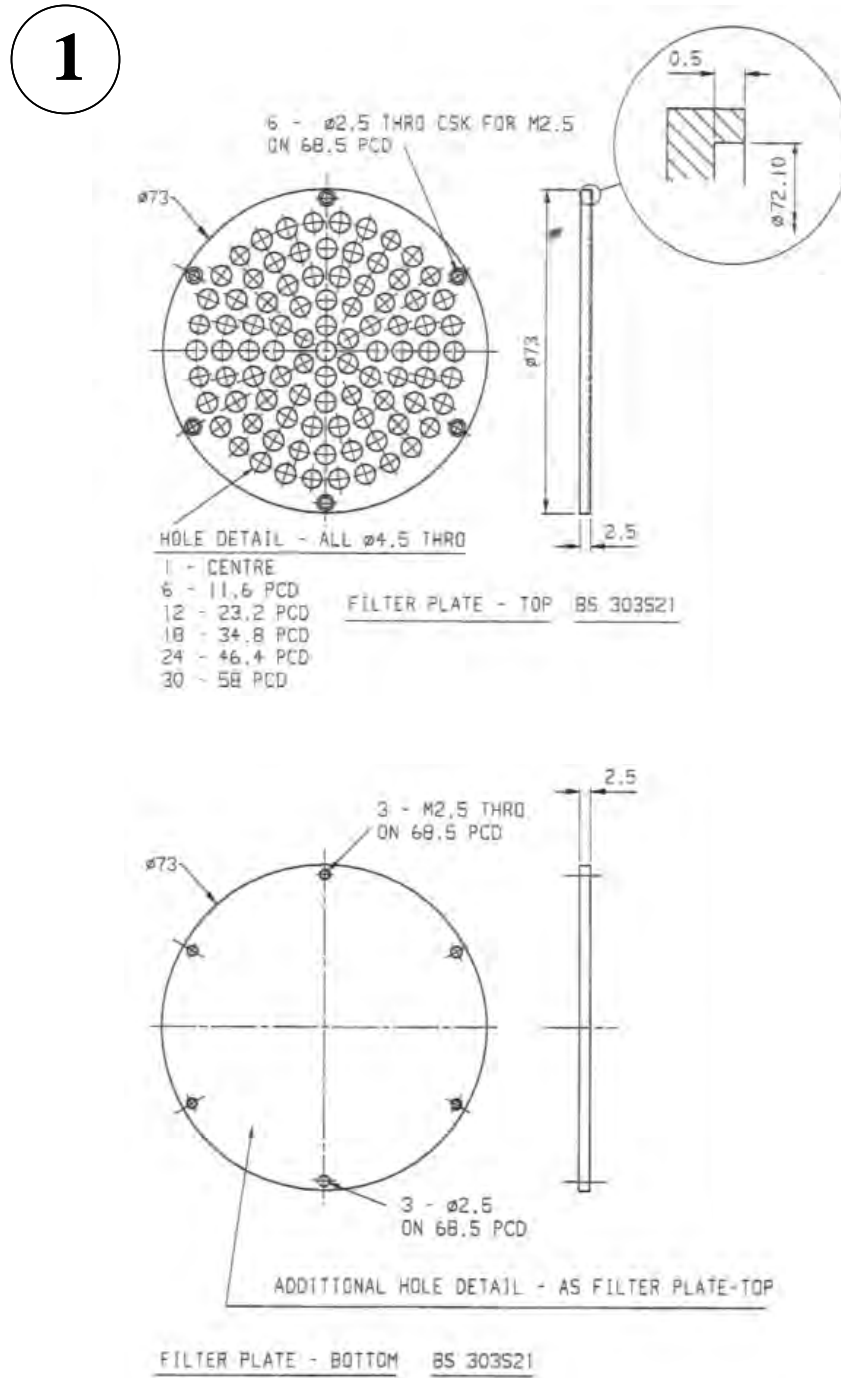


Figure A2: Perforated stainless steel plates used to sandwich ceramic filter.

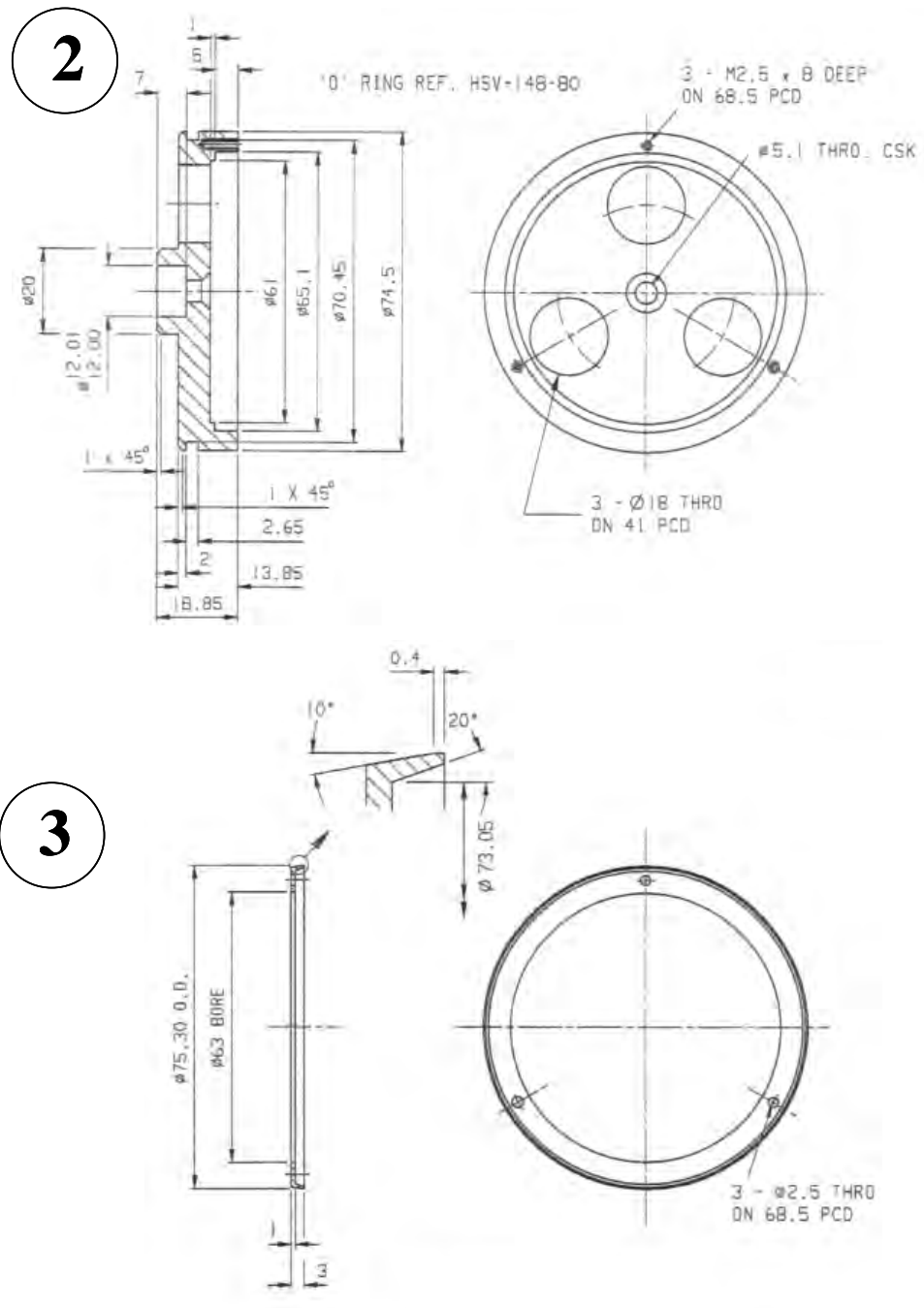


Figure A3: (1) Piston Head and (2) nylon wiper seal.

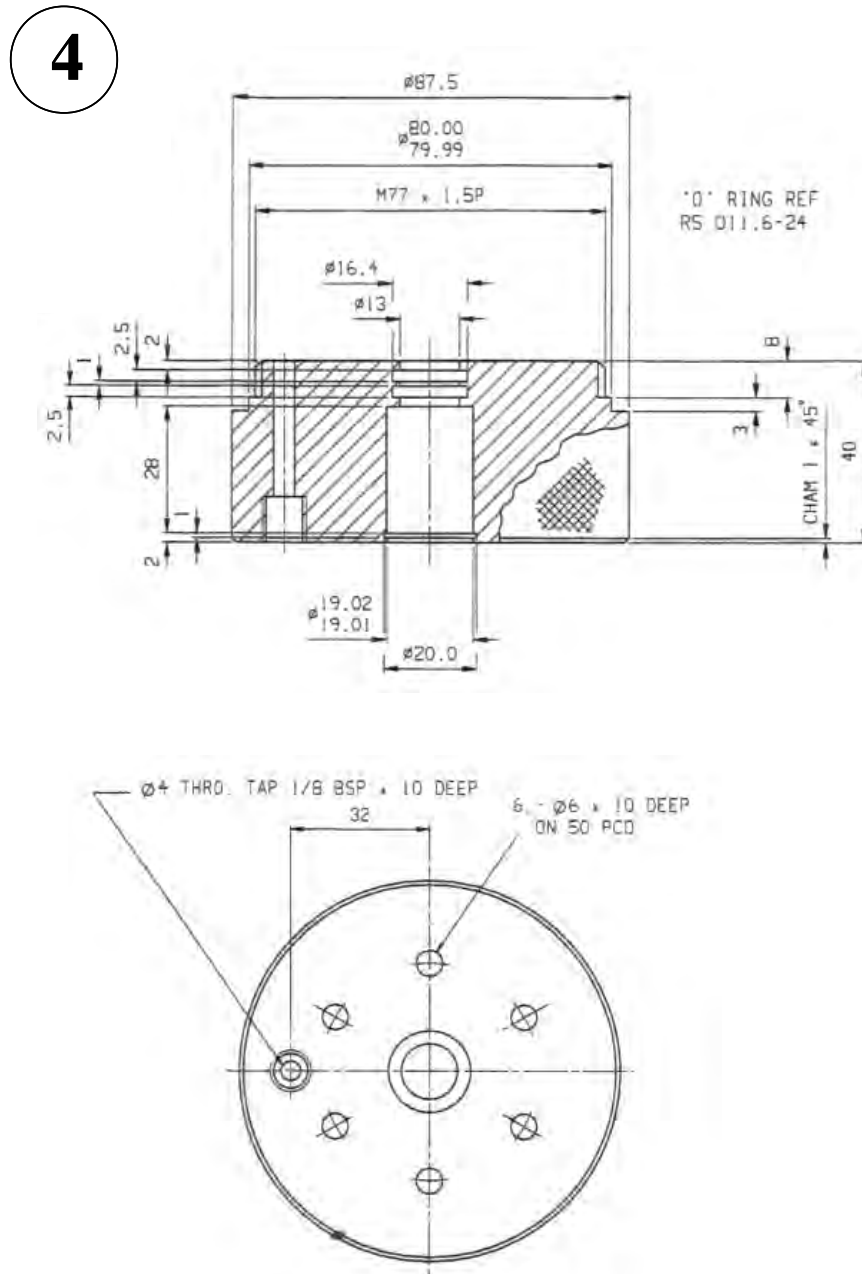


Figure A4: Piston assembly end cap.

A2 Pin Fixture Array

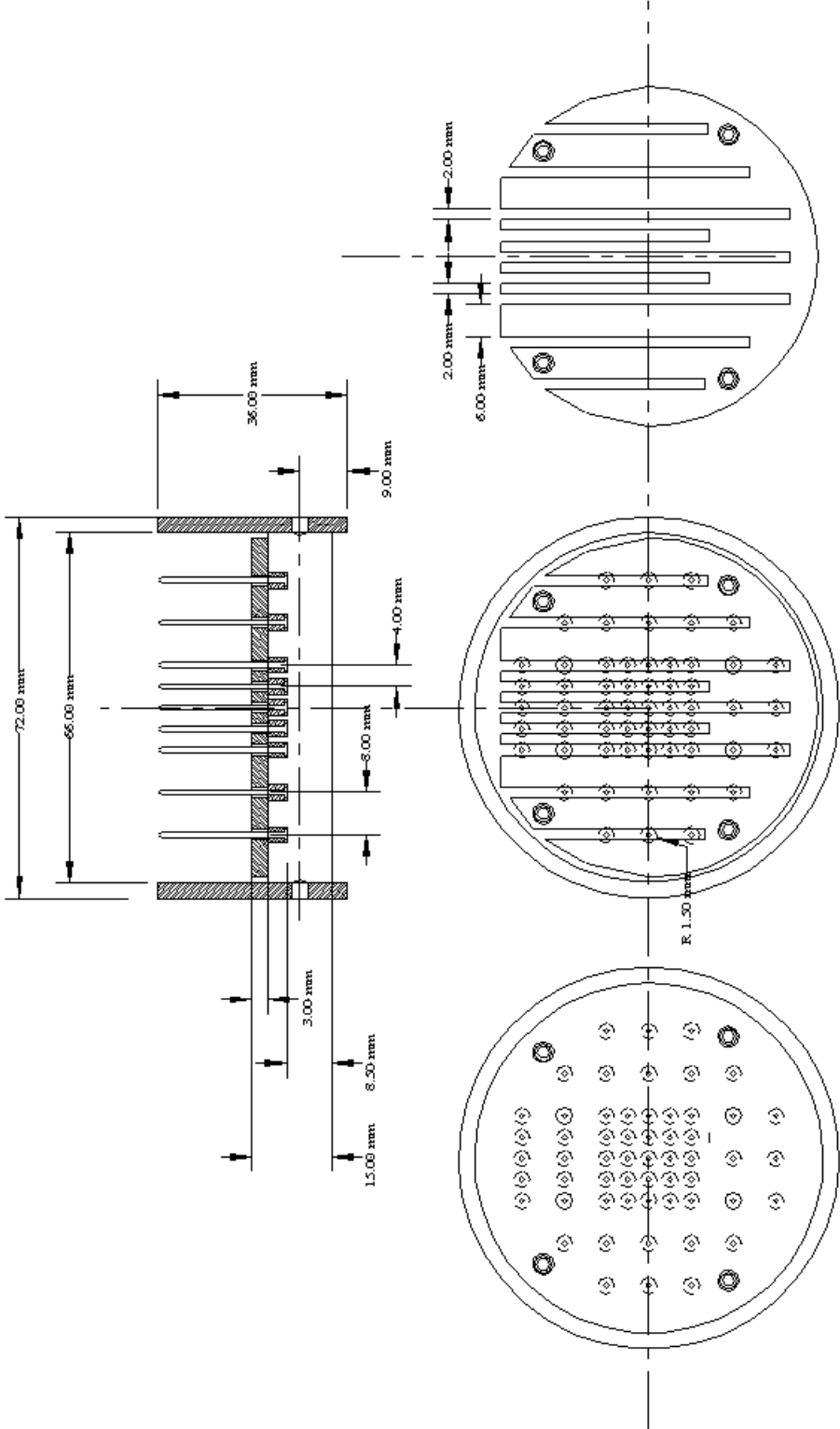


Figure A5: Engineering drawing of pin fixture array.

A3 Powder Mixer Assembly and Rotational Speed Calculations

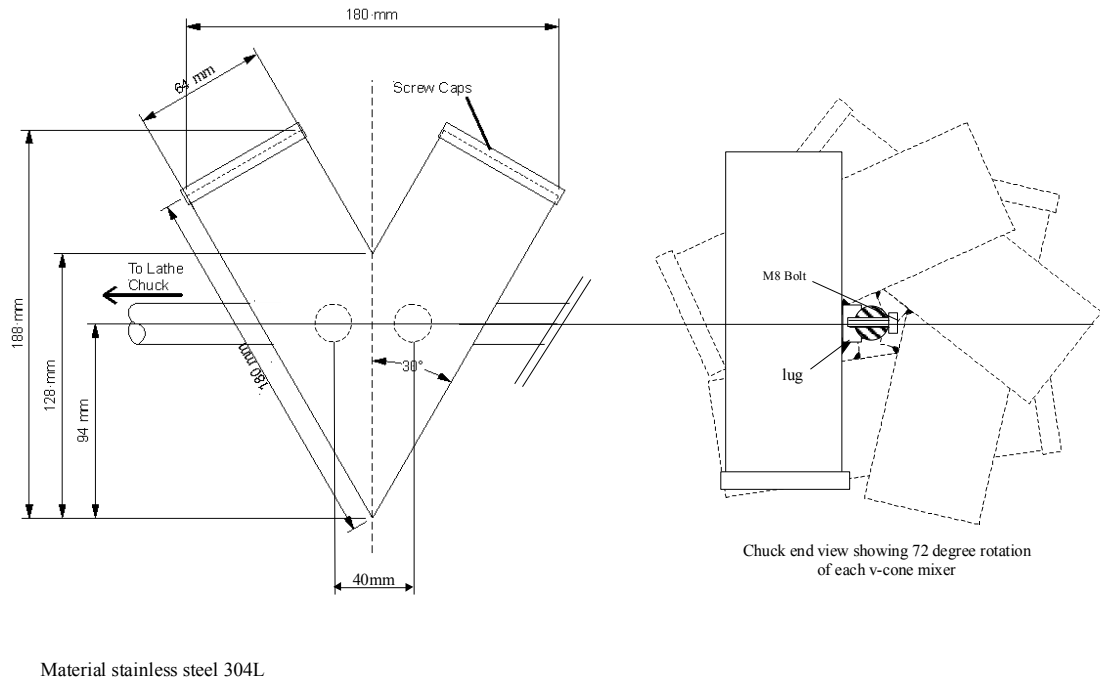
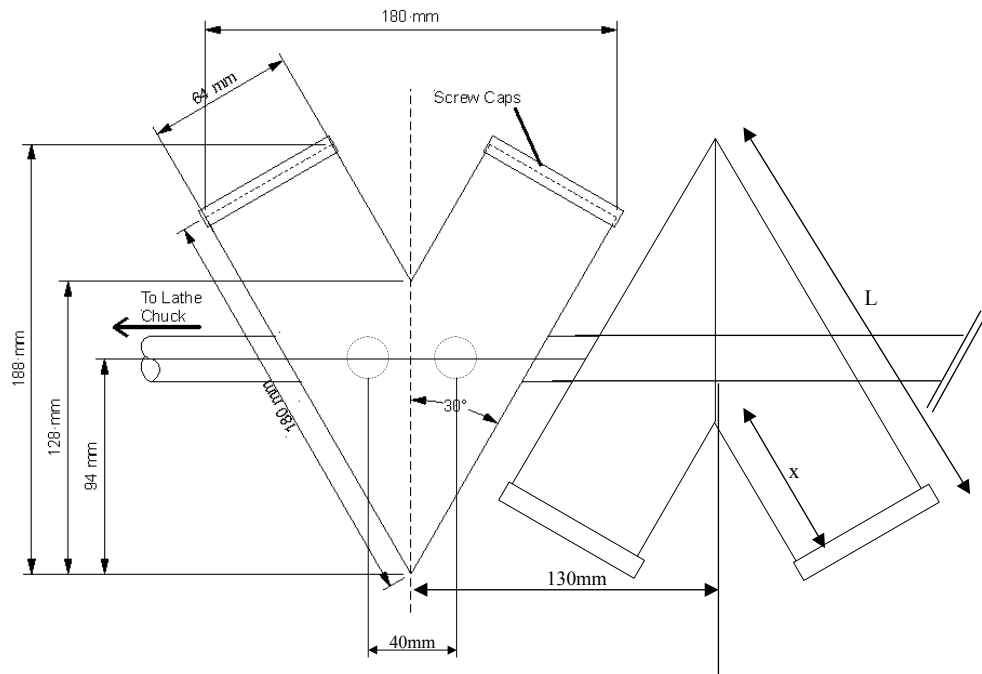


Figure A6: Engineering drawing of a V-cone mixer.



For clarity the second v-cone mixer is drawn at a rotation of 180° with respect to the first (the actual rotation required is 72°)

Figure A7: Engineering drawing showing coupling between two V-cone mixers.

Calculations 1 (powder volume):

The volume, V , of a V-cone mixer is:

$$V = \pi r^2 (L + x) = \pi(0.032)^2 (0.188 + 0.067) = 8.2 \times 10^{-4} \text{ m}^3 \quad (\text{A1})$$

at 40% capacity the required powder volume = $3.28 \times 10^{-4} \text{ m}^3$ (approx. 1.6Kg of powder)*

at 25% capacity the required powder volume = $2.05 \times 10^{-4} \text{ m}^3$ (approx. 1.0Kg of powder)*

at 20% capacity the required powder volume = $1.64 \times 10^{-4} \text{ m}^3$ (approx. 0.8Kg of powder)*

*Mass calculations were based on the average density of the powder in all batches tested. This was found to be 4750Kg/m³.

Calculations 2:

The critical rotational speed of a cylindrical mixer represents a balance between centrifugal and gravitational forces. At higher speeds mixing will not occur. At the critical rate N_c , the forces will balance. Let, d , be the rotational diameter of the mixer and, V , be the rotational velocity. The centrifugal force on a particle of mass, m , at the mixer wall is given as F_c ,

$$F_c = \frac{2mV^2}{d} \quad (\text{A2})$$

and the gravitational force is given as F_g ,

$$F_g = mg \quad (\text{A3})$$

and the velocity of the mixer, V , at the outer wall depends on the rotational speed, N , and the rotational diameter, d , such that;

$$V = \frac{\pi d N_c}{2} \quad (\text{A4})$$

At the critical condition $F_g = F_c$ giving;

$$mg = \frac{2m}{d} \left(\frac{\pi^2 d^2 N_c^2}{4} \right) \quad (\text{A5})$$

$$\text{or; } N_c = \sqrt{\left[\frac{2g}{\pi^2 d} \right]} \quad (\text{A6})$$

Therefore, the rotational speed of the mixer in rpm as a function of mixer diameter is;

$$N_c = \frac{84}{\sqrt{d}} \quad (\text{A7})$$

German, (1994) suggests that optimal mixing of a powder occurs when the mixer is run at approx. 75% of N_c , hence;

$$N_o = \frac{63}{\sqrt{d}} \quad (\text{A8})$$

where, N_o , is the optimal rotational speed (in RPM) and, d , is the diameter of the mixer (in meters) in a direction perpendicular to the direction of rotation. Assuming the eccentricity of the v-cone mixer assembly in Figures A6 and A7 is negligible (which is justified at such low speeds), the rotational speed can be calculated as follows;

$$N_o = \frac{63}{\sqrt{.188}} = 145\text{rpm} \quad (\text{A9})$$

The closest matching rotational speed of the Harrison lathe is 120rpm.

Appendix B

HPGL Source Code

B1 An example of HPGL code

The data is written in columns.

```

←. (;←.I81;;17:
←.N;19:
IN;SC;PU;PU;SP7;
LT;VS36
PU;
SP1;
PA-1530,1530;
PD;
PA1530,1530;
PU;
PA1530,1446;
PD;
PA-1530,1446;
PU;
PU;
PA-1530,1362;
PD;
PA1530,1362;
PU;
PU;
PA1530,1278;
PD;
PA-1530,1278;
PU;
PU;
PA-1530,1193;
PD;
PA1530,1193;
PU;
PU;
PA1530,1109;
PD;
PA-1530,1109;
PU;
PU;
PA-1530,1025;
PD;
PA1530,1025;
PU;
PU;
PA1530,941;
PD;
PA-1530,941;
PU;
PU;
PA-1530,857;
PD;
PA1530,857;
PU;
PA1530,773;
PD;
PA-1530,773;

PU;
PU;
PA-1530,688;
PD;
PA1530,688;
PU;
PU;
PA1530,604;
PD;
PA-1530,604;
PU;
PU;
PA-1530,520;
PD;
PA1530,520;
PU;
PU;
PA1530,436;
PD;
PA-1530,436;
PU;
PU;
PA-1530,352;
PD;
PA1530,352;
PU;
PU;
PA1530,268;
PD;
PA-1530,268;
PU;
PU;
PA-1530,184;
PD;
PA1530,184;
PU;
PU;
PA1530,99;
PD;
PA-1530,99;
PU;
PU;
PA-1530,15;
PD;
PA1530,15;
PU;
PU;
PA1530,-69;
PD;
PA-1530,-69;
PU;
PU;
PA-1530,-153;

PD;
PA1530,-153;
PU;
PU;
PA1530,-237;
PD;
PA-1530,-237;
PU;
PU;
PA-1530,-321;
PD;
PA1530,-321;
PU;
PU;
PA1530,-405;
PD;
PA-1530,-405;
PU;
PU;
PA-1530,-490;
PD;
PA1530,-490;
PU;
PU;
PA-1530,-574;
PD;
PA1530,-574;
PU;
PU;
PA-1530,-658;
PD;
PA1530,-658;
PU;
PU;
PA-1530,-742;
PD;
PA1530,-742;
PU;
PU;
PA-1530,-826;
PD;
PA1530,-826;
PU;
PU;
PA-1530,-910;
PD;
PA-1530,-910;
PU;
PU;
PA-1530,-995;
PD;
PA1530,-995;
PU;

```

The above source code creates a rastered layer of dimensions 20mm x 20mm and with a scan spacing of 0.5mm when created using the build zone.

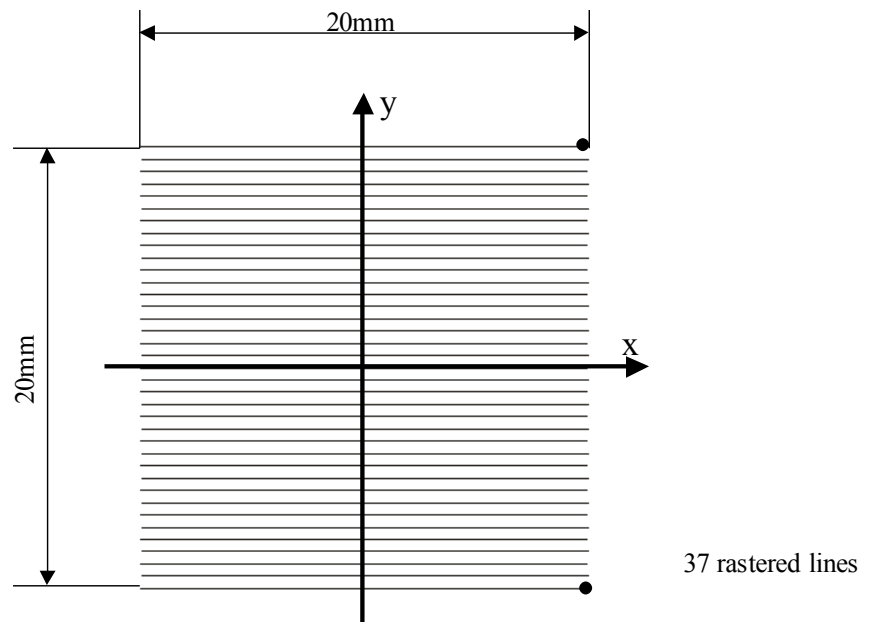


Figure B1: Raster layered generated by the above program.

Appendix C

Machine Parameter Settings and Beam Velocity Calculations

C1 Machine Parameter Settings

Table C1 displays a list of all the system level commands used during all scanning routines. Parameters 1-3, controlled the rotational speed of the mirror galvanometers and therefore determined the speed of scan of the laser across the powder surface. Look up tables were generated which listed the parameter combinations required to generate scan speeds in the range 0.5mm/s to 50mm/s (see Section C.2). All other parameters were kept at their default settings.

Table C2: System level commands

Number	Name	Units	Default	Range	Function
1	mark step size	LSB	50	0 to 65535	Micro-vector size for imprinting vectors.
2	jump step size	LSB	100	0 to 65535	Micro-vector size for non-imprinting vectors.
3	step period	μsec	168	0 to 65535	Micro-vector output rate.
4	mark delay	μsec	500	0 to 65535	End of imprinting vector delay.
5	jump delay	μsec	500	0 to 65535	End of non-imprinting vector delay.
6	stroke delay	μsec	500	0 to 65535	End of imprinting vector sequence delay.
7	laser on delay	μsec	500	0 to 65535	Turn on delay for laser at start of stroke.
8	laser off delay	μsec	500	0 to 65535	Turn off delay for laser at end of stroke.
9	q-switch width	μsec	500	0 to 65535	Pulse width of Q-switch pulse.
10	q-switch period	μsec	500	0 to 65535	Rep-rate of the Q-switch pulse train.
11	laser power	bytes	50	0 to 255	Digital output to control laser power.
12	autosegmentation		1	1 or 0	Enable/disable autosegmentation.
13	break angle	°(deg)	180	0 to 180	Included angle that breaks a stroke.
14	dither width	LSB	0	0 to 65535	Diameter of the circle described by the laser.
15	dither feed	LSB	0	0 to 65535	Distance between subsequent circles. Defines the rate of feed.
16	power change delay	msec	0	0 to 65535	Settle time for laser power supply.
17	FPS		0	1 or 0	Enable first pulse suppression if required.
18	message			0-235 characters	String of characters.

C2 Scan Speed Calculations

The velocity of the galvanometers, and therefore the scan speed was calculated using equation C1:

$$\text{Velocity} = \frac{\text{Distance}}{\text{Time}} \quad (\text{C1})$$

where:

Distance = step size = number of steps of the galvanometer per

DAC command [LSB]

Time = step period = time for one DAC command [μsecs]

Hence:

$$\text{Galvo velocity} = \frac{\text{Step Size}}{\text{Step Period}} \quad (\text{C2})$$

Since the maximum scan field is 65535 LSB the beam velocity (marking speed) at the powder surface is:

$$\text{marking speed (mm)} = \frac{\text{Step Size (LSB)}}{\text{Step Period } (\mu\text{secs})} \times \frac{\text{Field Size (mm)}}{65535} \times \frac{1 \mu\text{sec}}{1 \text{sec}} \quad (\text{C3})$$

Where the Field size is the maximum mark area. This had two values: 75mm for the build zone and 120mm for the build plate. Equation C3 was used to generate look-up tables for both build areas (see Tables C2/3). Both the Field size and the working distance (distance from the powder surface to the centre of the Y mirror) were set in the PC-MarkMT configuration file (default.asc) using PostGrid. PostGrid is General Scanning's software for the generation of grid correction files for scanning systems; the working distance had values of 680mm and 590mm for the build zone and the build plate respectively.

Table C3: Look-up table for mark speed selection (build zone).**Table C4:** Look-up table for mark speed selection (build tray).**C2**

Mark speed (mm/s)	Step Size (LSB)	Step period (micro secs)
0.5	20	42725
1	20	21363
2	20	10681
3	20	7121
4	20	5341
5	20	4273
6	20	3560
7	20	3052
8	20	2670
9	20	2374
10	20	2136
11	20	1942
12	20	1780
13	20	1643
14	20	1526
15	20	1424
16	20	1335
17	20	1257
18	20	1187
19	20	1124
20	20	1068
21	20	1017
22	20	971
23	20	929
24	20	890
25	20	855
26	20	822
27	20	791
28	20	763
29	20	737
30	20	712
31	20	689
32	20	668
33	20	647
34	20	628
35	20	610
36	20	593
37	20	577
38	20	562
39	20	548
40	20	534
41	20	521
42	20	509
43	20	497
44	20	486
45	20	475
46	20	464
47	20	455
48	20	445
49	20	436
50	20	427

C3

Mark speed (mm/s)	Step Size (LSB)	Step period (micro secs)
0.5	10	36622
1	20	36622
2	20	18311
3	20	12207
4	20	9155
5	20	7324
6	20	6104
7	20	5232
8	20	4578
9	20	4069
10	20	3662
11	20	3329
12	20	3052
13	20	2817
14	20	2616
15	20	2441
16	20	2289
17	20	2154
18	20	2035
19	20	1927
20	20	1831
21	20	1744
22	20	1665
23	20	1592
24	20	1526
25	20	1465
26	20	1409
27	20	1356
28	20	1308
29	20	1263
30	20	1221
31	20	1181
32	20	1144
33	20	1110
34	20	1077
35	20	1046
36	20	1017
37	20	990
38	20	964
39	20	939
40	20	916
41	20	893
42	20	872
43	20	852
44	20	832
45	20	814
46	20	796
47	20	779
48	20	763
49	20	747
50	20	732

Appendix D

Melt track Dimensional and Mass Measurements

D1 Air Atmosphere Results

D.1.1 300/150 Powder Batch

Table D 1

150/75 Air (Single tracks measured using callipers)									
Laser Power (W)	Scan Speed (mm/s)	Experiment 1		Experiment 2		Experiment 3		Average Width (mm)	Average Depth (mm)
		Width (mm)	Depth (mm)	Width (mm)	Depth (mm)	Width (mm)	Depth (mm)		
58	0.5	1.96	1.71	1.94	1.73	1.97	1.71	1.96	1.72
58	1	1.78	1.60	1.78	1.60	1.82	1.57	1.79	1.59
58	2	1.52	1.41	1.50	1.37	1.50	1.38	1.51	1.38
58	3	1.20	1.09	1.16	1.04	1.19	1.13	1.18	1.09
58	4	0.98	0.91	1.00	0.94	0.99	0.93	0.99	0.93

Table D 2

150/75 Air (Single tracks measured using callipers)									
Laser Power (W)	Scan Speed (mm/s)	Experiment 1		Experiment 2		Experiment 3		Average Width (mm)	Average Depth (mm)
		Width (mm)	Depth (mm)	Width (mm)	Depth (mm)	Width (mm)	Depth (mm)		
89	0.5	2.49	2.26	2.59	2.22	2.54	2.25	2.54	2.25
89	1	2.24	2.04	2.22	2.03	2.25	2.05	2.24	2.04
89	2	1.88	1.73	1.86	1.71	1.89	1.73	1.88	1.72
89	3	1.59	1.43	1.53	1.46	1.58	1.42	1.57	1.44
89	4	1.35	1.28	1.36	1.29	1.33	1.27	1.35	1.28
89	5	1.17	1.10	1.11	1.09	1.16	1.08	1.15	1.09
89	6	1.04	0.95	1.00	0.95	1.01	0.97	1.02	0.96

Table D 3

150/75 Air (Single tracks measured using callipers)									
Laser Power (W)	Scan Speed (mm/s)	Experiment 1		Experiment 2		Experiment 3		Average Width (mm)	Average Depth (mm)
		Width (mm)	Depth (mm)	Width (mm)	Depth (mm)	Width (mm)	Depth (mm)		
110	0.5	2.95	2.89	2.95	2.88	2.90	2.92	2.93	2.89
110	1	2.68	2.66	2.70	2.66	2.65	2.67	2.68	2.66
110	2	2.28	2.22	2.30	2.24	2.27	2.22	2.28	2.23
110	3	1.86	1.83	1.90	1.80	1.92	1.78	1.89	1.80
110	4	1.64	1.53	1.70	1.53	1.65	1.51	1.66	1.52
110	5	1.43	1.37	1.47	1.40	1.47	1.40	1.46	1.39
110	6	1.30	1.25	1.34	1.23	1.32	1.20	1.32	1.23
110	7	1.30	1.23	1.38	1.23	1.35	1.20	1.34	1.22

Table D 4

150/75 Air (Single tracks measured using callipers)									
Laser Power (W)	Scan Speed (mm/s)	Experiment 1		Experiment 2		Experiment 3		Average Width (mm)	Average Depth (mm)
		Width (mm)	Depth (mm)	Width (mm)	Depth (mm)	Width (mm)	Depth (mm)		
125	0.5	3.29	3.53	3.38	3.40	3.22	3.48	3.30	3.47
125	1	2.93	3.02	2.89	2.99	2.95	3.08	2.92	3.03
125	2	2.53	2.62	2.55	2.56	2.50	2.57	2.53	2.58
125	3	2.18	2.11	2.20	2.05	2.14	2.12	2.17	2.09
125	4	1.83	1.74	1.80	1.74	1.82	1.72	1.82	1.73
125	5	1.72	1.61	1.65	1.57	1.71	1.59	1.69	1.59
125	6	1.63	1.55	1.60	1.52	1.62	1.49	1.62	1.52
125	7	1.50	1.42	1.51	1.45	1.52	1.39	1.51	1.42
125	8	1.41	1.28	1.39	1.32	1.38	1.33	1.39	1.31

Table D 5

150/75 Air (Single tracks measured using callipers)									
Laser Power (W)	Scan Speed (mm/s)	Experiment 1		Experiment 2		Experiment 3		Average Width (mm)	Average Depth (mm)
		Width (mm)	Depth (mm)	Width (mm)	Depth (mm)	Width (mm)	Depth (mm)		
152	0.5	3.27	4.15	3.27	4.19	3.32	4.27	3.29	4.20
152	1	3.12	3.62	3.09	3.58	3.10	3.64	3.10	3.61
152	2	2.79	2.94	2.80	2.91	2.83	2.95	2.81	2.93
152	3	2.54	2.42	2.58	2.45	2.57	2.53	2.56	2.47
152	4	2.24	2.21	2.26	2.14	2.24	2.18	2.25	2.18
152	5	2.05	1.91	1.96	1.85	2.00	1.90	2.00	1.89
152	6	1.80	1.70	1.85	1.70	1.84	1.71	1.83	1.70
152	7	1.64	1.53	1.62	1.53	1.65	1.50	1.64	1.52
152	8	1.56	1.40	1.57	1.46	1.59	1.49	1.57	1.45

Table D 6

150/75 Air (Single tracks measured using callipers)									
Laser Power (W)	Scan Speed (mm/s)	Experiment 1		Experiment 2		Experiment 3		Average Width (mm)	Average Depth (mm)
		Width (mm)	Depth (mm)	Width (mm)	Depth (mm)	Width (mm)	Depth (mm)		
189	0.5	3.42	4.14	3.47	4.17	3.33	4.05	3.41	4.12
189	1	3.31	3.52	3.35	3.56	3.34	3.53	3.33	3.54
189	2	3.14	3.21	3.18	3.22	3.16	3.22	3.16	3.22
189	3	2.88	2.87	2.91	2.88	2.91	2.83	2.90	2.86
189	4	2.58	2.54	2.54	2.50	2.58	2.52	2.57	2.52
189	5	2.24	2.12	2.18	2.16	2.23	2.22	2.22	2.17
189	6	2.02	1.93	2.00	1.93	2.03	1.95	2.02	1.94
189	7	1.82	1.70	1.80	1.71	1.80	1.74	1.81	1.72
189	8	1.64	1.50	1.61	1.55	1.62	1.50	1.62	1.52

D1.2 150/75 Powder Batch

Table D 7

150/75 Air (Single tracks measured using callipers)											
Laser Power (W)	Scan Speed (mm/s)	Experiment 1		Experiment 2		Experiment 3		Average Width (mm)	Average Depth (mm)	Track Length (mm)	Track Mass (grams)
		Width (mm)	Depth (mm)	Width (mm)	Depth (mm)	Width (mm)	Depth (mm)				
58	0.5	2.27	2.28	2.29	2.30	2.27	2.29	2.28	2.29	15.82	0.5368
58	1	2.06	2.07	2.05	2.03	2.04	2.03	2.05	2.04	25.34	0.6512
58	2	1.80	1.77	1.82	1.77	1.81	1.78	1.81	1.77	27.20	0.5343
58	3	1.46	1.38	1.43	1.40	1.45	1.37	1.45	1.38	27.51	0.5307
58	4	1.16	1.04	1.11	1.10	1.13	1.12	1.13	1.09	26.80	0.2679

Table D 8

150/75 Air (Single tracks measured using callipers)											
Laser Power (W)	Scan Speed (mm/s)	Experiment 1		Experiment 2		Experiment 3		Average Width (mm)	Average Depth (mm)	Track Length (mm)	Track Mass (grams)
		Width (mm)	Depth (mm)	Width (mm)	Depth (mm)	Width (mm)	Depth (mm)				
89	0.5	2.49	2.64	2.52	2.60	2.43	2.56	2.48	2.60	27.29	1.3323
89	1	2.41	2.48	2.33	2.47	2.32	2.46	2.35	2.47	27.57	1.0545
89	2	2.11	2.15	2.04	2.18	2.07	2.13	2.07	2.15	26.90	0.7111
89	3	1.81	1.75	1.71	1.73	1.74	1.72	1.75	1.73	26.58	0.5942
89	4	1.46	1.35	1.42	1.39	1.35	1.37	1.41	1.37	27.18	0.4259
89	5	1.07	1.05	1.10	1.07	1.12	1.03	1.10	1.05	27.02	0.3274

Table D 9

150/75 Air (Single tracks measured using callipers)											
Laser Power (W)	Scan Speed (mm/s)	Experiment 1		Experiment 2		Experiment 3		Average Width (mm)	Average Depth (mm)	Track Length (mm)	Track Mass (grams)
		Width (mm)	Depth (mm)	Width (mm)	Depth (mm)	Width (mm)	Depth (mm)				
110	0.5	2.75	2.97	2.70	3.00	2.77	3.01	2.74	2.99	28.01	1.5381
110	1	2.60	2.80	2.64	2.82	2.61	2.78	2.62	2.80	24.55	0.9911
110	2	2.42	2.50	2.40	2.52	2.41	2.48	2.41	2.50	26.80	0.8762
110	3	2.08	2.19	2.17	2.15	2.14	2.15	2.13	2.16	26.97	0.7380
110	4	1.76	1.73	1.75	1.75	1.73	1.74	1.75	1.74	27.31	0.5432
110	5	1.50	1.48	1.52	1.46	1.49	1.46	1.50	1.47	27.28	0.4205
110	6	1.26	1.25	1.30	1.21	1.34	1.24	1.30	1.23	26.82	0.3348

Table D 10

150/75 Air (Single tracks measured using callipers)											
Laser Power (W)	Scan Speed (mm/s)	Experiment 1		Experiment 2		Experiment 3		Average Width (mm)	Average Depth (mm)	Track Length (mm)	Track Mass (grams)
		Width (mm)	Depth (mm)	Width (mm)	Depth (mm)	Width (mm)	Depth (mm)				
125	0.5	2.82	3.07	2.85	3.11	2.79	3.09	2.82	3.09	18.46	0.9971
125	1	2.71	2.92	2.74	2.91	2.75	2.89	2.73	2.91	17.30	0.7724
125	2	2.52	2.67	2.56	2.63	2.55	2.61	2.54	2.64	27.15	0.9931
125	3	2.24	2.32	2.28	2.36	2.26	2.27	2.26	2.32	27.13	0.8124
125	4	1.93	1.93	1.95	1.97	1.97	1.97	1.95	1.96	27.19	0.5761
125	5	1.60	1.59	1.60	1.60	1.64	1.57	1.61	1.59	27.20	0.4444
125	6	1.34	1.33	1.37	1.30	1.38	1.27	1.36	1.30	27.49	0.3698
125	7	1.11	1.07	1.15	1.09	1.13	1.08	1.13	1.08	27.26	0.3138

Table D 11

150/75 Air (Single tracks measured using callipers)											
Laser Power (W)	Scan Speed (mm/s)	Experiment 1		Experiment 2		Experiment 3		Average Width (mm)	Average Depth (mm)	Track Length (mm)	Track Mass (grams)
		Width (mm)	Depth (mm)	Width (mm)	Depth (mm)	Width (mm)	Depth (mm)				
152	0.5	3.05	3.60	3.07	3.55	3.04	3.64	3.05	3.60	28.63	1.9841
152	1	2.83	3.16	2.83	3.18	2.80	3.14	2.82	3.16	28.38	1.6664
152	2	2.91	3.00	2.95	3.03	2.90	3.04	2.92	3.02	27.84	1.3212
152	3	2.52	2.60	2.46	2.55	2.58	2.52	2.52	2.56	27.13	0.9815
152	4	2.25	2.25	2.21	2.21	2.24	2.28	2.23	2.25	26.95	0.7026
152	5	1.93	1.89	1.96	1.89	1.99	1.95	1.96	1.91	26.98	0.5480
152	6	1.66	1.57	1.64	1.58	1.66	1.61	1.65	1.59	27.28	0.4553
152	7	1.45	1.36	1.37	1.35	1.45	1.41	1.42	1.37	27.43	0.3809
152	8	1.17	1.10	1.21	1.10	1.17	1.11	1.18	1.10	27.09	0.3341

Table D 12

150/75 Air (Single tracks measured using callipers)											
Laser Power (W)	Scan Speed (mm/s)	Experiment 1		Experiment 2		Experiment 3		Average Width (mm)	Average Depth (mm)	Track Length (mm)	Track Mass (grams)
		Width (mm)	Depth (mm)	Width (mm)	Depth (mm)	Width (mm)	Depth (mm)				
189	0.5	3.21	3.90	3.22	3.85	3.21	3.89	3.21	3.88	29.08	1.9074
189	1	3.14	3.60	3.18	3.64	3.17	3.69	3.16	3.64	28.24	1.6652
189	2	3.11	3.24	3.12	3.20	3.07	3.22	3.10	3.22	28.39	1.4584
189	3	2.66	2.69	2.72	2.65	2.60	2.70	2.66	2.68	28.02	1.3905
189	4	2.40	2.34	2.42	2.28	2.32	2.29	2.38	2.30	28.05	0.9245
189	5	2.04	1.99	2.11	1.98	2.07	2.03	2.07	2.00	27.94	0.8114
189	6	1.78	1.76	1.78	1.77	1.80	1.78	1.79	1.77	27.92	0.5910
189	7	1.60	1.50	1.55	1.51	1.64	1.51	1.60	1.51	28.06	0.4630
189	8	1.39	1.34	1.39	1.30	1.34	1.39	1.37	1.34	27.76	0.4211
189	10	1.08	1.07	1.02	1.03	1.08	1.05	1.06	1.05	27.16	0.3425

D1.3 75/38 Powder Batch

Table D 13

75/38 Air (Single tracks measured using callipers)											
Laser Power (W)	Scan Speed (mm/s)	Experiment 1		Experiment 2		Experiment 3		Average Width (mm)	Average Depth (mm)	Track Length (mm)	Track Mass (grams)
		Width (mm)	Depth (mm)	Width (mm)	Depth (mm)	Width (mm)	Depth (mm)				
58	0.5	2.21	2.26	2.27	2.29	2.17	2.26	2.22	2.27	29.08	0.9074
58	1	2.03	2.09	2.00	2.08	2.00	2.08	2.01	2.08	28.24	0.6652
58	2	1.73	1.82	1.77	1.80	1.73	1.83	1.74	1.82	28.39	0.4584
58	3	1.52	1.60	1.60	1.62	1.57	1.60	1.56	1.61	28.02	0.3905
58	4	1.25	1.33	1.28	1.31	1.23	1.29	1.25	1.31	28.05	0.2944
58	5	1.07	1.10	1.07	1.12	1.05	1.10	1.06	1.11	27.94	0.2291
58	6	0.93	0.93	0.91	0.90	0.92	0.95	0.92	0.93	27.92	0.1830

Table D 14

75/38 Air (Single tracks measured using callipers)											
Laser Power (W)	Scan Speed (mm/s)	Experiment 1		Experiment 2		Experiment 3		Average Width (mm)	Average Depth (mm)	Track Length (mm)	Track Mass (grams)
		Width (mm)	Depth (mm)	Width (mm)	Depth (mm)	Width (mm)	Depth (mm)				
89	0.5	2.74	2.83	2.77	2.87	2.81	2.81	2.77	2.84	29.84	1.3263
89	1	2.54	2.65	2.55	2.67	2.54	2.66	2.54	2.66	28.55	1.1999
89	2	2.33	2.41	2.38	2.38	2.36	2.44	2.36	2.41	29.08	0.8358
89	3	2.05	2.04	1.99	2.01	1.99	2.02	2.01	2.02	28.13	0.6487
89	4	1.76	1.74	1.7	1.78	1.79	1.73	1.75	1.75	27.86	0.4369
89	5	1.61	1.57	1.57	1.59	1.63	1.62	1.60	1.59	27.88	0.3419
89	6	1.46	1.48	1.44	1.49	1.47	1.52	1.46	1.50	27.84	0.3031
89	7	1.37	1.34	1.33	1.4	1.38	1.38	1.36	1.37	27.85	0.2544

Table D 15

75/38 Air (Single tracks measured using callipers)											
Laser Power (W)	Scan Speed (mm/s)	Experiment 1		Experiment 2		Experiment 3		Average Width (mm)	Average Depth (mm)	Track Length (mm)	Track Mass (grams)
		Width (mm)	Depth (mm)	Width (mm)	Depth (mm)	Width (mm)	Depth (mm)				
110	0.5	2.98	3.11	2.97	3.16	3.07	3.18	3.01	3.15	29.37	1.8033
110	1	2.76	2.98	2.84	2.94	2.87	3.02	2.82	2.98	13.20	0.7860
110	2	2.50	2.75	2.57	2.83	2.62	2.80	2.56	2.79	28.34	1.3290
110	3	2.28	2.38	2.27	2.43	2.33	2.42	2.29	2.41	27.46	0.8854
110	4	2.18	2.18	2.16	2.22	2.14	2.14	2.16	2.18	27.86	0.5944
110	5	2.01	1.93	1.89	2.02	1.95	1.98	1.95	1.98	27.69	0.4625
110	6	1.92	1.76	1.80	1.81	1.86	1.79	1.86	1.79	28.01	0.3735
110	7	1.76	1.68	1.73	1.61	1.69	1.66	1.73	1.65	27.47	0.3116
110	8	1.60	1.52	1.57	1.57	1.54	1.56	1.57	1.55	27.83	0.2684

Table D 16

75/38 Air (Single tracks measured using callipers)											
Laser Power (W)	Scan Speed (mm/s)	Experiment 1		Experiment 2		Experiment 3		Average Width (mm)	Average Depth (mm)	Track Length (mm)	Track Mass (grams)
		Width (mm)	Depth (mm)	Width (mm)	Depth (mm)	Width (mm)	Depth (mm)				
125	0.5	3.08	3.36	3.07	3.42	3	3.33	3.05	3.37	30.06	1.9129
125	1	2.94	3.22	2.91	3.14	2.85	3.16	2.90	3.17	28.73	2.0743
125	2	2.55	3.01	2.58	2.92	2.60	2.99	2.58	2.97	21.11	0.9975
125	3	2.34	2.39	2.25	2.47	2.31	2.42	2.30	2.43	28.10	1.0463
125	4	2.04	2.21	2.10	2.24	2.12	2.17	2.09	2.21	27.91	0.7581
125	5	1.99	2.01	2.07	2.07	2.05	1.98	2.04	2.02	27.68	0.5920
125	6	1.92	1.85	1.81	1.77	1.88	1.83	1.87	1.82	27.64	0.5021
125	7	1.70	1.66	1.74	1.62	1.68	1.68	1.71	1.65	27.36	0.4270
125	8	1.50	1.51	1.54	1.49	1.47	1.55	1.50	1.52	27.19	0.3823

Table D 17

75/38 Air (Single tracks measured using callipers)											
Laser Power (W)	Scan Speed (mm/s)	Experiment 1		Experiment 2		Experiment 3		Average Width (mm)	Average Depth (mm)	Track Length (mm)	Track Mass (grams)
		Width (mm)	Depth (mm)	Width (mm)	Depth (mm)	Width (mm)	Depth (mm)				
152	0.5	3.13	3.74	3.2	3.81	3.1	3.79	3.14	3.78	29.66	2.1700
152	1	2.95	3.55	2.99	3.6	3.03	3.54	2.99	3.56	30.54	2.2577
152	2	2.71	3.14	2.74	3.1	2.7	3.11	2.72	3.12	27.15	1.7760
152	3	2.49	2.54	2.54	2.6	2.43	2.55	2.49	2.56	27.88	1.3385
152	4	2.12	2.16	2.12	2.29	2.14	2.25	2.13	2.23	27.97	0.9421
152	5	1.98	2.01	1.93	1.96	1.96	2.01	1.96	1.99	27.71	0.7520
152	6	1.74	1.79	1.76	1.75	1.77	1.74	1.76	1.76	27.64	0.6327
152	7	1.65	1.57	1.61	1.53	1.61	1.61	1.62	1.57	27.43	0.5518
152	8	1.52	1.43	1.53	1.5	1.55	1.46	1.53	1.46	27.22	0.4911

Table D 18

75/38 Air (Single tracks measured using callipers)											
Laser Power (W)	Scan Speed (mm/s)	Experiment 1		Experiment 2		Experiment 3		Average Width (mm)	Average Depth (mm)	Track Length (mm)	Track Mass (grams)
		Width (mm)	Depth (mm)	Width (mm)	Depth (mm)	Width (mm)	Depth (mm)				
189	0.5	3.36	4.37	3.39	4.28	3.4	4.26	3.38	4.30	29.99	2.5459
189	1	3.23	4.11	3.27	4.1	3.27	4.04	3.26	4.08	30.61	2.4256
189	2	2.93	3.48	2.99	3.48	2.93	3.46	2.95	3.47	27.45	2.1206
189	3	2.71	2.84	2.74	2.86	2.67	2.87	2.71	2.86	28.27	1.5705
189	4	2.35	2.42	2.39	2.38	2.3	2.35	2.35	2.38	27.76	1.1564
189	5	2.02	2.04	2.03	2.06	2	1.97	2.02	2.02	27.43	0.8869
189	6	1.82	1.8	1.77	1.85	1.86	1.75	1.82	1.80	27.28	0.7265
189	7	1.63	1.66	1.66	1.59	1.66	1.59	1.65	1.61	27.28	0.6213
189	8	1.57	1.51	1.57	1.45	1.53	1.55	1.56	1.50	27.26	0.5617

D1.4 38 Powder Batch**Table D 19**

38 Air (Single tracks measured using callipers)									
Laser Power (W)	Scan Speed (mm/s)	Experiment 1		Experiment 2		Experiment 3		Average Width (mm)	Average Depth (mm)
		Width (mm)	Depth (mm)	Width (mm)	Depth (mm)	Width (mm)	Depth (mm)		
32	3	1.23	1.42	1.25	1.36	1.21	1.40	1.23	1.39
32	4	1.15	1.23	1.13	1.17	1.14	1.28	1.14	1.23
32	5	1.01	1.10	0.99	1.08	1.01	1.03	1.00	1.07
32	6	0.92	0.90	0.90	0.84	0.92	0.95	0.91	0.89
32	7	0.87	0.84	0.86	0.78	0.88	0.83	0.87	0.82
32	8	0.81	0.77	0.83	0.72	0.82	0.74	0.82	0.74
32	10	0.71	0.70	0.68	0.74	0.69	0.66	0.69	0.70

Table D 20

38 Air (Single tracks measured using callipers)									
Laser Power (W)	Scan Speed (mm/s)	Experiment 1		Experiment 2		Experiment 3		Average Width (mm)	Average Depth (mm)
		Width (mm)	Depth (mm)	Width (mm)	Depth (mm)	Width (mm)	Depth (mm)		
58	3	1.40	1.77	1.4	1.80	1.42	1.86	1.41	1.81
58	4	1.30	1.34	1.33	1.27	1.3	1.38	1.31	1.33
58	5	1.19	1.27	1.2	1.2	1.22	1.23	1.20	1.23
58	6	1.04	1.24	1.01	1.19	1.06	1.16	1.04	1.19
58	7	0.98	1.13	1.02	1.06	0.99	1.05	0.99	1.08
58	8	0.91	1.01	0.96	0.93	0.95	0.97	0.94	0.97
58	10	0.86	0.89	0.9	0.93	0.81	0.91	0.86	0.91
58	12	0.85	0.86	0.8	0.79	0.89	0.84	0.85	0.83
58	15	0.83	0.84	0.89	0.78	0.83	0.82	0.85	0.81
58	18	0.72	0.76	0.7	0.73	0.77	0.78	0.73	0.76

Table D 21

38 Air (Single tracks measured using callipers)									
Laser Power (W)	Scan Speed (mm/s)	Experiment 1		Experiment 2		Experiment 3		Average Width (mm)	Average Depth (mm)
		Width (mm)	Depth (mm)	Width (mm)	Depth (mm)	Width (mm)	Depth (mm)		
89	3	2.42	2.80	2.26	2.50	2.49	2.90	2.39	2.73
89	4	1.82	2.04	1.90	1.96	1.78	1.85	1.83	1.95
89	5	1.61	1.92	1.70	1.72	1.68	1.79	1.66	1.81
89	6	1.32	1.77	1.41	1.60	1.38	1.50	1.37	1.62
89	7	1.24	1.48	1.27	1.40	1.18	1.33	1.23	1.40
89	8	1.20	1.34	1.13	1.23	1.26	1.20	1.20	1.26
89	10	1.04	1.12	1.07	1.07	1.06	1.03	1.06	1.07
89	12	0.93	0.94	0.95	0.98	0.87	0.91	0.92	0.94
89	15	0.87	0.83	0.90	0.86	0.82	0.81	0.86	0.83
89	18	0.80	0.81	0.83	0.84	0.77	0.75	0.80	0.80

Table D 22

38 Air (Single tracks measured using callipers)									
Laser Power (W)	Scan Speed (mm/s)	Experiment 1		Experiment 2		Experiment 3		Average Width (mm)	Average Depth (mm)
		Width (mm)	Depth (mm)	Width (mm)	Depth (mm)	Width (mm)	Depth (mm)		
110	3	3.35	3.46	3.15	3.04	3.02	3.28	3.17	3.26
110	4	2.38	2.56	2.53	2.32	2.49	2.25	2.47	2.38
110	5	1.64	1.96	1.85	2.04	1.80	1.92	1.76	1.97
110	6	1.54	1.69	1.52	1.68	1.59	1.77	1.55	1.71
110	7	1.44	1.62	1.40	1.68	1.47	1.55	1.44	1.62
110	8	1.31	1.59	1.31	1.52	1.32	1.41	1.31	1.51
110	10	1.25	1.31	1.20	1.24	1.25	1.35	1.23	1.30
110	12	1.08	1.15	1.06	1.24	1.03	1.06	1.06	1.15
110	15	1.01	1.02	0.97	0.98	0.95	1.15	0.98	1.05

Table D 23

38 Air (Single tracks measured using callipers)									
Laser Power (W)	Scan Speed (mm/s)	Experiment 1		Experiment 2		Experiment 3		Average Width (mm)	Average Depth (mm)
		Width (mm)	Depth (mm)	Width (mm)	Depth (mm)	Width (mm)	Depth (mm)		
125	3	3.32	3.75	3.49	3.34	3.68	3.60	3.50	3.56
125	4	2.50	2.84	2.72	2.66	2.88	2.90	2.70	2.80
125	5	2.13	2.28	2.22	2.12	2.36	2.40	2.24	2.27
125	6	1.82	2.12	2.01	1.84	1.95	2.00	1.93	1.99
125	7	1.63	1.93	1.77	1.69	1.69	1.82	1.70	1.81
125	8	1.57	1.66	1.68	1.51	1.62	1.72	1.62	1.63
125	10	1.34	1.36	1.40	1.40	1.31	1.48	1.35	1.41
125	12	1.29	1.30	1.33	1.22	1.23	1.22	1.28	1.25
125	15	1.13	1.11	1.15	1.06	1.09	0.95	1.12	1.04

Table D 24

38 Air (Single tracks measured using callipers)									
Laser Power (W)	Scan Speed (mm/s)	Experiment 1		Experiment 2		Experiment 3		Average Width (mm)	Average Depth (mm)
		Width (mm)	Depth (mm)	Width (mm)	Depth (mm)	Width (mm)	Depth (mm)		
152	3	4.08	4.21	3.58	3.86	3.85	3.57	3.84	3.88
152	4	3.30	2.86	2.52	3.23	2.94	3.08	2.92	3.06
152	5	2.62	2.55	2.35	2.82	2.86	2.75	2.61	2.71
152	6	2.08	2.24	2.08	2.05	2.12	2.45	2.09	2.25
152	7	1.93	2.00	2.04	2.11	1.84	1.81	1.94	1.97
152	8	1.83	1.82	1.68	1.70	1.92	1.75	1.81	1.76
152	10	1.51	1.72	1.37	1.58	1.61	1.83	1.50	1.71
152	12	1.51	1.66	1.46	1.53	1.46	1.61	1.48	1.60
152	15	1.35	1.51	1.34	1.44	1.31	1.34	1.33	1.43

Table D 25

38 Air (Single tracks measured using callipers)									
Laser Power (W)	Scan Speed (mm/s)	Experiment 1		Experiment 2		Experiment 3		Average Width (mm)	Average Depth (mm)
		Width (mm)	Depth (mm)	Width (mm)	Depth (mm)	Width (mm)	Depth (mm)		
189	3	4.71	5.22	5.00	5.06	4.87	5.4	4.86	5.23
189	4	4.12	4.37	4.22	4.00	4.34	4.11	4.23	4.16
189	5	3.39	3.32	3.19	3.64	3.5	3.44	3.36	3.47
189	6	2.77	2.67	2.53	3.2	2.73	2.92	2.68	2.93
189	7	2.41	2.48	2.28	2.79	2.42	2.67	2.37	2.65
189	8	2.02	2.17	2.13	2.27	2.08	2.32	2.08	2.25
189	10	1.71	2.01	1.85	1.89	1.78	2.06	1.78	1.99
189	12	1.65	1.72	1.54	1.63	1.67	1.8	1.62	1.72
189	15	1.54	1.56	1.43	1.6	1.67	1.49	1.55	1.55

D2 Argon Atmosphere Results

D2.1 300/150 Powder Batch

Table D 26

300/150 Argon (Single tracks measured using callipers)											
Laser Power (W)	Scan Speed (mm/s)	Experiment 1		Experiment 2		Experiment 3		Average Width (mm)	Average Depth (mm)	Track Length (mm)	Track Mass (grams)
		Width (mm)	Depth (mm)	Width (mm)	Depth (mm)	Width (mm)	Depth (mm)				
16	0.5	1.2	0.99	1.21	1.02	1.21	1.01	1.21	1.01	19.66	0.0658
16	1	1.09	0.96	1.11	0.95	1.11	0.95	1.10	0.95	11.61	0.0286
16	2	0.91	0.91	0.95	0.91	0.93	0.91	0.93	0.91	16.94	0.0224
16	3	0.97	0.77	0.98	0.77	0.99	0.79	0.98	0.78	x	x
16	4	0.99	0.56	1.02	0.56	1.01	0.57	1.01	0.56	x	x

Table D 27

300/150 Argon (Single tracks measured using callipers)											
Laser Power (W)	Scan Speed (mm/s)	Experiment 1		Cross Section Pics		Experiment 3		Average Width (mm)	Average Depth (mm)	Track Length (mm)	Track Mass (grams)
		Width (mm)	Depth (mm)	Width (mm)	Depth (mm)	Width (mm)	Depth (mm)				
32	0.5	1.92	1.08	1.98	1.12	1.94	1.1	1.95	1.10	30.34	0.1628
32	1	1.77	1.04	1.82	1.04	1.82	1.07	1.80	1.05	30	0.1408
32	2	1.55	1.3	1.58	1.33	1.56	1.32	1.56	1.32	30.8	0.2339
32	3	1.47	1.08	1.51	1.11	1.53	1.11	1.50	1.10	30.16	0.1479
32	4	1.5	1	1.54	1.04	1.53	1.04	1.52	1.03	29.47	0.1148
32	5	1.18	0.73	1.22	0.76	1.24	0.75	1.21	0.75	x	x
32	6	1.09	0.7	1.13	0.68	1.14	0.7	1.12	0.69	x	x

Table D 28

300/150 Argon (Single tracks measured using callipers)											
Laser Power (W)	Scan Speed (mm/s)	Experiment 1		Experiment 2		Experiment 3		Average Width (mm)	Average Depth (mm)	Track Length (mm)	Track Mass (grams)
		Width (mm)	Depth (mm)	Width (mm)	Depth (mm)	Width (mm)	Depth (mm)				
58	0.5	2.68	1.4	2.72	1.38	2.72	1.46	2.71	1.41	20.37	0.251
58	1	2.51	1.35	2.56	1.34	2.56	1.33	2.54	1.34	20.19	0.2271
58	2	2.37	1.42	2.33	1.42	2.34	1.37	2.35	1.40	19.58	0.1996
58	3	2.14	1.29	2.14	1.28	2.15	1.33	2.14	1.30	19.01	0.144
58	4	2	1.14	1.99	1.14	1.99	1.16	1.99	1.15	16.19	0.1008
58	5	1.68	1.07	1.62	1.08	1.65	1.11	1.65	1.09	11.51	0.0447
58	6	1.4	0.97	1.38	0.96	1.44	0.99	1.41	0.97	x	x
58	7	1.27	0.91	1.28	0.95	1.28	0.97	1.28	0.94	x	x
58	8	1.11	0.87	1.17	0.86	1.14	0.91	1.14	0.88	x	x

Table D 29

300/150 Argon (Single tracks measured using callipers)											
Laser Power (W)	Scan Speed (mm/s)	Experiment 1		Experiment 2		Experiment 3		Average Width (mm)	Average Depth (mm)	Track Length (mm)	Track Mass (grams)
		Width (mm)	Depth (mm)	Width (mm)	Depth (mm)	Width (mm)	Depth (mm)				
77	0.5	2.9	1.53	2.99	1.56	2.96	1.64	2.95	1.58	20.62	0.2983
77	1	2.7	1.58	2.77	1.63	2.75	1.62	2.74	1.61	19.77	0.2662
77	2	2.65	1.72	2.58	1.68	2.62	1.71	2.28	1.70	19.36	0.2295
77	3	2.44	1.64	2.38	1.73	2.41	1.71	2.41	1.69	18.94	0.187
77	4	2.16	1.48	2.22	1.55	2.2	1.53	2.19	1.52	19.05	0.1379
77	5	2.04	1.28	1.97	1.33	1.97	1.34	1.99	1.32	18.76	0.1054
77	6	1.91	1.41	1.85	1.37	1.86	1.36	1.87	1.38	8.66	0.0384
77	7	1.6	1.18	1.67	1.2	1.65	1.27	1.64	1.22	x	x
77	8	1.36	1.12	1.39	1.16	1.44	1.16	1.40	1.15	x	x
77	10	1.33	1.06	1.29	1.07	1.29	1.06	1.30	1.06	x	x
77	12	1.17	1.01	1.19	1.01	1.17	0.99	1.18	1.00	x	x
77	15	1.12	0.92	1.12	0.96	1.11	0.95	1.12	0.94	x	x

Table D 30

300/150 Argon (Single tracks measured using callipers)											
Laser Power (W)	Scan Speed (mm/s)	Experiment 1		Experiment 2		Experiment 3		Average Width (mm)	Average Depth (mm)	Track Length (mm)	Track Mass (grams)
		Width (mm)	Depth (mm)	Width (mm)	Depth (mm)	Width (mm)	Depth (mm)				
89	0.5	3.23	1.61	3.28	1.59	3.22	1.68	3.24	1.63	19.28	0.3316
89	1	2.95	1.49	3.05	1.56	3.02	1.58	3.01	1.54	18.44	0.3218
89	2	2.79	1.71	2.91	1.63	2.86	1.62	2.85	1.65	18.71	0.2957
89	3	2.5	1.51	2.57	1.46	2.66	1.41	2.58	1.46	17.95	0.2345
89	4	2.21	1.31	2.28	1.39	2.27	1.37	2.25	1.36	17.91	0.1694
89	5	1.99	1.28	2.08	1.25	2.07	1.24	2.05	1.26	17.6	0.1285
89	6	1.87	1.11	1.96	1.15	1.95	1.14	1.93	1.13	11.8	0.0523
89	7	1.58	1.07	1.62	1.03	1.71	1.03	1.64	1.04	9.36	0.0382
89	8	1.34	0.97	1.26	1.01	1.32	1	1.31	0.99	x	x
89	10	1.18	0.9	1.25	0.9	1.23	0.95	1.22	0.92	x	x
89	12	1.17	0.86	1.15	0.86	1.15	0.86	1.16	0.86	x	x
89	15	1.09	0.77	1.14	0.77	1.11	0.79	1.11	0.78	x	x

Table D 31

300/150 Argon (Single tracks measured using callipers)											
Laser Power (W)	Scan Speed (mm/s)	Experiment 1		Experiment 2		Experiment 3		Average Width (mm)	Average Depth (mm)	Track Length (mm)	Track Mass (grams)
		Width (mm)	Depth (mm)	Width (mm)	Depth (mm)	Width (mm)	Depth (mm)				
110	0.5	3.5	1.57	3.59	1.62	3.53	1.66	3.54	1.62	21.21	0.5257
110	1	3.34	1.51	3.51	1.65	3.46	1.65	3.44	1.60	20.41	0.4893
110	2	3.25	1.82	3.29	1.77	3.44	1.7	3.33	1.76	19.36	0.4014
110	3	2.88	1.57	3.02	1.51	2.94	1.65	2.95	1.58	19.19	0.335
110	4	2.62	1.72	2.51	1.77	2.49	1.62	2.54	1.70	18.46	0.2477
110	5	2.22	1.47	2.33	1.52	2.26	1.4	2.27	1.46	18.7	0.1921
110	6	1.96	1.39	1.9	1.37	1.82	1.4	1.89	1.39	10.98	0.0871
110	7	1.66	1.4	1.51	1.48	1.53	1.42	1.57	1.43	9.17	0.0524
110	8	1.47	1.22	1.38	1.29	1.41	1.35	1.42	1.29	12.04	0.0514
110	10	1.3	1.18	1.35	1.24	1.3	1.23	1.32	1.22		
110	12	1.14	1.05	1.14	1.01	1.22	1.02	1.17	1.03	x	x
110	15	1.04	0.91	1.03	0.92	1.05	0.91	1.04	0.91	x	x

Table D 32

300/150 Argon (Single tracks measured using callipers)											
Laser Power (W)	Scan Speed (mm/s)	Experiment 1		Experiment 2		Experiment 3		Average Width (mm)	Average Depth (mm)	Track Length (mm)	Track Mass (grams)
		Width (mm)	Depth (mm)	Width (mm)	Depth (mm)	Width (mm)	Depth (mm)				
125	0.5	3.45	1.5	3.62	1.62	3.6	1.64	3.56	1.59	20.95	0.4476
125	1	3.64	1.66	4.02	1.79	3.85	1.77	3.84	1.74	20.23	0.5286
125	2	3.38	1.69	3.62	1.6	3.44	1.46	3.48	1.58	19.72	0.4776
125	3	2.71	1.77	2.91	1.74	2.85	1.61	2.82	1.71	18.77	0.4037
125	4	2.45	1.41	2.43	1.41	2.34	1.52	2.41	1.45	18.16	0.3057
125	5	2.19	1.31	2.28	1.33	2.14	1.27	2.20	1.30	18.5	0.2404
125	6	1.84	1.29	1.77	1.31	1.78	1.31	1.80	1.30	18.43	0.1964
125	7	1.79	1.48	1.8	1.5	1.8	1.52	1.80	1.50	18.37	0.0824
125	8	1.4	1.21	1.49	1.23	1.44	1.17	1.44	1.20	17.8	0.1328
125	10	1.37	1.15	1.37	1.15	1.39	1.15	1.38	1.15	15.82	0.1011
125	12	1.47	1.04	1.51	1.04	1.53	1.06	1.50	1.05	16.84	0.0564
125	15	1	0.97	1.01	0.97	1	0.99	1.00	0.98	9.36	0.027

Table D 33

300/150 Argon (Single tracks measured using callipers)											
Laser Power (W)	Scan Speed (mm/s)	Experiment 1		Experiment 2		Experiment 3		Average Width (mm)	Average Depth (mm)	Track Length (mm)	Track Mass (grams)
		Width (mm)	Depth (mm)	Width (mm)	Depth (mm)	Width (mm)	Depth (mm)				
143	0.5	3.91	2.08	4.18	1.88	4.21	1.85	4.10	1.94	21.04	0.6057
143	1	4.25	2.41	4.54	2.45	4.45	2.66	4.41	2.51	20.55	0.701
143	2	3.58	2.19	3.77	2.38	3.74	2.34	3.70	2.30	19.66	0.5555
143	3	2.99	2.03	3.11	2.08	3.06	1.96	3.05	2.02	19.14	0.4479
143	4	2.61	1.69	2.71	1.64	2.64	1.66	2.65	1.66	18.7	0.3444
143	5	2.29	1.55	2.33	1.57	2.34	1.59	2.32	1.57	18.09	0.2747
143	6	2.1	1.57	2.01	1.51	2.03	1.48	2.05	1.52	17.9	0.2259
143	7	1.75	1.54	1.71	1.45	1.79	1.65	1.75	1.55	18.18	0.1879
143	8	1.88	1.22	1.91	1.27	1.91	1.25	1.90	1.25	18.47	0.1627
143	10	1.58	1.16	1.57	1.16	1.59	1.18	1.58	1.17	15.41	0.0989
143	12	1.31	1.13	1.31	1.14	1.31	1.14	1.31	1.14	x	x
143	15	1.14	0.99	1.14	1.03	1.13	1.03	1.14	1.02	x	x

Table D 34

300/150 Argon (Single tracks measured using callipers)											
Laser Power (W)	Scan Speed (mm/s)	Experiment 1		Experiment 2		Experiment 3		Average Width (mm)	Average Depth (mm)	Track Length (mm)	Track Mass (grams)
		Width (mm)	Depth (mm)	Width (mm)	Depth (mm)	Width (mm)	Depth (mm)				
162	0.5	4.18	2.58	4.45	2.78	4.41	2.51	4.35	2.62	21.19	0.5252
162	1	4.28	3.15	4.66	3.44	4.41	3.21	4.45	3.27	20.63	0.7594
162	2	3.36	2.5	3.31	2.51	3.12	2.7	3.26	2.57	18.96	0.5755
162	3	2.88	1.89	2.76	1.8	2.69	1.82	2.78	1.84	18.85	0.4955
162	4	2.59	1.55	2.48	1.63	2.38	1.66	2.48	1.61	18.09	0.3634
162	5	2.24	1.55	2.14	1.6	2.35	1.67	2.24	1.61	18.48	0.2893
162	6	2.04	1.6	2.08	1.55	2.05	1.58	2.06	1.58	18.46	0.2337
162	7	1.93	1.47	2.04	1.44	1.98	1.43	1.98	1.45	18.55	0.1925
162	8	1.73	1.22	1.75	1.24	1.74	1.28	1.74	1.25	17.95	0.1644
162	10	1.62	1.09	1.57	1.08	1.58	1.09	1.59	1.09	14.96	0.1015
162	12	1.33	0.99	1.34	1.02	1.27	1.02	1.31	1.01	10.02	0.0522
162	15	1.1	0.93	1.13	0.93	1.14	0.93	1.12	0.93	x	x

Table D 35

300/150 Argon (Single tracks measured using callipers)											
Laser Power (W)	Scan Speed (mm/s)	Experiment 1		Experiment 2		Experiment 3		Average Width (mm)	Average Depth (mm)	Track Length (mm)	Track Mass (grams)
		Width (mm)	Depth (mm)	Width (mm)	Depth (mm)	Width (mm)	Depth (mm)				
170	0.5	4.2	2.02	3.85	2.21	4.11	2.12	4.05	2.12	30.85	2.3658
170	1	3.98	3.6	4.22	3.83	4.16	3.64	4.12	3.69	31.5	2.5641
170	2	3.32	2.38	3.22	2.4	3.01	2.16	3.18	2.31	30.77	1.7584
170	3	2.96	1.85	3.12	1.89	3.16	1.75	3.08	1.83	32.68	1.2547
170	4	2.66	1.64	2.68	1.7	2.53	1.59	2.62	1.64	29.75	1.1389
170	5	2.3	1.73	2.31	1.71	2.24	1.66	2.28	1.70	28.34	0.6582
170	6	2.22	1.6	2.24	1.6	2.25	1.68	2.24	1.63	27.75	0.4752
170	7	2.18	1.55	2.18	1.59	2.2	1.64	2.19	1.59	29.05	0.5526
170	8	1.88	1.31	1.88	1.31	1.89	1.36	1.88	1.33	28.43	0.3256
170	10	1.77	1.25	1.77	1.22	1.71	1.26	1.75	1.24	28.37	0.2563
170	12	1.16	1.01	1.16	1.01	1.16	0.96	1.16	0.99	13.78	0.0553
170	15	1.03	0.9	1.04	0.92	1.07	0.92	1.05	0.91	x	x

D2.2 150/75 Powder Batch

Table D 36

150/75 Argon (Single tracks measured using callipers)											
Laser Power (W)	Scan Speed (mm/s)	Experiment 1		Experiment 2		Experiment 3		Average Width (mm)	Average Depth (mm)	Track Length (mm)	Track Mass (grams)
		Width (mm)	Depth (mm)	Width (mm)	Depth (mm)	Width (mm)	Depth (mm)				
16	0.5	1.58	0.69	1.58	0.72	1.62	0.67	1.59	0.69	18.64	0.0437
16	1	1.4	0.56	1.44	0.55	1.38	0.57	1.41	0.56	19.47	0.0331
16	2	1.22	0.48	1.25	0.44	1.24	0.46	1.24	0.46	14.98	0.0166
16	3	1.08	0.46	1.11	0.46	1.12	0.45	1.10	0.46	x	x
16	4	0.95	0.42	0.97	0.43	0.97	0.41	0.96	0.42	x	x

Table D 37

150/75 Argon (Single tracks measured using callipers)											
Laser Power (W)	Scan Speed (mm/s)	Experiment 1		Cross Section Pics		Experiment 3		Average Width (mm)	Average Depth (mm)	Track Length (mm)	Track Mass (grams)
		Width (mm)	Depth (mm)	Width (mm)	Depth (mm)	Width (mm)	Depth (mm)				
32	0.5	2.11	0.98	2.09	0.96	2.1	0.94	2.10	0.96	20.2	0.1134
32	1	1.7	0.81	1.64	0.77	1.72	0.8	1.69	0.79	19.83	0.0936
32	2	1.6	0.78	1.62	0.75	1.71	0.77	1.64	0.77	17.26	0.0637
32	3	1.45	0.74	1.4	0.73	1.42	0.77	1.42	0.75	12.5	0.0352
32	4	1.13	0.63	1.16	0.64	1.14	0.61	1.14	0.63	9.2	0.019
32	5	1.02	0.63	0.99	0.64	1.08	0.6	1.03	0.62	x	x
32	6	0.88	0.55	0.91	0.52	0.92	0.51	0.90	0.53	x	x

Table D 38

150/75 Argon (Single tracks measured using callipers)											
Laser Power (W)	Scan Speed (mm/s)	Experiment 1		Experiment 2		Experiment 3		Average Width (mm)	Average Depth (mm)	Track Length (mm)	Track Mass (grams)
		Width (mm)	Depth (mm)	Width (mm)	Depth (mm)	Width (mm)	Depth (mm)				
58	0.5	2.58	1.09	2.55	1.11	2.56	1.08	2.56	1.09	20.51	0.2545
58	1	2.5	0.98	2.52	1.02	2.48	1.01	2.50	1.00	20.07	0.2092
58	2	2.16	0.82	2.15	0.83	2.15	0.82	2.15	0.82	19.63	0.1643
58	3	1.85	0.77	1.82	0.79	1.84	0.82	1.84	0.79	18.9	0.1392
58	4	1.48	0.72	1.44	0.73	1.52	0.73	1.48	0.73	18.85	0.1132
58	5	1.25	0.7	1.26	0.71	1.22	0.72	1.24	0.71	18.87	0.0913
58	6	1.11	0.65	1.09	0.66	1.12	0.66	1.11	0.66	18.42	0.0753
58	7	1.04	0.62	1.01	0.58	1.01	0.6	1.02	0.60	x	x
58	8	0.93	0.55	0.94	0.58	0.87	0.52	0.91	0.55	x	x

Table D 39

150/75 Argon (Single tracks measured using callipers)											
Laser Power (W)	Scan Speed (mm/s)	Experiment 1		Experiment 2		Experiment 3		Average Width (mm)	Average Depth (mm)	Track Length (mm)	Track Mass (grams)
		Width (mm)	Depth (mm)	Width (mm)	Depth (mm)	Width (mm)	Depth (mm)				
77	0.5	2.77	1.41	2.7	1.44	2.85	1.47	2.77	1.44	31.56	0.4247
77	1	2.48	1.21	2.55	1.18	2.51	1.19	2.51	1.19	31.06	0.3198
77	2	2.16	1.11	2.17	1.15	2.19	1.12	2.17	1.13	30.54	0.2392
77	3	2	1.08	2.01	1.09	2.07	1.13	2.03	1.10	30.21	0.2662
77	4	2.21	1.06	2.14	1.01	2.15	0.96	2.17	1.01	30.74	0.2572
77	5	1.58	0.97	1.54	0.97	1.6	1.06	1.57	1.00	29.29	0.2216
77	6	1.23	0.91	1.19	0.99	1.29	0.92	1.24	0.94	29.16	0.132
77	7	1.23	0.83	1.2	0.9	1.28	0.92	1.24	0.88	28.92	0.1001
77	8	1.09	0.75	1.12	0.68	1.21	0.77	1.14	0.73	24.41	0.0701
77	10	0.99	0.71	0.95	0.68	0.95	0.67	0.96	0.69	x	x
77	12	0.91	0.68	0.88	0.69	0.87	0.65	0.89	0.67	x	x
77	15	0.83	0.62	0.84	0.59	0.81	0.6	0.83	0.60	x	x

Table D 40

150/75 Argon (Single tracks measured using callipers)											
Laser Power (W)	Scan Speed (mm/s)	Experiment 1		Experiment 2		Experiment 3		Average Width (mm)	Average Depth (mm)	Track Length (mm)	Track Mass (grams)
		Width (mm)	Depth (mm)	Width (mm)	Depth (mm)	Width (mm)	Depth (mm)				
89	0.5	3	1.58	3.11	1.64	3.15	1.51	3.09	1.58	20.71	0.3221
89	1	2.81	1.72	2.77	1.69	2.81	1.74	2.80	1.72	20.21	0.2879
89	2	2.41	1.44	2.54	1.36	2.64	1.39	2.53	1.40	19.48	0.225
89	3	2.48	1.31	2.39	1.24	2.41	1.25	2.43	1.27	19.24	0.1854
89	4	2.42	1.18	2.38	1.22	2.47	1.17	2.42	1.19	18.98	0.1508
89	5	1.89	1.18	1.77	1.29	1.98	1.19	1.88	1.22	18.91	0.1233
89	6	1.58	1.2	1.59	1.17	1.51	1.21	1.56	1.19	18.16	0.0985
89	7	1.24	1.04	1.21	0.91	1.26	0.94	1.24	0.96	14.4	0.064
89	8	1.17	1.02	1.23	1	1.19	1.08	1.20	1.03	13.85	0.0543
89	10	1.05	0.94	1.01	0.98	1.05	0.97	1.04	0.96	x	x
89	12	0.99	0.94	0.94	0.95	0.93	0.91	0.95	0.93	x	x
89	15	0.87	0.84	0.85	0.85	0.86	0.82	0.86	0.84	x	x

Table D 41

150/75 Argon (Single tracks measured using callipers)											
Laser Power (W)	Scan Speed (mm/s)	Experiment 1		Experiment 2		Experiment 3		Average Width (mm)	Average Depth (mm)	Track Length (mm)	Track Mass (grams)
		Width (mm)	Depth (mm)	Width (mm)	Depth (mm)	Width (mm)	Depth (mm)				
110	0.5	3.4	1.77	3.37	1.82	3.45	1.82	3.41	1.80	21.05	0.4984
110	1	3.2	1.60	3.22	1.58	3.18	1.7	3.20	1.63	19.83	0.7348
110	2	2.85	1.73	2.86	1.78	2.82	1.79	2.84	1.77	19.67	0.45
110	3	2.97	1.55	2.91	1.62	2.84	1.51	2.91	1.56	19.21	0.2957
110	4	2.71	1.3	2.65	1.24	2.67	1.41	2.68	1.32	19.29	0.2226
110	5	2.12	1.42	2.2	1.38	2.24	1.39	2.19	1.40	18.44	0.1795
110	6	1.65	1.24	1.65	1.23	1.68	1.3	1.66	1.26	18.07	0.149
110	7	1.42	1.17	1.41	1.14	1.47	1.11	1.43	1.14	14.74	0.098
110	8	1.4	1.1	1.33	1.11	1.39	1.21	1.37	1.14	18.05	0.1044
110	10	1.18	0.99	1.13	1.08	1.18	1.07	1.16	1.05	13.98	0.06
110	12	1.11	0.86	1.12	0.91	1.09	0.9	1.11	0.89	x	x
110	15	0.98	0.78	1.02	0.78	1.05	0.76	1.02	0.77	x	x

Table D 42

150/75 Argon (Single tracks measured using callipers)											
Laser Power (W)	Scan Speed (mm/s)	Experiment 1		Experiment 2		Experiment 3		Average Width (mm)	Average Depth (mm)	Track Length (mm)	Track Mass (grams)
		Width (mm)	Depth (mm)	Width (mm)	Depth (mm)	Width (mm)	Depth (mm)				
125	0.5	3.64	1.85	3.58	1.84	3.68	1.83	3.63	1.84	21.13	0.554
125	1	3.41	2.38	3.39	2.36	3.37	2.3	3.39	2.35	20.02	0.8674
125	2	3.18	2.28	3.02	2.15	3.08	2.18	3.09	2.20	19.09	0.523
125	3	2.95	1.87	2.84	1.81	2.97	1.89	2.92	1.86	19.28	0.3353
125	4	2.64	1.6	2.42	1.58	2.61	1.42	2.56	1.53	18.33	0.2238
125	5	2.19	1.53	2.25	1.3	2.21	1.25	2.22	1.36	15.14	0.1506
125	6	1.74	1.42	1.68	1.4	1.62	1.22	1.68	1.35	18.2	0.1491
125	7	1.45	1.29	1.4	1.21	1.38	1.25	1.41	1.25	16.33	0.1179
125	8	1.38	1.11	1.45	1.16	1.36	1.08	1.40	1.12	12.92	0.0843
125	10	1.31	1.02	1.29	0.99	1.3	0.98	1.30	1.00	x	x
125	12	1.25	0.91	1.18	0.86	1.18	0.88	1.20	0.88	x	x
125	15	1.12	0.86	1.1	0.87	1.07	0.83	1.10	0.85	x	x

Table D 43

150/75 Argon (Single tracks measured using callipers)											
Laser Power (W)	Scan Speed (mm/s)	Experiment 1		Experiment 2		Experiment 3		Average Width (mm)	Average Depth (mm)	Track Length (mm)	Track Mass (grams)
		Width (mm)	Depth (mm)	Width (mm)	Depth (mm)	Width (mm)	Depth (mm)				
143	0.5	3.9	2	4.02	1.96	3.91	1.94	3.94	1.97	32.24	0.9587
143	1	3.62	2.7	3.58	2.61	3.64	2.8	3.61	2.70	30.53	1.5807
143	2	3.1	2.25	3.18	2.19	3.17	2.18	3.15	2.21	30.66	1.3643
143	3	2.99	1.85	2.95	1.97	3.08	1.96	3.01	1.93	31.3	0.6271
143	4	2.51	1.9	2.45	1.87	2.44	1.82	2.47	1.86	23.66	0.9383
143	5	1.91	1.41	1.84	1.48	1.82	1.52	1.86	1.47	28.72	0.5845
143	6	1.6	1.44	1.78	1.52	1.66	1.41	1.68	1.46	28.74	0.2966
143	7	1.42	1.27	1.34	1.28	1.5	1.33	1.42	1.29	28.46	0.2322
143	8	1.3	1.12	1.41	1.15	1.31	1.2	1.34	1.16	9.18	0.0621
143	10	1.08	0.9	1.01	0.95	1.13	0.88	1.07	0.91	7.11	0.0422
143	12	0.97	0.79	0.95	0.82	0.92	0.77	0.95	0.79	x	x
143	15	0.87	0.72	0.85	0.74	0.82	0.69	0.85	0.72	x	x

Table D 44

150/75 Argon (Single tracks measured using callipers)											
Laser Power (W)	Scan Speed (mm/s)	Experiment 1		Experiment 2		Experiment 3		Average Width (mm)	Average Depth (mm)	Track Length (mm)	Track Mass (grams)
		Width (mm)	Depth (mm)	Width (mm)	Depth (mm)	Width (mm)	Depth (mm)				
162	0.5	4.3	2.18	4.15	2.09	4.45	2.25	4.30	2.17	20.88	0.6277
162	1	4.11	3.79	4.34	3.89	4.22	4.08	4.22	3.92	19.82	1.2682
162	2	3.63	2.63	3.69	2.51	3.51	2.54	3.61	2.56	11.71	0.4073
162	3	3.51	2.24	3.38	2.4	3.4	2.41	3.43	2.35	9.14	0.2006
162	4	3.08	1.65	2.97	1.55	3.08	1.61	3.04	1.60	18.75	0.307
162	5	2.35	1.81	2.41	1.77	2.4	1.85	2.39	1.81	18.73	0.2468
162	6	1.98	1.45	1.91	1.28	2.02	1.32	1.97	1.35	18.45	0.2075
162	7	1.49	1.21	1.55	1.18	1.42	1.28	1.49	1.22	18.99	0.1722
162	8	1.38	1.15	1.45	1.25	1.44	1.18	1.42	1.19	19.02	0.1467
162	10	1.44	1.19	1.38	1.08	1.36	1.29	1.39	1.19	12.78	0.0786
162	12	1.37	1.08	1.33	1.05	1.32	1.07	1.34	1.07	x	x
162	15	1.22	0.92	1.18	0.95	1.15	0.93	1.18	0.93	x	x

Table D 45

150/75 Argon (Single tracks measured using callipers)											
Laser Power (W)	Scan Speed (mm/s)	Experiment 1		Experiment 2		Experiment 3		Average Width (mm)	Average Depth (mm)	Track Length (mm)	Track Mass (grams)
		Width (mm)	Depth (mm)	Width (mm)	Depth (mm)	Width (mm)	Depth (mm)				
170	0.5	4.28	2.15	4.36	2.21	4.3	2.2	4.31	2.19	19.3	0.8676
170	1	3.98	3.68	4.2	4.21	4.11	4.28	4.10	4.06	21.2	1.387
170	2	3.22	3.4	3.38	3.59	3.35	3.12	3.32	3.37	6.74	0.24775934
170	3	2.97	2.41	2.91	2.52	3.09	2.59	2.99	2.51	5.55	0.138927505
170	4	2.68	2.05	2.61	2.06	2.63	2.17	2.64	2.09	7.12	0.134621525
170	5	2.47	1.66	2.42	1.58	2.56	1.48	2.48	1.57	8.22	0.124343598
170	6	2.05	1.31	2.11	1.39	2.09	1.28	2.08	1.33	19.29	0.237
170	7	1.66	1.21	1.71	1.25	1.71	1.24	1.69	1.23	18.36	0.1925
170	8	1.54	1.09	1.5	1.11	1.59	1.19	1.54	1.13	18.8	0.1684
170	10	1.35	1.05	1.44	1.11	1.39	1.15	1.39	1.10	18.23	0.1272
170	12	1.26	0.96	1.25	0.99	1.18	1.02	1.23	0.99	x	x
170	15	1.14	0.84	1.11	0.83	1.11	0.84	1.12	0.84	x	x

D2.3 75/38 Powder Batch

Table D 46

75/38 Argon (Single tracks measured using callipers)											
Laser Power (W)	Scan Speed (mm/s)	Experiment 1		Experiment 2		Experiment 3		Average Width (mm)	Average Depth (mm)	Track Length (mm)	Track Mass (grams)
		Width (mm)	Depth (mm)	Width (mm)	Depth (mm)	Width (mm)	Depth (mm)				
16	0.5	1.88	0.71	1.92	0.74	1.91	0.73	1.90	0.73	20.44	0.0638
16	1	1.55	0.61	1.59	0.62	1.6	0.59	1.58	0.61	19.73	0.0444
16	2	1.41	0.51	1.4	0.5	1.34	0.54	1.38	0.52	x	x
16	3	1.23	0.55	1.24	0.54	1.27	0.54	1.25	0.54	x	x
16	4	1.17	0.51	1.2	0.5	1.2	0.5	1.19	0.50	x	x
16	5	1.14	0.46	1.08	0.47	1.08	0.47	1.10	0.47		
16	6	1.03	0.44	1.02	0.47	1.02	0.47	1.02	0.46		

Table D 47

75/38 Argon (Single tracks measured using callipers)											
Laser Power (W)	Scan Speed (mm/s)	Experiment 1		Cross Section Pics		Experiment 3		Average Width (mm)	Average Depth (mm)	Track Length (mm)	Track Mass (grams)
		Width (mm)	Depth (mm)	Width (mm)	Depth (mm)	Width (mm)	Depth (mm)				
32	0.5	2.55	0.93	2.54	0.95	2.55	0.93	2.55	0.94	19.1	0.1383
32	1	2.31	0.79	2.36	0.77	2.38	0.77	2.35	0.78	19.89	0.1079
32	2	2.14	0.61	2.1	0.65	2.08	0.66	2.11	0.64	19.39	0.0683
32	3	1.9	0.63	1.93	0.64	1.93	0.63	1.92	0.63	19.31	0.0538
32	4	1.82	0.6	1.79	0.59	1.74	0.63	1.78	0.61	19.39	0.0459
32	5	1.66	0.57	1.66	0.59	1.66	0.56	1.66	0.57	11.15	0.0202
32	6	1.41	0.57	1.41	0.55	1.46	0.56	1.43	0.56	x	x
32	7	1.34	0.52	1.33	0.53	1.39	0.54	1.35	0.53		
32	8	1.21	0.54	1.22	0.55	1.22	0.55	1.22	0.55		
32	10	1.16	0.48	1.16	0.47	1.17	0.53	1.16	0.49		

Table D 48

75/38 Argon (Single tracks measured using callipers)											
Laser Power (W)	Scan Speed (mm/s)	Experiment 1		Experiment 2		Experiment 3		Average Width (mm)	Average Depth (mm)	Track Length (mm)	Track Mass (grams)
		Width (mm)	Depth (mm)	Width (mm)	Depth (mm)	Width (mm)	Depth (mm)				
58	0.5	3.24	1.01	3.26	1.07	3.26	1.05	3.25	1.04	20.57	0.2614
58	1	3.1	1.16	3.16	1.17	3.16	1.2	3.14	1.18	20.63	0.2612
58	2	2.69	0.73	2.69	0.77	2.77	0.74	2.72	0.75	19.55	0.1459
58	3	2.07	1.17	2.13	1.18	2.1	1.24	2.10	1.20	17.23	0.1566
58	4	1.93	1.15	1.92	1.15	1.92	1.1	1.92	1.13	18.51	0.1245
58	5	1.74	0.9	1.75	0.93	1.72	0.98	1.74	0.94	19.1	0.095
58	6	1.45	0.82	1.44	0.81	1.47	0.83	1.45	0.82	18.85	0.0786
58	7	1.7	0.62	1.7	0.66	1.64	0.68	1.68	0.65	11.3	0.0427
58	8	1.6	0.62	1.6	0.64	1.72	0.61	1.64	0.62	19.2	0.0587

Table D 49

75/38 Argon (Single tracks measured using callipers)											
Laser Power (W)	Scan Speed (mm/s)	Experiment 1		Experiment 2		Experiment 3		Average Width (mm)	Average Depth (mm)	Track Length (mm)	Track Mass (grams)
		Width (mm)	Depth (mm)	Width (mm)	Depth (mm)	Width (mm)	Depth (mm)				
77	0.5	3.61	1.10	3.82	1.2	3.7	1.14	3.71	1.15	20.2	0.3256
77	1	3.62	1.24	3.39	1.33	3.48	1.36	3.50	1.31	19.79	0.3139
77	2	2.95	1.14	3.12	1.16	3.09	1.27	3.05	1.19	5.28	0.0714
77	3	2.24	0.99	2.51	1.09	2.6	1.16	2.45	1.08	7.22	0.076
77	4	2.38	1.13	2.3	0.98	2.04	1.08	2.24	1.06	6.33	0.0485
77	5	2.09	0.75	1.97	0.91	2.18	0.8	2.08	0.82	9.52	0.0526
77	6	1.92	0.66	1.99	0.78	1.78	0.74	1.90	0.73	18.93	0.0934
77	7	1.9	0.74	1.88	0.72	1.98	0.71	1.92	0.72	19.17	0.0784
77	8	1.68	0.71	1.68	0.7	1.77	0.7	1.71	0.70	17.79	0.0685
77	10	1.66	0.67	1.67	0.68	1.63	0.68	1.65	0.68	18.91	0.0559
77	12	1.61	0.71	1.65	0.71	1.68	0.69	1.65	0.70	15.47	0.0382

Table D 50

75/38 Argon (Single tracks measured using callipers)											
Laser Power (W)	Scan Speed (mm/s)	Experiment 1		Experiment 2		Experiment 3		Average Width (mm)	Average Depth (mm)	Track Length (mm)	Track Mass (grams)
		Width (mm)	Depth (mm)	Width (mm)	Depth (mm)	Width (mm)	Depth (mm)				
89	0.5	3.81	1.41	4.22	1.48	4.11	1.59	4.05	1.49	19.77	0.5088
89	1	3.21	1.39	3.58	1.35	3.4	1.55	3.40	1.43	19.95	0.5084
89	2	2.51	1.06	2.59	1.15	2.32	1.11	2.47	1.11	18.76	0.3479
89	3	2.21	1.09	2.29	0.99	2.42	1.02	2.31	1.03	18.18	0.2332
89	4	2.32	0.92	2.15	0.96	2.14	0.88	2.20	0.92	19.01	0.1899
89	5	2.02	1.05	2.08	1.08	2.14	1.01	2.08	1.05	19.04	0.1483
89	6	2.06	0.99	2.01	0.98	1.92	0.96	2.00	0.98	18.92	0.129
89	7	1.46	1	1.49	1.02	1.32	1.01	1.42	1.01	15.1	0.0879
89	8	1.33	0.72	1.24	0.83	1.42	0.81	1.33	0.79	18.11	0.0969
89	10	1.3	0.71	1.22	0.79	1.36	0.83	1.29	0.78	13.63	0.0556

Table D 51

75/38 Argon (Single tracks measured using callipers)											
Laser Power (W)	Scan Speed (mm/s)	Experiment 1		Experiment 2		Experiment 3		Average Width (mm)	Average Depth (mm)	Track Length (mm)	Track Mass (grams)
		Width (mm)	Depth (mm)	Width (mm)	Depth (mm)	Width (mm)	Depth (mm)				
110	0.5	4.51	1.52	5.12	1.88	4.68	1.63	4.77	1.68	21.12	0.7511
110	1	4.27	2.25	3.42	1.86	4.18	2.11	3.96	2.07	19.67	0.7443
110	2	2.77	1.77	2.71	1.86	2.38	1.54	2.62	1.72	19.63	0.467
110	3	2.62	1.49	2.31	1.41	2.71	1.58	2.55	1.49	19.34	0.3225
110	4	2.49	1.18	2.41	1.16	2.42	1.15	2.44	1.16	14.22	0.19669
110	5	2.06	1.12	2.01	1.19	1.89	1.1	1.99	1.14	11.11	0.13011
110	6	2.14	1.07	1.99	1.01	2.07	1.11	2.07	1.06	8.88	0.08161
110	7	1.93	1.07	1.87	1.05	2.01	1.1	1.94	1.07	5.67	0.04833
110	8	1.75	0.99	1.99	0.84	2.05	1.03	1.93	0.95	4.66	0.03073
110	10	2	0.77	2.06	0.79	2.08	0.77	2.05	0.78	4.1	0.01788

Table D 52

75/38 Argon (Single tracks measured using callipers)											
Laser Power (W)	Scan Speed (mm/s)	Experiment 1		Experiment 2		Experiment 3		Average Width (mm)	Average Depth (mm)	Track Length (mm)	Track Mass (grams)
		Width (mm)	Depth (mm)	Width (mm)	Depth (mm)	Width (mm)	Depth (mm)				
125	0.5	4.51	2.66	5.21	2.72	4.82	2.98	4.85	2.79	21.11	1.1208
125	1	3.77	2.59	3.88	2.61	4.21	2.38	3.95	2.53	20.15	0.8806
125	2	2.71	1.79	2.93	2.1	2.48	2.1	2.71	2.00	19.76	0.5299
125	3	2.63	1.59	2.54	1.53	2.41	1.43	2.53	1.52	18.75	0.3716
125	4	2.24	1.47	2.38	1.48	2.39	1.56	2.34	1.50	19.45	0.2947
125	5	2.29	1.43	2.21	1.48	2.38	1.4	2.29	1.44	9.12	0.11832
125	6	2.21	1.3	2.29	1.38	2.26	1.34	2.25	1.34	8.62	0.09072
125	7	2.21	1.22	2.29	1.29	2.19	1.3	2.23	1.27	5.77	0.05398
125	8	1.88	1.01	2.11	1.07	2.09	1.06	2.03	1.05	7.22	0.05921
125	10	1.66	1.31	1.69	1.32	1.75	1.32	1.70	1.32	3.55	0.02309

Table D 53

75/38 Argon (Single tracks measured using callipers)											
Laser Power (W)	Scan Speed (mm/s)	Experiment 1		Experiment 2		Experiment 3		Average Width (mm)	Average Depth (mm)	Track Length (mm)	Track Mass (grams)
		Width (mm)	Depth (mm)	Width (mm)	Depth (mm)	Width (mm)	Depth (mm)				
143	0.5	4.89	3.62	5.41	3.59	5.32	4.31	5.21	3.84	21.23	1.6019
143	1	3.55	3.02	4.12	3.45	4.53	3.55	4.07	3.34	20.24	1.2337
143	2	2.77	2.55	3.12	2.33	3.21	2.39	3.03	2.42	18.83	0.6552
143	3	2.66	1.99	2.33	1.99	2.62	1.67	2.54	1.88	6.42	0.14813
143	4	2.19	1.51	2.49	1.59	2.24	1.68	2.31	1.59	5.98	0.10509
143	5	2.29	1.44	2.29	1.35	2.21	1.51	2.26	1.43	5.36	0.07766
143	6	2.37	1.33	2.39	1.37	2.44	1.36	2.40	1.35	4.22	0.05231

Table D 54

75/38 Argon (Single tracks measured using callipers)											
Laser Power (W)	Scan Speed (mm/s)	Experiment 1		Experiment 2		Experiment 3		Average Width (mm)	Average Depth (mm)	Track Length (mm)	Track Mass (grams)
		Width (mm)	Depth (mm)	Width (mm)	Depth (mm)	Width (mm)	Depth (mm)				
162	0.5	4.72	3.46	5.56	3.12	5	3.39	5.09	3.32	20.72	1.5814
162	1	4.29	3.21	4.42	3.11	4.03	3.49	4.25	3.27	20	1.2689
162	2	3.1	2.32	3.39	2.36	3.12	2.14	3.20	2.27	19.88	0.6649
162	3	2.77	1.61	2.79	1.69	2.59	1.75	2.72	1.68	7.22	0.1735
162	4	2.44	1.32	2.45	1.51	2.34	1.47	2.41	1.43	6.66	0.1230
162	5	2.22	1.52	2.47	1.41	2.3	1.44	2.33	1.46	8.13	0.1319
162	6	2.02	1.5	2.01	1.5	1.86	1.56	1.96	1.52	5.66	0.0745
162	7	2.11	1.33	2.12	1.32	2.17	1.31	2.13	1.32	4.33	0.0477
162	8	2.15	1.28	2.15	1.32	2.15	1.33	2.15	1.31	6.02	0.0592

D2.4 -38 Powder Batch

Table D 55

38 Argon (Single tracks measured using callipers)											
Laser Power (W)	Scan Speed (mm/s)	Experiment 1		Cross Section Pics		Experiment 3		Average Width (mm)	Average Depth (mm)	Track Length (mm)	Track Mass (grams)
		Width (mm)	Depth (mm)	Width (mm)	Depth (mm)	Width (mm)	Depth (mm)				
16	0.5	2.14	0.77	2.1	0.79	2.08	0.77	2.11	0.78	16.41	0.0682
16	1	1.88	0.66	1.94	0.66	1.93	0.68	1.92	0.67	15.23	0.0562
16	2	1.77	0.66	1.71	0.58	1.76	0.57	1.75	0.60	15.28	0.0421
16	3	1.55	0.53	1.61	0.51	1.57	0.54	1.58	0.53	15.83	0.0297
16	4	1.38	0.51	1.39	0.52	1.39	0.52	1.39	0.52	14.64	0.0241
16	5	1.23	0.49	1.23	0.5	1.21	0.5	1.22	0.50	13.55	0.0124
16	6	1.07	0.43	1.09	0.44	1.11	0.45	1.09	0.44	14.21	0.0118

Table D 56

38 Argon (Single tracks measured using callipers)											
Laser Power (W)	Scan Speed (mm/s)	Experiment 1		Cross Section Pics		Experiment 3		Average Width (mm)	Average Depth (mm)	Track Length (mm)	Track Mass (grams)
		Width (mm)	Depth (mm)	Width (mm)	Depth (mm)	Width (mm)	Depth (mm)				
32	0.5	3.01	1.22	3.09	1.26	3.07	1.29	3.06	1.26	10.05	0.1248
32	1	2.71	0.9	2.72	0.92	2.74	0.91	2.72	0.91	20.22	0.1523
32	2	2.25	0.73	2.35	0.74	2.31	0.71	2.30	0.73	19.61	0.0927
32	3	2.14	0.71	2.1	0.76	2.16	0.76	2.13	0.74	19.27	0.0735
32	4	2.07	0.72	2.05	0.69	2.05	0.7	2.06	0.70	19.2	0.0533
32	5	1.75	0.7	1.74	0.7	1.76	0.7	1.75	0.70	12.38	0.0295
32	6	1.75	0.62	1.75	0.63	1.78	0.62	1.76	0.62	19.13	0.0408

Table D 57

38 Argon (Single tracks measured using callipers)											
Laser Power (W)	Scan Speed (mm/s)	Experiment 1		Experiment 2		Experiment 3		Average Width (mm)	Average Depth (mm)	Track Length (mm)	Track Mass (grams)
		Width (mm)	Depth (mm)	Width (mm)	Depth (mm)	Width (mm)	Depth (mm)				
58	0.5	3.96	1.69	3.99	1.63	3.91	1.61	3.95	1.64	21.14	0.4548
58	1	3.47	1.2	3.42	1.18	3.43	1.21	3.44	1.20	20.46	0.2679
58	2	3.05	0.92	3.01	0.96	2.94	0.88	3.00	0.92	20.2	0.1637
58	3	2.83	0.74	2.85	0.75	2.76	0.79	2.81	0.76	19.86	0.1207
58	4	2.71	0.69	2.72	0.69	2.71	0.67	2.71	0.68	19.7	0.1006
58	5	2.52	0.61	2.47	0.63	2.56	0.64	2.52	0.63	19.51	0.0845
58	6	2.33	0.61	2.33	0.61	2.31	0.6	2.32	0.61	19.44	0.0729
58	7	2.38	0.58	2.37	0.59	2.45	0.54	2.40	0.57	19.31	0.0717
58	8	2	0.61	2.02	0.6	2.02	0.61	2.01	0.61	18.91	0.0622

Table D 58

38 Argon (Single tracks measured using callipers)											
Laser Power (W)	Scan Speed (mm/s)	Experiment 1		Experiment 2		Experiment 3		Average Width (mm)	Average Depth (mm)	Track Length (mm)	Track Mass (grams)
		Width (mm)	Depth (mm)	Width (mm)	Depth (mm)	Width (mm)	Depth (mm)				
77	0.5	3.87	1.51	4.05	1.63	4.09	1.61	4.00	1.58	21.2	0.462
77	1	3.32	1.21	3.68	1.39	3.71	1.32	3.57	1.31	20.61	0.2951
77	2	3.03	1.39	3.31	1.42	3.35	1.25	3.23	1.35	19.82	0.2799
77	3	3.11	0.77	3.08	0.83	2.74	0.84	2.98	0.81	19.98	0.131
77	4	2.7	0.65	2.83	0.73	2.74	0.74	2.76	0.71	13.83	0.0725
77	5	2.61	0.66	2.68	0.61	2.62	0.69	2.64	0.65	19.6	0.0966
77	6	2.39	0.76	2.37	0.71	2.28	0.72	2.35	0.73	18.84	0.0998
77	7	2.35	0.55	2.39	0.51	2.42	0.65	2.39	0.57	14.24	0.0622
77	8	2.14	0.82	2.17	0.84	2.25	0.77	2.19	0.81	19.22	0.0804

Table D 59

38 Argon (Single tracks measured using callipers)											
Laser Power (W)	Scan Speed (mm/s)	Experiment 1		Experiment 2		Experiment 3		Average Width (mm)	Average Depth (mm)	Track Length (mm)	Track Mass (grams)
		Width (mm)	Depth (mm)	Width (mm)	Depth (mm)	Width (mm)	Depth (mm)				
89	0.5	4.19	1.61	4.41	1.71	4.39	1.95	4.33	1.76	21.27	0.5736
89	1	3.92	1.21	3.61	1.14	3.68	1.48	3.74	1.28	20.79	0.3465
89	2	2.98	1.69	3.14	1.81	3.45	2.08	3.19	1.86	20.1	0.3555
89	3	2.65	1.47	2.79	1.58	2.51	1.34	2.65	1.46	19.53	0.2472
89	4	2.52	0.89	2.34	1.15	2.9	1.04	2.59	1.03	19.28	0.1358
89	5	2.35	0.96	2.67	0.95	2.5	0.94	2.51	0.95	18.45	0.1285
89	6	2.45	0.93	2.45	0.88	2.34	0.92	2.41	0.91	19.15	0.1189
89	7	2.62	0.98	2.64	1.03	2.68	1	2.65	1.00	15.66	0.077

Table D 60

38 Argon (Single tracks measured using callipers)											
Laser Power (W)	Scan Speed (mm/s)	Experiment 1		Experiment 2		Experiment 3		Average Width (mm)	Average Depth (mm)	Track Length (mm)	Track Mass (grams)
		Width (mm)	Depth (mm)	Width (mm)	Depth (mm)	Width (mm)	Depth (mm)				
110	0.5	4.25	2.25	5.02	2.31	5.1	2.84	4.79	2.47	21.75	0.7917
110	1	4.18	3.38	4.35	3.52	4.67	3.17	4.40	3.36	21.02	0.6251
110	2	3.59	2.59	3.5	2.84	3.45	2.91	3.51	2.78	20	0.5668
110	3	3.19	2.67	3.12	2.71	3.4	2.47	3.24	2.62	19.54	0.4192
110	4	2.96	2.51	3.21	2.63	3.32	2.6	3.16	2.58	18.32	0.3204
110	5	2.64	2.09	2.58	2.12	2.6	2.22	2.61	2.14	4.33	0.0587
110	6	2.54	2.39	2.56	2.52	2.57	2.59	2.56	2.50	4.11	0.0487

Table D 61

38 Argon (Single tracks measured using callipers)											
Laser Power (W)	Scan Speed (mm/s)	Experiment 1		Experiment 2		Experiment 3		Average Width (mm)	Average Depth (mm)	Track Length (mm)	Track Mass (grams)
		Width (mm)	Depth (mm)	Width (mm)	Depth (mm)	Width (mm)	Depth (mm)				
125	0.5	4.22	1.97	4.67	2.11	4.84	2.53	4.58	2.20	21.95	0.7619
125	1	3.02	2.92	3.28	3.01	3.77	2.64	3.36	2.86	20.23	0.6317
125	2	3.99	1.47	4.1	1.65	4.35	1.71	4.15	1.61	21.07	0.4707
125	3	3.39	2.31	3.16	2.26	3.42	2.32	3.32	2.30	18.8	0.454
125	4	2.55	2.72	2.51	2.59	2.74	2.62	2.60	2.64	18.29	0.3583
125	5	2.77	2.33	2.68	2.43	2.68	2.45	2.71	2.40	19.15	0.2343
125	6	2.92	2.14	2.81	2.26	3	2.25	2.91	2.22	6.32	0.0671
125	7	2.23	1.72	2.2	1.71	2.18	1.72	2.20	1.72	6	0.0417

Table D 62

38 Argon (Single tracks measured using callipers)											
Laser Power (W)	Scan Speed (mm/s)	Experiment 1		Experiment 2		Experiment 3		Average Width (mm)	Average Depth (mm)	Track Length (mm)	Track Mass (grams)
		Width (mm)	Depth (mm)	Width (mm)	Depth (mm)	Width (mm)	Depth (mm)				
143	0.5	3.99	2.33	5.14	2.48	5.34	3.1	4.82	2.64	21.81	0.8399
143	1	4.12	2.11	4.89	2.05	4.42	1.74	4.48	1.97	20.87	0.5639
143	2	3.54	3.02	4.01	3.09	4.19	3.28	3.91	3.13	20.3	0.6909
143	3	3.21	2.7	3.25	2.72	3.43	2.83	3.30	2.75	5.15	0.1347
143	4	3.23	2.84	2.83	2.59	2.66	2.49	2.91	2.64	4.76	0.061
143	5	2.39	2.45	2.68	2.38	2.77	2.36	2.61	2.40	4	0.0463
143	6	2.56	2.3	2.55	2.34	2.38	2.47	2.50	2.37	3.89	0.0478
143	7	2.51	2.11	2.56	2.11	2.57	2.19	2.55	2.14	5.7	0.0648

Table D 63

38 Argon (Single tracks measured using callipers)											
Laser Power (W)	Scan Speed (mm/s)	Experiment 1		Experiment 2		Experiment 3		Average Width (mm)	Average Depth (mm)	Track Length (mm)	Track Mass (grams)
		Width (mm)	Depth (mm)	Width (mm)	Depth (mm)	Width (mm)	Depth (mm)				
162	0.5	4.79	3.95	5.37	4.12	5.62	3.57	5.26	3.88	22.06	1.1991
162	1	4.87	3.4	4.82	3.77	4.35	3.28	4.68	3.48	21.24	0.8984
162	2	3.77	3.18	4.17	3.22	4.1	3.39	4.01	3.26	20.16	0.8256
162	3	3.31	2.62	3.49	2.68	3.44	2.53	3.41	2.61	20.03	0.5356
162	4	3.14	2.59	3.07	2.56	3.09	2.51	3.10	2.55	19.2	0.4345
162	5	1.92	2.5	1.93	2.5	1.86	2.5	1.90	2.50	8.25	0.1412
162	6	2.21	2.36	2.2	2.38	2.2	2.4	2.20	2.38	6.32	0.0984

Appendix E

Powder Density Data and Particle Grain Size Measurements

E1 Powder Bed Density Data

Time (min)	Powder size fraction	Density measurements of powder														
		Experiment A (position number)					Experiment B (position number)									
		1a	2a	3a	4a	5a	1b	2b	3b	4b	5b					
0		4830.854	4742.881	4730.500	4621.040	4675.852	4772.826	4739.668	4760.320	4678.660	4752.845					
7.5		4860.885	4879.453	4844.578	4886.217	4877.192	4869.038	4877.370	4863.603	4880.359	4876.056					
15	-300 + 150	4926.725	4916.772	4929.258	4896.865	4924.193	4925.459	4918.509	4926.303	4916.631	4917.299					
30		4891.579	4888.091	4894.809	4881.114	4888.349	4889.964	4888.465	4841.041	4887.911	4888.764					
45		4893.178	4909.669	4904.876	4902.120	4881.481	4932.330	4905.201	4891.229	4909.019	4912.106					
60		4889.597	4862.063	4872.305	4806.995	4906.890	4898.243	4889.299	4892.479	4863.024	4858.460					
0		4720.349	4821.545	4675.351	4821.523	4758.237	4831.298	4819.919	4786.325	4760.300	4786.288					
7.5		4837.479	4862.888	4865.038	4855.135	4851.258	4844.369	4852.982	4883.962	4854.369	4827.006					
15		4927.076	4936.287	4897.733	4903.218	4917.405	4921.241	4936.941	4903.350	4919.014	4915.934					
30	-150 + 75	4877.433	4904.971	4940.392	4905.932	4878.413	4900.923	4889.130	4901.583	4863.322	4911.969					
45		4921.802	4926.982	4865.967	4888.227	4868.850	4895.326	4889.647	4877.675	4891.169	4877.195					
60		4857.771	4899.864	4912.007	4889.880	4884.889	4871.330	4886.170	4880.369	4888.374	4895.530					
0		4639.159	4586.214	4605.500	4583.005	4588.365	4641.988	4638.017	4726.982	4620.311	4594.262					
7.5		4739.739	4712.510	4711.829	4759.054	4717.649	4696.194	4713.247	4740.224	4712.672	4711.904					
15		4732.241	4712.407	4729.075	4732.739	4715.407	4726.324	4751.190	4730.269	4731.750	4734.872					
30	-75 + 38	4711.594	4700.495	4700.666	4679.296	4738.521	4724.058	4708.807	4669.989	4698.324	4691.385					
45		4709.978	4708.291	4681.975	4725.918	4718.981	4758.512	4709.529	4745.478	4727.792	4696.416					
60		4716.018	4699.374	4753.607	4666.086	4725.430	4720.724	4759.644	4717.587	4740.897	4697.414					
0		4588.003	4564.606	4556.254	4597.484	4581.255	4592.881	4599.674	4557.372	4598.775	4597.861					
7.5		4486.045	4547.892	4561.318	4526.085	4533.681	4546.999	4538.268	4545.121	4525.565	4525.786					
15		4419.128	4493.687	4433.767	4448.860	4426.447	4430.107	4445.110	4427.667	4449.267	4447.336					
30	-38	4512.217	4429.876	4516.957	4486.350	4514.587	4515.772	4492.234	4514.982	4486.482	4485.856					
45		4421.718	4322.703	4337.374	4360.598	4379.546	4322.214	4360.171	4372.517	4358.256	4369.384					
60		4367.366	4386.714	4259.165	4337.748	4313.266	4286.215	4327.442	4304.249	4334.743	4349.019					

Table E1: Powder bed density vs. mixing time results for experiments A and B.

Time (min)	Powder size fraction	Density measurements of powder													
		Experiment C (position number)							Experiment D (position number)						
		1c	2c	3c	4c	5c	1d	2d	3d	4d	5d				
0	-300 + 150	4731.351	4687.608	4647.291	4672.296	4643.776	4794.054	4757.062	4724.815	4640.211	4704.665				
7.5		4873.416	4880.805	4870.557	4876.810	4875.168	4862.692	4874.472	4871.981	4877.55	4872.206				
15		4922.422	4913.615	4922.552	4914.518	4917.802	4921.436	4921.08	4919.516	4913.806	4919.763				
30		4872.494	4886.366	4884.179	4877.150	4873.162	4890.588	4888.983	4885.65	4885.631	4889.22				
45		4894.126	4900.572	4897.502	4902.245	4900.929	4902.724	4898.337	4907.075	4904.232	4903.576				
60		4887.144	4859.743	4882.014	4857.395	4867.920	4880.393	4872.684	4854.192	4869.493					
0	-150 + 75	4824.001	4767.195	4830.074	4780.929	4708.066	4798.888	4765.102	4814.456	4771.588	4728.14				
7.5		4855.861	4861.856	4854.366	4852.468	4858.859	4853.163	4849.56	4849.31	4854.483	4858.753				
15		4919.782	4902.437	4921.853	4931.399	4911.215	4921.768	4916.678	4927.754	4911.487	4914.566				
30		4899.113	4898.636	4887.508	4887.914	4894.982	4897.922	4881.275	4898.395	4900.453	4914.153				
45		4895.709	4892.164	4884.799	4907.045	4895.901	4893.877	4892.512	4894.656	4889.082	4886.506				
60		4889.181	4885.851	4882.355	4883.972	4876.007	4884.966	4880.228	4890.98	4889.366	4897.99				
0	-75 + 38	4633.854	4594.474	4637.010	4602.348	4627.504	4599.987	4608.512	4615.161	4613.074	4598.238				
7.5		4723.461	4725.471	4725.482	4729.980	4727.046	4718.65	4720.643	4719.156	4727.422	4717.268				
15		4719.361	4723.076	4734.264	4734.429	4725.045	4726.075	4722.951	4728.834	4738.267	4720.478				
30		4703.002	4704.159	4707.801	4690.727	4691.342	4702.413	4712.233	4705.831	4696.822	4705.047				
45		4724.250	4720.245	4714.586	4719.517	4723.383	4701.11	4716.26	4722.794	4711.612	4708.554				
60		4714.130	4707.947	4729.931	4709.736	4708.661	4730.777	4720.43	4719.823	4713.269	4716.86				
0	-38	4570.363	4559.252	4583.764	4583.771	4574.465	4573.627	4573.414	4578.659	4586.476	4568.138				
7.5		4544.174	4540.215	4538.708	4539.456	4537.719	4513.13	4536.662	4535.702	4537.663	4525.292				
15		4436.765	4456.395	4436.107	4454.039	4446.740	4437.761	4439.585	4442.882	4445.56	4442.069				
30		4506.096	4479.916	4504.306	4480.573	4490.455	4496.067	4501.094	4495.327	4478.068	4494.503				
45		4356.830	4344.733	4365.516	4353.902	4357.938	4383.225	4358.944	4353.918	4354.443	4367.589				
60		4300.387	4329.592	4313.698	4339.403	4327.748	4348.479	4311.23	4323.478	4344.218	4332.486				

Table E2: Powder bed density vs. mixing time results for experiments C and D.

Time (min)	Particle size fraction	Density variance calculations for experiments A, B, C and D							
		Max density	Min density	Average density	Max variance (%)	Min variance %	Average variance (+/- %)		
0	-300 + 150	4794.054	4621.040	4715.43	1.64	2.00	1.82		
7.5		4886.217	4844.578	4872.52	0.28	0.57	0.43		
15		4929.258	4896.865	4919.23	0.20	0.45	0.33		
30		4894.809	4841.041	4883.68	0.23	0.87	0.55		
45		4932.330	4881.481	4902.63	0.60	0.43	0.52		
60		4906.890	4806.995	4870.82	0.74	1.31	1.02		
0	-150 + 75	4831.298	4675.351	4778.48	1.09	2.16	1.63		
7.5		4883.962	4827.006	4854.16	0.61	0.56	0.58		
15		4936.941	4897.733	4917.86	0.39	0.41	0.40		
30		4940.392	4863.322	4896.72	0.88	0.68	0.78		
45		4926.982	4865.967	4891.75	0.71	0.53	0.62		
60		4912.007	4871.330	4886.35	0.52	0.31	0.41		
0	-75 + 38	4726.982	4583.005	4617.70	2.31	0.75	1.53		
7.5		4759.054	4696.194	4722.48	0.77	0.56	0.66		
15		4751.190	4712.407	4728.45	0.48	0.34	0.41		
30		4738.521	4669.989	4702.13	0.77	0.68	0.73		
45		4758.512	4681.975	4717.26	0.87	0.75	0.81		
60		4759.644	4666.086	4718.42	0.87	1.11	0.99		
0	-38	4599.674	4556.254	4579.30	0.44	0.50	0.47		
7.5		4561.318	4513.130	4534.27	0.59	0.47	0.53		
15		4493.687	4426.447	4443.46	1.12	0.38	0.75		
30		4516.957	4429.876	4494.09	0.51	1.43	0.97		
45		4383.225	4322.214	4360.08	0.53	0.87	0.70		
60		4386.714	4259.165	4326.83	1.37	1.56	1.46		

Table E3: Powder density variance calculations using experiments A, B,C and D.

E2 Particle Grain Size Measurements

Table E4: Particle grain size measurement data (set 1)

Particle diameter and grain size measurements					
Batch	Sample				Grain size (microns)
	Particle Size (microns)				
	1	2	3	Average	
-300 + 150	274	274	273	273.7	7.2
	262	265	263	263.3	7.0
	258	258	259	258.3	6.8
	255	252	255	254.0	6.9
	238	238	238	238.0	6.8
	222	224	221	222.3	6.6
	202	201	198	200.3	6.1
	190	188	191	189.7	6.2
	176	172	177	175.0	5.9
	165	167	164	165.3	5.5
-150 + 75	128	129	130	129.0	5.3
	114	114	118	115.3	4.9
	105	106	109	106.7	4.2
	99	92	98	96.3	3.2
	82	86	85	84.3	2.4
-75 + 38	65	61	61	62.3	2.0
	59	63	57	59.7	1.5
	48	42	43	44.3	1.9
	46	48	42	45.3	1.0

Table E5: Particle grain size measurement data (set 2)

Particle diameter and grain size measurements					
Batch	Sample				Grain size (microns)
	Particle Size (microns)				
	1	2	3	Average	
-300 + 150	269	269	271	269.7	7.3
	264	264	264	264.0	7.2
	258	258	257	257.7	7.0
	224	221	226	223.7	6.7
	215	211	209	211.7	6.6
	211	209	207	209.0	6.2
	198	195	195	196.0	6.1
	174	169	160	167.7	5.7
	168	165	168	167.0	5.4
	166	166	162	164.7	5.2
	-150 + 75	141	136	134	137.0
122		125	128	125.0	5.1
115		114	114	114.3	4.8
101		101	106	102.7	4.1
72		71	69	70.7	2.9
-75 + 38	71	71	73	71.7	2.4
	52	51	55	52.7	1.9
	48	52	52	50.7	1.6
	44	44	47	45.0	1.3

Table E6: Particle grain size measurement data (set 3)

Particle diameter and grain size measurements					
Batch	Sample				Grain size (microns)
	Particle Size (microns)				
	1	2	3	Average	
-300 + 150	268	268	268	268.0	6.9
	259	259	258	258.7	7.2
	242	251	252	248.3	7
	238	231	232	233.7	7
	205	206	206	205.7	6.6
	200	201	201	200.7	6.3
	198	192	192	194.0	5.9
	160	160	161	160.3	5.6
	181	182	183	182.0	5.6
	147	148	149	148.0	4.8
-150 + 75	138	135	135	136.0	5.1
	118	120	121	119.7	5
	111	111	113	111.7	4.6
	95	96	98	96.3	3.7
	82	81	78	80.3	3.2
-75 + 38	68	68	67	67.7	2.1
	52	51	47	50.0	1.3
	47	54	54	51.7	1.1
	40	36	37	37.7	0.9